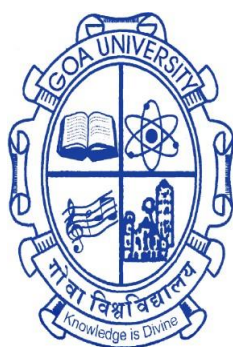


NANOPOROUS TiO₂, Ni_{1-x}O AND THEIR NANOCOMPOSITES FOR ENVIRONMENTAL AND ENERGY APPLICATIONS

A THESIS SUBMITTED IN PARTIAL FULFILLMENT FOR THE DEGREE OF

DOCTOR OF PHILOSOPHY

IN THE SCHOOL OF CHEMICAL SCIENCES
GOA UNIVERSITY



By

AMARJA PRASHANT NAIK
GOA UNIVERSITY
TALEIGAO
GOA

JUNE 2022

DECLARATION

I, Miss. Amarja Prashant Naik hereby declare that this thesis represents work which has been carried out by me and that it has not been submitted, either in part or full, to any other University or Institution for the award of any research degree.

Place: Taleigao Plateau.

Date: 01-06-2022



Miss. Amarja Prashant Naik
Research Scholar
School of Chemical Sciences
Goa University, Goa.

CERTIFICATE

I hereby certify that the above Declaration of the candidate, Miss. Amarja Prashant Naik is true and the work was carried out under my supervision.



Dr. Pranay P. Morajkar
Research Guide
School of Chemical sciences
Goa University, Goa.

ACKNOWLEDGEMENT

Ph.D. is not just a degree; it's a learning process of logically handling the ups and downs of our life. It teaches us how to see a given problem from a different angle. It helps us to face our weakness and conquer them. The research work carried out during my Ph.D. course has not been possible without the guidance, unconditional help and support of many people during this journey. I owe a BIG thanks to all of them.

*I want to express my sincere gratitude to my thesis advisor **Dr. Pranay P. Morajkar**, for allowing me to work under his inspiring mentorship. His constant encouragement, positive approach, enthusiasm, patience, constructive criticism, and helpful discussion enabled me to pursue my research interest. His brilliant, skillful supervision enriched this study greater than my expectations. This research work would not be possible without his stimulation, inspiration, and cooperation. I thank my co-guide, **Prof. Sheshanath V. Bhosale**, for being very supportive throughout my Ph.D. tenure. Special thank to my subject experts, **Prof. J. B. Fernandes** and **Prof. V. M. S. Verenkar** for their valuable advices. Your encouraging words and thoughtful, detailed feedback have been significant to me. Your knowledge and ingenuity are something I will always keep aspiring.*

*I express my sincere gratitude to our Honorable Vice-chancellor, **Prof. Harilal B. Menon**, Registrar **Prof. Vishnu Nadkarni**, and also to our former Vice-chancellor **Prof. V. Sahni** and former Registrar, **Prof. Y. V. Reddy**, Goa University for allowing me to conduct my research work in this institute and frequent support during all the needy times. I am indeed thankful to **Prof. V. M. S. Verenkar** (Dean School of Chemical Sciences), **Prof. V. S. Nadkarni** (former Dean School of Chemical Sciences), **Prof. B. R. Srinivasan** (former Head, Department of Chemistry, Goa University), for providing all the necessary facilities for my research work.*

*I take this opportunity to thank all my teachers and faculty members of the School of Chemical Sciences, **Prof. A. V. Salker**, **Prof. B. R. Srinivasan**, **Prof. S. G. Tilve**, **Prof. V. S. Nadkarni**, **Prof. R. N. Shirsat**, **Prof. S. N. Dhuri** and **Mrs. S. V. Girkar**, for their encouragement and support. I also thank **Dr. Mahesh Majik**, **Dr. Rupesh Patre** and*

Dr. Santosh Shetgaunkar for helping me with the LCMS analysis required for my research work. A special thank to **Dr. Purnakala Samant** and **Dr. Jyoti Sawant** for all their help, support and motivation during my research journey. I also thank, **Dr. Vrushali Joshi**, **Dr. P. Payaswini**, **Dr. Sandesh Bugde**, **Dr. Rohan Kunkalekar**, and **late Dr. Pankaj R. Singh** for their timely motivation, help, and constant support.

I wish to thank **Prof. Balasubramanian Viswanathan** (NCCR, IIT Madras) and **Prof. Chandrashekhar V. Rode** (NCL, Pune) for initial lab training provided at their research laboratory on various catalytic reactors. I also thank **Prof. Ravi Fernandes** (PTB, Germany) for hosting me as visiting research student at PTB Germany and for providing hands-on training with RCM.

I would also like to thank my T.Y. B.Sc. project guide **Dr. Sachin Kakodkar**, and my College teachers **Dr. Ganpat Naik**, **Dr. Manjita Porob**, **Dr. Roopa Belurkar**, **Mrs. Padmini Raikar**, **Dr. Lactina Gonsalves** for their timely encouragement.

I owe my sincere gratitude to my research group member and my best friend **Mr. Akshay V. Salkar**, for being extremely helpful and supportive throughout the ups and downs of my Ph.D. work. I also thank **Ms. Sarvesha D. Shetgaonkar**, and **Ms. Samantha da Costa**, for creating a positive and friendly working environment which provided the moral boost in tough situations. I am also thankful to all my seniors **Dr. Meera**, **Dr. Madhavi**, **Dr. Satu**, **Dr. Shambu**, **Dr. Durga**, **Dr. Johnross**, **Dr. Dattaprasad**, **Dr. Kiran**, **Dr. Savita**, **Dr. Rita**, **Dr. Mithil**, **Dr. Prajesh**, **Dr. Sagar**, **Dr. Daniel**, **Dr. Mayuri**, **Dr. Chandan**, **Dr. Sudarshana**, **Dr. Pooja**, **Dr. Sudesh**, **Dr. Celia**, **Mr. Vishnu**, **Dr. Madhavi**, **Dr. Vishal**, **Dr. Abhijeet**, **Dr. Jeyakanthan**, **Dr. Apurva**, **Dr. Prajyoti**, **Dr. Rahul**, **Dr. Pratik**, and **Dr. Kedar**, for all their help during my Ph.D. tenure.

I would also like to extend my thank to other research colleagues from the department **Ms. Lima**, **Ms. Luann**, **Mr. Ketan**, **Dr. Sarvesh**, **Mr. Shashank**, **Ms. Neha**, **Mr. Dinesh**, **Ms. Mangala**, **Ms. Seneca**, **Ms. Sonam**, **Ms. Geeta**, **Mr. Pritesh**, **Ms. Sanjali**, **Mr. Ratan**, **Mr. Dinesh**, **Mr. Kerba**, **Ms. Gayatri**, **Mr. Vishal**, **Mr. Vilas** and **Mr. Harshad** for their support.

*A special thank to my buddies, **Mr. Akshay V. Salkar, Ms. Lima Rodrigues, Dr. Sankrita Gaunkar, Dr. Rutuja Palkar, Mrs. Atiba Shaik and Mrs. Nupur Phadte,** for creating beautiful memories for life during this journey. I would also like to thank **Dr. Velu Jeyalakshmi** for all her help and support during my stay at NCCR IIT Madras. I am also thankful to all my cousins for their constant support and encouragement during my Ph.D. journey.*

*I sincerely thank the **non-teaching staff** of the School of Chemical Sciences-Goa University, the **librarian** and other teams in the library, and the **AR (PG) and staff** of Goa University for being kind and helpful. Special gratitude goes out to the funding agencies namely **DST-SERB-ECR and UGC-BSR** for providing research fellowship and infrastructure needed for my Ph.D. work. I am also grateful to **Goa University** for providing financial support through Ph.D. research studentship.*

*Last but not least, I would like to thank my family; my father, **Shri Prashant Sadanand Naik**, my mother, **Smt. Shobha Prashant Naik**, my uncle **Shri Ghanshyam Sadanand Naik**, and my brother **Mr. Amarjeet Prashant Naik** for their constant support and encouragement in every step to bring me to this present stage.*

Finally, I thank God for all the bounties and blessings he bestowed upon me and for granting me the strength and patience to complete my research.

.....Ms. Amarja Prashant Naik

*Dedicated to my parents
Shri Prashant Sadanand
Naik*

&

*Smt. Shobha Prashant
Naik*

*On their 31st Wedding
Anniversary.*

Contents

List of Abbreviations.....	i
List of Tables.....	v
List of Figures.....	xi

CHAPTER I: INTRODUCTION

1.0 Introduction to environmental impact of energy.....	01
1.1 Dyes as water pollutant.....	02
1.2 Chemistry of Amaranth dye.....	03
1.3 Toxicity and treatment of Amaranth dye polluted water.....	04
1.4 Adsorptive removal of Amaranth dye.....	05
1.5 Photocatalytic degradation of Amaranth dye.....	07
1.5.1 TiO ₂ as an n-type semiconductor photocatalyst.....	08
1.5.2 Photocatalytic degradation mechanism over TiO ₂	10
1.5.3 Ni _{1-x} O as p-type semiconductor photocatalyst.....	13
1.5.4 Ni _{1-x} O/TiO ₂ as heterojunction catalyst	17
1.6 Supercapacitors	19
1.6.1 Ni _{1-x} O, TiO ₂ and their nanocomposites for supercapacitor application.....	20
1.7 Thesis objectives	23
1.8 References.....	24

CHAPTER II: SYNTHESIS, CHARACTERIZATION AND CATALYTIC

APPLICATION OF NANOPOROUS TiO₂ CATALYST

2.1 Prologue.....	39
2.2 Chemicals used.....	39
2.3 Instrumentation	39
2.3.1 Characterization Techniques	
➤ Thermogravimetric-Differential Thermal Analysis	
➤ Infrared Spectroscopy	
➤ Powder X-ray Diffraction	

	➤ <i>Field Emission Scanning Electron Microscopy & Energy Dispersive X-ray Spectroscopy</i>	
	➤ <i>High Resolution Transmission Electron Microscopy & Selected Area Electron Diffraction Analysis</i>	
	➤ <i>UV-Diffuse Reflectance Spectroscopy</i>	
	➤ <i>X-ray Photoelectron Spectroscopy</i>	
	➤ <i>N₂ Adsorption – Desorption isotherms & Surface Area Analysis</i>	
2.3.2	Photocatalytic reactor design.....	43
2.4	Experimental: Synthesis Strategies & Procedures.....	44
2.4.1	Synthesis of TiO ₂ using urea as a fuel for sol-gel combustion synthesis.....	44
2.4.2	Synthesis of TiO ₂ using carboxylic acids as structure-directing agents.....	45
2.4.3	Synthesis of TiO ₂ using carboxylic acids and urea mixtures.....	46
2.4.4	Protocol of adsorption isotherm and kinetic experiments.....	47
2.4.5	Protocol of photocatalytic degradation studies.....	49
2.5	Results and discussion.....	50
2.5.1	Characterization of synthesized TiO ₂ catalysts.....	50
	➤ <i>Effect of Ti: Urea ratio on surface area of TiO₂</i>	
	➤ <i>Effect of number of carboxylic group on porosity and surface area of TiO₂</i>	
	➤ <i>Tuneability of TiO₂ pore structure using carboxylic acids and urea mixture as SDA</i>	
2.5.2	Adsorptive removal of Amaranth dye from water using synthesized TiO ₂ catalysts.....	69
	➤ <i>Adsorption isotherm studies</i>	
	➤ <i>Adsorption kinetic studies</i>	
2.5.3	Photocatalytic degradation of Amaranth dye using synthesized TiO ₂ catalysts.....	77
	➤ <i>Kinetic studies</i>	
	➤ <i>Catalyst regeneration</i>	
2.6	Conclusion.....	84
2.7	References.....	86

CHAPTER III: SYNTHESIS CHARACTERIZATION AND CATALYTIC APPLICATION OF NANOPOROUS Ni_{1-x}O CATALYST

3.1	Prologue	93
3.2	Chemicals used	93
3.3	Experimental: Synthesis Strategies & Procedures	93
3.3.1	Synthesis of Ni _{1-x} O from nickel coordination compound precursors....	93
	➤ [Ni(H ₂ O) ₆].(4-nba) ₂ .2H ₂ O	
	➤ [Ni(H ₂ O) ₄ (4-nba) ₂].2H ₂ O	
	➤ [Ni(H ₂ O) ₂ (Im) ₂ (4-nba) ₂]	
	➤ [Ni(Im) ₆].(4-nba) ₂ .2H ₂ O	
3.3.2	Synthesis of Ni _{1-x} O from Ni(OH) ₂ -urea mixture.....	97
3.3.3	Protocol of Amaranth dye adsorption isotherm and kinetic studies....	97
3.4	Results and discussion	98
3.4.1	Characterization of synthesized Ni_{1-x}O catalysts	98
	➤ Effect of <i>p</i> -nitrobenzoate ligation with Ni ²⁺ on properties of Ni _{1-x} O	
	➤ Effect of imidazole ligation with Ni ²⁺ on properties of Ni _{1-x} O	
	➤ Effect of urea as structure directing agent on properties of Ni _{1-x} O	
	➤ Effect of structure directing agent on non-stoichiometry of Ni _{1-x} O	
3.4.2	Adsorptive removal of Amaranth dye from water using Ni_{1-x}O catalysts	116
	➤ Adsorption isotherm studies	
	➤ Adsorption kinetic studies	
3.4.3	Photocatalytic degradation of Amaranth dye using Ni_{1-x}O catalysts	121
	➤ Kinetic studies	
	➤ Catalyst regeneration	
3.5	Conclusion	125
3.6	References	127

CHAPTER IV: SYNTHESIS CHARACTERIZATION AND CATALYTIC APPLICATION OF NANOPOROUS Ni_{1-x}O/TiO₂ NANOCOMPOSITES

4.1	Prologue	131
4.2	Experimental: Synthesis Strategies & Procedures	131

4.2.1	Synthesis of Ni _{1-x} O/TiO ₂ nanocomposite.....	131
4.2.2	Protocol of adsorption isotherm and kinetic experiments.....	132
4.2.3	Protocol of photocatalytic degradation studies.....	133
4.2.4	Protocol of LCMS identification of Amaranth dye degradation products.....	133
4.3	Results and discussion.....	134
4.3.1	Characterization of synthesized Ni_{1-x}O/TiO₂ catalysts.....	134
	➤ <i>Effect of urea, 1,2,3,4-butanetetracarboxylic acid and nitrobenzoate hybrid gels on Ni_{1-x}O/TiO₂ catalyst.</i>	
	➤ <i>Non stoichiometric nature of NiO_{1-x}O/TiO₂ nanocomposites</i>	
4.3.2	Adsorptive removal of Amaranth dye from water using Ni_{1-x}O/TiO₂ catalysts.....	146
	➤ <i>Adsorption isotherm studies</i>	
	➤ <i>Adsorption kinetic studies</i>	
4.3.3	Photocatalytic degradation of Amaranth dye using Ni_{1-x}O/TiO₂ catalysts.....	150
	➤ <i>Kinetic studies</i>	
	➤ <i>Free radical Scavenging studies</i>	
	➤ <i>Catalyst regeneration</i>	
	➤ <i>Identification of Amaranth degradation products</i>	
	➤ <i>Plausible degradation mechanism</i>	
4.4	Conclusion.....	162
4.5	References.....	163

CHAPTER V: SUPERCAPACITOR APPLICATIONS OF Ni_{1-x}O, TiO₂ AND Ni_{1-x}O/TiO₂ NANOCOMPOSITES

5.1	Prologue	167
5.2	Chemicals used.....	167
5.3	Experimental: Procedures.....	167
5.4	Results and discussion.....	167
5.4.1	Effect of ligation on supercapacitor behavior of Ni _{1-x} O.....	167
	➤ <i>Cyclic voltammetry</i>	
	➤ <i>Galvanostatic charge discharge study</i>	

➤ <i>Cyclic stability study</i>	
5.4.2 Supercapacitor performance of TiO₂ catalysts	174
➤ <i>Cyclic voltammetry</i>	
➤ <i>Galvanostatic charge discharge study</i>	
➤ <i>Cyclic stability study</i>	
5.4.3 Supercapacitor performance of Ni_{1-x}O/TiO₂ nanocomposites	178
➤ <i>Cyclic voltammetry</i>	
➤ <i>Galvanostatic charge discharge study</i>	
➤ <i>Cyclic stability study</i>	
5.5 Conclusion	185
5.6 References	187
CHAPTER VI: CONCLUSION OF THE THESIS	191
Appendix I	197
Appendix II	203
Appendix III	207

List of abbreviations

AC	Activated Carbon
CV	Cyclic Voltammetry
DEG	Degussa P-25
EDLC	Electric Double Layer Capacitor
EDS	Energy Dispersive X-ray Spectroscopy
GCD	Galvanostatic Charge-Discharge
HRTEM	High Resolution Transmission Electron Microscopy
IR	Infrared Spectroscopy
JCPDS	Joint Committee on Powder Diffraction Standards
MPMVL	Medium Pressure Mercury-Vapour Lamp
MWCNT	Multi-Walled Carbon Nanotube
4-nba	para-Nitrobenzoate
4-nbaH	para-Nitrobenzoic acid
NU	Ni _{1-x} O synthesized using Urea
N1	Ni _{1-x} O synthesized using Hexaaquanickel(II) bis(p-nitrobenzoate) dihydrate
N2	Ni _{1-x} O synthesized using Tetra-aquobis(para-nitrobenzoato)nickel(II) dihydrate
N3	Ni _{1-x} O synthesized using Diaquabis(imidazole-κN)bis(nitrobenzoate-κO)nickel(II)
N4	Ni _{1-x} O synthesized using Hexakis(imidazole)nickel(II) bis(4-nitrobenzoate) dehydrate
NT	Ni _{1-x} O/TiO ₂ composite
1NT	1% Ni _{1-x} O/TiO ₂ composite
3NT	3% Ni _{1-x} O/TiO ₂ composite
5NT	5% Ni _{1-x} O/TiO ₂ composite
10 NT	10% Ni _{1-x} O/TiO ₂ composite
20NT	20% Ni _{1-x} O/TiO ₂ composite
50NT	50% Ni _{1-x} O/TiO ₂ composite
PN	Pristine Ni _{1-x} O
PT	Pristine TiO ₂
PC	Pseudocapacitor

PXRD	Powder X-ray Diffraction
q _e	Adsorption capacity at equilibrium
R-P	Redlich-Peterson
rGO	Reduced Graphene Oxide
SEM	Scanning Electron Microscopy
SAED	Selected Area Electron Diffraction
SDA	Structure Directing Agent
TG-DTA	Thermogravimetric-Differential Thermal Analysis
TU	TiO ₂ synthesized using Urea
TOA	TiO ₂ synthesized using Oxalic acid
TTC	TiO ₂ synthesized using Tricarballic acid
TBTC	TiO ₂ synthesized using Butanetetracarboxylic acid
TOAU	TiO ₂ synthesized using Oxalic acid and Urea
TTCU	TiO ₂ synthesized using Tricarballic acid and Urea
TBTCU	TiO ₂ synthesized using Butanetetracarboxylic acid and Urea
UV-DRS	Ultra-Violet Diffuse Reflectance Spectroscopy
XPS	X-ray Photoelectron Spectroscopy

List of Tables

CHAPTER I: INTRODUCTION

1.1	Botanical classification of Amaranth dye.....	04
1.2	Crystal parameters and properties of anatase, rutile and brookite TiO ₂	09
1.3	Literature overview on TiO ₂ & its nanocomposites for photocatalytic dye degradation.....	12
1.4	Literature report on Ni _{1-x} O based catalysts and their photocatalytic performance.....	16
1.5	Literature reports on supercapacitor performance of Ni _{1-x} O, TiO ₂ and their composites.....	21

CHAPTER II: SYNTHESIS, CHARACTERIZATION AND CATALYTIC APPLICATION OF NANOPOROUS TiO₂ CATALYST.

2.1	Mathematical equations of different adsorption isotherm models.....	48
2.2	Mathematical equations of different adsorption kinetic models.....	49
2.3	Surface area, average pore size, and average pore volume of pristine TiO ₂ and TiO ₂ with urea at different ratio.....	54
2.4	Band gap, surface area, pore size, and pore volume of all the synthesized TiO ₂ catalysts.....	62
2.5	Comparative analysis of surface properties of all the synthesized TiO ₂ catalysts.....	66
2.6	Adsorption isotherm parameters obtained using different adsorption isotherm models.....	73
2.7	Adsorption kinetic parameters obtained using different adsorption kinetic models.....	76
2.8	Correlation between material properties with that of photocatalytic performance of the synthesized catalysts.....	78

2.9	Comparative analysis of the Amaranth degradation efficiency, corresponding photocatalytic rate constant and material properties of all the synthesized catalysts	82
2.10	Comparative analysis of Amaranth dye degradation efficiency of TBTCU with that of literature reported catalysts.....	83

CHAPTER III: SYNTHESIS, CHARACTERIZATION AND CATALYTIC APPLICATION OF NANOPOROUS Ni_{1-x}O CATALYSTS

3.1	The percentage of species obtained from the XPS peak area integration of narrow scan spectra of Ni _{1-x} O catalysts.....	115
3.2	Parameters obtained from different adsorption isotherm models of Amaranth adsorption over Ni _{1-x} O catalysts.....	117
3.3	Parameters obtained from adsorption kinetic analysis.....	120
3.4	Comparative analysis of the Amaranth degradation efficiency, photo catalytic rate constant, bandgap energies and surface area of synthesized N1, N2, N3, N4, PN and NU catalyst.....	123
3.5	Comparison of amaranth degradation efficiency of Ni _{1-x} O with respect to literature reported catalysts.....	124

CHAPTER IV: SYNTHESIS, CHARACTERIZATION AND CATALYTIC APPLICATION OF NANOPOROUS Ni_{1-x}O/TiO₂ NANOCOMPOSITES

4.1	Optimized eluent gradient conditions for HPLC separation.....	133
4.2	Surface area, pore size and pore volume of Ni _{1-x} O/TiO ₂ nanocomposites.....	138
4.3	The percentage of species obtained from the XPS peak area integration of narrow scan spectra of Ni _{1-x} O catalyst.....	145
4.4	Parameters obtained from different adsorption isotherm study.....	148
4.5	Parameters obtained from adsorption kinetic analysis.....	151

4.6	Comparative analysis of Amaranth dye degradation efficiency of TBTCU, $Ni_{1-x}O$ and $Ni_{1-x}O/TiO_2$ with that of literature reported catalysts.....	154
-----	---	-----

CHAPTER V: SUPERCAPACITOR APPLICATIONS OF $Ni_{1-x}O$, TiO_2 AND $Ni_{1-x}O/TiO_2$ NANOCOMPOSITES

5.1	Comparative surface area and specific capacitance values of N1, N2, N3, N4, PN and NU.....	170
5.2	Comparative analysis of specific capacitance and cyclic performance of synthesized mesoporous $Ni_{1-x}O$ nanosponge with that of literature reported $Ni_{1-x}O$ catalyst.....	172
5.3	Comparative analysis of BET surface area, specific capacitance and Ni^{3+}/Ni^{2+} ratio of a synthesized and physically mixed $Ni_{1-x}O/TiO_2$ nanocomposites.....	184

List of Figures

CHAPTER I: INTRODUCTION

1.1	(a) Image of the Amaranth plant, (b) Amaranth dye powder and c) Structure of Amaranth dye.....	03
1.2	The crystal structure of rutile, brookite and anatase TiO ₂	09
1.3	Crystal structure of Ni _{1-x} O.....	14
1.4	p-n junction & charge carrier separation in Ni _{1-x} O/TiO ₂ catalyst.....	17

CHAPTER II: SYNTHESIS, CHARACTERIZATION AND CATALYTIC APPLICATION OF NANOPOROUS TiO₂ CATALYST.

2.1	Photocatalytic reactor system.....	44
2.2	Scheme of TiO ₂ synthesis using urea as structure directing agent.....	45
2.3	Synthesis of TiO ₂ using carboxylic acids (OA, TC and BTC) as SDA.....	46
2.4	Synthesis of TiO ₂ using carboxylic acid and urea mixture as SDA.....	47
2.5	Schematic representation of photocatalytic Amaranth dye degradation Experiment.....	49
2.6	(a, b) TG-DTA and (c, d) IR spectra of titanium precursor gel without and with urea as SDA.....	51
2.7	N ₂ adsorption-desorption plots for (a) Pristine TiO ₂ , (b) TU2, (c) TU4, (d) TU6, (e) TU8, (f) TU10, (g) TU12 and h) variation in surface area as a function of Ti: urea ratio.....	53
2.8	(a) XRD and (b) UV- DRS of PT and TU8.....	54
2.9	SEM and elemental characterization of Pristine TiO ₂ (PT) and TiO ₂ (TU8) synthesized using urea directing agent.....	56
2.10	(a) Low resolution TEM, (b) Particle size distribution (c) HRTEM and (d) SAED analysis of PT and TU8.....	56
2.11	(a-c) TG-DTA and (d, e) IR analysis of as synthesized hybrid gel precursors and the post calcined TiO ₂ labelled as TOA, TTC and TBTC respectively.....	58
2.12	(a) XRD and (b) UV-DRS of TOA, TTC and TBTC.....	59

2.13	Measured BET surface area of TOA, TTC and TBTC.....	60
2.14	FESEM of TiO ₂ obtained after calcination of titanium hydroxide gel modified with different carboxylic acid.....	61
2.15	(a, e and i) Low resolution TEM micrographs, (b, f and j) histogram of particle size distribution (c, g and k) HRTEM micrographs and (d, h and l) SAED pattern of TiO ₂ synthesized using carboxylic acids.....	61
2.16	TG-DTA analysis of titanium hydroxide gel with (a) oxalic acid & urea (b) tricarballic acid & urea (c) 1,2,3,4 butanetetracarboxylic acid & urea. (d & e) IR analysis of all precursors and their corresponding calcined TiO ₂ : TOAU, TTCU and TBTCU.....	64
2.17	(a) XRD (b) UV-DRS of TOAU, TTCU and TBTCU.....	65
2.18	N ₂ adsorption-desorption isotherms and pore size distribution (as inset) of TOAU, TTCU and TBTCU.....	66
2.19	FESEM micrographs of the TiO ₂ obtained after calcination of titanium hydroxide gel modified with different carboxylic acid and urea mixture.....	67
2.20	(a, e and i) Low resolution TEM micrographs, (b, f and j) histogram of particle size distribution (c, g and k) HRTEM micrographs and (d, h and l) SAED of TiO ₂ synthesized using carboxylic acids and urea.....	68
2.21	(a-c) Amaranth dye adsorption isotherms for DEG, PT and TU8.....	71
2.22	(a-f) Amaranth dye adsorption isotherms for TOA, TTC, TBTC, TOAU, TTCU and TBTCU.....	72
2.23	(a-d) Amaranth dye adsorption kinetic profiles over all the synthesized TiO ₂ catalysts.....	75
2.24	(a) & (b): Kinetic profile for photocatalytic degradation of Amaranth dye using TU8 catalyst in comparison with PT and DEG.....	78
2.25	Effect of (a) catalyst dosage (b) initial Amaranth dye concentration and (c) pH of the dye solution.....	79
2.26	(a) Kinetic profiles and (b) logarithmic plots for photocatalytic degradation of Amaranth dye using TiO ₂ photocatalysts.....	82
2.27	Catalyst regeneration study of Degussa P-25, PT, TU8, TBTC and TBTCU.....	84

**CHAPTER III: SYNTHESIS, CHARACTERIZATION AND
CATALYTIC APPLICATION OF NANOPOROUS Ni_{1-x}O CATALYST**

3.1	Structure of (I) [Ni(H ₂ O) ₆](4-nba) ₂ .2H ₂ O and (II) [Ni(H ₂ O) ₄ (4-nba) ₂].2H ₂ O.....	94
3.2	Schematic representation of synthesis of Ni _{1-x} O from compounds a) I and b) II...	95
3.3	Structures of (III) [Ni(Im) ₂ (4-nba) ₂ (H ₂ O) ₄].2H ₂ O and (IV) [Ni(Im) ₆](4-nba) ₂ .2H ₂ O.....	95
3.4	Synthesis of Ni _{1-x} O from compounds a) III and b) IV.....	96
3.5	Schematic of Ni _{1-x} O synthesis by precipitation method.....	97
3.6	(a) TG-DTA analysis and (b) IR analysis of compounds I and II	98
3.7	(a) XRD and (b) UV-DRS spectra of N1 and N2.....	99
3.8	Morphological analysis of N1 and N2 using FESEM.....	100
3.9	(a, b) HRTEM analysis, (c, d) particle size distribution and (e, f) SAED analysis of N1 and N2 respectively.....	101
3.10	N ₂ adsorption-desorption and the pore size distribution in N1 and N2.....	101
3.11	(a) TG-DTA analysis and (b) IR spectra of III & IV respectively.....	103
3.12	(a) XRD and (b) UV-DRS of N3 & N4.....	104
3.13	FESEM analysis of N3 and N4.....	105
3.14	(a, b) HRTEM analysis, (c, d) particle size distribution, (e, f) SAED of N3 and N4 respectively.....	106
3.15	BET surface area analysis of (a) N3 and (b) N4.....	107
3.16	(a, b) TG-DTA and (c) IR analysis of Ni(OH) ₂ , Ni(OH) ₂ with urea and Ni _{1-x} O after calcination at 400 °C.....	109
3.17	(a) XRD and (b) UV-DRS spectra of PN and NU.....	110
3.18	Morphological analysis of PN and NU.....	111
3.19	(a-b) Low resolution TEM, (c-d) Particle size distribution, (e-f) SAED analysis of PN and NU respectively.....	111
3.20	N ₂ adsorption-desorption analysis of a) PN and b) NU respectively.....	112
3.21	XPS spectra of N4 (a-c), PN (d-f) and NU (g-i).....	113
3.22	XPS spectra of N4 (j-l), PN (m-o) and NU (p-r).....	114
3.23	Amaranth dye adsorption isotherms profiles over Ni _{1-x} O (N1, N2, N3, N4, PN and NU) catalysts.....	118

3.24	Amaranth adsorption kinetics on Ni _{1-x} O; a) Pseudo first order, b) Pseudo second order, c) Elovich model and d) Intra particle diffusion model.....	119
3.25	(a) Kinetic profiles, (b) Linear fit $\ln[\text{Amaranth}]_o/[\text{Amaranth}]_t$ as a function of time for Amaranth dye degradation using Ni _{1-x} O catalyst.....	122
3.26	Catalyst regeneration study of the synthesized Ni _{1-x} O catalysts.....	125

CHAPTER IV: SYNTHESIS, CHARACTERIZATION AND CATALYTIC APPLICATION OF NANOPOROUS Ni_{1-x}O/TiO₂ NANOCOMPOSITES

4.1	Schematic representation of Ni _{1-x} O/TiO ₂ catalyst synthesis protocol using reflux assisted sol-gel method.....	132
4.2	(a-e) TG-DTA analysis of titanium hydroxide hybrid gel with butanetetracarboxylic acid, urea and [Ni(H ₂ O) ₄ (4-nba) ₂].2H ₂ O.....	135
4.3	(a) IR analysis (b) XRD and (c) UV-DRS analysis of Ni _{1-x} O/TiO ₂ nanocomposites.....	136
4.4	(a-e) N ₂ adsorption-desorption analysis of synthesized Ni _{1-x} O/TiO ₂ nanocomposites.....	137
4.5	SEM analyses of synthesized Ni _{1-x} O/TiO ₂ nanocomposites.....	138
4.6	(a) Low resolution TEM, (b) particle size distribution, (c) HRTEM and (d) SAED analysis of 1NT.....	139
4.7	(a) Low resolution TEM, (b) particle size distribution, (c) HRTEM and (d) SAED analysis of 3NT.....	140
4.8	(a) Low resolution TEM, (b) particle size distribution, (c) HRTEM and (d) SAED analysis of 20NT.....	140
4.9	(a) Low resolution TEM, (b) particle size distribution, (c) HRTEM and (d) SAED analysis of 50NT.....	141
4.10	(a-f) Full scan spectra Ni _{1-x} O/TiO ₂ nanocomposites.....	142
4.11	XPS spectra of 1NT (a-c), 3NT (d-f) and 5NT (g-i).....	143
4.12	XPS spectra of 10NT (j-l), 20NT (m-o) and 50NT (p-r).....	144
4.13	(a-f) Adsorption isotherm study of all the synthesized Ni _{1-x} O/TiO ₂ nanocomposites.....	147
4.14	(a-d) Adsorption kinetic study of synthesized Ni _{1-x} O/TiO ₂ nanocomposites.....	149

4.15	(a-b) Photocatalytic degradation study of synthesized Ni _{1-x} O/TiO ₂ nanocomposites.....	152
4.16	(a) Comparative free radical scavenging study of TiO ₂ , Ni _{1-x} O and Ni _{1-x} O /TiO ₂ nanocomposites and (b) Schematic of photocatalytic degradation mechanism using free radical species.....	153
4.17	Liquid chromatogram of the Amaranth dye.....	156
4.18	Ultra-performance chromatogram of the Amaranth dye.....	157
4.19	Impurity peak corresponding to m/z value 144.....	157
4.20	Impurity peak corresponding to m/z value 301.....	157
4.21	Sodium 4-aminobenzenesulfonate corresponding to m/z value 172.....	158
4.22	5, 6, 7 Trihydroxynaphthalene-2-sulfonic acid corresponding to m/z value 274...	158
4.23	2-Hydroxymalonic acid corresponding to m/z value 143.....	159
4.24	Plausible mechanism for the photocatalytic degradation of Amaranth dye.....	161

CHAPTER V: SUPERCAPACITOR APPLICATIONS OF Ni_{1-x}O, TiO₂ AND Ni_{1-x}O/TiO₂ NANOCOMPOSITES

5.1	Cyclic voltammogram of the Ni _{1-x} O samples N1, N2, N3, N4, PN and NU.....	169
5.2	Galvanostatic charge discharge study of the Ni _{1-x} O samples N1, N2, N3, N4 PN and NU.....	171
5.3	Cyclic stability study of the Ni _{1-x} O samples N1, N2, N3, N4, PN and NU.....	173
5.4	Cyclic voltammogram of the TiO ₂ samples DEG, TU and TBCTU.....	175
5.5	Galvanostatic charge discharge study of the TiO ₂ samples DEG, TU and TBCTU.....	176
5.6	Cyclic stability study of TiO ₂ samples, DEG, TU and TBTCU.....	177
5.7	Cyclic voltammogram of the synthesized Ni _{1-x} O/TiO ₂ nanocomposites.....	180
5.8	Galvanostatic charge discharge study of all synthesized Ni _{1-x} O/TiO ₂ nanocomposites.....	181
5.9	Cyclic stability study of all synthesized Ni _{1-x} O /TiO ₂ nanocomposites.....	183

5.10	(a) Comparative CV and (b) GCD plots of 1-50 % Ni _{1-x} O/TiO ₂ nanocomposites at 5 mV.s ⁻¹ and 1 A.g ⁻¹	184
5.11	(a) Comparative cyclic voltammetry at 5 mV.s ⁻¹ (b) Galvanostatic charge discharge at 1 A.g ⁻¹	185
5.12	Specific capacitance of 1-50 % Ni _{1-x} O/TiO ₂ nanocomposites.....	185

CHAPTER I:
INTRODUCTION

1.0 Introduction to environmental impact of energy

Today's world stands divided into two classes: the developed and the developing! Each of which has its own share of challenges to address. In developed countries, the basic necessities of food, clothing and shelter are largely addressed by rapid economic growth through industrialization. However, a great share of this progress has been made by satisfying the energy needs for this rapid industrialization through unsustainable and polluting sources of energy such as fossil fuels. While the energy needs keep on increasing in such countries, this also results in a significant rise in air pollution and climate change which threatens the very existence of life on earth. Therefore, a great deal of focus has now shifted towards the utilization of sustainable, clean and green energy sources such as wind and solar energy generation technologies. The majority of the research community has now centered its efforts towards developing energy efficient, smart nanomaterials which have the capability to harness and store these energies in the form of chemical/electronic energy [1]. Energy storage in itself is a challenge worth paying attention to. Batteries and capacitors have emerged as the potential solutions to these problems but are limited by the energy storage density of the available materials for large scale production and application.

While batteries have several advantages, its low cycling stability and inability to deliver high power performance results in its limited utility in less energy intensive applications. On the contrary, capacitors have the ability to charge and discharge at a rapid rate but are limited in the energy density that they can store [2]. Therefore, in recent times, development of supercapacitors which can overcome these limitations of traditional capacitors as well as batteries is being extensively researched especially in the developed countries [3]. In section 1.6, more details about the working principle of a supercapacitor and the advancements in metal oxide nano systems as electrodes for supercapacitor devices is presented. While the research on improving the energy density of supercapacitor grows in the laboratory, the use of fossil fuels for energy still continues in the developed nations with stricter norms on pollutant emission and mitigations.

With the increasing stringent norms on pollutant emission, environmental regulations and its associated economic burden, several of the heavily polluting industries from the developed

nations have largely shifted their production units to the developing countries. These developing countries wherein the basic necessities of life are still a major challenge, readily welcome such industries as it brings with it opportunities of jobs and with it the hopes of a better quality of life merely through the economic perspective. However, with the rapid rise in industrialization with not so stringent norms and regulations on environmental protection, the fundamental elements of life such as air, water and earth get extensively polluted making the survival of life itself a major challenge. Among the several challenges faced by the developing world today, one of the most important concern is the availability and affordability of clean drinking water. Water is one such natural resource that has been extensively polluted by the uncontrolled and untreated discharge of industrial organic/inorganic waste into the natural water bodies. This has resulted in water borne diseases affecting thousands of lives especially the children [4].

There are numerous ways by which water pollution is caused. Some of these are oil spills, improper sewage disposal, radioactive waste discharge, fertilizer run-off, rapid urban development and chemical waste dumping [5]. The most common industrially discharged chemical pollutants are, pesticides, polyaromatic hydrocarbons, pharmaceutical drugs and dyes [6]. Among these pollutants, dyes and pigments are the major water pollutants as they are largely being discharged untreated into water bodies by the food, cosmetic and clothing industry [7]. The next section highlights some of the intricate details of pollution caused by azo dyes, in particular the Amaranth dye and its associated toxicological effects.

1.1 Dyes as water pollutant

Dyes are excessively used in the dyeing process in inks, paints, varnishes, rubbers, drugs, cosmetics, food, paper, textile, leather, and plastic industries [8]. They are used to impart color to the food which makes the product appealing to the customer. As per the recent financial reports the annual global production of the dye is approximately 700,000 tons manufactured worldwide and the market share of the dye industry appears to be skyrocketing each year. Among several dyes, the azo dyes are one of the largest classes of dyes which are used in industries. These organic dyes have an azo ($N = N$) group along with other chromophores which help them in harvesting photon energy from the visible region of the solar spectrum and

re-emit the complimentary colors [8,9]. During azo dye production process, approximately 1-2 % of it is lost and at least 10-15 % of it gets discarded as industrial effluent during dye application processes [10]. The discharge of the dye into the natural water bodies leads to serious threat to the aquatic life especially the phytoplanktons. Thus, through the food chain these dyes find an entry into the living systems. There is direct as well as indirect effect of the discharge of dye into the aquatic system. The direct effects include reduced dissolved oxygen levels, minimization of sunlight penetration into water which inhibits photosynthesis and finally the bioaccumulation effect. On the other hand, the indirect effects caused by dye effluents are more severe which include death of aquatic organisms, genotoxicity and microtoxicity imposed by colored allergens, suppression of human immune system, allergic reactions, hyperactivity in kids, cancer in humans, etc. [11]. The organic azo dyes have aromatic centers in their molecular structures, and their metabolic and degradation products like aromatic amines (anilines), benzidines and benzene sulphonic acids are well-established as carcinogens and mutagens which induce subsequent toxicological effects on cellular life [12]. Among various azo dyes, Amaranth dye is one such anionic dye which is widely used in food, textile and cosmetic industries.

1.2 Chemistry of Amaranth dye

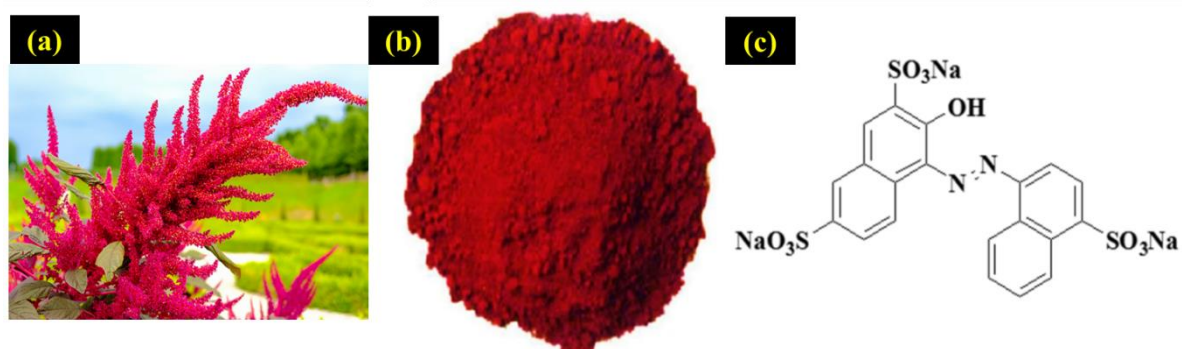


Figure 1.1: a) Image of the Amaranth plant, b) Amaranth dye powder and c) Structure of Amaranth dye [12]

Amaranth dye is commonly termed as Acid red 27 and Food Red 9, while the accepted IUPAC name is Trisodium (4E)-3-oxo-4-[(4-sulfonato-1-naphthyl)hydrazono]naphthalene-2,7-disulfonate. The presence of extended conjugation and the azo group in its structure allows absorption in the visible region with a λ_{\max} at 520 nm. In olden times, Amaranth dye was

extracted from the ornamental *Amaranthus* plant species (as shown in Figure 1.1 a). Its botanical classification is given in the Table 1.1. However, in recent times it is commercially synthesized as a trisodium salt with higher solubility in water and improved dyeing efficiency for fabrics, paper, leather etc. Amaranth dye is a widely used food colorant in several countries, United States of America (USA) being the major consumer. However, its untreated waste discharge caused severe water pollution and later it was suspected to be a carcinogen in the USA [13].

Kingdom	Plantae
Clade	Angiosperm
Family	Amaranthaceous
Genus	<i>Amaranthus</i>

Table 1.1: Botanical Classification of Amaranth dye

1.3 Toxicity and treatment of Amaranth dye polluted water

In the early 1971, the Soviet Union reported for the first time the carcinogenic effects of Amaranth dye [13,14]. Since then many research groups have evaluated the toxicity of Amaranth dye. For instance in 2001 Tsuda et al. [15] conducted genotoxicity study on a group of pregnant mice with a daily dose of $2000 \text{ mg.kg}^{-1}.\text{day}^{-1}$. The samples were collected from various organs such as kidney, colon, embryo, urinary bladder, liver etc. and the DNA damages were measured using a comet assay. The positive results confirming cellular damages were found after Amaranth administration. The $10 \text{ mg.kg}^{-1}.\text{day}^{-1}$ dose of Amaranth was reported to cause DNA damages in the male mice. Further, Clode et al.[16] carried out another study wherein Amaranth was incorporated into the food diet and subsequently in utero for long-term evaluation on a group of 90 (control) and 50 (treated) rats with doses from 0 to $250 \text{ mg.kg}^{-1}.\text{day}^{-1}$ but no carcinogenic effects were observed in this study. However, renal calcification and pelvic epithelial hyperplasia with degenerative changes were observed in female rats after 18 months from exposure to Amaranth dye. Further, the metabolites of Amaranth dye, such as sodium naphthionate and R-amino salts, were injected into Osborne Mendel pregnant female rats at doses of $15\text{-}200 \text{ mg.kg}^{-1}.\text{day}^{-1}$ by Collins et al.[17]. An increase in fetuses with sternebra abnormalities were observed at $100 \text{ mg.kg}^{-1}.\text{day}^{-1}$ dose level of sodium naphthionate.

Similar observations have been reported in the case of R-amino salts with higher dose of 200 mg.kg⁻¹.day⁻¹. DNA interaction and cytogenic in vitro evaluation studies using Amaranth dye (0.02- 8 mM) were conducted by Mpountoukas et al.[11] in human peripheral blood cells and they found high toxic potential of Amaranth dye to human lymphocytes. Mutagenic and genotoxic investigation of Amaranth was also conducted by Das et al. [18] using Ames mutagenicity assay and bone marrow of the mouse (in vivo). They concluded that Amaranth doses from 50 to 200 mg.kg⁻¹ body weight do not show any mutagenic or genotoxic effects. Other indirect effects such as allergic and asthmatic issues of Amaranth when given in conjunction with aspirin drug in certain patients have also been reported. The European Food Safety Authority in 2010 proposed ADI of 0.15 mg.kg⁻¹.bw⁻¹.day⁻¹.

Although there is disagreement in several studies about the carcinogenic and genotoxicity effects of Amaranth dye, it is well agreed that the reduction of azo group of Amaranth into free sulfonated aromatic amines, cause both carcinogenic, and mutagenic effects on living systems. This led to a complete ban on the use of Amaranth dye as food additive in the United States. However, in developing countries it is still being used extensively. Therefore, the treatment of water polluted with Amaranth dye is extremely essential.

Till date, several efforts have been made towards the use of conventional and biological treatment methods such as flocculation-coagulation, separation using membrane filters or precipitation, enzyme/microbial degradation etc. for treating waters contaminated with Amaranth dye. Since Amaranth dye has a high solubility in water, its removal from water streams by chemical/physical methods such as coagulation and froth floatation becomes extremely difficult. Adsorptive separation of Amaranth dye has been one of the widely employed technique for the effective removal of the dye from wastewater. An overview of these adsorption process is presented in the next section.

1.4 Adsorptive removal of Amaranth dye.

Adsorption is one of the simplest and effective method for removal of dye from polluted water because of its simplicity and cost-effectiveness. Adsorption is defined as the affinity of the adsorbate molecules for accumulation on the surface of the adsorbent, leading to higher concentration of adsorbate on the surface. A typical adsorption mechanism takes place in three

different stages. At first, the diffusion of the adsorbate from the bulk of the solvent to the surface of adsorbent occurs under the influence of the intermolecular forces between the adsorbent and the adsorbate. At second stage, the migration of the adsorbate into the pores of the adsorbent is evident. Finally, the monolayer or multilayer formation of the adsorbate on the adsorbent surface takes place. There are several factors which affect the rate of the adsorption such as, the surface area of the adsorbent, pH of the solution, initial concentration of the dye and the temperature of the solution. To understand the equilibrium relation between the adsorbate and the adsorbent, various adsorption isotherm models are studied such as Langmuir, Freundlich, Sip, Temkin, Redlich-Peterson (R-P), Toth, Dubinin-Radushkevich isotherm models etc.[19] Moreover, the kinetics of adsorption phenomenon is well described by different adsorption kinetic models such as pseudo-first-order, pseudo-second-order, Elovich and intraparticle diffusion model which are described in details in Chapter 2, section 2.5.2 of this thesis.

For effective Amaranth dye removal from the water, researchers have tried different adsorbents which includes activated carbon derived from *Trapa Natan* seeds [20], deoiled soya [21], peanut hull [22], pineapple peelings, coconut shells, [23] Ahmad et al. [24] used alumina reinforced polystyrene for removal and recovery of Amaranth dye from the waste streams. Various high surface area adsorbents such as $\text{Fe}_3\text{O}_4/\text{MgO}$ nanoparticles [25], Mg/Al double layered hydroxides [26] and clay based adsorbents such as Smectite clay etc. were also used for adsorption of Amaranth dye. These materials showed excellent adsorptive removal of Amaranth dye with high adsorption capacity up to 86.29 mg.g^{-1} . However, this method generates secondary Amaranth waste which needs post treatment of the adsorbed dye on the adsorbent. This becomes one of the serious drawback which makes the adsorptive separation technology less sustainable [27]. There are various other methods adopted for removal of Amaranth dye from wastewater such as electrochemical, sonocatalytic degradation of Amaranth dye. For instance, Song et al. [28] used La^{3+} doped TiO_2 for sonocatalytic degradation of Amaranth dye and obtained 100 % degradation of Amaranth in 90 minutes. Alwash et al. [29] used zeolite encapsulated with Fe- TiO_2 for ultrasound assisted degradation of Amaranth dye and obtained 97.5 % degradation of Amaranth in 120 minutes. However, the need of sophisticated instrumental techniques increase the cost of the overall process. Thus, in

recent times advanced photocatalytic oxidation processes using semiconductor photocatalysts have emerged as the most promising and cost effective solution for the complete removal of dyes from wastewater.

1.5 Photocatalytic degradation of Amaranth dye

The advanced oxidation process is a method of oxidizing the organic pollutant using in situ generated strong oxidizing agents such as $\cdot\text{OH}$ radicals. The different advanced oxidation techniques reported so far are Photo-Fenton process [30,31], Sonolysis [32], Ozonation process [33], biodegradation [34] and photocatalytic degradation methods [35]. Among all these physico-chemical techniques available, photocatalysis is considered to be one of the most promising method. The process of photocatalysis includes irradiation of photosensitive semiconductor metal oxides using a UV-visible light source, having energy greater than the bandgap energy of the semiconductor. This leads to the excitation of electrons from valence band to the conduction band thus leaving behind holes in the valence band. These photogenerated electrons and holes together contribute in oxidation of the adsorbed species on the surface of the semiconductor metal oxides.

Semiconductor metal oxides are basically of two type n-type and p-type semiconductor. The n-type semiconductor mainly possess excess electrons as the major charge carrier. On the other hand in a p-type semiconductor, holes are the majority charge carriers. Both n-type and p-type semiconductor metal oxides can be used as photocatalyst to carry out photocatalytic degradation of Amaranth dye. For instance, Karkmaz et al. [36] used TiO_2 and obtained 75 % degradation of Amaranth dye in 60 minutes. Divya et al.[37] and Ameta et al. [38] used ZnO catalyst and obtained 100 % degradation in 120 minutes and 92.5 % degradation in 300 minutes respectively for different initial concentration of Amaranth dye. Researchers have also tried incorporating non-metals such as N and S to improve the photocatalytic performance of TiO_2 . For example, Sudrajat et al. [12, 39] carried out photocatalytic degradation of Amaranth dye using N-doped WO_3 and N-doped ZrO_2 and obtained 100 % and 84.5 % degradation in 120 minutes and 240 minutes respectively under different light source irradiation. Further, Jain et al.[40] used N,S doped TiO_2 and obtained 59.3 % degradation of Amaranth dye in 90 minutes.

Researchers have further tried to enhance the photocatalytic degradation of Amaranth dye by coupling n-type semiconductor with p-type semiconductor for photocatalytic degradation of Amaranth dye. For example Benaissa et al. [41] coupled g-C₃N₄ with BiVO₃ and obtained degradation of 90 % in 120 minutes. In another example Wang et al. [30] coupled g-C₃N₄ with Fe₂O₃ and obtained degradation of 97.6 % within 10 minutes of irradiation. Some of the researchers also tried coupling semiconductor metal oxides with plasmonic material such as Ag because of its multi-coloring capability in order to increase the visible light absorption capacity and enhance the photocatalytic Amaranth dye degradation efficiency. For example Hamza et al. [42] used Ag@RGO/g-C₃N₄ ternary 0D@2D/2D nanocomposites and obtained degradation of 80.54 % in 120 minutes. Pascariu et al.[43] used 1 % Ag/ZnO and obtained degradation of 98.4 % in 10 hours of irradiation.

Among all these catalysts, TiO₂ is considered to be the best photocatalyst so far for all practical applications in dye polluted waste water treatment. This is because of its low band gap, and its high physical/chemical stability, high catalytic activity and inertness. These superior photocatalytic properties of TiO₂ arise from its crystal structure, band structure and morphology. Therefore, in the next section a brief discussion on structure and morphology dependent properties of TiO₂ as a semiconductor photocatalyst is presented.

1.5.1 TiO₂ as an n-type semiconductor photocatalyst

TiO₂ is an n-type semiconductor which exist in three polymorphic forms, namely, anatase, rutile and brookite. The crystal structure of anatase, rutile and brookite is shown in Figure 1.2. Among the three polymorphs of TiO₂, macrocrystalline rutile phase of TiO₂ is thermodynamically stable as compared to macrocrystalline brookite and anatase phase. However, the thermodynamic stability is mostly dependent on the particle size of the TiO₂ [44–46]. For lower particle diameter, anatase is more stable which can reversibly transform to rutile upon heat treatment.

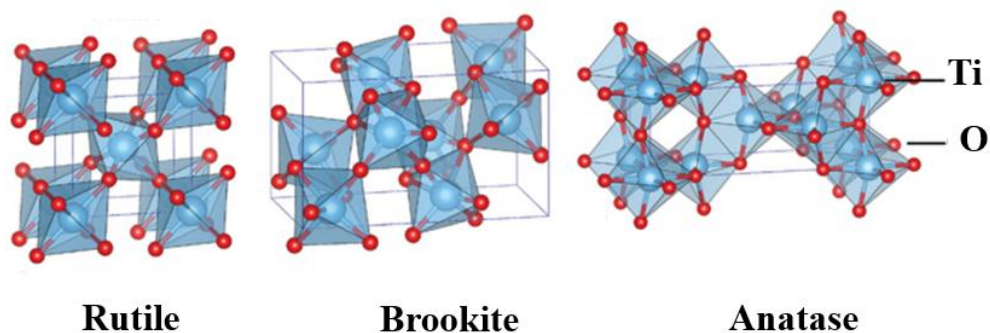


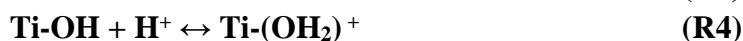
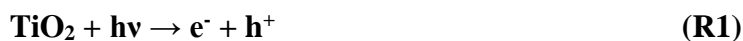
Figure 1.2: The crystal structure of rutile, brookite and anatase TiO_2 . Image reproduced with permission from reference [46].

The structure of TiO_2 is formed by chains of distorted TiO_6 octahedral where each Ti atom is surrounded by 6 oxygen atoms. The three-dimensional stacking of the octahedra in anatase, rutile and brookite is shown in Figure 1.2. The unit cell of anatase TiO_2 contains four octahedral units, while the unit cell of rutile TiO_2 contains two octahedral units, and the unit cell of brookite TiO_2 contains eight octahedral units [47]. Among these three phases, anatase or rutile are preferred over brookite for catalytic applications as brookite is the least stable phase. Among anatase and rutile, literature reports suggest that mesoporous anatase TiO_2 serves as a promising catalyst for remediation of dye polluted wastewater [48–52]. For example, the pilot-scale plants such as the SOLARDETOX plant in Arganda del Rey, Spain, and the PhoRTex plant in Augsburg, Germany, utilize mesoporous TiO_2 for photocatalytic treatment for dye waste. This high photocatalytic efficiency of mesoporous TiO_2 therefore depends on the lifetime of photo generated charge carriers.

Property	Anatase	Rutile	Brookite
Crystal structure	Tetragonal	Tetragonal	Orthorhombic
Octahedra per unit cell	4	2	8
Lattice parameters (nm)	a = b = 0.3785, c = 0.9514	a = b = 0.4594, c = 0.2959	a = c = 0.5436, b = 0.9166
Unit cell volume (nm^3)	0.1363	0.0624	0.2574
Density (g/cm^3)	3.83	4.24	4.17
Band gap (eV)	3.26	3.05	3.10

Table 1.2: Crystal parameters & properties of anatase, rutile and brookite TiO_2 [46].

1.5.2 Photocatalytic dye degradation mechanism over TiO₂



The above reaction steps depict the photocatalytic mechanism of TiO₂. When TiO₂ is irradiated with photon energy greater than its bandgap energy, the electrons from the valence band are excited to conduction band keeping behind holes in the valence band. These electrons then interact with the adsorbed oxygen to generate superoxide anion radicals while the holes interact with the adsorbed water molecules to produce hydroxyl radicals. These reactive oxygen species react with the adsorbed dye pollutants and oxidize them into water and CO₂. Therefore, the high efficiency and sustainability of photocatalytic performance of TiO₂ depends entirely on the concentration and lifetime of photo-generated charge carriers. However, two major factors lead to the reduction in the photocatalytic activity of TiO₂; these are i) its low surface area that limits its dye adsorption capacity and ii) the inherent recombination rate of photogenerated charge carriers. For instance, the commercial Degussa P25 which is most commonly used for photocatalytic applications, has an effective surface area of only 50 m².g⁻¹. This limits the dye adsorption capacity of the photocatalytic surface and also lowers the photocatalytic efficiency.

Many researchers [10,53,54] have therefore preferred to synthesize TiO₂ composites with multi-walled carbon nanotubes (MWCNT), reduced graphene oxide (rGO), carbon nitride (C₃N₄) and precious metal composites of high surface area (some of which are listed in Table 1.3). However, most of these composites are prepared with costly materials and therefore the overall cost of the synthesis limits its application for commercial purpose. In order to make TiO₂ a self-sustainable catalyst there is a need to synthesize TiO₂ of high surface area via a cost effective method with robust, structural porosity to enhance the dye adsorption rates and hence the catalytic activity.

Over two decades of research on TiO₂ synthesis has been reported in the literature so far. It is too exhaustive to cover all of these in this section but a few important ones have been listed in

Table 1.3 and discussed below. Interestingly, only a few research groups have actually succeeded in synthesizing TiO_2 of high surface area (SA). For instance, Nagaveni et al. [35] used glycine as template and obtained surface area of $156 \text{ m}^2.\text{g}^{-1}$. This resulted in a photocatalytic activity of 100 % degradation of methylene blue dye in 65 minutes. Bakre et al. [55] used dicarboxylic acids as templates and obtained maximum surface area of $297 \text{ m}^2.\text{g}^{-1}$ with 100 % degradation efficiency of methylene blue dye in 150 minutes. Tayade et al. [56] synthesized TiO_2 of surface area $124 \text{ m}^2.\text{g}^{-1}$ by hydrolysis of titanium isopropoxide by ultrasonication method and obtained 100 % degradation of methylene blue and malachite green within 60 minutes of irradiation.

Lu et al. [57] synthesized TiO_2 with surface area of $119 \text{ m}^2.\text{g}^{-1}$ using urea as structure directing agent by hydrothermal method and obtained 47.8 % degradation in 240 minutes. Oliveira et al. [65] synthesized TiO_2 using TiCl_4 hydrolysis using dilute H_2SO_4 and obtained surface area of $213 \text{ m}^2.\text{g}^{-1}$ and obtained 66 % degradation in 180 minutes. Dong et al. [59] synthesized mesoporous TiO_2 encapsulated on polyimide nanofiber with surface area of $213 \text{ m}^2.\text{g}^{-1}$ which resulted in 100 % degradation of methylene blue within 40 minutes. In addition to this, researchers have tried to increase the surface area of TiO_2 by coupling it with other metal oxides, for example Abdi et al. [60] synthesized $\text{TiO}_2/\text{ZrO}_2$ using titanium precursor and zirconium metalorganic framework. They obtained surface area of $916 \text{ m}^2.\text{g}^{-1}$ which contributed to 90 % degradation of Rhodamine B dye (20 ppm) in 180 minutes.

Catalyst	Surface area (m ² .g ⁻¹)	Band gap (eV)	[Model dye]	Light source	% Degradation /time (min)
TiO ₂ [36]	52	3.2	[Amaranth] = 84 μmol.L ⁻¹	125 W UV lamp	75/60
N,S doped TiO ₂ [40]	50	3.2	[Amaranth] = 3.9×10 ⁻⁵ mol.L ⁻¹	200W tungsten lamp	59/90
TiO ₂ [35]	156	2.18	[Methylene blue] = 25 ppm [Orange G] = 25ppm [Remazol brill blue] = 25ppm	Solar	100/65 90/100 72/150
TiO ₂ [55]	297	3.38	[Methylene blue] = 10 ppm	Solar	100/120
TiO ₂ [56]	124	3.10	[Methylene blue] = 50 ppm	125 W mercury vapor lamp	100/60
TiO ₂ [57]	119	2.98	[Malachite green] = 50 ppm [Methylene blue] = 10 ppm	UV lamp 33 W.m ⁻²	100/60 48/240
TiO ₂ [58]	213	3.2	[Methylene blue] = 20 ppm	15 W UV lamp	66/180
TiO ₂ /porphyrin [58]	233	3.2	[Methylene blue] = 20 ppm	15 W UV lamp	74/180
TiO ₂ [59]	213	3.2	[Methylene blue] = 9 ppm	30 W UV lamp	100/40
TiO ₂ /ZrO ₂ [60]	916	3.88	[Rhodamine B] = 20 ppm	100 W LED visible light	90/180
GO/TiO ₂ [61]	80	3.2	[Methyl orange] = 10 ppm	20 W UV light	90/9
MWCNTs-TiO ₂ /γ-Al ₂ O ₃ [10]	--	3.2	[Acid orange 7] = 0.050	Pulsed discharge plasma system	100/60
C-TiO ₂ /g-C ₃ N ₄ [54]	--	2.73	[Methyl orange] = 0.020	300 W Xe lamp	98.6/60
TiO ₂ /rGO [53]	78	3.2	[Rhodamine B] = 0.030	300 W Hg lamp	96/60
Ag-TiO ₂ @Fe ₂ O ₄ [62]	55	1.163	[Methyl orange] = 0.025	30 W Simulated visible light	93/120
TiO ₂ - Lignocellulosic Biomass@Fe ₃ O ₄ [63]	104	2.55	[Rhodamine B] = 10 ppm [Methylene blue] = 10 ppm [Congo red] = 10 ppm	300 W Xenon	100/60 75/60 81/60
Hydrotalcite-TiO ₂ -Fe ₃ O ₄ [64]	--	3.3	[Methylene blue] = 0.024	125 W Hg Vapor lamp	96/120

Table 1.3: Literature overview on TiO₂ & its nanocomposites for photocatalytic dye degradation.

All these results are quite promising for photocatalytic application of TiO₂ composites in water purification technology. However, the major limitation of these studies is that they have achieved high surface area either by reduction in particle size or by using a high surface area support material. Most of these reports claim mesoporosity in TiO₂, which refers to intraparticle agglomerate porosity formed merely due to the random agglomeration of fine particle clusters of TiO₂. Therefore, in spite of the gross high surface area, such materials do not provide facile, accessible paths for diffusion and adsorption of bulky reactant molecules due to lack of ordered porous structure. Thus limiting the effective surface adsorption and photocatalytic performance [66]. This provided the motivation for the present thesis to devise a simple methodology to transform the agglomerate porosity into robust, structurally ordered mesoporosity in TiO₂. A detailed investigation and outcomes of this study is presented in Chapter 2.

Furthermore, the second major limiting factor is the high electron-hole recombination rate of TiO₂. Researchers across the globe have constructed different methodologies to enhance the photocatalytic performance by reducing electron-hole recombination rate. Some of them include metal doping into TiO₂ to form interstitial donor or acceptor level which can enhance visible light absorption. Secondly, coupling of TiO₂ with other p-type semiconductor metal oxides such as NiO, ZnO, Ag₂O and CuO etc. have also been attempted [67], which could substantially lower the recombination rate of electrons and holes thus enhancing the photocatalytic performance. Among these metal oxides, NiO in particular serves as an excellent p-type semiconductor having a wide band gap of 3-4 eV. However, there are several factors that limits its utility in photocatalytic applications as well. A brief account of the semiconductor properties of NiO is presented in the next section.

1.5.3 Ni_{1-x}O as p-type semiconductor

NiO exist as a bunsenite mineral in nature. It basically crystalizes in NaCl like (i.e. Rock salt) structure with Ni²⁺ and O²⁻ occupying the octahedral sites (as shown in Figure 1.3). The major difference with respect to NaCl being that NiO is highly non-stoichiometric in nature and exists as Ni_{1-x}O where x represents the number of cation vacancies. Another interesting property of NiO is that its colour changes as a function of Ni:O ratio. Highly stoichiometric NiO usually

exist in green colour whereas nonstoichiometric NiO exist in either grey or black colour depending on the number of Ni^{2+} vacancies. NiO has been extensively studied over the years because of its unique characteristic features such as low cost, low toxicity, significant catalytic activity, and abundant availability [68]. The existence of $\text{Ni}^{2+}/\text{Ni}^{3+}$ redox surface states serve as excellent catalytic centers for several applications. Therefore, it has been widely utilized in different areas of application such as energy storage, as sensors, as catalyst, as electrochromic materials, and in optically active filters [69]. Moreover, it is also used as photocatalyst due to its semiconducting behavior and its antiferromagnetic property aids in easy catalyst recovery [70].

NiO is the first reported p-type semiconductor with a wide bandgap of 3.6–4 eV [71], which restricts its visible light response and hence limits its use as a photocatalyst. Literature studies suggest that NiO nanoparticles as photocatalyst have low activity for remediation of dye polluted wastewater as compared to TiO_2 . Some of these studies on NiO and its performance is listed in Table 1.4. For instance, Lalithambika et al. [72] utilized NiO nanoparticles for photodegradation of methylene blue dye and estimated removal efficiency of 79.5 % in 60 minutes using 300 W Xenon arc lamp. Sabouri et al. [73] studied the degradation of Methylene blue dye using NiO nanoparticles which exhibited 79% degradation after 4 h of reaction under UV light. The poor photocatalytic performance is largely attributed to its low surface area due to nanoparticle agglomeration and also the wide band gap limiting the visible light absorption.

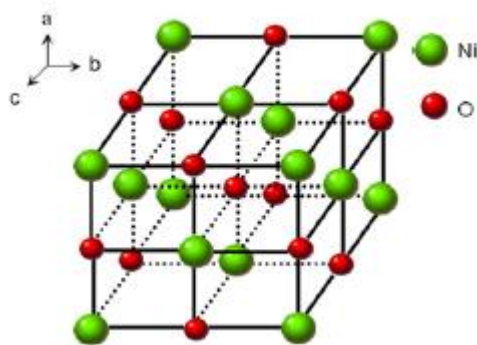


Figure 1.3: Crystal structure of Ni_{1-x}O . Image reproduced with permission from reference [87]

Therefore, in recent times, a lot of research effort has been directed towards the nanostructuring of NiO to tune the surface heterostructure and facilitate the generation of active sites, surface area, reduced bandgap and enhanced light response [74]. For instance, Fazlali et al. [75] synthesized NiO nanostructures such as nanoflowers, nanoplates, nanopshere and nanowoods using multiple synthetic strategies such as thermal decomposition, sol-gel, hydrothermal and emulsion nano-reactor method. Many researcher have also tried to explore the role of urea to synthesized different morphologies of NiO with moderate surface area such as NiO nanoflowers ($66 \text{ m}^2.\text{g}^{-1}$), nanotetrahedra ($114 \text{ m}^2.\text{g}^{-1}$), nanosheets ($120 \text{ m}^2.\text{g}^{-1}$) ultrathin and ultrathick nanosheets ($173 \text{ m}^2.\text{g}^{-1}$ and $81.9 \text{ m}^2.\text{g}^{-1}$) and NiO microspheres ($64 \text{ m}^2.\text{g}^{-1}$). Furthermore, Su et al. [76] synthesized crescent shaped nanoplates with surface area of $68.5 \text{ m}^2.\text{g}^{-1}$ using polyvinylpyrrolidone as nanoplate directing agent. Tian et al.[77] used pollens as microsphere directing agent to synthesize NiO microspheres. Yan et al. [78] synthesized NiO nanoflakes using hexamethylenetetramine with surface area of $185 \text{ m}^2.\text{g}^{-1}$ as structure directing agent. Abbas et al. [79] synthesized NiO microspheres with surface area of $91 \text{ m}^2.\text{g}^{-1}$ using oleylamine as structure directing agent. In addition to this, ultrathin and ultrathick nanosheets with surface area of $173.2 \text{ m}^2.\text{g}^{-1}$ and $81.9 \text{ m}^2.\text{g}^{-1}$ were synthesized using NaBH_4 as a morphology directing agent [80]. Zhang et al. obtained NiO nanocolumns, nanoslice and nanoplates with surface area of $102.4 \text{ m}^2.\text{g}^{-1}$, $11.4 \text{ m}^2.\text{g}^{-1}$ and $20.2 \text{ m}^2.\text{g}^{-1}$ by pH optimization studies [81] .

Some of these nanostructures of NiO have shown improved photocatalytic activity as compared to the 0D particles. For instance, Safa et al. [82] synthesized NiO nanoparticles, nanorods and nanoworms using the hydrothermal method and tested their performance for photodegradation of 4-nitrophenol. The highest degradation efficiency of 65 % was recorded for nanoworm-like NiO in 180 minutes. Vahini et al. [71] synthesized NiO nanospheres with a partially reduced bandgap (3.3 eV) leading to improved photocatalytic degradation activity (98 %) for crystal violet dye in 60 minutes under UV light illumination. Adinaveen et al. [83] synthesized NiO using plant extract and obtained 92.3 % degradation in 180 minutes. Malwal et al. [84] used NiO nanofibers which exhibited Congo red degradation performance of 98 % but it took 6 h of reaction time to achieve it. In another study, Motahari et al. [85] synthesized NiO nanostructures using 1,3 propylenediamine as structure directing agent and obtained 80

% degradation of Rhodamine B in 120 minutes. Qing et al. [86] synthesized mesoporous NiO nanostructures and obtained 99.4 % degradation in 140 minutes. Though, using different synthesis methodologies various morphologies of NiO have been synthesized, the need for expensive equipment and reactors such as in hydrothermal/solvothermal and its associated safety hazards for bulk synthesis limits its large scale production. Moreover, the need of additional templates and surfactants to direct the nanostructural morphology and its post-synthesis separation treatment adds to the complexity of the synthesis procedure. Therefore, there is a need to design a simple and scalable method for the synthesis of nanostructured NiO of high catalytic activity. This provided the motivation to design simple and scalable strategies to obtain highly porous NiO catalyst of high surface area and catalytic activity. The interesting results of this synthesis strategy are presented in Chapter 3.

Catalyst	Surface area (m ² .g ⁻¹)	Band gap (eV)	[Model dye]	Light source	% Degradation/time (min)
NiO [71]	62	3.31	[Crystal violet] = 20 ppm	UV light	98/60
NiO [83]	67.7	3.8	Rhodamine B] = 10 ppm	8W UV light	92.3/180
NiO [70]	306.4	3.6	[Methylene blue] = 10 ppm [Congo red] = 10 ppm [Eosin red] = 10 ppm	500W halogen lamp	94.3/50 98/30 81/60
NiO [84]	33.4	3.5	[Congo red] = 10 ppm	UV lamp	98/360
NiO [87]	52.57	2.83	[Rhodamine B] = 10 ppm	400 W UV	80/120
NiO [86]	187	3.4	[Methylene blue] = 20 ppm	Xe arc lamp	99.4/140
NiO/TiO ₂ [88]	146.8	2.5	[Methylene blue] = 2 × 10 ⁻⁵ mol L ⁻¹	400 W metal halide	97/100
NiO/TiO ₂ [89]	106.4	2.86	[Methylene blue] = 20 ppm	400 W visible light lamp	90/150
NiO/TiO ₂ [90]	90	–	[Methyl orange]= 10 ppm	15 W UV lamp	100/90
NiO/TiO ₂ [91]	53	2.9	[Methyl orange]= 10 ppm	375 W high pressure Hg lamp	100/20
NiO/TiO ₂ [92]	60.5	2.7	[Methyl orange]= 30 μ M	250 W Xe arc lamp	92/140
carbon /NiO/TiO ₂ [93]	169	–	[Methylene blue] = 2.0 × 10 ⁻⁵ mol L ⁻¹	400 W metal halide lamp	98/100
Ni/NiO/TiO ₂ [94]	154.7	2.78	[Rhodamine B] = 2 ppm	Simulated solar lamp	99/60

Table 1.4: Literature report on Ni_{1-x}O based catalysts and their photocatalytic performance.

1.5.4 Ni_{1-x}O/TiO₂ as heterojunction catalyst.

In recent years, enormous efforts have been made in surface modification of TiO₂ with other p-type semiconductors such as ZnO [95], Cu₂O [67], NiO [96] and Ag₂O [97] which could substantially reduce the band gap and enhance the photocatalytic activity. Most of these systems possess enhanced charge separation efficiency, an extended light absorption range, high dye degradation capacity and promote mass-transfer, thus enhancing the photocatalytic efficiency. As discussed earlier, NiO is a p-type semiconductor and TiO₂ is an n-type semiconductor. The individual photocatalytic performance of both these catalysts is limited due factors such as low chemical/photo stability and high electron-hole recombination rate respectively. The efficient separation of the electrons and holes is an important step in enhancing the photocatalytic performance. Therefore, a combination of NiO and TiO₂ could form a formidable p-n heterojunction photocatalyst which could lead to further enhancement in photocatalytic activity by reducing the electron-hole recombination rate. A heterojunction is defined as an interface between the two hybrid layers of dissimilar electronic band structures of a semiconductor. Overall, there are four types of heterojunction photocatalyst namely, i) the semiconductor metal oxide heterojunction photocatalyst wherein both the metal oxides are semiconductor in nature, ii) the semiconductor combined with metal heterojunction photocatalyst, iii) the semiconductor-carbon heterojunction catalyst and iv) the multicomponent heterojunction photocatalyst. Out of these four, the heterojunction photocatalyst formed by combining two semiconductor metal oxide is mostly preferred because of its high charge carrier performance and excellent stability.

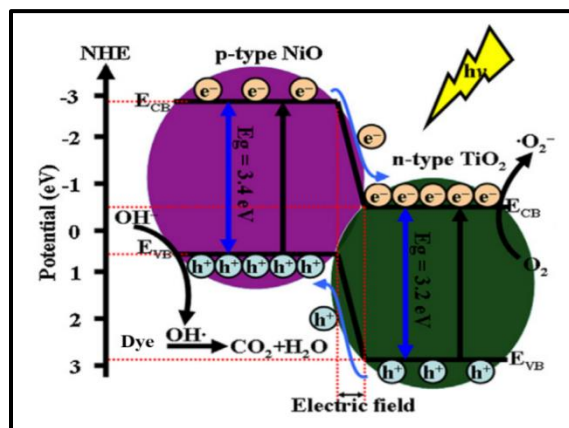


Figure 1.4: p-n junction & charge carrier separation in NiO@ TiO₂ catalyst Image reproduced with permission from reference [91]

When the p- and n-type semiconductor is in contact with each other they form a p-n junction with a space charge separation at the interface due to the diffusion of electrons and holes as shown in Figure 1.4. This creates a built-in electrical potential that can direct the electrons and holes to travel in the opposite direction. When the formed p-n heterojunction is irradiated with photons having energy higher or equal to the bandgap energy of the photocatalyst, there is a quick transfer of photogenerated electrons and holes which are separated by built-in electric field within the space charge region. The built-in electric field acts as a driving force for the photogenerated electrons to be transferred to conduction band (CB) of the n-type semiconductors and the photogenerated holes to the valence band (VB) of the p-type semiconductor. The various associated advantages of p-n junction photocatalyst are as follows: i) effective charge separation ii) rapid charge transfer to the catalyst, iii) long lifetime of the charge carriers and iv) the ability to extend the visible light absorption characteristics of the composite catalyst.

Different NiO/TiO₂ nanocomposites in particular have been the most promising heterojunction catalyst. Several research groups have fabricated NiO/TiO₂ nanocomposites through hydrothermal, sol-gel, electrospinning, anodization, wetness impregnation and electrodeposition method. For instance, NiO/TiO₂ nanocomposites synthesized using polyvinylpyrrolidone as structure directing agent via electrospinning method gave surface area of 41 m².g⁻¹ [98]. Predominantly NiO/TiO₂ have been synthesized using hydrothermal method with varying surface area of about 53-146 m².g⁻¹ [88,91,93]. Researchers have also used bulky structure directing agents such as lauryl amine hydrochloride, triblock copolymer and acetic acid using sol-gel method of synthesis with surface area as high as 180 m².g⁻¹ [89]. The high surface area also contributed to high photocatalytic degradation activity in several studies, some of which are listed in Table 1.4. For instance, Chen et al. [96] synthesized NiO/TiO₂ with surface area of 146 m².g⁻¹ and obtained photocatalytic activity of 97 % for methylene blue degradation in 100 minutes. Faisal et al. [89] synthesized NiO/TiO₂ with surface area 106 m².g⁻¹ and obtained 90 % degradation of methylene blue dye in 150 minutes. Furthermore, NiO/TiO₂ has been synthesized with surface area ranging from 53 to 90 m².g⁻¹ and obtained photocatalytic degradation of approximately 100 % for methyl orange dye on an average time of in 100 minutes. In another study, Wang et al.[93] synthesized carbon encapsulated NiO/TiO₂

nanocomposites having surface area of $169 \text{ m}^2.\text{g}^{-1}$ and obtained 98 % photocatalytic degradation within 100 minutes. Zhu et al. [94] incorporated Ni in NiO/TiO₂ nanocomposites having surface area of $154 \text{ m}^2.\text{g}^{-1}$ resulting in photocatalytic degradation of 99 % in 60 minutes. Therefore, attempts have been made in this thesis to develop a simple and scalable method to produce NiO/TiO₂ nanocomposites heterojunction photocatalyst of higher photocatalytic performance, the results of which are presented in Chapter 4.

Apart from the photocatalytic application of NiO, TiO₂ and their nanocomposites, they are also widely used as candidate for energy storage application such as in supercapacitors. The next section therefore presents in brief, the mechanism of energy storage using the supercapacitor technology and the capacitive performance of some of the reported NiO, TiO₂ and its composite catalysts.

1.6 Supercapacitors

The most abundant sustainable energy resources such as solar energy, wind power and hydropower are available for only a certain period of time in a given day. Therefore, there is a need to develop a system that can store this energy instantly [99]. Hence, many efforts have been made on the energy storage systems that can harvest the intermittent energy, store and utilize this energy as per the human need. Among the diverse energy storage systems existing currently, the batteries and supercapacitors are the most promising and important energy storage systems [100]. Supercapacitors are very well known nowadays because of their high cycling performance, safety and low maintenance cost. They can be fully charged/discharged at a faster rate with enlarged cycling lifetime. According to the charge storage mechanism, supercapacitors can be classified into two types i.e. electrical double-layer capacitors (EDLCs) and pseudo-capacitors (PCs), [101]. The EDLCs can store charges mainly through the adsorption and desorption of ions, which take place in the electric double layer formed at the interface between electrode and electrolyte [102]. The entire process is purely a physical change without any occurrence of chemical reactions, which makes EDLCs possess high power density. However, the low capacitance hinders its broad applications. The carbon-based materials, such as activated carbon (AC), graphene, and carbon nanotubes (CNTs) are usually used as the electrode materials for EDLCs owing to their good conductivity and large surface

area [103–105]. The pseudo-capacitors often possess higher specific capacitance compared to that of EDLCs, due to its faradaic redox reactions occurring at the surface of active materials [106]. Thus, transition metal oxides are gaining more attention for their application in energy storage application because of their abundance and high stability [107].

An eminent scientist Thierry Brousse [108] reported that the MnO_2 electrode shows a similar electrochemical behavior as that of capacitive carbon electrode and can be termed as pseudocapacitive material. It is now confirmed that the transition metal oxides such as RuO_2 [109], [110] do exhibit pseudocapacitor behavior. Apart from this many metal oxide-based materials such as NiO [111–113], NiCo_2O_4 [114–116], Co_3O_4 [117–119], CuCo_2O_4 [120–122], Fe_2O_3 [123–125], NiFe_2O_4 [126,127], have been widely studied as the pseudocapacitor material owing to their conducting nature and multiple oxidation states. It is well established that the performance of any material/catalyst is largely dependent on its phase composition, crystallinity, morphology, electronic and optical properties, and these properties are tuned based on the applied synthesis methodology. Tuneability of surface heterostructure and mesoporosity have emerged as the key factors that render exceptional catalytic activity. Many available literature reports highlight that nanostructured materials show better supercapacitor behavior as compared to 0D nanoparticles. Nanostructured transition metal oxides have found utility in drug delivery, biomedical, tissue engineering, photocatalysis and supercapacitor applications.

1.6.1 Ni_{1-x}O , TiO_2 and their nanocomposites for supercapacitor application.

Among the various transition metal oxide-based electrode materials with supercapacitor properties, NiO and TiO_2 both have very high theoretical capacitance of 2584 F.g^{-1} [128] and 2295 F.g^{-1} [129] respectively. However, the practically obtained specific capacitance of both these oxides is significantly low for practical applications. For instance, NiO exhibits a practically achievable specific capacitance in the range of 39 F.g^{-1} to 1140 F.g^{-1} as can be seen from Table 1.5. Therefore, several researchers have attempted to improve its capacitive performance by synthesizing nanostructured NiO based electrodes. For instance Yan et al. [78] synthesized NiO nanoflakes with surface area of $185 \text{ m}^2.\text{g}^{-1}$ having specific capacitance of 400 F.g^{-1} .

Catalyst	Specific capacitance	Current density	Electrolyte
NiO [78]	400 F.g ⁻¹	2 A.g ⁻¹	2 M KOH
NiO [79]	1140 F.g ⁻¹	10 A.g ⁻¹	2 M KOH
NiO [130]	39 F.g ⁻¹	0.3 A.g ⁻¹	1 M KOH
NiO [131]	62 F.g ⁻¹	5 mV.s ⁻¹	6 M KOH
NiO [132]	97 F.g ⁻¹	0.1 A.g ⁻¹	1 M KOH
NiO [133]	184.6 F.g ⁻¹	0.3 A.g ⁻¹	1 M KOH
NiO [134]	260 F.g ⁻¹	0.5 A.g ⁻¹	2 M KOH
NiO [135]	423 F.g ⁻¹	0.5 mA.cm ⁻²	1M Na ₂ SO ₄
NiO [136]	810 F.g ⁻¹	5 mV.s ⁻¹	6 M KOH
La ³⁺ doped NiO [137]	253 F.g ⁻¹	1 A.g ⁻¹	1 M KOH
NiO [138]	390 F.g ⁻¹	5 A.g ⁻¹	1 M KOH
TiO ₂ /MnO ₂ [139]	231.2 F.g ⁻¹	0.2 A.g ⁻¹	1M Na ₂ SO ₄
TiO ₂ /V ₂ O ₅ [140]	310 F.g ⁻¹	2 mV.s ⁻¹	1M Na ₂ SO ₄
TiO ₂ /RuO ₂ [141]	1200 F.g ⁻¹	0.5 A.g ⁻¹	1M H ₂ SO ₄
TiVN [142]	15 mF.cm ⁻²	2 mV.s ⁻¹	1M KOH
Ni(OH) ₂ /TiO ₂ [143]	22 mF.cm ⁻²	10 mV.s ⁻¹	1 M NaOH
Co(OH) ₂ /TiO ₂ [144]	229 F.g ⁻¹	2 mA	6 M KOH
TiO ₂ /polyaniline [145]	897.35 F.g ⁻¹	0.21 A.g ⁻¹	0.05 M H ₂ SO ₄
TiO ₂ /polypyrrole [146]	446 F.g ⁻¹	15 A.g ⁻¹	1M H ₂ SO ₄
NiO/TiO ₂ [147]	40 – 100 F.g ⁻¹	0.4 mA.cm ⁻²	1 M KOH
NiO@TiO ₂ core-shell [148]	50-211 F.g ⁻¹	0.83 A.g ⁻¹	6 M KOH
TiO ₂ @Ni(OH) ₂ [149]	181 F.g ⁻¹	5 mV.s ⁻¹	6 M KOH
TiO ₂ /NiO [150]	689.28 F.g ⁻¹	1.5 A.g ⁻¹	1 M KOH
NiO/TiO ₂ [151]	72.7 mF.cm ⁻²	0.5mA.cm ⁻²	1 M KOH
NiO/TiO ₂ [151]	42.3 mF.cm ⁻²	0.5mA.cm ⁻²	1 M KOH

Table 1.5: Literature reports on supercapacitor performance of Ni_{1-x}O, TiO₂ and their composites.

In another study, Han et al. [137] synthesized La³⁺ doped NiO microspheres using colloidal carbon spheres as hard templates via hydrothermal method and obtained a high surface area of 227.5 m².g⁻¹ with specific capacitance of 253 F.g⁻¹. In another investigation, Zhang et al. [138] synthesized NiO nanocolumns, nanoslices and nanoplates and obtained specific capacitance of 390 F.g⁻¹, 176 F.g⁻¹ and 285 F.g⁻¹ respectively. However, the major drawback of the NiO is its electro-corrosion effects which result in its poor electrochemical performance and reduced cycling stability making it less sustainable material for this applications. Researchers have tried to address this issue by supporting NiO with other conducting material such as graphene oxide and g-C₃N₄ [152]. An increase in specific capacitance is observed in these studies due to the uniform distribution of the NiO on to the conducting support material. However, very limited attention has been given to tailoring the properties of NiO and making it self-sustainable for

supercapacitor application. In comparison to NiO, the capacitor properties of TiO₂ have barely been explored in the literature.

As mentioned earlier, TiO₂ has a high theoretical specific capacitance of 2295 F.g⁻¹. However, its poor conductivity renders it as an unsuitable material for electrochemical performance. Therefore, researchers have tried combining TiO₂ with electroactive materials such as MnO₂ [139], V₂O₅ [140], RuO₂ [141], NiO [153] and obtained specific capacitance in the range of 231 to 1200 F.g⁻¹. Some of these studies are listed in Table 1.5. For instance, Chen et al. [143] and Tao et al. [144] coupled TiO₂ with metal hydroxides such as (Co(OH)₂, Ni(OH)₂) and obtained the specific capacitance of 22 mF.cm⁻² and 229 F.g⁻¹ respectively. Further, Achour et al. [142] tried coupling TiO₂ with titanium vanadium nitride (TiVN) due to its high electronic conductivity as compared to metal oxides and obtained the specific capacitance of 15 mF.cm⁻². In another study, Jiang et al. [129] and Shao et al. [145] combined TiO₂ with conducting polymers such as polypyrrole, polyaniline and obtained the specific capacitance upto 897 F.g⁻¹ [129,145]. In addition to this, various other modification of TiO₂ has been carried out such as synthesizing TiO₂ nanocomposite using different conducting substrates such as reduced graphene oxide [154], carbon nanotube [155], graphene, graphitic carbon [156], which could help in accelerating the charge transfer process and could help in enhancing the charge storage performance. However, it was observed that the use of conducting materials were not applicable for long cycling stability of the electrode in comparison to metal oxide supported TiO₂ catalysts.

Among these mixed metal oxide composites, NiO-TiO₂ is considered to be one of the promising composite material for supercapacitor application. For instance, Kim et al. [147] synthesized microstructure NiO@TiO₂ for supercapacitor application and measured specific capacitance in the range of 40-100 F.g⁻¹. Lee et al. [148] synthesized NiO@TiO₂ core-shell structures and obtained a specific capacitance of 211 F.g⁻¹. In another study, Ke et al. [149] synthesized TiO₂@Ni(OH)₂ nanowire array and the obtained specific capacitance was 181 F.g⁻¹. Cui et al. [150] synthesized hydrogenated TiO₂ nanotube array decorated with nickel oxide and the obtained specific capacitance of 689.28 F.g⁻¹. Xie et al.[151] synthesized NiO@TiO₂ composite flowers having specific capacitance of 72.7 mF.cm² which was almost twice as that

of NiO/TiO₂ nanoparticle. However, most of the methods employed for synthesis such as hydrothermal, electro-deposition, electrochemical anodization etc. are not truly conducive for large scale industrial production. Moreover, the obtained SC performance is also very limited. Therefore, there is a need to design a simple and scalable methodology by which NiO/TiO₂ nanocomposite of high conductivity and improved electrochemical cycling stability can be achieved for application in supercapacitor technology. This provided the motivation to undertake a study on TiO₂, NiO and their composite catalyst for supercapacitor application. The results of this investigation are presented in detail in Chapter 5.

Based on the above literature survey, the major objectives of this thesis were defined as follows:

1.7 Thesis objectives

- To synthesize nanoporous TiO₂ catalysts and perform their detailed material characterization.
- To synthesize nanoporous Ni_{1-x}O catalysts and perform their detailed material characterization.
- To synthesize nanoporous Ni_{1-x}O/TiO₂ nanocomposites and perform their detailed material characterization.
- To evaluate the Amaranth dye adsorptive separation and photocatalytic degradation efficiency of all the synthesized catalysts.
- To evaluate the supercapacitive energy storage performance of all the synthesized catalysts.

The outcome of the systematic research methodology employed to achieve the above objectives is discussed in detail in the individual Chapters 2-5 while the overall summary of the findings of these investigations is presented in Chapter 6.

1.8 References

- [1] Q. Zhang, E. Uchaker, S.L. Candelaria, G. Cao, Nanomaterials for energy conversion and storage, *Chem. Soc. Rev.* 42 (2013) 3127–3171.
- [2] Y. Wang, J. Guo, T. Wang, J. Shao, D. Wang, Y.W. Yang, Mesoporous transition metal oxides for supercapacitors, *Nanomaterials*. 5 (2015) 1667–1689.
- [3] S.A. Delbari, L.S. Ghadimi, R. Hadi, S. Farhoudian, M. Nedaei, A. Babapoor, A. Sabahi Namini, Q. Van Le, M. Shokouhimehr, M. Shahedi Asl, M. Mohammadi, Transition metal oxide-based electrode materials for flexible supercapacitors: A review, *J. Alloys Compd.* 857 (2021) 158281.
- [4] M. Choudhary, R. Kumar, S. Neogi, Activated biochar derived from *Opuntia ficus-indica* for the efficient adsorption of malachite green dye, Cu^{+2} and Ni^{+2} from water, *J. Hazard. Mater.* 392 (2020) 122441.
- [5] J. Ahmed, A. Thakur, A. Goyal, and Industrial waste water and its Toxic Effects, *RSC* (2022) 1–14.
- [6] Shivaraju HP, Removal of Organic Pollutants in the Municipal Sewage Water by TiO_2 based Heterogeneous Photocatalysis, *Int. J. Environ. Sci.* 1 (2011) 911-923.
- [7] I.M. Banat, P. Nigam, D. Singh, R. Marchant, Microbial decolorization of textile-dye-containing effluents : a review, *Bioresour. Technol.* 58 (1997) 217–227.
- [8] S. Benkhaya, M. Souad, A. El, Harfi Classifications , properties , recent synthesis and applications of azo dyes, *Heliyon* 6 (2020) 1-26.
- [9] K. Chung, Environmental Carcinogenesis and Ecotoxicology Reviews Azo dyes and human health : A review, *J. Environ. Sci. Heal. Part C.* 34 (2016) 233–261.
- [10] X. Li, T. Wang, G. Qu, D. Liang, S. Hu, Enhanced degradation of azo dye in wastewater by pulsed discharge plasma coupled with MWCNTs- $\text{TiO}_2/\gamma\text{-Al}_2\text{O}_3$ composite photocatalyst, *J. Environ. Manage.* 172 (2016) 186–192.
- [11] P. Mpountoukas, A. Pantazaki, E. Kostareli, P. Christodoulou, D. Kareli, S. Poliliou, C. Mourelatos, V. Lambropoulou, T. Lialiaris, Cytogenetic evaluation and DNA interaction studies of the food colorants amaranth, erythrosine and tartrazine, *Food Chem. Toxicol.* 48 (2010) 2934–2944.
- [12] H. Sudrajat, S. Babel, Rapid photocatalytic degradation of the recalcitrant dye amaranth by highly active N- WO_3 , *Environ. Chem. Lett.* 14 (2016) 243–249.

- [13] P. Verma, S.K. Samanta, Degradation kinetics of pollutants present in a simulated wastewater matrix using UV/TiO₂ photocatalysis and its microbiological toxicity assessment, *Res. Chem. Intermed.* 43 (2017) 6317–6341.
- [14] J. Gomes, A. Lopes, K. Bednarczyk, M. Gmurek, M. Stelmachowski, A. Zaleska-Medynska, M. Quinta-Ferreira, R. Costa, R. Quinta-Ferreira, R. Martins, Effect of Noble Metals (Ag, Pd, Pt) Loading over the Efficiency of TiO₂ during Photocatalytic Ozonation on the Toxicity of Parabens, *ChemEngineering*. 2 (2018) 1-14.
- [15] S. Tsuda, M. Murakami, N. Matsusaka, K. Kano, K. Taniguchi, Y.F. Sasaki, DNA Damage induced by red food dyes orally administered to pregnant and male mice, *Toxicol. Sci.* 61 (2001) 92–99.
- [16] S.A. Clode, J. Hooson, D. Grant, W.H. Butler, Long-term toxicity study of amaranth in rats using animals exposed in utero, *Food Chem. Toxicol.* 25 (1987) 937–946.
- [17] T.F.X. Collins, J. Mclaughlin, Teratology Studies on Food Colourings. Part II. Embryotoxicity of R Salt and Metabolites of Amaranth (FD & C Red No. 2) in Rats 11 *Fd Cosmet. Toxicol.* Vol. 11 (1973) 355–365.
- [18] A. Das, A. Mukherjee, Genotoxicity Testing of the Food Colours Amaranth and Tartrazine Genotoxicity Testing of the Food Colours Amaranth and Tartrazine, *Int. J. Hum.Genet.* 4 (2017) 277-280
- [19] N. Ayawei, A.N. Ebelegi, D. Wankasi, Modelling and Interpretation of Adsorption Isotherms, *J. Chem.* 2017 (2017) 1–11.
- [20] M. Singh, D.P. Tiwari, M. Bhagat, Batch Adsorption Studies on the Removal of Amaranth Red Dye From Aqueous Solution Using Activated Trapa Natans Peels, *Environ. biotech. J.* 39 (2020) 130–137.
- [21] A. Mittal, L. Kurup, V.K. Gupta, Use of waste materials - Bottom Ash and De-Oiled Soya, as potential adsorbents for the removal of Amaranth from aqueous solutions, *J. Hazard. Mater.* 117 (2005) 171–178.
- [22] R. Gong, Y. Ding, M. Li, C. Yang, H. Liu, Y. Sun, Utilization of powdered peanut hull as biosorbent for removal of anionic dyes from aqueous solution, *Dyes Pigm.* 64 (2005) 187–192.
- [23] I.T. Kuete, Biosorption of amaranth red in aqueous solution onto treated and untreated lignocellulosic materials (pineapple peelings and coconut shells), *Indian J. Eng. Mater.*

- Sci. 8 (2017) 4199-4212.
- [24] R. Ahmad, R. Kumar, Adsorption of Amaranth Dye onto Alumina Reinforced Polystyrene, *Clean - Soil, Air, Water*. 39 (2011) 74–82.
- [25] A.N.M. Salem, M.A. Ahmed, M.F. El-Shahat, Selective adsorption of amaranth dye on Fe₃O₄/MgO nanoparticles, *J. Mol. Liq.* 219 (2016) 780–788.
- [26] K. Abdellaoui, I. Pavlovic, M. Bouhent, A. Benhamou, C. Barriga, A comparative study of the amaranth azo dye adsorption/desorption from aqueous solutions by layered double hydroxides, *Appl. Clay Sci.* 143 (2017) 142–150.
- [27] N. Kumar, H. Mittal, S.M. Alhassan, S.S. Ray, Bionanocomposite Hydrogel for the Adsorption of Dye and Reusability of Generated Waste for the Photodegradation of Ciprofloxacin: A Demonstration of the Circularity Concept for Water Purification, *ACS Sustain. Chem. Eng.* 6 (2018) 17011–17025.
- [28] L. Song, C. Chen, S. Zhang, Q. Wei, Sonocatalytic degradation of amaranth catalyzed by La³⁺ doped TiO₂ under ultrasonic irradiation, *Ultrason. Sonochem.* 18 (2011) 1057–1061.
- [29] A.H. Alwash, A.Z. Abdullah, N. Ismail, Elucidation of Reaction Behaviors in Sonocatalytic Decolorization of Amaranth Dye in Water Using Zeolite Y Co-Incorporated with Fe and TiO₂, *Adv. Chem. Eng. Sci.* 3 (2013) 113–122.
- [30] L. Wang, Y. Wang, X. Li, T. He, R. Wang, Y. Zhao, H. Song, H. Wang, 3D/2D Fe₂O₃/g-C₃N₄ Z-scheme heterojunction catalysts for fast, effective and stable photo Fenton degradation of azo dyes, *J. Environ. Chem. Eng.* 9 (2021) 105907.
- [31] Y. Deng, R. Zhao, Advanced Oxidation Processes (AOPs) in Wastewater Treatment, *Curr. pollution Rep* (2015) 167–176.
- [32] M. Pirsaeheb, N. Moradi, Sonochemical degradation of pesticides in aqueous solution : investigation on the influence of operating parameters and degradation pathway, *RSC Adv.* 10 (2020) 7396–7423.
- [33] R. Gnirss, T. Wintgens, Environmental Science Water Research & Technology microbiological quality parameters *Environ. Sci. Water Res. Technol.* 7 (2021) 1643–1656.
- [34] P. Van Aken, N. Lambert, Environmental Science Water Research & Technology processes to enhance chlorophenol abatement in, *Environ. Sci. Water Res. Technol.* 5

- (2019) 444–481.
- [35] K. Nagaveni, G. Sivalingam, M.S. Hegde, G. Madras, Solar photocatalytic degradation of dyes: High activity of combustion synthesized nano TiO₂, *Appl. Catal. B Environ.* 48 (2004) 83–93.
- [36] M. Karkmaz, E. Puzenat, C. Guillard, J.M. Herrmann, Photocatalytic degradation of the alimentary azo dye amaranth: Mineralization of the azo group to nitrogen, *Appl. Catal. B Environ.* 51 (2004) 183–194.
- [37] N. Divya, A. Bansal, A.K. Jana, Photocatalytic activity of transition metal ion doped titania for Amaranth dye degradation, *Mater. Sci. Forum.* 712 (2012) 85–104.
- [38] R. Ameta, N. Jain, S. Kothari, Photocatalytic bleaching of amaranth dye over ZnO powder, *Indian J. Chem. Technol.* 11 (2004) 423–426.
- [39] H. Sudrajat, S. Babel, H. Sakai, S. Takizawa, Rapid enhanced photocatalytic degradation of dyes using novel N-doped ZrO₂, *J. Environ. Manage.* 165 (2016) 224–234.
- [40] A.K. Jain, S. Sharma, R. Ameta, Enhanced photocatalytic activity of N , S-doped titania for degradation of amaranth, *Merit Res. J. Environ. Sci. Toxicol.* 3 (2015) 25–30.
- [41] M. Benaissa, N. Abbas, S. Al Arni, N. Elboughdiri, A. Moumen, M.S. Hamdy, H.S.M. Abd-Rabboh, A.H. Galal, M.G. Al-Metwaly, M.A. Ahmed, BiVO₃/g-C₃N₄ S-scheme heterojunction nanocomposite photocatalyst for hydrogen production and amaranth dye removal, *Opt. Mater. (Amst).* 118 (2021) 111237.
- [42] M.A. Hamza, S.A. Abd El-Rahman, A.N. El-Shazly, E.M. Hashem, R.T. Mohamed, E.M. El-Tanany, M.G. Elmahgary, Facile one-pot ultrasonic-assisted synthesis of novel Ag@RGO/g-C₃N₄ ternary 0D@2D/2D nanocomposite with enhanced synergetic tandem adsorption-photocatalytic degradation of recalcitrant organic dyes: Kinetic and mechanistic insights, *Mater. Res. Bull.* 142 (2021) 111386.
- [43] P. Pascariu, C. Cojocaru, P. Samoila, A. Airinei, N. Olaru, D. Rusu, I. Rosca, M. Sucheaa, Photocatalytic and antimicrobial activity of electrospun ZnO:Ag nanostructures, *J. Alloys Compd.* 834 (2020) 155144.
- [44] H. Zhang, J.F. Banfield, Understanding polymorphic phase transformation behavior during growth of nanocrystalline aggregates: Insights from TiO₂, *J. Phys. Chem. B.* 104 (2000) 3481–3487.

- [45] H. Zhang, J.F. Banfield, Thermodynamic analysis of phase stability of nanocrystalline titania, *J. Mater. Chem.* 8 (1998) 2073–2076.
- [46] J. E. S. Haggerty, L. T. Schelhas, D. A. Kitchaev, J. S. Mangum, L. M. Garten, W. Sun, K. H. Stone, J. D. Perkins, M. F. Toney, G. Ceder, D. S. Ginley, B. P. Gorman, J. Tate High-fraction brookite films from amorphous precursors, *Sci Rep* 7 (2017) 15232.
- [47] D.A.H. Hanaor, C.C. Sorrell, Review of the anatase to rutile phase transformation, *J. Mater. Sci.* 46 (2011) 855–874.
- [48] H.G. Jung, Y.S. Kang, Y.K. Sun, Anatase TiO₂ spheres with high surface area and mesoporous structure via a hydrothermal process for dye-sensitized solar cells, *Electrochim. Acta.* 55 (2010) 4637–4641.
- [49] T. V. Gerasimova, O.L. Evdokimova (Galkina), A.S. Kraev, V.K. Ivanov, A. V. Agafonov, Micro-mesoporous anatase TiO₂ nanorods with high specific surface area possessing enhanced adsorption ability and photocatalytic activity, Elsevier Ltd, 2016.
- [50] S.S. Muniandy, N.H. Mohd Kaus, Z.T. Jiang, M. Altarawneh, H.L. Lee, Green synthesis of mesoporous anatase TiO₂ nanoparticles and their photocatalytic activities, *RSC Adv.* 7 (2017) 48083–48094.
- [51] W. Zhou, W. Li, J.Q. Wang, Y. Qu, Y. Yang, Y. Xie, K. Zhang, L. Wang, H. Fu, D. Zhao, Ordered mesoporous black TiO₂ as highly efficient hydrogen evolution photocatalyst, *J. Am. Chem. Soc.* 136 (2014) 9280–9283.
- [52] W. Li, Z. Wu, J. Wang, A.A. Elzatahry, D. Zhao, A perspective on mesoporous TiO₂ materials, *Chem. Mater.* 26 (2014) 287–298.
- [53] M.H.H. Ali, A.D. Al-Afify, M.E. Goher, Preparation and characterization of graphene – TiO₂ nanocomposite for enhanced photodegradation of Rhodamine-B dye, *Egypt. J. Aquat. Res.* 44 (2018) 263–270.
- [54] Z. Lu, L. Zeng, W. Song, Z. Qin, D. Zeng, C. Xie, In situ synthesis of C-TiO₂/g-C₃N₄ heterojunction nanocomposite as highly visible light active photocatalyst originated from effective interfacial charge transfer, *Appl. Catal. B Environ.* 202 (2017) 489–499.
- [55] P. V. Bakre, S.G. Tilve, Dicarboxylic Acids as Soft Templates for the Sol-Gel Synthesis of Mesoporous Nano TiO₂ with Enhanced Photocatalytic Activity, *ChemistrySelect.* 2 (2017) 7063–7072.
- [56] R.J. Tayade, P.K. Surolia, R.G. Kulkarni, R. V. Jasra, Photocatalytic degradation of

- dyes and organic contaminants in water using nanocrystalline anatase and rutile TiO₂, *Sci. Technol. Adv. Mater.* 8 (2007) 455–462.
- [57] T. Lu, Y. Wang, Y. Wang, L. Zhou, X. Yang, Y. Su, Synthesis of Mesoporous Anatase TiO₂ Sphere with High Surface Area and Enhanced Photocatalytic Activity, *J. Mater. Sci. Technol.* 33 (2017) 300–304.
- [58] C.P.M. de Oliveira, A.L.A. Lage, D.C. da S. Martins, N.D.S. Mohallem, M.M. Viana, High surface area TiO₂ nanoparticles: impact of carboxylporphyrin sensitizers in the photocatalytic activity, *Surfaces and Interfaces.* 21 (2020) 100774.
- [59] G. Dong, Y. Wang, H. Lei, G. Tian, S. Qi, D. Wu, Hierarchical mesoporous titania nanoshell encapsulated on polyimide nanofiber as flexible, highly reactive, energy saving and recyclable photocatalyst for water purification, *J. Clean. Prod.* 253 (2020) 120021.
- [60] J. Abdi, M. Yahyanezhad, S. Sakhaie, M. Vossoughi, I. Alemzadeh, Synthesis of porous TiO₂/ZrO₂ photocatalyst derived from zirconium metal organic framework for degradation of organic pollutants under visible light irradiation, *J. Environ. Chem. Eng.* 7 (2019) 103096.
- [61] G. Jiang, Z. Lin, C. Chen, L. Zhu, Q. Chang, N. Wang, W. Wei, H. Tang, TiO₂ nanoparticles assembled on graphene oxide nanosheets with high photocatalytic activity for removal of pollutants, *Carbon N. Y.* 49 (2011) 2693–2701.
- [62] W.J. Chung, D.D. Nguyen, X.T. Bui, S.W. An, J.R. Banu, S.M. Lee, S.S. Kim, D.H. Moon, B.H. Jeon, S.W. Chang, A magnetically separable and recyclable Ag-supported magnetic TiO₂ composite catalyst: Fabrication, characterization, and photocatalytic activity, *J. Environ. Manage.* 213 (2018) 541–548.
- [63] R. Djellabi, B. Yang, H.M. Adeel Sharif, J. Zhang, J. Ali, X. Zhao, Sustainable and easy recoverable magnetic TiO₂-Lignocellulosic Biomass@Fe₃O₄ for solar photocatalytic water remediation, *J. Clean. Prod.* 233 (2019) 841–847.
- [64] L.D.L. Miranda, C.R. Bellato, J.L. Milagres, L.G. Moura, A.H. Munteer, M.F. de Almeida, Hydrotalcite-TiO₂ magnetic iron oxide intercalated with the anionic surfactant dodecylsulfate in the photocatalytic degradation of methylene blue dye, *J. Environ. Manage.* 156 (2015) 225–235.
- [65] C.P.M. de Oliveira, A.L.A. Lage, D.C. da S. Martins, N.D.S. Mohallem, M.M. Viana,

- High surface area TiO₂ nanoparticles: impact of carboxylporphyrin sensitizers in the photocatalytic activity, *Surfaces and Interfaces*. 21 (2020) 100774.
- [66] A.A. Ismail, D.W. Bahnemann, Mesoporous titania photocatalysts: Preparation, characterization and reaction mechanisms, *J. Mater. Chem.* 21 (2011) 11686–11707.
- [67] L. Yang, S. Luo, Y. Li, Y. Xiao, Q. Kang, Q. Cai, High efficient photocatalytic degradation of p-nitrophenol on a unique Cu₂O/TiO₂ p-n heterojunction network catalyst, *Environ. Sci. Technol.* 44 (2010) 7641–7646.
- [68] M. Bonomo, Synthesis and characterization of NiO nanostructures: a review, *J. Nanoparticle Res.* 20 (2018) 1-26.
- [69] A. Barakat, M. Al-Noaimi, M. Suleiman, A.S. Aldwayyan, B. Hammouti, T. Ben Hadda, S.F. Haddad, A. Boshala, I. Warad, One step synthesis of NiO nanoparticles via solid-state thermal decomposition at low-temperature of novel aqua(2,9-dimethyl-1,10-phenanthroline)NiCl₂ complex, *Int. J. Mol. Sci.* 14 (2013) 23941–23954.
- [70] W. Sun, L. Xiao, X. Wu, Facile synthesis of NiO nanocubes for photocatalysts and supercapacitor electrodes, *J. Alloys Compd.* 772 (2019) 465–471.
- [71] R. Vahini, P.S. Kumar, S. Karuthapandian, Bandgap-tailored NiO nanospheres: an efficient photocatalyst for the degradation of crystal violet dye solution, *Appl. Phys. A Mater. Sci. Process.* 122 (2016) 1–8.
- [72] K.C. Lalithambika, A. Thayumanavan, K. Ravichandran, S. Sriram, Photocatalytic and antibacterial activities of eco-friendly green synthesized ZnO and NiO nanoparticles, *J. Mater. Sci. Mater. Electron.* 28 (2017) 2062–2068.
- [73] Z. Sabouri, A. Akbari, H.A. Hosseini, A. Hashemzadeh, M. Darroudi, Bio-based synthesized NiO nanoparticles and evaluation of their cellular toxicity and wastewater treatment effects, *J. Mol. Struct.* 1191 (2019) 101–109.
- [74] X. Wang, L. Chen, F. Li, S. Zhang, X. Chen, J. Yin, Synthesis of hollow NiO nanostructures and their application for supercapacitor electrode, *Ionics (Kiel)*. 25 (2019) 697–705.
- [75] F. Fazlali, A.R. Mahjoub, R. Abazari, A new route for synthesis of spherical NiO nanoparticles via emulsion nano-reactors with enhanced photocatalytic activity, *Solid State Sci.* 48 (2015) 263–269.
- [76] C. Su, L. Zhang, Y. Han, C. Ren, X. Chen, J. Hu, M. Zeng, N. Hu, Y. Su, Z. Zhou, Z.

- Yang, Controllable synthesis of crescent-shaped porous NiO nanoplates for conductometric ethanol gas sensors, *Sensors Actuators, B Chem.* 296 (2019) 126642.
- [77] K. Tian, X.X. Wang, H.Y. Li, R. Nadimicherla, X. Guo, Lotus pollen derived 3-dimensional hierarchically porous NiO microspheres for NO₂ gas sensing, *Sensors Actuators, B Chem.* 227 (2016) 554–560.
- [78] X. Yan, X. Tong, J. Wang, C. Gong, M. Zhang, L. Liang, Synthesis of mesoporous NiO nanoflake array and its enhanced electrochemical performance for supercapacitor application, *J. Alloys Compd.* 593 (2014) 184–189.
- [79] S.A. Abbas, K.D. Jung, Preparation of mesoporous microspheres of NiO with high surface area and analysis on their pseudocapacitive behavior, *Electrochim. Acta.* 193 (2016) 145–153.
- [80] Y. Wang, Y. Chen, J. Wang, X. Xv, X. Yang, J. Zhou, S. Li, F. Cao, G. Qin, Novel porous ultrathin NiO nanosheets for highly efficient water vapor adsorption-desorption, *Sep. Purif. Technol.* 226 (2019) 299–303.
- [81] X. Zhang, W. Shi, J. Zhu, W. Zhao, J. Ma, S. Mhaisalkar, T.L. Maria, Y. Yang, H. Zhang, H.H. Hng, Q. Yan, Synthesis of porous NiO nanocrystals with controllable surface area and their application as supercapacitor electrodes, *Nano Res.* 3 (2010) 643–652.
- [82] S. Safa, R. Hejazi, M. Rabbani, R. Azimirad, Hydrothermal synthesis of NiO nanostructures for photodegradation of 4-nitrophenol, *Desalin. Water Treat.* 57 (2016) 21982–21989.
- [83] T. Adinaveen, T. Karnan, S.A. Samuel Selvakumar, Photocatalytic and optical properties of NiO added *Nephelium lappaceum* L. peel extract: An attempt to convert waste to a valuable product, *Heliyon.* 5 (2019) 1-10.
- [84] D. Malwal, P. Gopinath, Fabrication and characterization of poly(ethylene oxide) templated nickel oxide nanofibers for dye degradation, *Environ. Sci. Nano.* 2 (2015) 78–85.
- [85] F. Motahari, M.R. Mozdianfard, F. Soofivand, M. Salavati-Niasari, NiO nanostructures: Synthesis, characterization and photocatalyst application in dye wastewater treatment, *RSC Adv.* 4 (2014) 27654–27660..
- [86] Z. Qing, L. Haixia, L. Huali, L. Yu, Z. Huayong, L. Tianduo, Solvothermal synthesis

- and photocatalytic properties of NiO ultrathin nanosheets with porous structure, *Appl. Surf. Sci.* 328 (2015) 525–530.
- [87] L. Lin, T. Liu, B. Miao, W. Zeng, Hydrothermal fabrication of uniform NiO nanosheets: structure, growth and response *Mater. Lett.* 102-103 (2013) 43-46.
- [88] J. Chen, M. Wang, J. Han, R. Guo, TiO₂ nanosheet/NiO nanorod hierarchical nanostructures: p–n heterojunctions towards efficient photocatalysis, *J. Colloid Interface Sci.* 562 (2020) 313–321.
- [89] M. Faisal, F.A. Harraz, A.A. Ismail, A.M. El-Toni, S.A. Al-Sayari, A. Al-Hajry, M.S. Al-Assiri, Novel mesoporous NiO/TiO₂ nanocomposites with enhanced photocatalytic activity under visible light illumination, *Ceram. Int.* 44 (2018) 7047–7056.
- [90] T. Sreethawong, S. Ngamsinlapasathian, S. Yoshikawa, Surfactant-aided sol-gel synthesis of mesoporous-assembled TiO₂-NiO mixed oxide nanocrystals and their photocatalytic azo dye degradation activity, *Chem. Eng. J.* 192 (2012) 292–300.
- [91] B. Sun, G. Zhou, T. Gao, H. Zhang, H. Yu, NiO nanosheet/TiO₂ nanorod-constructed p-n heterostructures for improved photocatalytic activity, *Appl. Surf. Sci.* 364 (2016) 322–331.
- [92] R. Vinoth, P. Karthik, K. Devan, B. Neppolian, M. Ashokkumar, TiO₂-NiO p–n nanocomposite with enhanced sonophotocatalytic activity under diffused sunlight, *Ultrason. Sonochem.* 35 (2017) 655–663.
- [93] M. Wang, J. Han, Y. Hu, R. Guo, Y. Yin, Carbon-Incorporated NiO/TiO₂ Mesoporous Shells with p-n Heterojunctions for Efficient Visible Light Photocatalysis, *ACS Appl. Mater. Interfaces.* 8 (2016) 29511–29521.
- [94] Q. Zhu, N. Liu, N. Zhang, Y. Song, M.S. Stanislaus, C. Zhao, Y. Yang, Efficient photocatalytic removal of RhB, MO and MB dyes by optimized Ni/NiO/TiO₂ composite thin films under solar light irradiation, *J. Environ. Chem. Eng.* 6 (2018) 2724–2732.
- [95] J. Wang, J. Li, Y. Xie, C. Li, G. Han, L. Zhang, R. Xu, X. Zhang, Investigation on solar photocatalytic degradation of various dyes in the presence of Er³⁺: gamma-Al₂O₃/ZnO-TiO₂ composite, *J. Environ. Manage.* 91 (2010) 677–684.
- [96] C.J. Chen, C.H. Liao, K.C. Hsu, Y.T. Wu, J.C.S. Wu, P-N junction mechanism on improved NiO/TiO₂ photocatalyst, *Catal. Commun.* 12 (2011) 1307–1310.
- [97] D. Sarkar, C.K. Ghosh, S. Mukherjee, K.K. Chattopadhyay, Three dimensional

- Ag₂O/TiO₂ type-II (p-n) nanoheterojunctions for superior photocatalytic activity, *ACS Appl. Mater. Interfaces*. 5 (2013) 331–337.
- [98] L. Li, B. Cheng, Y. Wang, J. Yu, Enhanced photocatalytic H₂-production activity of bicomponent NiO/TiO₂ composite nanofibers, *J. Colloid Interface Sci.* 449 (2015) 115–121.
- [99] M. Khairy, S.A. El-Safty, Mesoporous NiO nanoarchitectures for electrochemical energy storage: Influence of size, porosity, and morphology, *RSC Adv.* 3 (2013) 23801–23809.
- [100] V. Augustyn, P. Simon, B. Dunn, Pseudocapacitive oxide materials for high-rate electrochemical energy storage, *Energy Environ. Sci.* 7 (2014) 1597–1614.
- [101] C. Zhong, Y. Deng, W. Hu, J. Qiao, L. Zhang, J. Zhang, A review of electrolyte materials and compositions for electrochemical supercapacitors, *Chem. Soc. Rev.* 44 (2015) 7484–7539.
- [102] B. Pal, S. Yang, S. Ramesh, V. Thangadurai, R. Jose, Electrolyte selection for supercapacitive devices: A critical review, *Nanoscale Adv.* 1 (2019) 3807–3835.
- [103] A. Borenstein, O. Hanna, R. Attias, S. Luski, T. Brousse, D. Aurbach, Carbon-based composite materials for supercapacitor electrodes: A review, *J. Mater. Chem. A*. 5 (2017) 12653–12672.
- [104] Y. Wang, L. Zhang, H. Hou, W. Xu, G. Duan, S. He, K. Liu, S. Jiang, Recent progress in carbon-based materials for supercapacitor electrodes: a review, *J. Mater. Sci.* 56 (2021) 173–200.
- [105] M. Ciszewski, A. Koszorek, T. Radko, P. Szatkowski, D. Janas, Review of the Selected Carbon-Based Materials for Symmetric Supercapacitor Application, *J. Electron. Mater.* 48 (2019) 717–744.
- [106] Z.S. Iro, C. Subramani, S.S. Dash, A brief review on electrode materials for supercapacitor, *Int. J. Electrochem. Sci.* 11 (2016) 10628–10643.
- [107] G. Zhang, X. Xiao, B. Li, P. Gu, H. Xue, H. Pang, Transition metal oxides with one-dimensional/one-dimensional-analogue nanostructures for advanced supercapacitors, *J. Mater. Chem. A*. 5 (2017) 8155–8186.
- [108] M. Toupin, T. Brousse, D. Bélanger, Charge storage mechanism of MnO₂ electrode used in aqueous electrochemical capacitor, *Chem. Mater.* 16 (2004) 3184–3190.

- [109] S. Jeon, J.H. Jeong, H. Yoo, H.K. Yu, B.H. Kim, M.H. Kim, RuO₂ Nanorods on Electrospun Carbon Nanofibers for Supercapacitors, *ACS Appl. Nano Mater.* 3 (2020) 3847–3858.
- [110] N. Jabeen, Q. Xia, S. V. Savilov, S.M. Aldoshin, Y. Yu, H. Xia, Enhanced Pseudocapacitive Performance of α -MnO₂ by Cation Preinsertion, *ACS Appl. Mater. Interfaces.* 8 (2016) 33732–33740.
- [111] X. Yan, X. Tong, J. Wang, C. Gong, M. Zhang, L. Liang, Rational synthesis of hierarchically porous NiO hollow spheres and their supercapacitor application, *Mater. Lett.* 95 (2013) 1–4.
- [112] W. Huang, L. Li, D. Liang, W. Zhou, H. Wang, Z. Lu, S. Yu, Y. Fan, In situ synthesis of a 3D highly porous NiO film electrode with enhanced performance for supercapacitors, *Inorg. Chem. Front.* 6 (2019) 2927–2934.
- [113] J. Zhao, Y. Tian, A. Liu, L. Song, Z. Zhao, The NiO electrode materials in electrochemical capacitor: A review, *Mater. Sci. Semicond. Process.* 96 (2019) 78–90.
- [114] C. Wang, E. Zhou, W. He, X. Deng, J. Huang, M. Ding, X. Wei, X. Liu, X. Xu, NiCo₂O₄-based supercapacitor nanomaterials, *Nanomaterials.* 7 (2017) 1–23.
- [115] Y. Zhu, X. Ji, Z. Wu, W. Song, H. Hou, Z. Wu, X. He, Q. Chen, C.E. Banks, Spinel NiCo₂O₄ for use as a high-performance supercapacitor electrode material: Understanding of its electrochemical properties, *J. Power Sources.* 267 (2014) 888–900.
- [116] Y. Li, X. Han, T. Yi, Y. He, X. Li, Review and prospect of NiCo₂O₄-based composite materials for supercapacitor electrodes, *J. Energy Chem.* (2019) 54–78.
- [117] X. Hu, L. Wei, R. Chen, Q. Wu, J. Li, Reviews and Prospectives of Co₃O₄-Based Nanomaterials for Supercapacitor Application, *ChemistrySelect.* 5 (2020) 5268–5288.
- [118] A. Umar, S.D. Raut, A.A. Ibrahim, H. Algadi, H. Albargi, M.A. Alsaiari, M.S. Akhtar, M. Qamar, S. Baskoutas, Perforated Co₃O₄ nanosheets as high-performing supercapacitor material, *Electrochim. Acta.* 389 (2021) 138661.
- [119] H.L. Zhu, Y.Q. Zheng, Mesoporous Co₃O₄ anchored on the graphitic carbon nitride for enhanced performance supercapacitor, *Electrochim. Acta.* 265 (2018) 372–378.
- [120] S. Vijayakumar, S.H. Lee, K.S. Ryu, Hierarchical CuCo₂O₄ nanobelts as a supercapacitor electrode with high areal and specific capacitance, *Electrochim. Acta.* 182 (2015) 979–986.

- [121] A.K. Das, N.H. Kim, S.H. Lee, Y. Sohn, J.H. Lee, Facile synthesis of CuCo_2O_4 composite octahedrons for high performance supercapacitor application, *Compos. Part B Eng.* 150 (2018) 269–276.
- [122] J. Sun, C. Xu, H. Chen, A review on the synthesis of CuCo_2O_4 -based electrode materials and their applications in supercapacitors, *J. Mater.* 7 (2021) 98–126.
- [123] P.M. Kulal, D.P. Dubal, C.D. Lokhande, V.J. Fulari, Chemical synthesis of Fe_2O_3 thin films for supercapacitor application, *J. Alloys Compd.* 509 (2011) 2567–2571.
- [124] V.D. Nithya, N.S. Arul, Review on $\alpha\text{-Fe}_2\text{O}_3$ based negative electrode for high performance supercapacitors, *J. Power Sources.* 327 (2016) 297–318.
- [125] T. Li, H. Yu, L. Zhi, W. Zhang, L. Dang, Z. Liu, Z. Lei, Facile Electrochemical Fabrication of Porous Fe_2O_3 Nanosheets for Flexible Asymmetric Supercapacitors, *J. Phys. Chem. C.* 121 (2017) 18982–18991.
- [126] N. Kumar, A. Kumar, S. Chandrasekaran, T.Y. Tseng, Synthesis of Mesoporous NiFe_2O_4 Nanoparticles for Enhanced Supercapacitive Performance, *J. Clean Energy Technol.* 6 (2018) 51–55.
- [127] X. Gao, W. Wang, J. Bi, Y. Chen, X. Hao, X. Sun, J. Zhang, Morphology-controllable preparation of NiFe_2O_4 as high performance electrode material for supercapacitor, *Electrochim. Acta.* 296 (2019) 181–189.
- [128] F. Liu, X. Wang, J. Hao, S. Han, J. Lian, Q. Jiang, High Density Arrayed Ni/NiO Core-shell Nanospheres Evenly Distributed on Graphene for Ultrahigh Performance Supercapacitor, *Sci. Rep.* 7 (2017) 1–10.
- [129] L. Jiang, D. Luo, Q. Zhang, S. Ma, G. Wan, X. Lu, Z. Ren, Electrochemical Performance of Free-Standing and Flexible Graphene and TiO_2 Composites with Different Conductive Polymers as Electrodes for Supercapacitors, *Chem. - A Eur. J.* 25 (2019) 7903–7911.
- [130] N. Duraisamy, A. Numan, S.O. Fatin, K. Ramesh, S. Ramesh, Facile sonochemical synthesis of nanostructured NiO with different particle sizes and its electrochemical properties for supercapacitor application, *J. Colloid Interface Sci.* 471 (2016) 136–144.
- [131] P. Pandurangan, T.N. Parvin, B. Soundiraraju, Y. Johnbosco, M. Ramalingam, M. Bhagavathiachari, S.A. Suthanthiraraj, S.S. Narayanan, Ultrasmall NiO nanoclusters modified with conical Ni(II)-SR staples for high performance supercapacitor

- applications, *New J. Chem.* 41 (2017) 6127–6136.
- [132] S. Pilban Jahromi, A. Pandikumar, B.T. Goh, Y.S. Lim, W.J. Basirun, H.N. Lim, N.M. Huang, Influence of particle size on performance of a nickel oxide nanoparticle-based supercapacitor, *RSC Adv.* 5 (2015) 14010–14019.
- [133] N. Duraisamy, K. Kandiah, R. Rajendran, S. Prabhu, R. Ramesh, G. Dhanaraj, Electrochemical and photocatalytic investigation of nickel oxide for energy storage and wastewater treatment, *Res. Chem. Intermed.* 44 (2018) 5653–5667.
- [134] S.I. Kim, J.S. Lee, H.J. Ahn, H.K. Song, J.H. Jang, Facile route to an efficient NiO supercapacitor with a three-dimensional nanonetwork morphology, *ACS Appl. Mater. Interfaces.* 5 (2013) 1596–1603.
- [135] B. Gnana Sundara Raj, B. Natesan, A.M. Asiri, J.J. Wu, S. Anandan, Pseudocapacitive properties of nickel oxide nanoparticles synthesized via ultrasonication approach, *Ionics (Kiel)*. (2019).
- [136] S. Chatterjee, R. Maiti, M. Miah, S.K. Saha, D. Chakravorty, NiO Nanoparticle Synthesis Using a Triblock Copolymer: Enhanced Magnetization and High Specific Capacitance of Electrodes Prepared from the Powder, *ACS Omega.* 2 (2017) 283–289.
- [137] D. Han, X. Jing, J. Wang, P. Yang, D. Song, J. Liu, Porous lanthanum doped NiO microspheres for supercapacitor application, *J. Electroanal. Chem.* 682 (2012) 37–44.
- [138] X. Zhang, W. Shi, J. Zhu, W. Zhao, J. Ma, S. Mhaisalkar, T.L. Maria, Y. Yang, H. Zhang, H.H. Hng, Q. Yan, Synthesis of porous NiO nanocrystals with controllable surface area and their application as supercapacitor electrodes, *Nano Res.* 3 (2010) 643–652.
- [139] X.L. Guo, M. Kuang, F. Li, X.Y. Liu, Y.X. Zhang, F. Dong, D. Losic, Engineering of three dimensional (3-D) diatom@TiO₂@MnO₂ composites with enhanced supercapacitor performance, *Electrochim. Acta.* 190 (2016) 159–167..
- [140] A. Ray, A. Roy, P. Sadhukhan, S.R. Chowdhury, P. Maji, S.K. Bhattacharya, S. Das, Electrochemical properties of TiO₂-V₂O₅ nanocomposites as a high performance supercapacitors electrode material, *Appl. Surf. Sci.* 443 (2018) 581–591.
- [141] S. Park, D. Shin, T. Yeo, B. Seo, H. Hwang, J. Lee, W. Choi, Combustion-driven synthesis route for tunable TiO₂/RuO₂ hybrid composites as high-performance electrode materials for supercapacitors, *Chem. Eng. J.* 384 (2020) 123269.

- [142] A. Achour, R. Lucio-Porto, M. Chaker, A. Arman, A. Ahmadpourian, M.A. Soussou, M. Boujtita, L. Le Brizoual, M.A. Djouadi, T. Brousse, Titanium vanadium nitride electrode for micro-supercapacitors, *Electrochem. Commun.* 77 (2017) 40–43.
- [143] P. Chen, C. Cao, C. Ding, Z. Yin, S. Qi, J. Guo, M. Zhang, Z. Sun, One-body style photo-supercapacitors based on Ni(OH)₂/TiO₂ heterojunction array: High specific capacitance and ultra-fast charge/discharge response, *J. Power Sources.* 521 (2022) 230920.
- [144] F. Tao, Y. Shen, Y. Liang, H. Li, Synthesis and characterization of Co(OH)₂/TiO₂ nanotube composites as supercapacitor materials, *J. Solid State Electrochem.* 11 (2007) 853–858.
- [145] Z. Shao, H. Li, M. Li, C. Li, C. Qu, B. Yang, Fabrication of polyaniline nanowire/TiO₂ nanotube array electrode for supercapacitors, *Energy.* 87 (2015) 578–585.
- [146] Y. Gao, Y. Wang, X. Xu, K. Ding, D. Yu, Synthesis of polypyrrole-titanium dioxide brush-like nanocomposites with enhanced supercapacitive performance, *RSC Adv.* 4 (2014) 63719–63724.
- [147] J.H. Kim, K. Zhu, Y. Yan, C.L. Perkins, A.J. Frank, Microstructure and pseudocapacitive properties of electrodes constructed of oriented NiO-TiO₂ nanotube arrays, *Nano Lett.* 10 (2010) 4099–4104.
- [148] S. Lee, J. Lee, K. Nam, W.G. Shin, Y. Sohn, Application of Ni-Oxide@TiO₂ core-shell structures to photocatalytic mixed dye degradation, CO oxidation, and supercapacitors, *Materials (Basel).* 9 (2016) 1–15.
- [149] Q. Ke, M. Zheng, H. Liu, C. Guan, L. Mao, J. Wang, 3D TiO₂ @Ni(OH)₂ Core-shell Arrays with Tunable Nanostructure for Hybrid Supercapacitor Application, *Sci. Rep.* 5 (2015) 1–11.
- [150] L.H. Cui, Y. Wang, X. Shu, J.F. Zhang, C.P. Yu, J.W. Cui, H.M. Zheng, Y. Zhang, Y.C. Wu, Supercapacitive performance of hydrogenated TiO₂ nanotube arrays decorated with nickel oxide nanoparticles, *RSC Adv.* 6 (2016) 12185–12192.
- [151] Y. Xie, C. Huang, L. Zhou, Y. Liu, H. Huang, Supercapacitor application of nickel oxide-titania nanocomposites, *Compos. Sci. Technol.* 69 (2009) 2108–2114.
- [152] M. Sumathi, A. Prakasam, P.M. Anbarasan, Fabrication of Hexagonal Disc Shaped Nanoparticles g-C₃N₄/NiO Heterostructured Nanocomposites for Efficient Visible

- Light Photocatalytic Performance, *J. Clust. Sci.* 6 (2019).
- [153] P. Anandhi, V.J.S. Kumar, S. Harikrishnan, Preparation and Improved Capacitive Behavior of NiO/TiO₂ Nanocomposites as Electrode Material for Supercapacitor, *Curr. Nanosci.* 16 (2019) 79–85.
- [154] Y. Lu, X.L. Liu, L. He, Y.X. Zhang, Z.Y. Hu, G. Tian, X. Cheng, S.M. Wu, Y.Z. Li, X.H. Yang, L.Y. Wang, J.W. Liu, C. Janiak, G.G. Chang, W.H. Li, G. Van Tendeloo, X.Y. Yang, B.L. Su, Spatial Heterojunction in Nanostructured TiO₂ and Its Cascade Effect for Efficient Photocatalysis, *Nano Lett.* 20 (2020) 3122–3129.
- [155] X. Sun, M. Xie, J.J. Travis, G. Wang, H. Sun, J. Lian, S.M. George, Pseudocapacitance of amorphous TiO₂ thin films anchored to graphene and carbon nanotubes using atomic layer deposition, *J. Phys. Chem. C.* 117 (2013) 22497–22508.
- [156] M. Anjum, R. Kumar, S.M. Abdelbasir, M.A. Barakat, Carbon nitride/titania nanotubes composite for photocatalytic degradation of organics in water and sludge: Pre-treatment of sludge, anaerobic digestion and biogas production, *J. Environ. Manage.* 223 (2018) 495–502.

CHAPTER II:
SYNTHESIS,
CHARACTERIZATION AND
CATALYTIC APPLICATION OF
NANOPOROUS TiO₂ CATALYTS

2.1 PROLOGUE

The nanoporous TiO₂ catalysts have been synthesized using reflux assisted sol-gel method. The different structure directing agents used for these syntheses are urea, oxalic acid, tricarballic acid and 1,2,3,4 butanetetracarboxylic acid. The details of chemicals used and synthesis procedures are presented in section 2.2 and 2.4 respectively. The effect of each structure directing agent as well as their desired combinations on morphological and catalytic properties of synthesized catalysts have been investigated. All the synthesized catalyst have been characterized in detail using the characterization techniques listed in section 2.3. Finally, the catalytic efficiency of all the synthesized TiO₂ catalysts were evaluated for adsorption and photocatalytic degradation of Amaranth dye. The novel findings of this investigation are presented in detail in the results and discussion section 2.5 along with conclusions of this study in section 2.6.

2.2 CHEMICALS USED

The chemicals such as Titanium isopropoxide (98 %), Ammonia solution (25 % in water), Urea (99.5 %), Oxalic acid (99.5 %), Tricarballic acid (99%) and Butanetetracarboxylic acid (99%) were purchased from Alfa Aesar. Amaranth dye (85 %) was purchased from Loba Chemie, India and used without any further purification.

2.3 INSTRUMENTATION

The principles of different instrumental techniques used in this thesis have been presented in brief in this section.

2.3.1 Characterization techniques

All the synthesized catalysts were characterized using different characterization techniques such as Thermogravimetric-Differential Thermal Analysis (TG-DTA), Infrared Spectroscopy (IR), Powder X-ray Diffraction (XRD), UV-Vis Diffuse Reflectance Spectroscopy (UV-DRS), Scanning Electron Microscopy (SEM), High Resolution-Transmission Electron Microscopy (HR-TEM), N₂-adsorption-desorption isotherm studies, (BET) Surface area analysis, Energy-Dispersive X-ray Spectroscopy (EDS) and X-ray Photoelectron Spectroscopy (XPS). The principles and the associated equations of these techniques are summarized below.

➤ **Thermogravimetric-Differential Thermal Analysis (TG-DTA)**

Thermogravimetric analysis measures the change in the weight of the sample associated with its decomposition or any other physical or chemical changes that results in sample weight gain or loss under controlled temperature and gas atmosphere. A plot of percent weight change as a function of temperature enables us to understand the physical or chemical changes that have caused the sample to gain or lose weight. DTA measures the difference in temperature (ΔT), between the inert reference material (alpha alumina) and the sample as a function of temperature. In the present study all the synthesized precursors were analyzed using NETZSCH TG/DTA STA 409 PC instrument in the temperatures range of 30 to 800 °C in air atmosphere at the heating rate of 10 °C.min⁻¹.

➤ **Infrared Spectroscopy (IR)**

It is a vibrational spectroscopy which determines the vibrational frequency of the bonds and functional groups present in a given molecule or compound. The essential criteria for a molecule to be IR active is the “change in dipole moment”. In a Fourier transform infrared technique a beam of infrared light passes through a sample under analysis. The absorption of radiation takes place when a frequency of particular vibration is equal to the frequency of IR radiation focused on the molecule and the transmitted light allows us to understand the energy absorbed at each incident frequency. In the present study all the samples were grounded with KBr and the spectrum was recorded under IR radiations in the vibration frequency range of 4000-400 cm⁻¹ at ambient temperature using the SHIMADZU IR-PRESTIGE-21 IR spectrophotometer.

➤ **Powder X-Ray Diffraction (XRD)**

XRD is a very reliable technique to know the crystal structure of the sample under investigation. It basically depends on the constructive interference of monochromatic X-rays and the crystalline sample. These generated X-rays by a cathode ray tube are filtered to produce a monochromatic radiations which are then collimated and are directed towards the sample. The interaction between the incident rays and the sample results in diffraction of X-rays. The constructive interference of these diffracted X-rays is produced upon satisfying the Bragg's law ($n\lambda = 2d\sin\theta$). This law relates the wavelength of electromagnetic radiation to

the diffraction angle and the lattice spacing in a crystalline sample. The diffracted X-rays are then detected, processed and counted by scanning the sample through a range of 2θ angles. The crystalline nature and phase purity analysis of all the synthesized catalysts in this thesis were performed in the diffraction region of $2\theta = 10 - 80^\circ$ on a RIGAKU ULTIMA IV X-Ray diffractometer using Cu $K\alpha$ (1.5418 Å) source and Ni filter.

➤ **Field Emission Scanning Electron Microscopy (FE-SEM) & Energy Dispersive X-ray spectroscopy (EDS)**

SEM is a popular technique to view or analyze the surface morphology of the samples. It works on the principle of applying kinetic energy to produce signals on the interaction of the electrons. These electrons are secondary electrons, backscattered electrons, and diffracted electrons which are used to view the surface morphology. These secondary electrons and backscattered electrons from the sample are used to produce an image. In EDS analysis, when the X-ray hits the target electron based on its source energy, the target electrons get knocked off from its shell leaving behind a positively charged hole. This hole attracts another electron from an outer shell to fill up the vacancy. As the electron moves from the outer higher energy to the inner lower energy shell of an atom the difference in the energy is released in the form of X-rays. The energy of this X-ray is unique to the specific element and hence can be used to identify the elements present in the sample.

The surface morphology of the synthesized metal oxides were analyzed using i) SEM Zeiss Evo 18 and ii) Field Emission scanning electron microscopy (FESEM) and elemental analysis using JEOL JSM-7610F coupled with Ametek edx PV6500 respectively. All the samples were mounted on a carbon tape and spray coated with Au/Pd prior to analysis.

➤ **High Resolution Transmission Electron Microscopy (HRTEM) and Selected Area Electron Diffraction (SAED) Analysis**

This is a very powerful technique capable of elucidating the morphology, inner structure and particle size of the material. It is a microscopic technique in which the transmitted electrons through a sample are detected and recorded in the form of an image. The particle size and selected area diffraction analysis (SAED) of the fringe structure of all the synthesized samples were determined using high-resolution transmission electron microscopy (Tecnai

TEM 200 kV). All the samples were sonicated in acetone for 15 minutes and subsequently coated on a Lacey carbon 400 mesh Cu TEM grid and dried under IR lamp prior to the analysis.

➤ UV-Diffuse Reflectance Spectroscopy (UV-DRS)

UV-DRS is a technique used for studying the spectral characteristics of the opaque solid samples. When the UV or visible light is incident on a material, it absorbs the incident light energy resulting in excitation of electrons from the valence band to conduction band of the sample. This causes relative decrease in the light intensity of the particular energy with respect to the reference source. In particular the diffused light intensity from the surface of the material is measured as a function of wavelength and processed subsequently.

The band gap of the synthesized catalysts were analyzed by recording the diffuse reflectance of the solid samples using SHIMADZU UV-Visible spectrophotometer (UV 2450) in the wavelength range of 200-800 nm. The reference compound used for the analysis was BaSO₄. By using the wavelength of absorption (λ), the band gap was calculated as per the equation E1.

$$E(eV) = \frac{1240}{\lambda} \quad (E1)$$

➤ UV-Visible Spectroscopy

It refers to the absorption spectroscopy which measures the absorbance/transmittance of a sample as a function of wavelength of electromagnetic radiation. In this thesis, the change in concentration of Amaranth dye solution during the adsorption and photocatalytic reaction were monitored by recording the absorbance of aliquots at different reaction times using Shimadzu UV2450 UV-visible spectrophotometer in the wavelength range of 200-800 nm. Concentrations were obtained from the measured absorbance using the Beer-Lamberts Law:

$$A = \epsilon lc \quad (E2)$$

wherein 'A' is the absorbance, ' ϵ ' is the molar absorptivity coefficient, ' l ' is the optical path length in cm and ' c ' is the concentration.

➤ X-ray Photoelectron Spectroscopy (XPS)

In XPS analysis, when X-rays are bombarded on the sample, some of the core electrons absorb this energy (\geq the binding energy of the electrons) and escape from the atom. By analyzing the energy of these electrons the oxidation state and binding energy of the sample is determined. The oxidation state of all the metal ion in the catalyst were confirmed using XPS analysis with a Kratos Axis Supra DLD spectrophotometer, equipped with a monochromatic Al K α X-ray source ($h\nu = 1486.6$ eV) operating at 150 with a multi-channel plate and delay line detector under a vacuum of $\sim 10^{-9}$ mbar. The calibration of the instrument was performed using the adventitious carbon C1s at 284.8 eV.

➤ N₂ adsorption-desorption isotherms & Surface area analysis

Brunauer-Emmett-Teller (BET) surface area analysis is the multipoint measurements of sample's surface area through gas adsorption-desorption analysis. The N₂ adsorption – desorption isotherms were recorded at varying adsorption pressures to construct the isotherm. The monolayer formation of the gas molecules on the solid surface is used to determine the specific surface area of the sample. The surface area, pore size and pore volume of the catalysts were analyzed using the Quantachrome NOVA-1000 surface area analyzer by N₂ adsorption/desorption method at -196 °C. All the samples were degassed at 200 °C for 2 hours prior to adsorption analysis so as to remove the pre-adsorbed gases and the moisture from the sample.

2.3.2 Photocatalytic reactor design and operation

Figure 2.1 showcases the different parts of the photocatalytic reactor which consists of a 300 mL quartz vessel equipped with a gas and liquid sampling port. Two additional port: one for temperature while other for catalyst loading is available. Double quartz jacketed 250 Watt, medium pressure mercury vapor UV lamp is immersed into the reactor maintaining circulation of cold water through the double jacketed chamber that allows maintaining steady temperature of the UV lamp. The entire assembly is placed on a Teflon coated magnetic stirrer operating at 1500 RPM. This assembly is placed in a UV safety cabinet with a built in exhaust fan and LED light source. The duration of exposure of UV light to the solution is controlled by a programmed digital UV lamp controller unit.

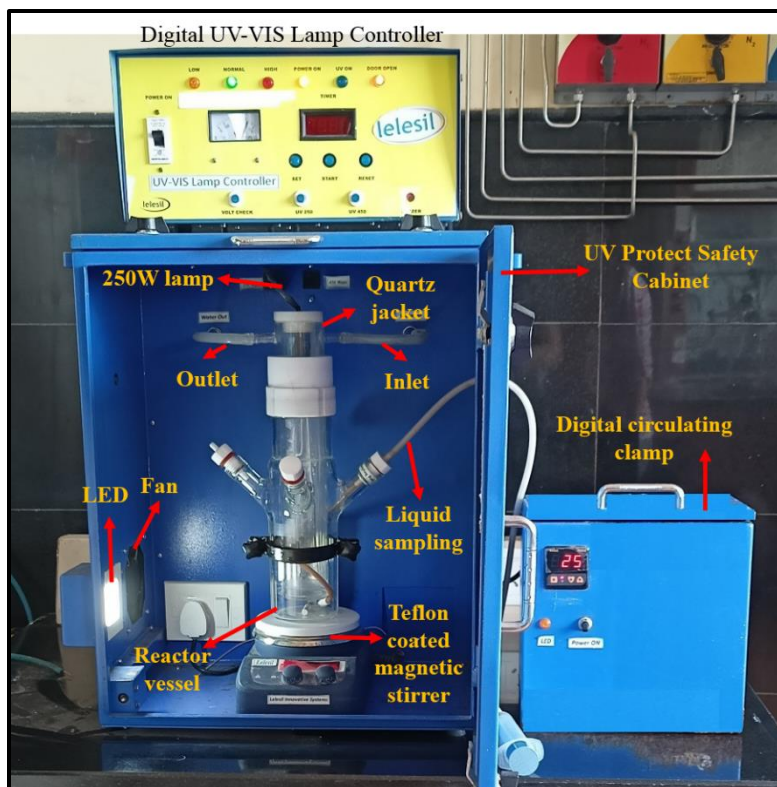


Figure 2.1: Photocatalytic reactor system.

2.4 EXPERIMENTAL: SYNTHESIS STRATEGY AND PROCEDURES

2.4.1. Synthesis of TiO_2 using urea as a fuel for sol-gel-combustion synthesis.

The TiO_2 synthesis procedure is schematically depicted in Figure 2.2. The syntheses were carried out by dispersing 4 mL titanium isopropoxide in isopropanol (60 mL) at 8 °C. To this mixture 1M NH_4OH (60 mL) was added dropwise for the formation of titanium hydroxide gel. The obtained $\text{Ti}(\text{OH})_4$ gel was modified with addition of aqueous urea solution (varying the titanium : urea ratio as 1:2 to 1:12). The resultant gel was then refluxed at 80 °C in 1M HNO_3 and ethanol mixture for 24 hours with continuous stirring. Further the refluxed gel was digested at 100 °C to obtain a dried semi-solid which was then calcined at 500°C in a preheated furnace for 1 hour. The calcination temperature was chosen based on the TG-DTA analysis as presented in Figure 2.6. The obtained TiO_2 synthesized using different urea ratios are labeled as TU2, TU4, TU6, TU8, TU10 and TU12. In a similar procedure pristine TiO_2 was also synthesized without the addition of urea and it is labeled as PT.

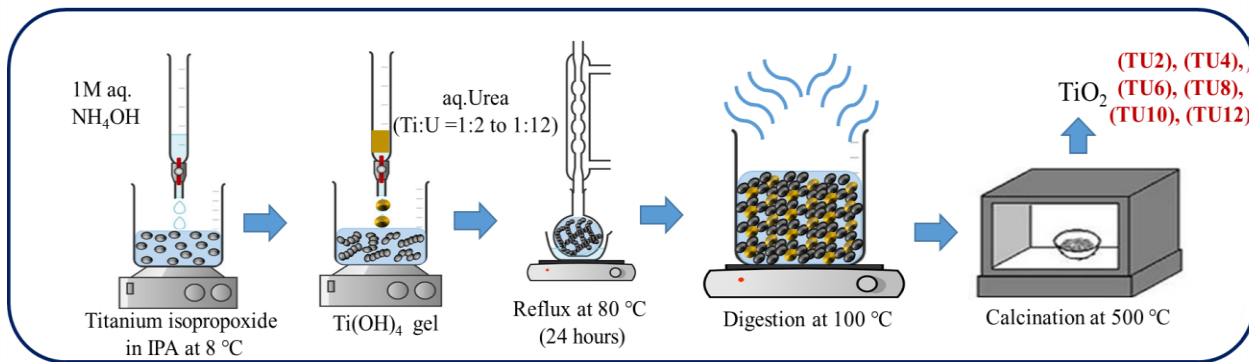


Figure 2.2: Scheme of TiO₂ synthesis using urea as structure directing agent.

2.4.2 Synthesis of TiO₂ using carboxylic acids as structure-directing agents.

The synthesis of TiO₂ was carried out using reflux assisted sol-gel method and carboxylic acids such as oxalic acid, tricarballic acid and butanetetracarboxylic acid were used as structure directing agents. In an experimental procedure 4 mL of titanium isopropoxide precursor was dispersed in isopropanol solvent (maintained at 8 °C). The solution was further hydrolyzed using 1M NH₄OH solution to form titanium hydroxide gel. This gel was further modified by addition of aqueous solution of each of the carboxylic acids (optimized Ti : carboxylic acids ratio of 1:8) as presented in Figure 2.3. The resultant gel was then refluxed at 80 °C in 1M HNO₃ and ethanol mixture for 24 hours with continuous stirring. Further the refluxed gel was digested at 100 °C to obtain a semi-solid which was then calcined at 550 °C in a preheated furnace for 1 hour. The calcination temperature was chosen based on the TG-DTA analysis presented in Figure 2.6. The obtained catalyst are labeled as TOA, TTC and TBTC.

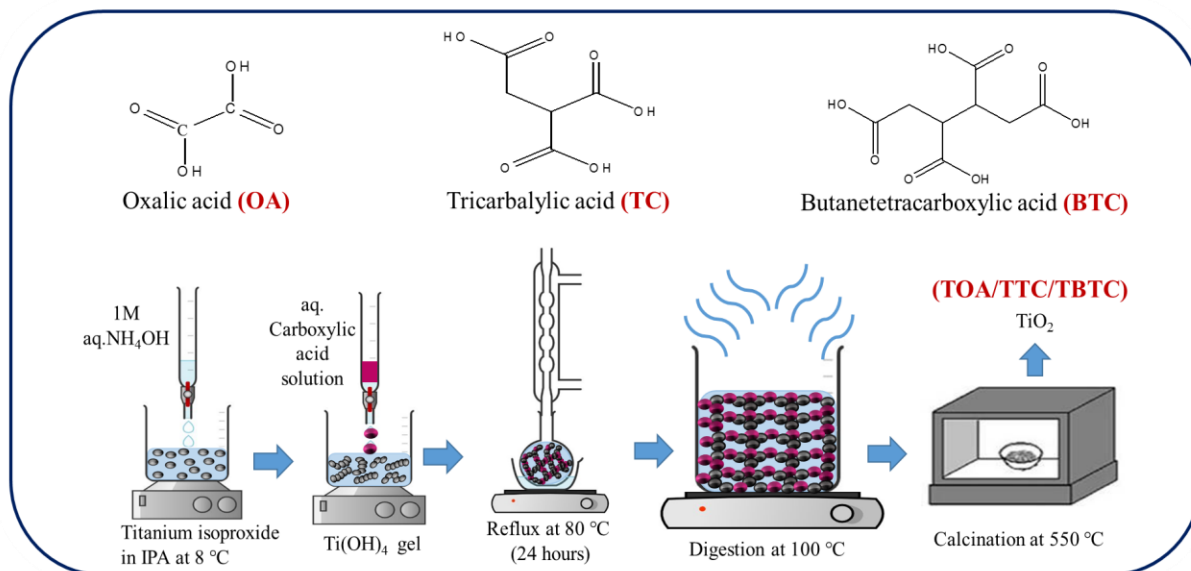


Figure 2.3: Synthesis of TiO_2 using carboxylic acids (OA, TC and BTC) as SDA.

2.4.3 Synthesis of TiO_2 using carboxylic acids and urea mixtures.

The synthesis of TiO_2 was carried out using reflux assisted sol-gel method using carboxylic acids such as oxalic acid, tricarballic acid, butanetetracarboxylic acid and urea as structure directing agents (SDA). In an experimental procedure 4 mL of titanium isopropoxide precursor was dispersed in isopropanol solvent (at 8 °C). The dispersed titanium isopropoxide was further hydrolyzed using 1M NH_4OH solution to form titanium hydroxide gel. This gel was further modified by addition of aqueous solution of each of the carboxylic acid followed by urea (in the ratio Ti: carboxylic acids: urea, 1:8:8) as presented in Figure 2.4. The resultant gel was then refluxed at 80 °C in 1M HNO_3 and ethanol mixture for 24 hours with continuous stirring. Further the reflux gel was digested at 100 °C to obtain a dried semi-solid which was then calcined at 550 °C in a preheated furnace for 1 hour as per the TG-DTA analysis. The obtained catalyst were labelled as TOAU, TTCU and TBTCU respectively.

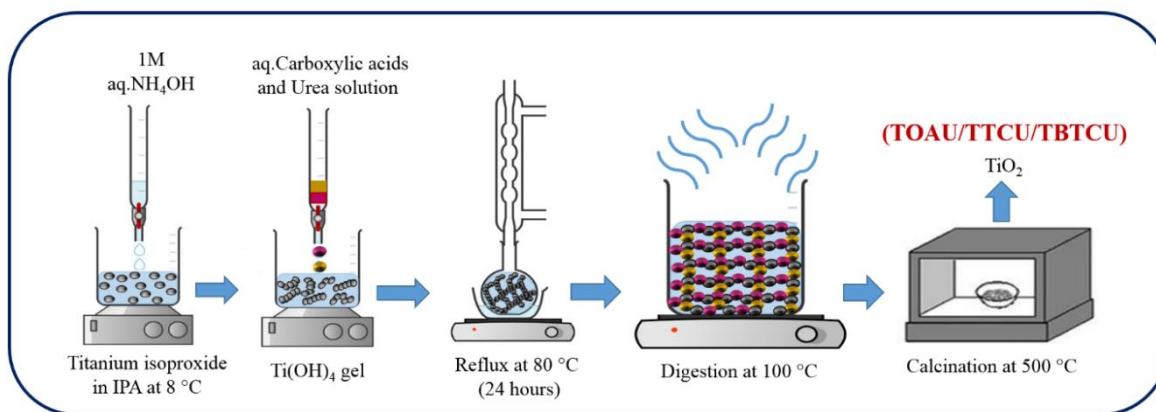


Figure 2.4: Synthesis of TiO₂ using carboxylic acid and urea mixture as SDA.

All the synthesized catalysts were then characterized using the techniques listed in section 2.3 and subsequently their adsorption capacities and photocatalytic dye degradation efficiencies were measured using the protocols as described below.

2.4.4 Protocol of adsorption isotherm and kinetic experiment.

In a typical adsorption experiment the pre-activated TiO₂ catalyst (0.3 g) was dispersed in 1L Amaranth dye solution of varied concentration from 10 to 110 ppm. The solution pH was adjusted to 2 using 1N HCl and it was then kept on shaker for 24 hours at room temperature. The absorbance of each of the solution was recorded at 520 nm using UV-Visible spectrophotometer. The adsorption capacity at equilibrium (q_e), and the Amaranth removal efficiency of each of the TiO₂ catalyst was determined using the standard adsorption isotherm models. [1,2] The graph of q_e as a function of initial concentration of Amaranth dye was fitted using non-linear forms of different adsorption isotherm models such as Langmuir, Freundlich, Sips and Temkin models [3–5].

Similarly the adsorption kinetic experiment were performed to know the reaction rate and the adsorption mechanism. In a typical experiment 0.3 g of each of the TiO₂ catalyst was dispersed in 1L of 30 ppm Amaranth dye solution. At regular interval of time an aliquots were taken and the absorbance of the solution was recorded using UV-Visible spectrophotometer at 520 nm. The obtained experimental data was fitted using different adsorption kinetic models such as pseudo first order, pseudo second order, Elovich model

and intraparticle diffusion model. The mathematical equations of all the above-mentioned isotherm models and adsorption kinetic models are presented in Table 2.1 and Table 2.2 respectively. The obtained results are discussed in detail in section 2.5.2.

Models	Equations	Parameters
Langmuir	$q_e = \frac{q_m K_L C_e}{1 + K_L C_e}$ $R_L = \frac{1}{1 + K_L C_0}$	q_m : Maximum capacity of adsorption, mg.g^{-1} K_L : Affinity of the binding sites, L.mg^{-1} R_L : Separation factor
Freundlich	$q_e = K_F C_e^{\frac{1}{n}}$	K_F : Freundlich parameter, $(\text{L.mg}^{-1})^{1/n}(\text{mg.g}^{-1})$ n : Heterogeneity parameter ($n < 1$)
Temkin	$q_e = B \ln(K_T C_e)$ $B = \frac{RT}{b_T}$	B : Temkin Parameter, mg.g^{-1} K_T : Adsorption capacity, L.mg^{-1} b : Heat of sorption, kJ.mol^{-1}
Sips	$q_e = \frac{q_m (K_S C_e)^m}{1 + (K_S C_e)^m}$	q_m : Maximum capacity of adsorption, mg.g^{-1} K_S : Sips isotherm model constant, L. mg^{-1} m : Exponent

Table 2.1: Mathematical equations of different adsorption isotherm models.

Name	Expression	Parameters
Pseudo-first-order	$q_t = q_e(1 - e^{-k_1 t})$	k_1 : Pseudo-first-order rate constant, min^{-1}
Pseudo-second-order	$q_t = \frac{k_2 q_e^2 t}{1 + k_2 q_e t}$	k_2 : Pseudo-second-order rate constant, $\text{g.mg}^{-1}.\text{min}^{-1}$
Elovich	$q_t = \frac{1}{\beta} \ln(\alpha\beta) + \frac{1}{\beta} \ln t$	α : Initial adsorption rate constant, $\text{mg.g}^{-1}.\text{min}^{-1}$ β : Adsorption rate constant during any one experiment, g.min^{-1}
Intraparticle diffusion	$q_t = k_{ID} t^{\frac{1}{2}} + C$	k_{ID} : Intraparticle diffusion rate constant, $\text{mg.g}^{-1}.\text{min}^{-1/2}$ C: Intercept, mg.g^{-1}

Table 2.2: Mathematical equations of different adsorption kinetic models.

2.4.5 Protocol of photocatalytic degradation studies.

The photocatalytic performance of all the synthesized TiO_2 were evaluated for Amaranth dye degradation study. 90 mg of the pre-activated TiO_2 catalyst was dispersed in 300 mL (30 ppm) dye solution and the mixture was transferred in a photocatalytic reactor. The solution was then irradiated with 250 watt MPMVL (Medium pressure mercury-vapour lamp) for 60 minutes at room temperature. The reaction was monitored by sampling the solution after every five minutes and recording its absorbance using UV-Visible spectrophotometer at 520 nm as presented in Figure 2.5. Furthermore the various reaction parameters were optimized such as catalyst dosage, initial concentration of Amaranth dye, and the pH of the solution. The obtained results are discussed in section 2.6.

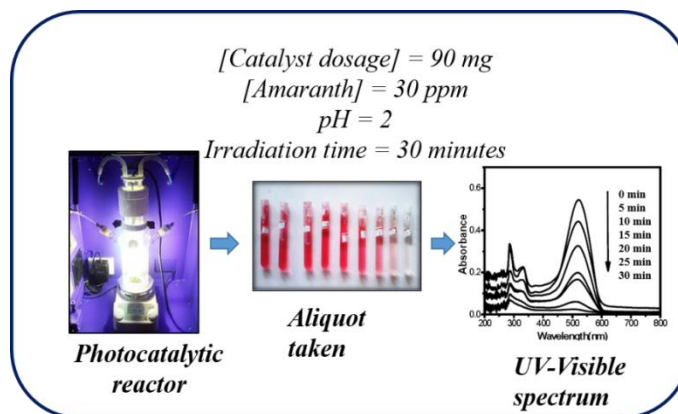


Figure 2.5: Schematic representation of Amaranth dye degradation experiment.

2.5 RESULT AND DISCUSSION

2.5.1 Characterization of synthesized TiO₂ catalysts

The effect of urea, oxalic acid, tricarballic acid, butanetetracarboxylic acid and the combination of these acids with urea on the phase purity, morphology, particle size and the surface area of TiO₂ has been investigated using different characterization techniques which are discussed in detail in the subsequent sections.

➤ Effect of Ti:urea ratio on surface area of TiO₂

The TiO₂ has been synthesized using urea as structure directing agent and its physicochemical properties are compared with that of pristine TiO₂. The obtained titanium hydroxide gel with and without urea were subjected to TG-DTA analysis. Figure 2.6 (a) and (b) represents the TG-DTA plot for titanium hydroxide gel without and with urea as SDA respectively. The TG-DTA analysis of the precursor gel was carried out from 30 to 800 °C in air at a heating rate of 10 °C.min⁻¹. The initial weight loss at 120 °C and 202 °C in titanium hydroxide gel and titanium hydroxide-urea gel accounts for the loss of physically adsorbed water. The second major weight loss is due to the decomposition of the organic component and phase transition of the titanium hydroxide gel into TiO₂. From temperature of 500 °C to 800 °C no major change in weight loss was seen which confirms the formation of stable phase of metal oxide. To confirm this observation, IR analysis of the precursor gel and of the calcined TiO₂ were carried out at room temperature in the range of 400 to 4000 cm⁻¹ and the observed different vibration modes were accounted. Figure 2.6 (c) represents the titanium hydroxide gel with vibration frequencies of C-H, O-H, and Ti-O stretching and bending vibration [6,7]. Similarly Figure 2.6 (d) represents the IR spectrum of titanium hydroxide/urea gel with characteristic stretching vibrations of O-H, C-H and N-H along with bending vibrations of O-H [8,9] at the corresponding wavenumbers marked in the Figure 2.6 c & d. However, upon calcination at 500 °C no characteristics peaks of organic functional groups corresponding to the precursors and SDA's were observed except OH stretching, OH bending and Ti-O-Ti stretching vibrations which confirms the complete removal of the SDA and transformation of the gel into TiO₂[10,11]. The effect of urea on the surface area of the synthesized TiO₂ catalysts were further investigated using N₂ adsorption-desorption analysis.

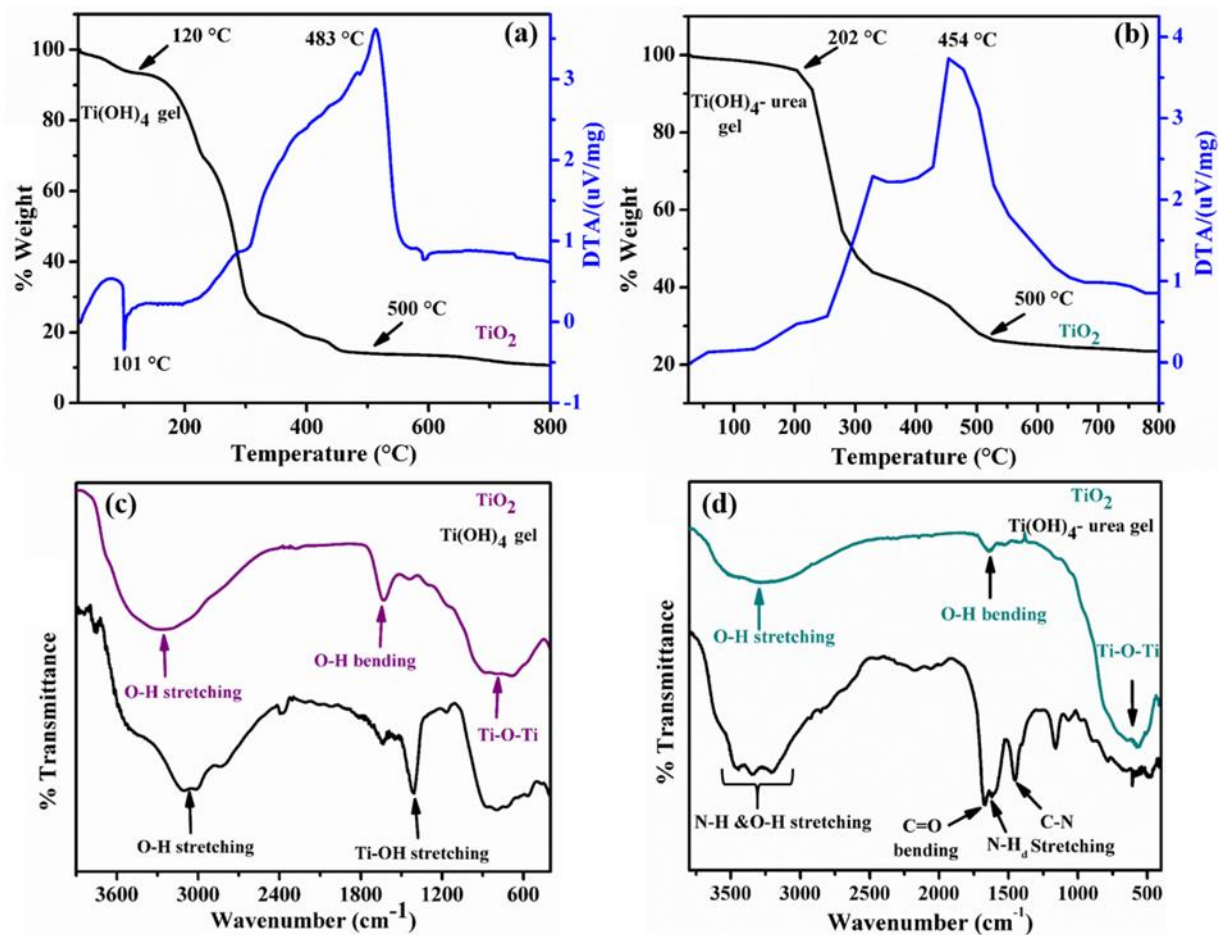


Figure 2.6: (a, b) TG-DTA and (c, d) IR spectra of titanium precursor gel without and with urea as SDA.

Figure 2.7 shows the N_2 adsorption-desorption isotherms of the TiO_2 synthesized with and without urea. All the as-synthesized TiO_2 catalysts displayed type IV isotherms with a hysteresis loop typical of mesoporous adsorbents as shown in Figure 2.7 (a) - (g). At lower pressure it represents the monolayer-multilayer adsorption in to the mesopores followed by the capillary condensation/ pore filling mechanism. [12] The surface area, pore size and pore volume obtained for PT and TiO_2 synthesized using urea (TU2 to TU12) is presented in Table 2.3. A noticeable effect of urea on surface area and mesoporous nature of TiO_2 has been observed. The surface area of TU2 ($112 \text{ m}^2 \cdot \text{g}^{-1}$) is comparatively higher than PT ($68 \text{ m}^2 \cdot \text{g}^{-1}$). As we increase the ratio of Ti: urea from 1:2 to 1:8 there was significant increase in surface area $112 \text{ m}^2 \cdot \text{g}^{-1}$ to $186 \text{ m}^2 \cdot \text{g}^{-1}$, reduction in pore size from 12.2 nm to 7.5 nm and increase in pore volume from $0.205 \text{ cc} \cdot \text{g}^{-1}$ to $0.353 \text{ cc} \cdot \text{g}^{-1}$ respectively. Further increase in Ti:

urea ratio exhibits no significant change in surface area, average pore size and average pore volume (see Figure 2.7 (h)). This is understandable, as urea acts as a fuel during heat treatment of the as-synthesized gels, resulting in rapid liberation of gases such as CO/CO₂, NO_x etc [13,14]. This may result in the randomly oriented agglomerate porosity in TiO₂. Thus, the optimized titanium to urea ratio fixed as 1:8 with a maximum surface area of 186 m².g⁻¹, average pore diameter of 7.5 nm and average pore volume of 0.353 cc.g⁻¹. Furthermore, the phase purity of TiO₂ was analyzed using powder X-ray diffraction studies (refer Figure 2.8 (a)). The characteristic peaks at 2θ values of 25.3°, 37.81°, 48.0°, 53.9°, 55.06°, 62.7°, 68.7° and 70.2° corresponds to the 101, 004, 200, 105, 211, 205, 116, 220 planes of TiO₂ which was further confirmed by comparing it with the JCPDS standard pattern (JCPDS number 21-1272). The highly crystalline nature of TiO₂ was characterized by peak at 2θ value = 25.3° corresponding to 101 plane of TiO₂. All the characteristics peaks obtained at corresponding 2θ values were attributed to anatase phase of TiO₂ with absence of rutile phase which is in good agreement with the literature reports. [15, 16]. Furthermore the effect of urea on the band gap of TiO₂ was determined using UV-DRS. Urea is a well-known nitrogen containing fuel. Literature reports [17–23] suggest that, when it is used as a fuel for TiO₂ synthesis, there is a possibility of N-doping resulting in decreasing the band gap of TiO₂ and the shift of absorption band to the visible region above 400 nm. In order to investigate such behavior, band gap analysis of the synthesized TiO₂ was carried out. Figure 2.8 (b) shows UV-DRS plots of the as-synthesized TiO₂ catalyst using urea (Ti: urea = 1:8) as structure directing agent in comparison to pristine TiO₂. The band gaps of the synthesized TiO₂ samples were found to be 3.24 and 3.29 (±0.5) eV (see Figure 2.8 (b)) which indicates no significant change in the band gap when urea was used as structure directing agent. Further, the effect of urea as structure directing agent on the morphology of as-synthesized TiO₂ was determined using FESEM analysis.

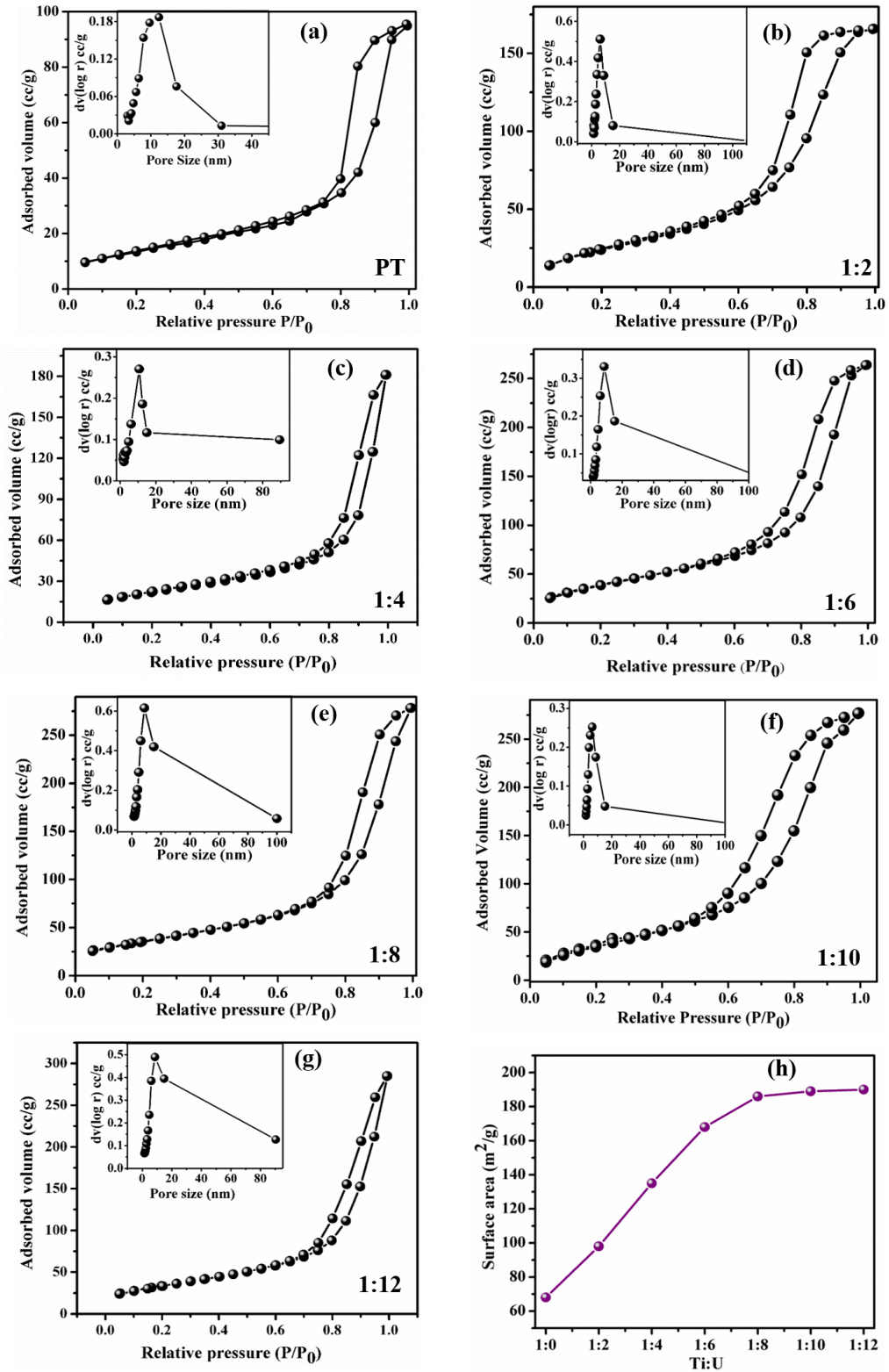


Figure 2.7: N₂ adsorption-desorption plots for (a) Pristine TiO₂, (b) TU2, (c) TU4, (d) TU6, (e) TU8, (f) TU10, (g) TU12 and (h) measured surface area versus Ti: Urea ratio.

Ti:urea	Surface area ($\pm 5 \text{ m}^2\cdot\text{g}^{-1}$)	Average. Pore size (nm)	Average. Pore volume ($\text{cc}\cdot\text{g}^{-1}$)
PT	68	11.6	0.190
TU2 (1:2)	112	12.2	0.205
TU4 (1:4)	135	10.9	0.263
TU6 (1:6)	168	8.6	0.297
TU8 (1:8)	186	7.5	0.353
TU10 (1:10)	189	7.2	0.362
TU12 (1:12)	190	7.1	0.425

Table 2.3: Surface area, average pore size, and average pore volume of pristine TiO₂ (PT) and TiO₂ with urea at different ratio.

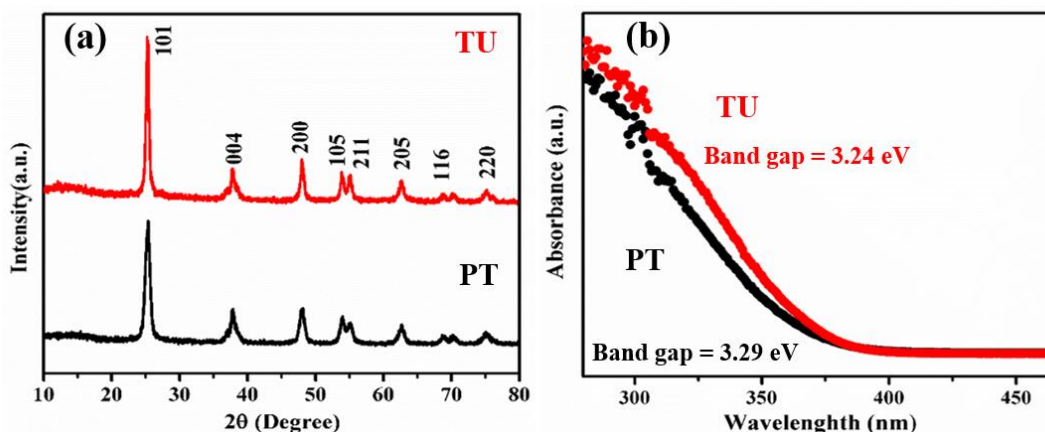


Figure 2.8: (a) XRD and (b) UV-DRS of PT and TU8.

The surface morphology, particle size and shape of the pristine TiO₂ and TiO₂ with urea (TU8) have been investigated by using SEM and HR-TEM analysis. Figure 2.9 shows the morphology and elemental analysis of the pristine TiO₂ (PT) and TiO₂ (TU8) synthesized using urea as structure directing agent. A high agglomeration of particles were observed in case of PT. The agglomeration was relatively lower in case of TU8. Both PT and TU8 showed presence of Ti and O with no other impurity peaks in EDS spectra. In addition to this the particle size of the TiO₂ was determined using HR-TEM analysis. Figure 2.10 illustrates

the formation of nano size TiO_2 particles. The low resolution TEM images (Figure 2.10 (a)) shows the formation of TiO_2 nanoparticles of varied shapes. The average particle size was found by measuring the particle sizes of approximately 100 particles using ImageJ software and the mean particle size of 25 nm and 18 nm for PT and TU8 respectively was recorded. Figure 2.10 (c) shows the HR-TEM images of PT and TU. The calculated d spacing value was 0.351 nm corresponding to (101) plane of TiO_2 . The selected area electron diffraction patterns of PT and TU is shown as in Figure 2.10 (d). The polymorphic rings were observed in both PT and TU8, which indicates polycrystalline nature of the catalyst surface.

Thus in summary, it is observed that the surface area of TiO_2 could be significantly altered by addition of urea during the synthesis. The optimal Ti:U ratio of 1:8 (TU8) exhibited maximum surface area for ($186 \text{ m}^2 \cdot \text{g}^{-1}$) which is greater than the pristine TiO_2 by a factor of 3 which is attributed to the reduction in particle size of TiO_2 particles confirmed through TEM analysis. The mesoporous nature of TU8 is due to the agglomeration of the tiny particles which produces agglomerate porosity as confirmed through FE-SEM and BET studies. However, the addition of urea did not alter significantly the band gap of TiO_2 as the calculated values were well within the error limits of the measurement. This limitation could be due to the fact that urea does not really act as a coordinating ligand to Ti^{4+} and can only serve as a fuel for combustion synthesis. If the structure of the Ti-hydroxide gel could be altered by using a suitable ligand, it could serve a greater purpose of modifying both the surface area as well as band properties of TiO_2 . Literature survey suggested that carboxylate groups serve as excellent coordination ligands that can bind to the metal ions in various modes [24–26]. Therefore, in the next synthesis strategy, it was indented to investigate the effect of various carboxylic acids with increasing number of COOH group as SDA in TiO_2 synthesis. The next section presents the results obtained from the above modification of synthesis strategy.

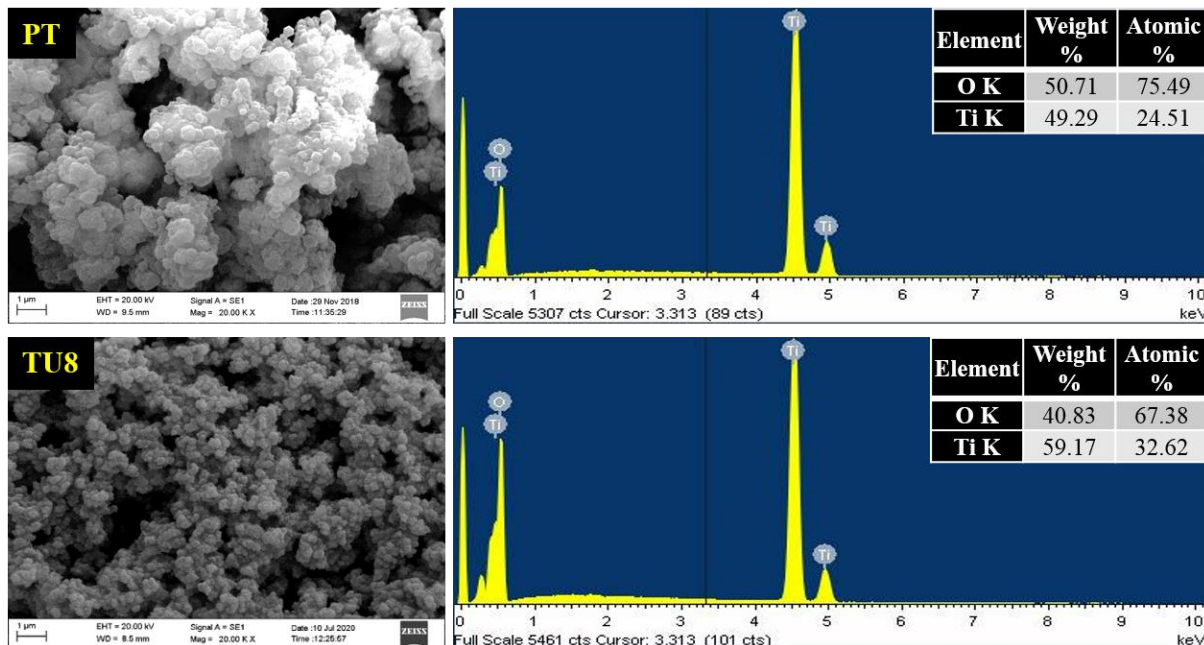


Figure 2.9: SEM and elemental characterization of Pristine TiO₂ (PT) and TiO₂ (TU8) synthesized using urea directing agent.

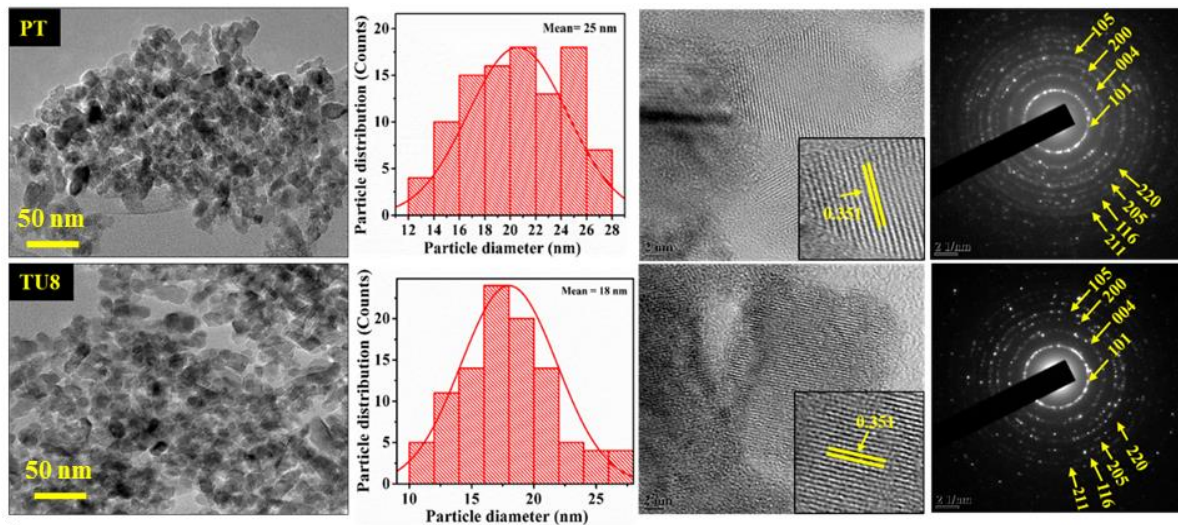


Figure 2.10: (a) Low resolution TEM, (b) Particle size distribution (c) HRTEM and (d) SAED analysis of PT and TU8.

➤ **Effect of number of carboxylic groups of SDA on porosity and surface area of TiO₂**

In order to investigate the effect of number of carboxylic groups in SDA on the porosity and surface area of TiO₂ catalyst, three different carboxylic acids were chosen namely, oxalic acid, tricarballylic acid, butanetetracarboxylic acid each having 2, 3 and 4 –COOH groups respectively. The synthesized titanium isopropoxide gel with each of the carboxylic acids were subjected to TG-DTA analysis, the results of which are presented in Figure 2.11 (a-c). The initial weight loss in all the three precursor were due to the loss of physical and chemical adsorbed water. A comparison between the TG-DTA profiles of TOA, TTC and TBTC revealed a striking difference in their decomposition pattern. The complete decomposition of the titanium isopropoxide gel with oxalic acid occurred at 500 °C. However, the higher temperature of 550 °C was required for complete decomposition of titanium hydroxide gel with tricarballylic acid and butanetetracarboxylic acid. This observation indicates the type of ligation between the Ti(OH)₄-oxalic acid and the Ti(OH)₄- tricarballylic acid/butanetetracarboxylic acid is significantly different. It is also expected that oxalic acid would coordinate via intramolecular ligation while the steric factor in case of tricarballylic acid and butanetetracarboxylic acid could result in intermolecular ligation [27]. Therefore, IR spectroscopic analysis of the titanium hydroxide with carboxylic acid hybrid gel precursors were performed and the obtained results are presented in Figure 2.11 (d).

The precursor of titanium hydroxide gel with oxalic acid, tricarballylic acid and butanetetracarboxylic acid showed a broad band at the region around 3450 to 2500 cm⁻¹ which is due to the presence of OH group from the acids convoluted with OH stretching of free water molecules present in the gel. In all the three precursors the characteristic peaks of C=O and C-O stretching vibrations were observed at 1710 cm⁻¹ to 1243 cm⁻¹ respectively. The symmetric and unsymmetrical carbonyl stretching vibrations were observed at 1568 and 1243 cm⁻¹ which indicates the intramolecular carboxylate linkage with Ti⁴⁺[27].

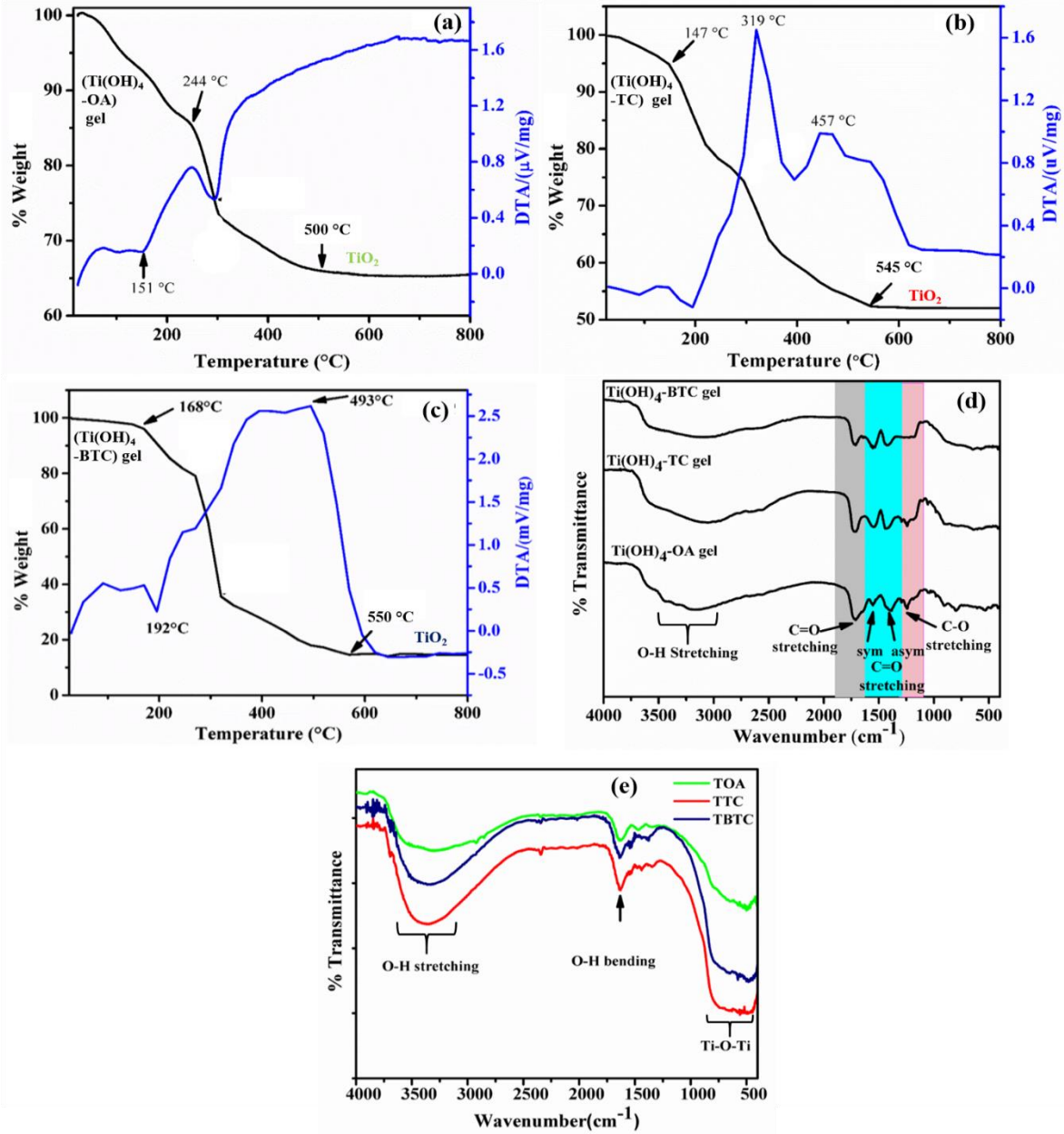


Figure 2.11: (a-c) TG-DTA and (d, e) IR analysis of as synthesized hybrid gel precursors and the post calcined TiO_2 labelled as TOA, TTC and TBTC respectively.

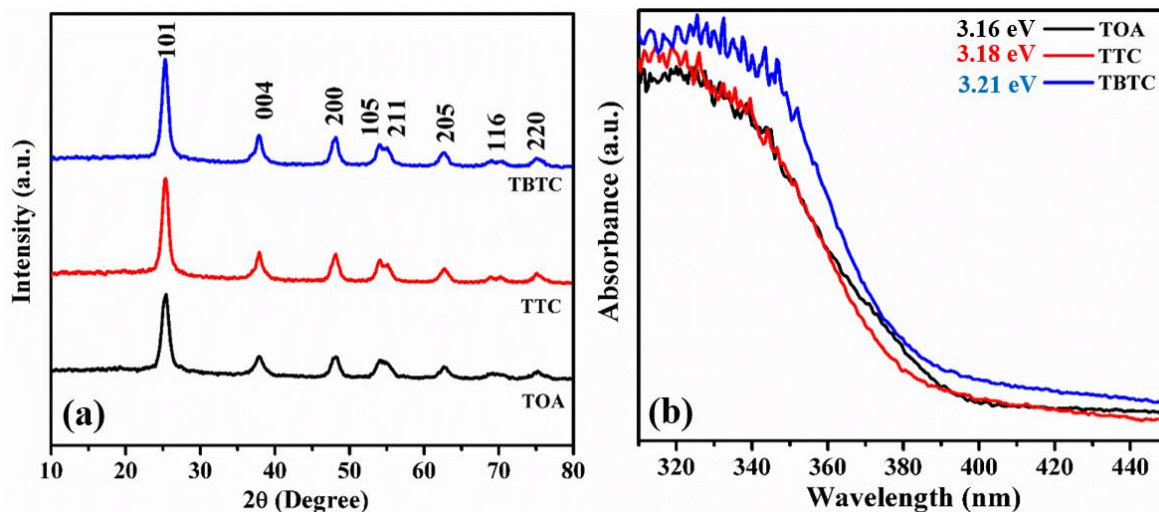


Figure 2.12: (a) XRD and (b) UV-DRS of TOA, TTC and TBTC.

Furthermore, the use of carboxylic acid as structure directing agent in titanium isopropoxide gel and its effect on the phase purity of the TiO_2 was determined using powder X-ray diffraction analysis (refer Figure 2.12 (a)). All the three synthesized TiO_2 i.e. TOA, TTC, and TBTC exhibited pure anatase phase of TiO_2 with characteristics planes such as 101, 004, 200, 105, 211, 205, 116, 220 corresponding to 2θ value of 25.3° , 37.81° , 48.0° , 53.9° , 55.06° , 62.7° , 68.7° and 70.2° which confirms the formation of anatase phase of TiO_2 . This also indicates that no carboxylic acid as structure directing agent could not induce any phase change in the material. Furthermore, the band gap analysis of the TiO_2 samples was performed. The obtained band gap of TOA, TTC and TBTC is 3.16, 3.18 and 3.21 eV (refer Figure 2.12 (b)). Thus, across the different carboxylic acids as SDA, there was no significant change in band gap of TiO_2 , however, when TOA is compared with PT, the band gap reduced from 3.29 to 3.16 eV signifying the alteration in optical properties of TiO_2 induced by carboxylic acids as SDA.

Furthermore, the influence of these carboxylic acids on surface area of TiO_2 was determined using N_2 adsorption-desorption isotherm analysis. Figure 2.13 shows N_2 adsorption-desorption isotherm analysis along with their pore size distribution graph (shown inset) for TOA, TTC and TBTC. All the three samples exhibited type IV isotherm with hysteresis loop

as per the IUPAC classification [12]. The obtained surface area were 107, 130 and 180 $\text{m}^2.\text{g}^{-1}$ respectively. It is observed that as we increase the number of carboxylic acid groups in the titanium hydroxide gel the surface area was observed to increase with wider mesoporous size distribution as observed in Table 2.4. This could be attributed to the increase in interaction of COO^- groups of carboxylic acid and possibly due to the change in their binding modes (intramolecular v/s intermolecular) with that of Ti^{+4} . The influence of these carboxylic acids on the morphology of synthesized TiO_2 was determined using FESEM analysis. Figure 2.14 shows the FESEM images of TOA, TTC and TBTC. All the three catalyst exhibited spherical shaped morphology of TiO_2 with cluster of tiny particles which represents the agglomerate porosity in the TiO_2 samples. Further the particle size of the synthesized TiO_2 was determined by measuring the particle size of approximately 100 nanoparticles using Image J software. Figure 2.15 (a) shows low resolution TEM of TOA, TTC and TBTC. The calculated particle size for TOA, TTC and TBTC was 11.4 nm, 13.6 nm, and 14.3 nm. The calculated d -spacing value for all three catalyst was ~ 0.35 which corresponds to 101 plane of TiO_2 . Bright rings in SAED as observed for all the three catalysts indicated highly polycrystalline nature of synthesized TiO_2 .

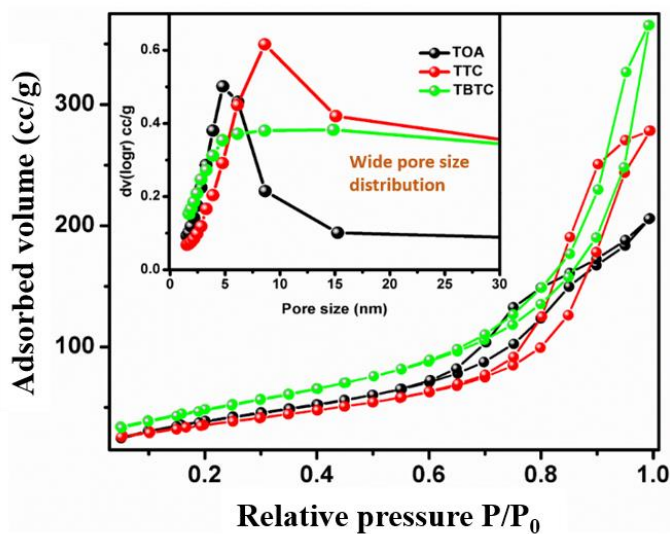


Figure 2.13: Measured BET surface area of TOA, TTC and TBTC

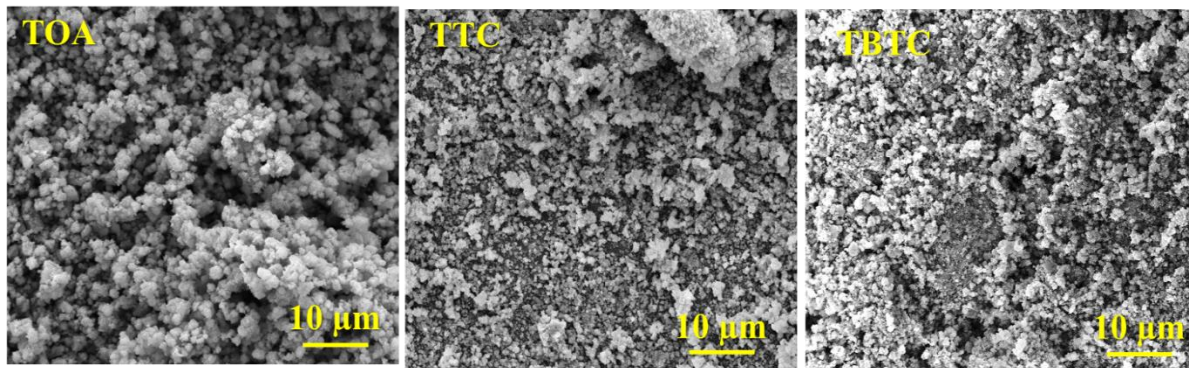


Figure 2.14: FESEM of TiO_2 obtained from calcined titanium hydroxide gel modified with different carboxylic acid.

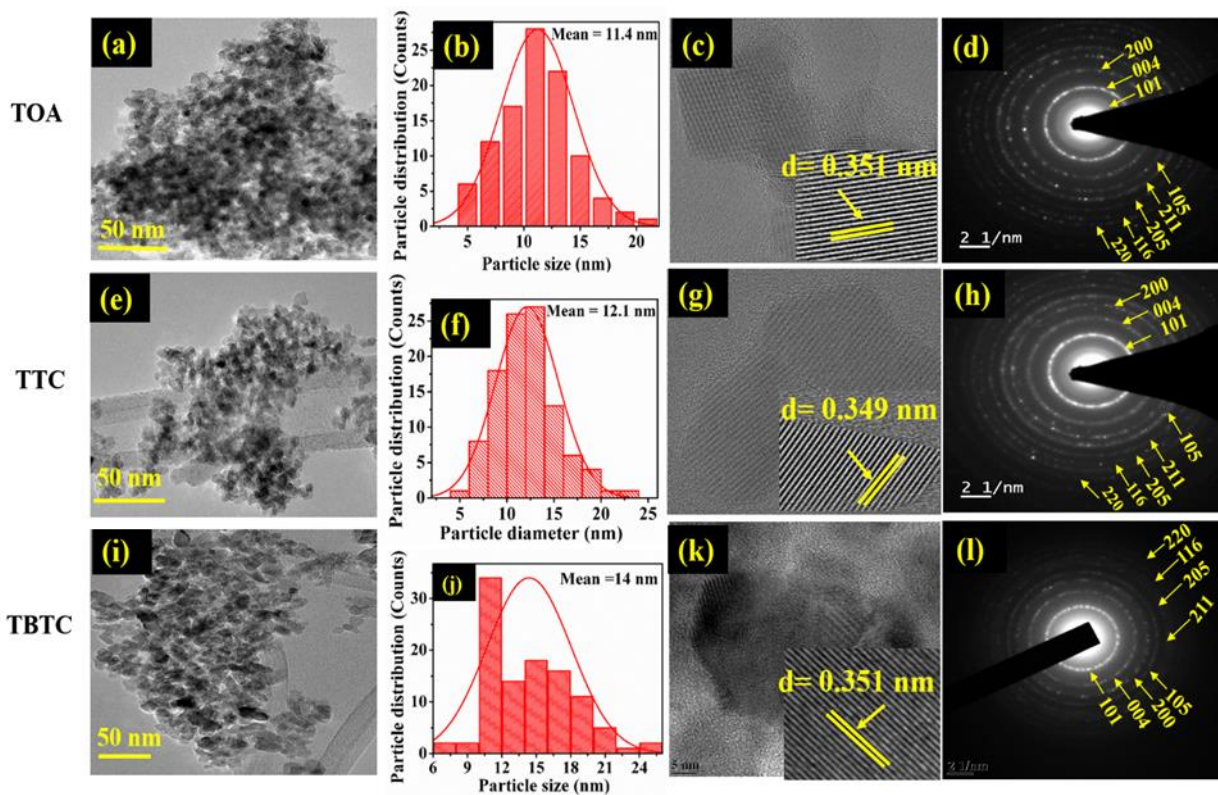


Figure 2.15: (a, e and i) Low resolution TEM micrographs, (b, f and j) histogram of particle size distribution (c, g and k) HRTEM micrographs and (d, h and l) SAED pattern of TiO_2 synthesized using carboxylic acids.

TiO₂	Band gap (± 0.05 eV)	Surface area (± 5 m ² .g ⁻¹)	Average Pore size (nm)	Average Pore volume (cc.g ⁻¹)
TOA	3.16	107	4.7	0.50
TTC	3.18	130	8.5	0.60
TBTC	3.21	180	14.8	0.68

Table 2.4: Band gap, surface area, pore size and pore volumes of the synthesized TiO₂ catalysts

In summary, butanetetracarboxylic acid as SDA significantly influenced the pore structure and surface area of TiO₂ compared to the oxalic and tricarballic acid, resulting in the highest surface area of 180 m².g⁻¹ with a wide pore size distribution. Though, the obtained surface area was not significantly different as compared to TU8 (186 m².g⁻¹), the obtained pore size of 14.3 nm was found to be almost double as compared to TU8 (7.5 nm). This indicates that the ligation of carboxylate group with Ti-hydroxide gel has a greater influence on the pore structure as compared to urea which merely influences the combustion characteristics of the gel.

Overall, the lower surface areas of TiO₂ catalysts in spite of altering the pore size with carboxylic acids as SDA in comparison to urea, suggests stronger ligation of carboxylate groups to Ti⁴⁺. This probably makes their removal difficult during calcination as it needs extended calcination time. Since urea act as a fuel and its exothermic decomposition via gas evolution is well documented [28–30], it was strategized to use urea and carboxylic acid mixtures as Fuel + SDA so that this could act as a driving force for facile and complete removal of carboxylic acids from the gel matrix during calcination. Very interesting results were obtained with this strategy which are presented in the next section.

➤ **Tuneability of TiO₂ pore structure using carboxylic acid (SDA) and urea (fuel) mixture.**

The TG-DTA of the modified titanium hydroxide gel with urea and each of the acids; oxalic acid, tricarballic acid and butanetetracarboxylic acid is presented in the Figure 2.16 (a) - (c). The initial weight loss is due to the loss of physisorbed water. The second major weight loss is due to the decomposition of the organic moiety. At temperature above 500 °C no significant weight loss was observed. Based on this all the samples were calcined at 500 °C. Thus using a combination of carboxylic acid with urea led to decrease in complete decomposition temperature of the gel i.e. oxalic-urea gel needed $\geq 420^{\circ}\text{C}$ while both tricarballic and butanetetracarboxylic acids with urea required $\geq 500^{\circ}\text{C}$ for complete removal of precursors and transformation into TiO₂. To further confirm this observation, IR analysis was carried out (refer Figure 2.16 (d)-(e)). The broad intense convoluted OH-stretching vibration of acids, water with NH stretching vibrations of urea was observed in the region 3200-2500 cm⁻¹ in all the precursor gels. The C=O and C-O stretching frequencies observed at 1553 cm⁻¹ and 1180 cm⁻¹ respectively were slightly shifted to lower wavenumbers in case of titanium (Ti(OH)₄-butanetetracarboxylic acid/urea gel.

This shift to a lower wavenumber indicates a weaker bonding interaction between Ti⁴⁺ and the butanetetracarboxylic acid group. Since the orientation of four COOH groups is in different planes, it is possible that butanetetracarboxylic acid coordinate with two Ti⁴⁺ which are present in adjacent planes in the titania gel matrix via intermolecular double ligation. Upon calcination of the gel matrix at 500 °C results in the complete removal of all the organic moiety leaving behind only the characteristic peaks of chemisorbed OH stretching and bending vibration at 3500-2500 cm⁻¹ and 1598 cm⁻¹ respectively. In addition to this, Ti-O-Ti stretching vibrations was also observed in the region 800 -500 cm⁻¹ in the calcined TiO₂. The lower calcination temperature needed in this case confirms that addition of urea indeed facilitates decomposition and facile removal of carboxylic acids from the hybrid gel.

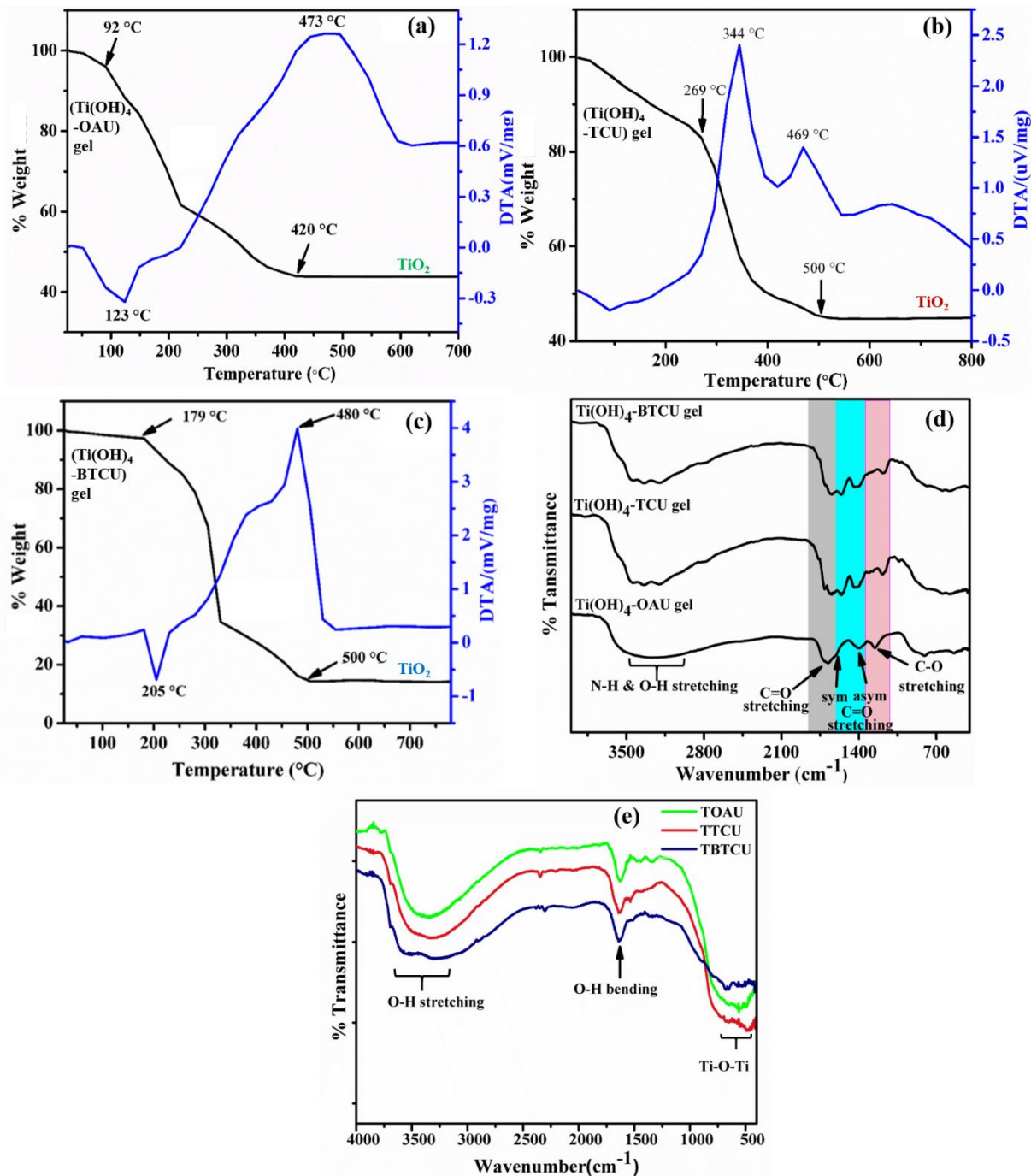


Figure 2.16: TG-DTA analysis of titanium hydroxide gel with (a) oxalic acid & urea (b) tricarballylic acid & urea (c) 1,2,3,4 butanetetracarboxylic acid & urea. (d & e) IR analysis of all precursors and their corresponding calcined TiO₂: TOAU, TTCU and TBTCU.

Further the effect of these urea-carboxylic acid modified hybrid gels on the phase formation of the TiO_2 was investigated using powder XRD studies (see Figure 2.17 (a)). All the calcined sample exhibited highly crystalline nature of TiO_2 . A pure anatase phase of TiO_2 was obtained with the major intensity peaks appearing at 25.3° , 37.8° , 48.0° , 53.9° , 55.06° , 62.7° , 68.7° , 70.2° corresponding to planes 101, 004, 200, 105, 211, 205, 116, 220 planes of TiO_2 which are in good agreement with the JCPDS number 84-1286. The calculated band gap of TOAU, TTCU and TBTCU is 3.14 eV, 3.15 eV and 3.19 eV as presented in Table 2.5 (see Figure 2.17 (b)). Thus not much change in the band gap is observed due to addition of urea to the carboxylic acid modified Ti-hydroxide gels. Furthermore the influence of these carboxylic acid/urea mixture on the porosity of TiO_2 was investigated using N_2 adsorption-desorption analysis.

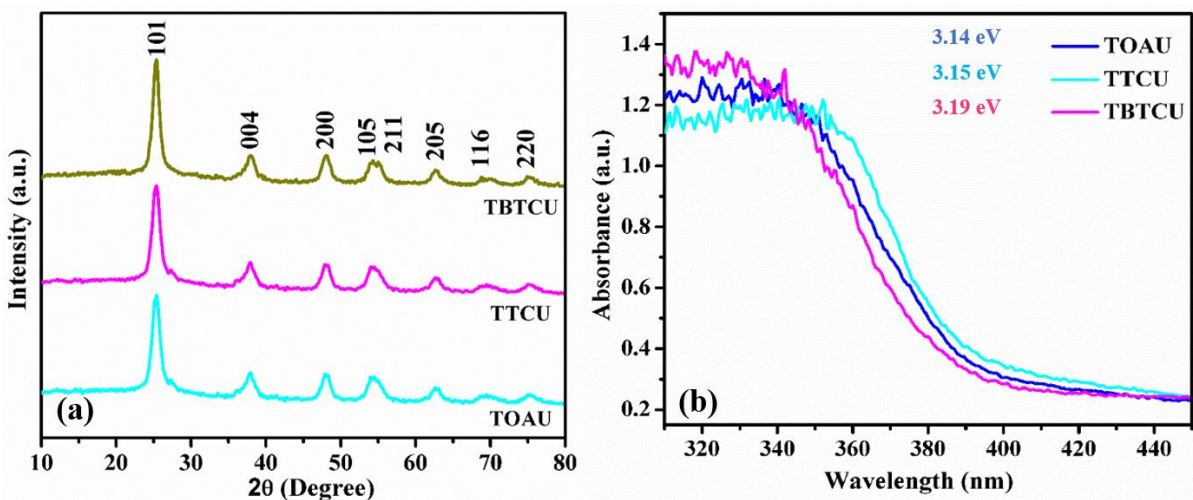


Figure 2.17 (a) XRD and (b) UV-DRS of TOAU, TTCU and TBTCU.

The influence of in-situ decomposition of $\text{Ti}(\text{OH})_4$ gel with carboxylic acid /urea mixture on the internal pore structure of TiO_2 was investigated using BET N_2 adsorption-desorption isotherm experiments and BJH pore size distribution analysis. All the measured values of average pore size, average pore volume, and surface area are presented in Table 2.5. As evident from Figure 2.18, all the synthesized TiO_2 displayed type IV adsorption isotherms. A clear distinction in the type of the hysteresis loop is evident when the TiO_2 catalysts prepared from urea-carboxylic acids gels is compared with those prepared with carboxylic acids alone (as presented earlier in Figure 2.13). At lower pressure it represents the monolayer-multilayer adsorption followed by the capillary condensation/pore-filling mechanism.

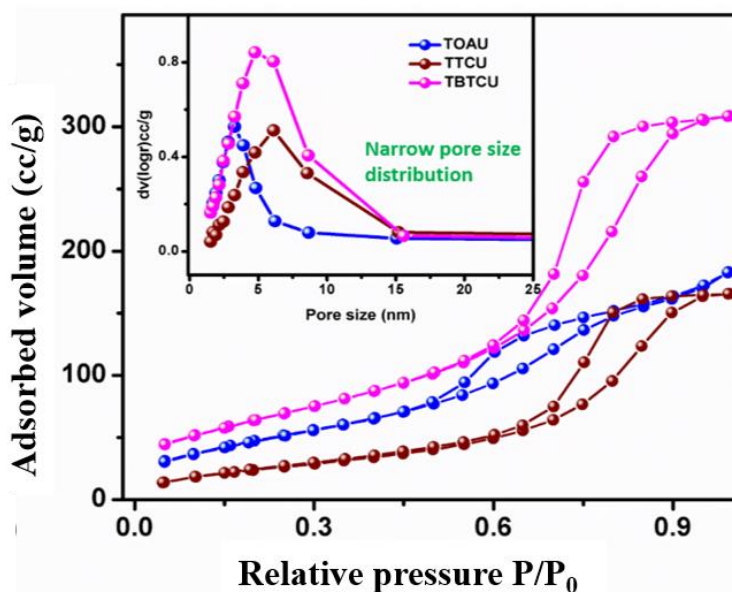


Figure 2.18: N₂ adsorption-desorption isotherms and pore size distribution (as inset) of TOAU, TTCU and TBTCU

TiO ₂	Band gap (eV)	Surface area (± 5 m ² .g ⁻¹)	Average pore size (nm)	Average pore volume (cc.g ⁻¹)
TOAU	3.14	116	3.2	0.55
TTCU	3.15	146	6.1	0.68
TBTCU	3.19	238	4.8	0.84

Table 2.5: Comparative analysis of surface properties of all the synthesized TiO₂ catalysts.

TTCU and TBTCU, displayed a significant reduction in average pore size distribution by a factor of more than 2 with largely ordered mesoporous structures. The reduction in pore size is further accompanied by an increase in pore volume from 0.55, 0.68 to 0.80 cc.g⁻¹, while the surface area increased tremendously from 116.8, 146.3 to 238.4 m².g⁻¹ in the case of TOAU, TTCU, and TBTCU respectively. TOAU is mostly composed of microporous structures. The steep desorption step, which is only observed in the case of H2(a) type hysteresis loop, is a characteristic of a complex interconnected pore structure wherein, either wide surface pore openings lead to subsequent percolation through narrow necks or cavitation induced evaporation mostly observed through spongy 3D gel-like interconnected mesoporous structures [12]. Further the influence of carboxylic acid and urea on the morphology of TiO₂ was determined using FESEM analysis.

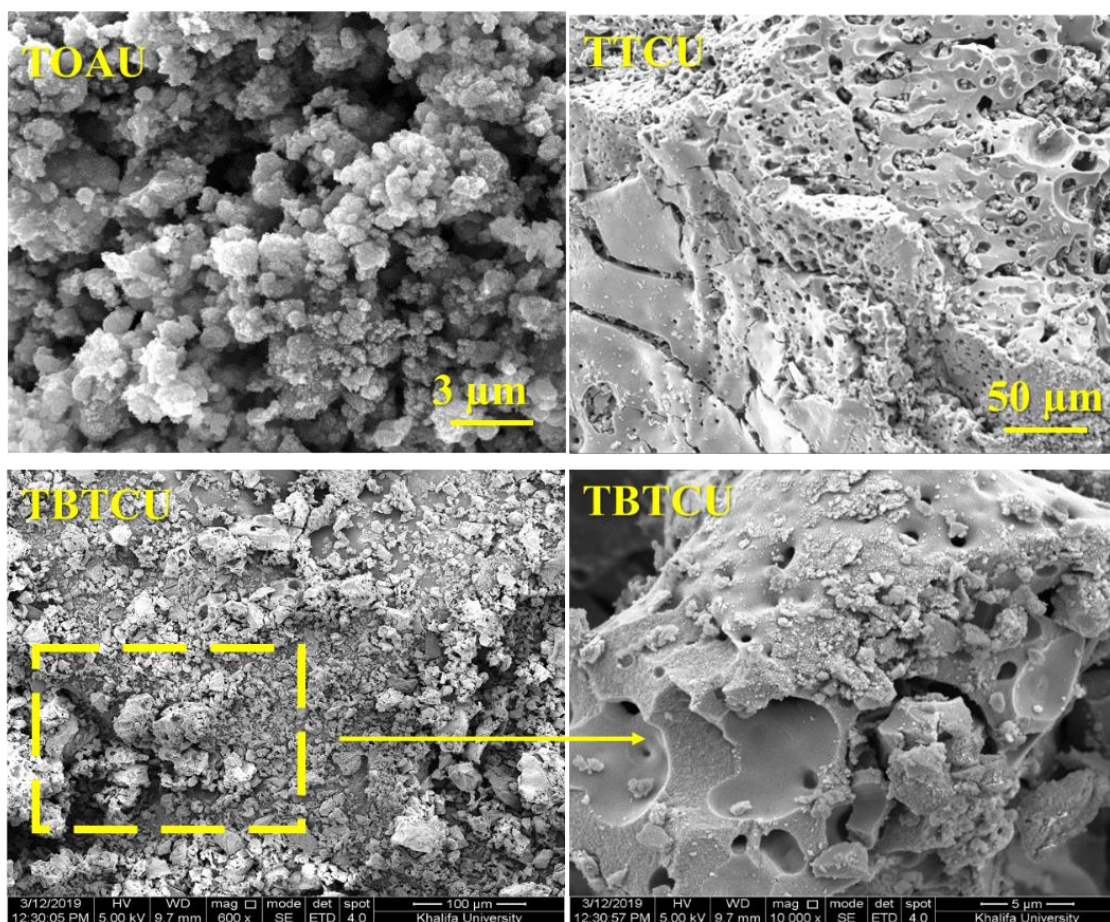


Figure 2.19: FESEM micrographs of the TiO₂ obtained after calcination of titanium hydroxide gel modified with different carboxylic acid and urea mixture.

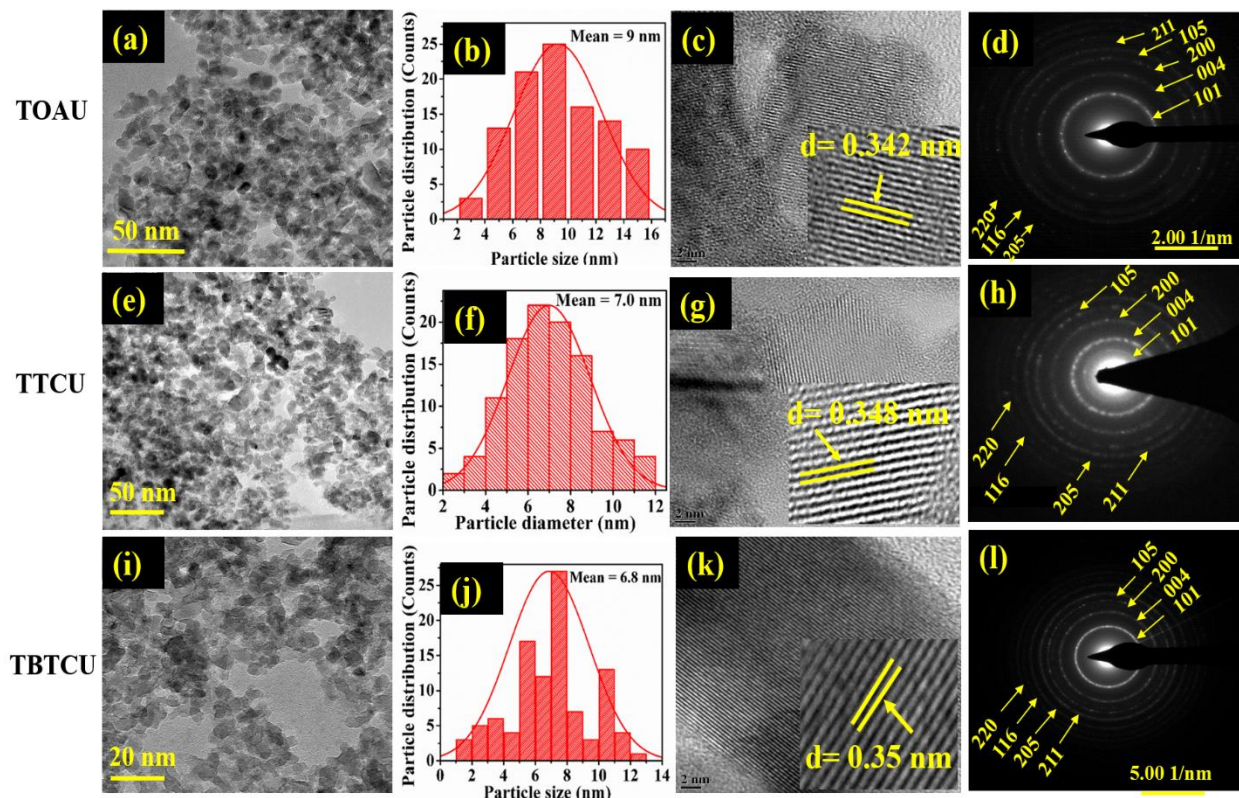


Figure 2.20 (a, e and i) Low resolution TEM micrographs, (b, f and j) histogram of particle size distribution (c, g and k) HRTEM micrographs and (d, h and l) SAED of TiO_2 synthesized using carboxylic acids and urea.

The surface morphology of the synthesized TiO_2 was found to be highly influenced by the nature of carboxylic acids and its combination with that of urea. Highly agglomerated nanoparticles were observed in the case of TOAU. On the contrary, porous structures were seen in case of TTCU and TBTCU. It was evident that greater number of carboxylic groups in TTC and TBTC probably stabilized greater number of TiO_2 particles while the presence of urea allowed transformation of these particles into highly robust, sponge-like super porous TiO_2 especially in the case of TBTCU. This structural porosity in TiO_2 could be due to the synergistic effect in enhancement of Ti^{+4} charge stabilization and in-situ decomposition of urea resulting in changing the internal pore structure of the TiO_2 catalyst. This observation is, therefore, in excellent agreement with the N_2 adsorption-desorption analysis presented earlier and explains the tremendous increase in measured surface area in the case of TiO_2 obtained from TBTCU. Further the Low resolution TEM analysis of TOAU, TTCU and TBTCU were carried out and presented in Figure 2.20 (a) (e) and (i). The calculated particle size was 9 nm,

7.2 nm and 6.6 nm for TOAU, TTCU and TBTCU which are comparatively lower than TOA, TTC and TBTC (see Figure 2.20 (b) (f) and (j)). HRTEM micrographs depicts the fringes spacing of 0.35 nm which corresponds to the (101) plane of TiO_2 which is indexed to the anatase phase of TiO_2 as observed from powder XRD pattern (see Figure 2.20 (c) (j) and (k)). All the synthesized TiO_2 were analyzed using SAED pattern (see Figure 2.20 (d) (h) and (l)) and it was observed to exhibit similar diffused ring patterns. Thus indicating polycrystalline nature of all the TiO_2 samples. The observed diffraction rings are indexed to (101), (004), (200), (105), (211), (205), (116) and (220) which are in good agreement with the powder XRD analysis. Thus, in summary, the modifications of Ti-hydroxide - carboxylic acid gels with urea could successfully produce highly porous TiO_2 nanostructures of high surface area. The band structure and phase remained an intrinsic property of TiO_2 which was not altered upon SDA modifications.

It was indeed interesting to investigate whether all the morphological changes introduced into the TiO_2 while converting it into extremely porous catalyst of high surface area, could have an effect on its adsorption capacity as well as photocatalytic properties. Therefore, all the synthesized catalysts were subjected to dye adsorption studies as presented in the next section.

2.5.2 Adsorptive removal of Amaranth dye from water using synthesized TiO_2 catalysts.

The catalytic efficiency of all the synthesized TiO_2 catalysts (PT, TU8, TOA, TTC, TBTC, TOAU, TTCU and TBTCU) in comparison to the commercial Degussa P-25 was determined for adsorptive removal of Amaranth dye from waste water. The nature of interaction between the adsorbate and adsorbent was investigated using adsorption isotherm and adsorption kinetic study.

➤ Adsorption isotherm studies

The procedure for adsorption isotherm study for all the synthesized TiO_2 was carried out as per the procedure mentioned in section 2.4.4 and the adsorption capacity at equilibrium (q_e), and the Amaranth removal efficiency of each of the TiO_2 catalyst was determined. The plot of adsorption equilibrium (q_e) as a function of initial concentration of Amaranth dye was

fitted using non-linear forms of different adsorption isotherm models such as Langmuir, Freundlich, Sips and Temkin models [3]. Figure 2.21 represents the adsorption isotherm plots for PT and TU8 in comparison with Degussa P-25 (DEG). Similarly Figure 2.22 represents the adsorption isotherm study for TOA, TTC, TBTC, TOAU, TTCU and TBTCU. It is a plot of maximum adsorption capacity q_e as a function of adsorbate concentration c_e . From the plots of all the TiO₂ catalysts we observe that at lower initial concentration of Amaranth dye there is near linear increase in the maximum adsorption capacity which subsequently enters into an equilibrium at higher initial concentration of Amaranth dye.

This could be due to the easy availability of the adsorptive sites for the Amaranth dye molecule to adsorb on the catalyst surface[4]. The analysis of adsorption data revealed that the Sips model best fitted the adsorption data with highest correlation coefficient values i.e. $R^2 \geq 0.98$ in the case of all TiO₂ catalysts (see Table 2.6). Sips model is a combination of both Freundlich and Langmuir adsorption isotherms which more reliably predicts the adsorption on any heterogeneous surface and overcomes the limitations of Freundlich isotherm model related to the higher concentrations of adsorbate [31]. Therefore, at lower concentrations of adsorbate, the Sips model agrees well with the Freundlich model, however, at higher concentrations of adsorbate it aligns well with the Langmuir's isotherm model [3].

The adsorption capacity of TU8 (65.5 mg.g⁻¹) observed to be higher as compared to PT (42.2 mg.g⁻¹) and DEG (26.3 mg.g⁻¹). The high adsorption capacity of TU8 was attributed to its high surface area of 186 m².g⁻¹ as compared to PT (50 m².g⁻¹) and DEG (68 m².g⁻¹). Furthermore the maximum adsorption capacity of TOA, TTC and TBTC were found to be in the order TBTC (73.8 mg.g⁻¹) > TTC (62.4 mg.g⁻¹) > TOA (48.6 mg.g⁻¹). The obtained adsorption capacity is in good agreement with the surface area of the TBTC (180 m².g⁻¹) > TTC (130 m².g⁻¹) > TOA (107 m².g⁻¹). Thus higher the surface area greater is the adsorption capacity. Similar observation was observed for TiO₂ synthesized using carboxylic acid and urea mixture as SDA. The maximum adsorption capacity was in the order TBTCU (87.8 mg.g⁻¹) > TTCU (80.9 mg.g⁻¹) > TOAU (62.4 mg.g⁻¹).

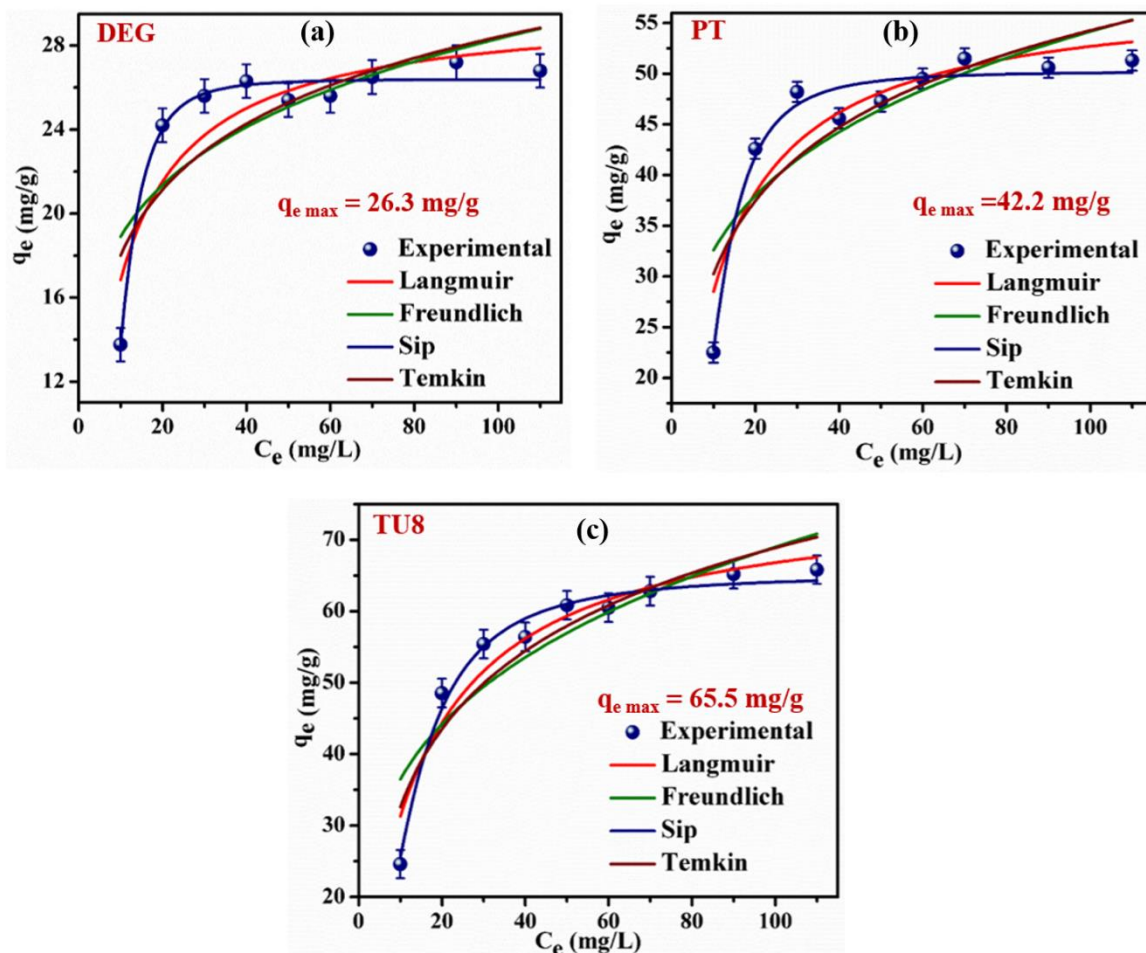


Figure 2.21: (a-c) Amaranth dye adsorption isotherms for DEG, PT and TU8.

Thus TBTCU exhibited maximum adsorption capacity of 87.8 mg.g^{-1} which was comparatively higher than that of TU8 and DEG. This trend of adsorption capacity was attributed to the increased ordered mesoporosity, presence of interconnected pore networks and increase in pore volume resulting in increased effective surface area in TBTCU based on BET analysis.

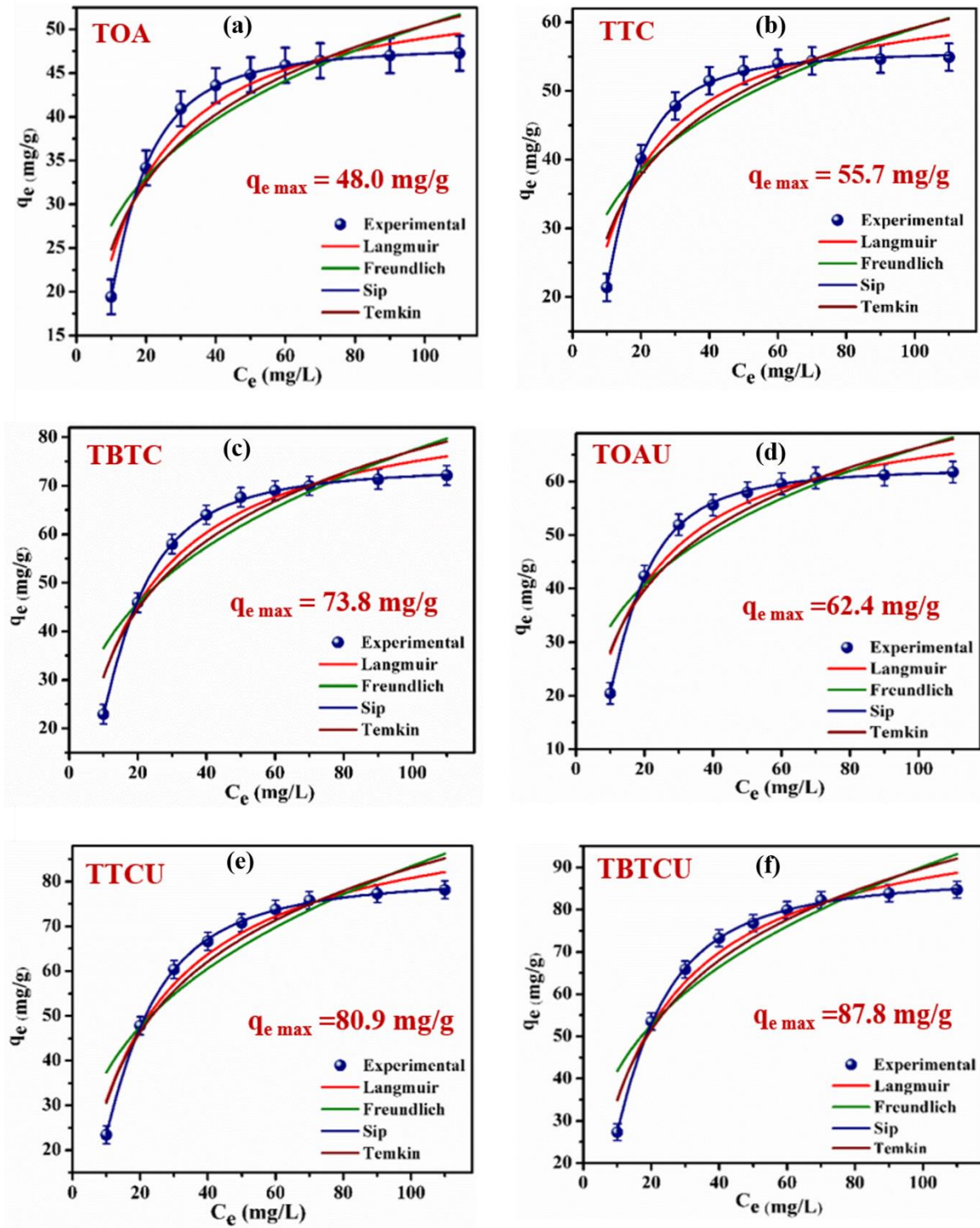


Figure 2.22: (a-f) Amaranth dye adsorption isotherms for TOA, TTC, TBTC, TOAU, TTCU and TBTCU.

Isotherm models	Parameters	Materials								
		DEG	PT	TU	TOA	TTC	TBTC	TOAU	TTCU	TBTCU
Langmuir	q_m (mg.g ⁻¹)	29.8	58.1	76.4	55.6	66.4	89.3	75.2	98.2	104.8
	K_L (L.mg ⁻¹)	0.091	0.086	0.069	0.073	0.071	0.051	0.058	0.046	0.049
	R_L	0.11-0.12	0.21-0.32	0.35-0.40	0.110-0.578	0.113-0.584	0.151-0.662	0.135-0.632	0.165-0.684	0.156-0.671
	R^2	0.80	0.84	0.92	0.97	0.97	0.97	0.97	0.97	0.95
Freundlich	K_F (L.mg ⁻¹)	12.6	19.6	19.3	15.1	17.4	17.2	16.4	16.7	19.3
	$1/n$ (mg.g ⁻¹)	0.175	0.220	0.276	0.262	0.265	0.330	0.302	0.348	0.334
	R^2	0.57	0.66	0.78	0.76	0.73	0.79	0.76	0.82	0.83
Sips	q_m (mg.g ⁻¹)	26.3	42.2	65.5	48.0	55.7	73.8	62.4	80.9	87.8
	K_S (L.mg ⁻¹)	0.068	0.052	0.010	0.081	0.079	0.065	0.070	0.060	0.063
	m	3.22	2.59	1.93	1.90	2.08	1.92	2.07	1.77	1.73
	R^2	0.97	0.95	0.98	0.98	0.98	0.98	0.98	0.98	0.98
Temkin	β (mg.g ⁻¹)	548.4	237.3	157.2	222.7	186.1	122.4	150.0	108.8	104.2
	K_T (L.mg ⁻¹)	5.378	1.808	0.790	0.931	0.854	0.453	0.554	0.383	0.436
	R^2	0.64	0.73	0.86	0.85	0.82	0.88	0.85	0.92	0.92

Table 2.6: Adsorption isotherm parameters obtained using different adsorption isotherm models

➤ **Adsorption kinetic studies**

The efficiency of any adsorbent is characterized by its excellent adsorption capacity over a short period of time under optimized condition. Thus kinetic study provides us the rate of adsorption process [1,32]. The experimental procedure for the adsorption kinetic analysis is explained in section 2.4.5. The obtained experimental data was fitted using different kinetic models such as pseudo-first-order (Figure 2.23 (a)), pseudo-second-order (Figure 2.23 (b)), Elovich model (Figure 2.23 (c)) and intraparticle diffusion model (Figure 2.23 (d)). The calculated adsorption kinetics parameters using these kinetic models are compiled under Table 2.7. The adsorption kinetic profile for all the TiO₂ catalysts depicted faster adsorption rate at initial stage of adsorption process and its subsequent decrease as it approaches towards the equilibrium.

The faster adsorption rate is ascribed to the large availability of the active sites on the catalyst surface and the strong electrostatic interaction of the active sites and the dye molecule at the beginning of the adsorption process (Mittal et al., 2018). Based on the values of correlation coefficient i.e. R^2 , it was decided that the adsorption of Amaranth dye on all the catalyst followed pseudo-first-order rate kinetics which predicted that, the rate of adsorption process depends on the initial concentration of the Amaranth dye and excess number of adsorptive sites present on the TiO_2 catalyst surface [35]. The experimental maximum adsorption capacity q_{e-exp} were found to be very close to q_{e-cal} for pseudo-first-order kinetic fit of all the TiO_2 catalysts [36,37]. It was also observed that the rate constant obtained using pseudo-first-order as well as pseudo-second-order rate equations followed the order $\text{DEG} < \text{PT} < \text{TU8} < \text{TOA} < \text{TTC} < \text{TBTC} < \text{TOAU} < \text{TTCU} < \text{TBTCU}$ which also predicts that with increasing ordered mesoporosity and surface area, the adsorption capacity, as well as the rate of adsorption increases significantly.

The complete process of the transfer of dye molecules from bulk solution to the adsorption sites is a combination of different steps involving the initial transfer to dye molecules from bulk solution to the boundary layer or outer surface of adsorbent followed by the transfer of dye molecules to the inner pores of adsorbent and finally attachment to the adsorption sites [38]. Therefore, to get further insights into the adsorption mechanism, the experimental adsorption kinetics data was fitted using the linear form of the intraparticle diffusion model (Figure 2.23 (d)) and different parameters calculated using this model are compiled under Table 2.7. It was observed that the plot of intraparticle diffusion model did not pass through the origin and had different slopes which ruled-out possibilities of the applicability of intraparticle diffusion model alone and predicted that the dye diffusion mechanism was not completely controlled by a single mechanism but it was a combination of two or more mechanisms.

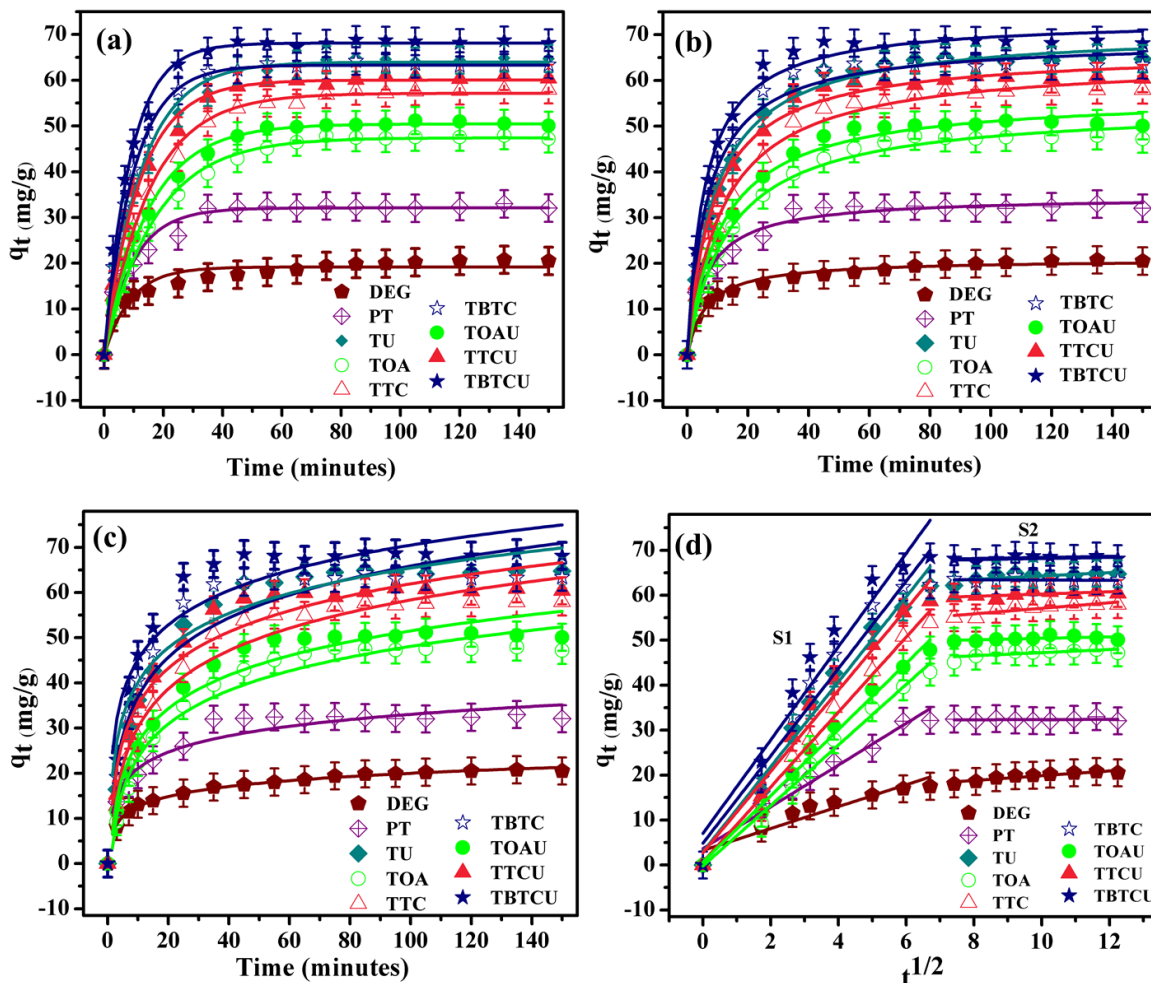


Figure 2.23: (a-d) Amaranth dye adsorption kinetic profiles over all the synthesized TiO_2 catalysts.

The plots of intraparticle diffusion model showed two regions with slope S1 and S2 with S1 being quite higher than S2, which suggested that the contribution of the steps involving the transfer of dye molecules from bulk solution to the internal pores is quite higher. Further, the value of the slope of region S1 also followed the order $\text{DEG} < \text{PT} < \text{TU} < \text{TOA} < \text{TTC} < \text{TBTC} < \text{TOAU} < \text{TTCU} < \text{TBTCU}$ (Table 2.7) which suggested that the dye uptake increased with increasing ordered porosity and surface area. A control experiment with HCl and Amaranth dye at pH 2 (without catalyst) resulted in a merely 1.5% decrease in Amaranth dye concentration even after 24 h, thus confirming that the porosity and surface area of the catalyst contributed significantly to adsorptive separation of Amaranth dye.

Models Parameters		Materials								
		DEG	PT	TU	TOA	TTC	TBTC	TOAU	TTCU	TBTCU
Pseudo- first-order	k_1 (min^{-1})	0.032	0.034	0.036	0.049	0.059	0.093	0.060	0.080	0.106
	$q_{e,\text{cal}}$ ($\text{mg}\cdot\text{g}^{-1}$)	24.1	51.2	66.0	50.3	58.2	63.4	50.9	59.8	68.3
	$q_{e,\text{exp}}$ ($\text{mg}\cdot\text{g}^{-1}$)	18.5	49.6	64.2	52.1	60.9	66.3	54.0	54.0	72.1
	R^2	0.98	0.96	0.97	0.98	0.98	0.97	0.98	0.98	0.97
Pseudo- second- order	K_2 ($\text{g}\cdot\text{mg}^{-1}$ $\cdot \text{min}^{-1}$)	7.68 $\times 10^{-3}$	6.62 $\times 10^{-4}$	5.49 $\times 10^{-4}$	1.02 $\times 10^{-3}$	1.12 $\times 10^{-3}$	1.84 $\times 10^{-3}$	1.30 $\times 10^{-3}$	1.58 $\times 10^{-3}$	2.04 $\times 10^{-3}$
	$q_{e,\text{cal}}$ ($\text{mg}\cdot\text{g}^{-1}$)	20.87	61.13	78.54	58.74	66.66	69.88	58.36	66.88	74.54
	R^2	0.92	0.94	0.95	0.96	0.97	0.97	0.96	0.97	0.96
Elovich	B ($\text{g}\cdot\text{mg}^{-1}$)	16.53	7.41	9.53	0.084	0.077	0.085	0.089	0.083	0.084
	k_E ($\text{mg}\cdot\text{g}^{-1}$ $\cdot \text{min}$)	0.31	0.08	0.06	8.48	12.80	32.0	11.43	21.04	48.66
	R^2	0.91	0.90	0.92	0.91	0.92	0.97	0.95	0.94	0.96
Intraparticle diffusion	$k_{\text{ID}}(\text{S1})$ ($\text{mg}\cdot\text{g}^{-1}$ $\cdot \text{min}^{-1/2}$)	2.02	5.17	6.83	6.73	8.40	11.03	6.93	10.25	12.25
	$C(\text{S1})$ ($\text{mg}\cdot\text{g}^{-1}$)	4.30	2.44	2.83	0.21	0.41	1.59	1.47	0.16	2.82
	$R^2(\text{S1})$	0.85	0.98	0.99	0.98	0.98	0.97	0.98	0.98	0.97
	$k_{\text{ID}}(\text{S2})$ ($\text{mg}\cdot\text{g}^{-1}$ $\cdot \text{min}^{-1/2}$)	0.33	0.81	0.36	1.02	1.30	1.13	1.05	1.26	1.13
	$C(\text{S2})$ ($\text{mg}\cdot\text{g}^{-1}$)	2.44	41.84	61.75	45.43	51.56	57.73	46.63	53.18	63.01
	$R^2(\text{S2})$	0.82	0.47	0.40	0.92	0.95	0.94	0.97	0.96	0.97

Table 2.7: Adsorption kinetic parameters obtained using different adsorption kinetic models.

2.6 Photocatalytic degradation of Amaranth dye using synthesized TiO₂ catalysts.

➤ Kinetic studies

The detailed experimental procedure for photocatalytic degradation of Amaranth dye is already presented in section 2.4.5. The change in Amaranth dye concentration as a function of irradiation time is as shown in Figure 2.25 (a). As observed from the Figure 2.24, the photocatalytic degradation experiment without catalyst, exhibited only ~4 % decrease in absorbance of the initial dye value after the irradiation of 60 minutes. On the other hand a significant decrease in initial concentration of dye was observed in presence of TiO₂ catalysts. The color of the Amaranth dye solution was observed to change from dark pink to pale pink to colorless at the end of 50 minutes in presence of all the TiO₂ catalyst i.e. PT, TU8 and DEG. The maximum degradation efficiency of 92.7 % was obtained using TU8 as compared to (PT 85.3 %) and DEG (80.6 %) as presented in Table 2.8 which is attributed to its high surface area as compared to PT (68 m².g⁻¹) and DEG (50 m².g⁻¹) and due to its relatively lower band gap of 3.24 eV compared to PT.

Figure 2.24 (b) shows a plot of $\ln[\text{Amaranth}]_0/[\text{Amaranth}]_t$ as a function of time which gives a straight line fit and from the slope of which the rate constant 'k' is calculated and is presented in Table 2.8. It was observed that photocatalytic degradation kinetics of Amaranth dye was best fitted using pseudo first order kinetic model [39,40] and the highest rate constant was $0.669 \times 10^{-1} \text{ min}^{-1}$ obtained using TU8 catalyst. For enhancement in photocatalytic degradation performance various parameters were optimized such as TiO₂ catalyst dosage, initial Amaranth dye concentration and the pH of the solution which has been discussed in detail in the following sections.

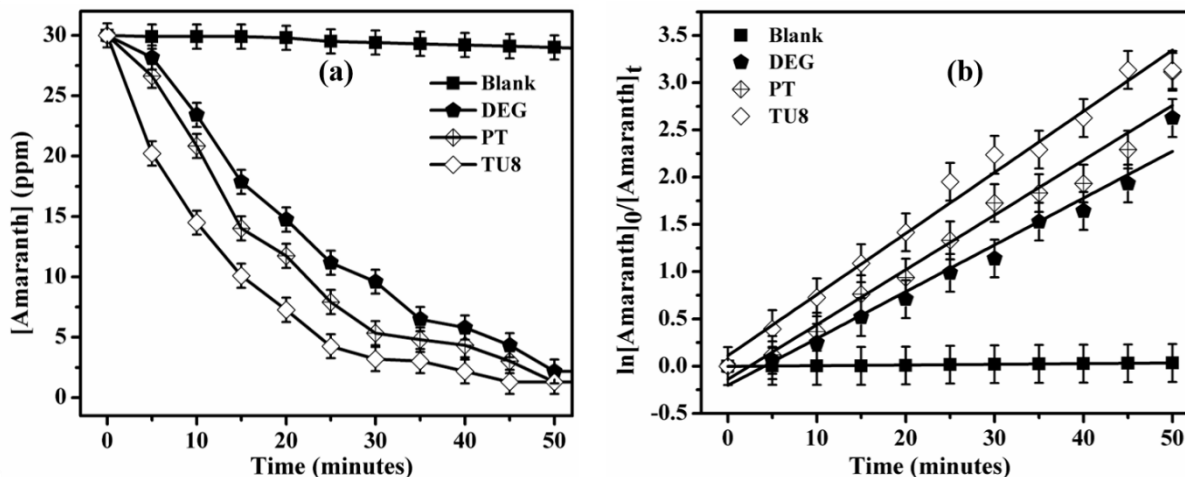


Figure 2.24 (a) & (b): Kinetic profiles for photocatalytic degradation of Amaranth dye using TU8 catalyst in comparison with PT and DEG.

Catalyst	Band gap (eV)	BET surface area ($\pm 5 \text{ m}^2 \cdot \text{g}^{-1}$)	% Degradation (in 40 min)	$k_{app} (\times 10^{-1}) (\text{min}^{-1})$
Blank	---	---	2.8	0.007
DEG	3.20	50	80.6	0.440
PT	3.23	68	85.3	0.539
TU8	3.22	186	92.7	0.669

Table 2.8: Correlation between material properties with that of photocatalytic performance of the synthesized catalysts.

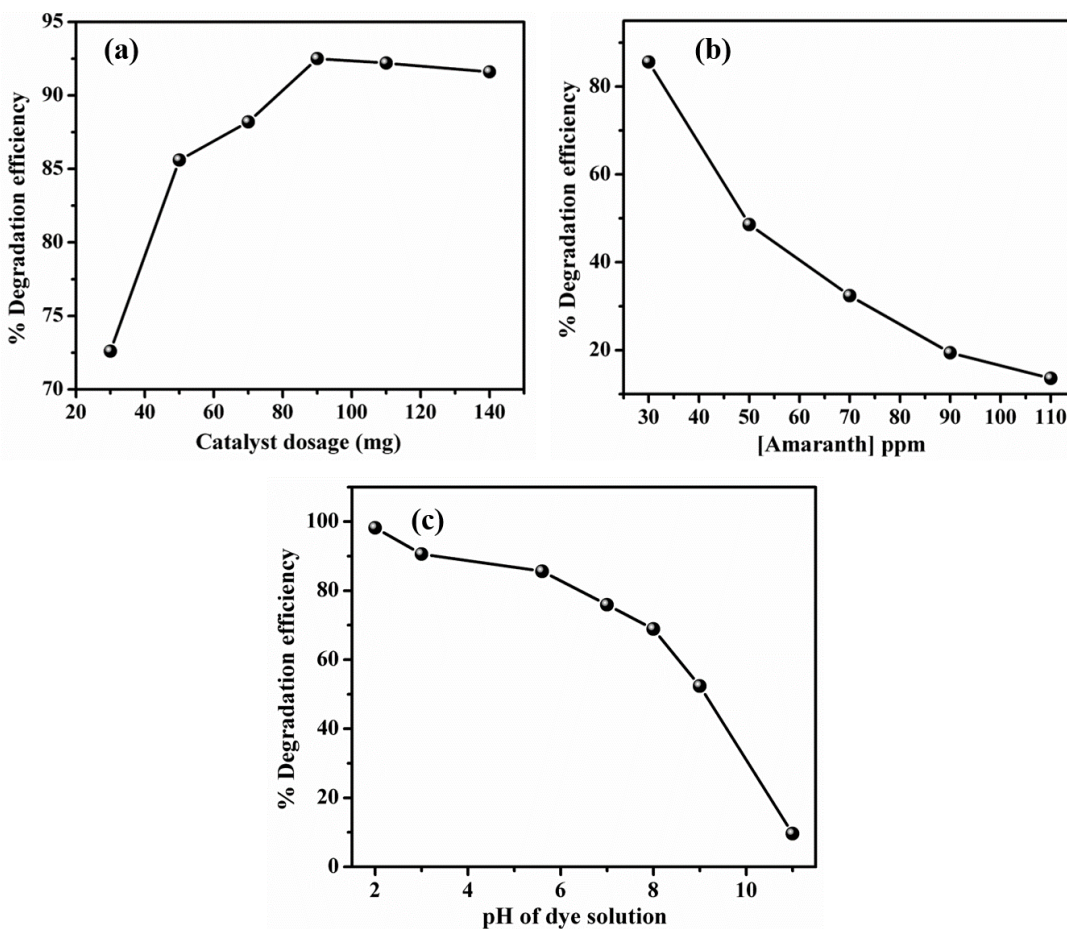


Figure 2.25: Effect of (a) catalyst dosage, (b) initial Amaranth dye concentration and (c) pH of the dye solution.

➤ **Effect of catalyst loading on photocatalytic activity of TiO₂.**

The optimum concentration of TiO₂ required for photocatalytic degradation of Amaranth dye was evaluated by varying the catalyst dosage in individual photocatalytic reactions. The amount of TiO₂ taken was 30, 50, 70, 90, 110 and 140 mg. Figure 2.25 (a) represents the % degradation efficiency as a function of catalyst dosage. The photocatalytic degradation efficiency was observed to increase with increase in the amount of catalyst up to 90 mg. This is attributed to the increase in number of active sites on the photocatalytic surface which leads to the increase in the photocatalytic activity [41]. However, with further increase in catalyst dosage the photocatalytic degradation efficiency did not improve any further, which could be due to the saturation of particles in the solution and less penetration of light due to the turbidity formed from the increased amount of the catalyst.

➤ **Effect of initial dye concentration on photocatalytic activity of TiO₂.**

The effect of initial dye concentration of photocatalytic degradation efficiency was evaluated experimentally. The different initial concentrations of the dye taken were 30 ppm, 50 ppm, 70 ppm, 90 ppm and 110 ppm as can be observed from Figure 2.25 (b). It is observed that at lower initial concentration of the dye, the rate of degradation is faster and with increase in initial dye concentration the rate of dye degradation decreases. This is attributed to the fact that at high concentrations, dye itself acts as an internal filter absorbing most of the light from the lamp [42]. Thus, reducing the number of photons available for excitation of the catalyst surface and hence leads to reduction in reactive oxygen species which are responsible for photocatalytic degradation of the dye.

➤ **Effect of pH on photocatalytic activity of TiO₂.**

The initial pH of the dye solution was observed to be 5.6. The efficiency of photocatalytic degradation of dye always depends on the pH of the dye solution and the point of zero charge of the catalyst. The effect of pH for photocatalytic degradation of Amaranth dye was investigated in the pH range from 2 to 11. It is observed from the Figure 2.25 (c) that the acidic pH shows better photocatalytic degradation as compared to alkaline pH. The highest photocatalytic degradation of Amaranth was obtained for pH = 2. Thus, the optimized conditions for photocatalytic degradation of Amaranth dye were [catalyst] = 90 mg, [Amaranth dye] = 30 ppm and pH = 2. Furthermore, these optimized conditions were used to investigate the photocatalytic degradation of Amaranth dye using TOA, TTC, TBTC, TOAU, TTCU and TBTCU catalysts and compared its activity with that of DEG-P25, PT and TU8.

➤ **Photocatalytic activity of TiO₂ synthesized using carboxylic acid-urea mixtures as structure directing agents.**

To investigate the influence of induced structural porosity in TiO₂ using carboxylic acid and urea combination as structure directing agent, the photocatalytic degradation of Amaranth dye was carried out under optimized conditions i.e [catalyst] = 90 mg, [Amaranth] = 30 ppm and pH=2. Figure 2.26 (a & b) shows the kinetic profiles of the photocatalytic degradation of Amaranth dye using DEG-P25, PT and TU8. TU8 exhibited maximum photocatalytic degradation efficiency of 88 % in 15 minutes as compared to DEG and PT. This enhanced

activity of TU8 was due to three main factors i) agglomerate porosity with average pore size of 7.5 nm and average pore volume of 0.35 cc.g^{-1} contributing to the high surface area of $186 \text{ m}^2.\text{g}^{-1}$ ii) the acidic pH of the solution which facilitates the faster adsorption of an anionic dye on the catalyst surface and iii) the lower band gap of TU8 compared to PT. Furthermore, the comparative photocatalytic degradation study was carried out for TiO_2 synthesized using carboxylic acid and carboxylic acid urea combination as SDA. The TiO_2 synthesized using only carboxylic acids as structure directing agent i.e. TOA, TTC and TBTC exhibited a gradual increase in photocatalytic degradation efficiency with the increase in the number of $-\text{COOH}$ groups. The order of photocatalytic performance was $\text{TBTC} (83.4 \%) > \text{TTC} (79.1 \%) > \text{TOA} (73.6 \%)$ respectively along with the corresponding increase in pseudo first order rate constant $\text{TBTC} (0.993 \times 10^{-1} \text{ min}^{-1}) > \text{TTC} (0.776 \times 10^{-1} \text{ min}^{-1}) > \text{TOA} (0.645 \times 10^{-1} \text{ min}^{-1})$ as can be seen from the Table 2.9. In comparison to TOA, TTC and TBTC corresponding % degradation efficiency of TOAU, TTCU and TBTCU was higher. TOAU showed marginal increase in % degradation efficiency of 76.9 % as compared to TOA. However, TTCU and TBTCU which showed robust structural porosity and high surface area exhibited enhanced photocatalytic performance of 89.9 % and 95.6 % respectively, within irradiation time of 15 minutes. On comparing the photocatalytic performance of TBTCU with that of DEG-P25, PT and TU8 the order of % degradation efficiency was found to be $\text{TBTCU} (95.6 \%) > \text{TU8} (88 \%) > \text{PT} (84.6 \%) > \text{DEG} (82.8 \%)$. So thus, the photocatalytic degradation efficiency of TBTCU was higher than that of TU8 which could be due to its interconnected structural porosity contributing to high surface area as compared to the agglomerate porosity in case of TU8. The improved % degradation efficiency of 95.6 % with maximum rate constant of $1.5 \times 10^{-1} \text{ min}^{-1}$ was compared with that of literature reports as summarized in Table 2.10. TBTCU exhibited highest % degradation of Amaranth dye within 15 minutes in comparison to other literature reported catalyst such as ZnO , N-WO_3 , N-ZrO_2 which requires around 100-300 minutes for complete degradation of the Amaranth dye under comparable experimental conditions. This signifies the importance of structural porosity in the catalyst for photocatalytic performance. Furthermore, the regeneration activity studies were carried out in order to evaluate the catalyst stability and cycling performance.

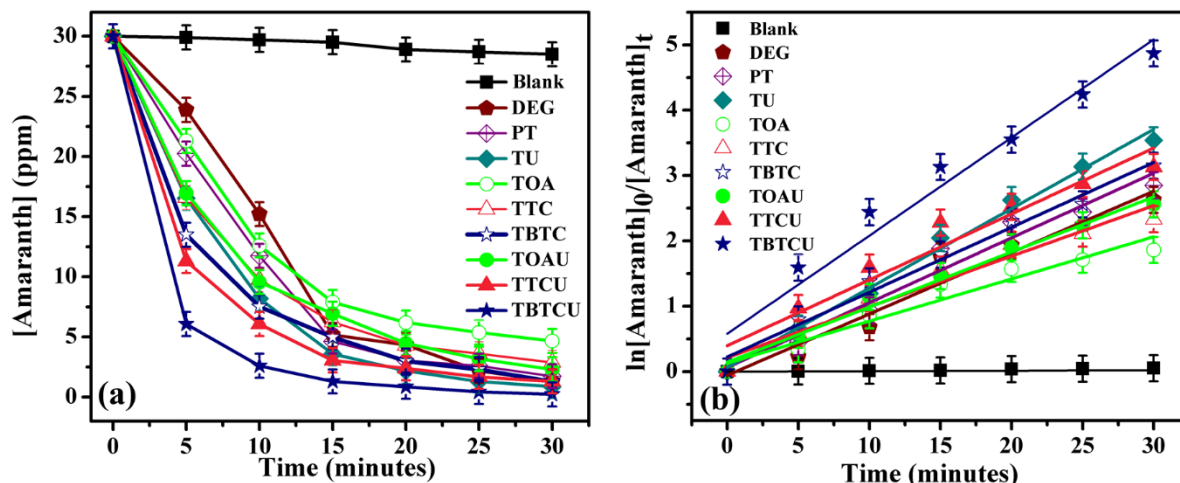


Figure 2.26: a) Kinetic profiles and b) logarithmic plots for photocatalytic degradation of Amaranth dye using TiO₂ photocatalysts.

Catalyst	Band gap (eV)	BET surface area ($\pm 5 \text{ m}^2 \cdot \text{g}^{-1}$)	% Degradation (in 15 min)	$k_{\text{app}} (\times 10^{-1}) (\text{min}^{-1})$
Blank	---	---	5.0	0.002
DEG	3.20	50	82.8	1.145
PT	3.23	80	84.6	1.108
TU	3.22	186	88.0	1.334
TOA	3.16	107	73.6	0.902
TTC	3.18	130	79.1	1.042
TBTC	3.21	180	83.4	1.190
TOAU	3.14	116	76.9	0.990
TTCU	3.15	146	89.8	1.492
TBTCU	3.19	238	95.6	2.048

Table 2.9: Comparative analysis of the Amaranth degradation efficiency, corresponding photocatalytic rate constant and material properties of all the synthesized catalysts.

Catalyst	Initial dye concentration	Light source	Reaction time (min)	% Degradation
N,S-doped Titania [43]	3.90×10^{-5} M	200 W tungsten lamp	90	59.3
N-WO ₃ [44]	25 mg.L ⁻¹	160 W Visible and UVA light	120	100
TiO ₂ [45]	84 μ mol.L ⁻¹	125 W	60	75.0
TiO ₂ [46]	30 ppm	Solar light	90	99.1
N-ZrO ₂ [47]	10 ppm	Fluorescent lamp (visible) 24 W and Low pressure Hg lamp(UV) of 15 W	120 240	26.4 84.5
ZnO [48]	20 ppm	250 W Hg medium pressure lamp	120	100
ZnO [49]	4.4×10^{-5} M	200 W tungsten lamp	300	92.5
TBTCU [This work]	30 ppm	250 W Hg Medium pressure Lamp	15	95.6

Table 2.10: Comparative analysis of Amaranth dye degradation efficiency of TBTCU with that of literature reported catalysts.

➤ **Catalyst regeneration studies**

The regeneration of the all the synthesized catalysts have been carried out under optimized conditions. Figure 2.27 shows the regeneration capacity of DEG, PT, TU8, TBTC and TBTCU was carried out for five consecutive cycles. After each reaction the dye adsorbed on the catalyst was desorbed by boiling it in a hot water for one hour with continuous stirring and then it was reactivated at 200 °C, and then the photocatalytic degradation was carried out. The obtained photocatalytic degradation efficiency is presented in Figure 2.26. Thus the TBTCU showed maximum efficiency as compared to the rest of the catalyst.

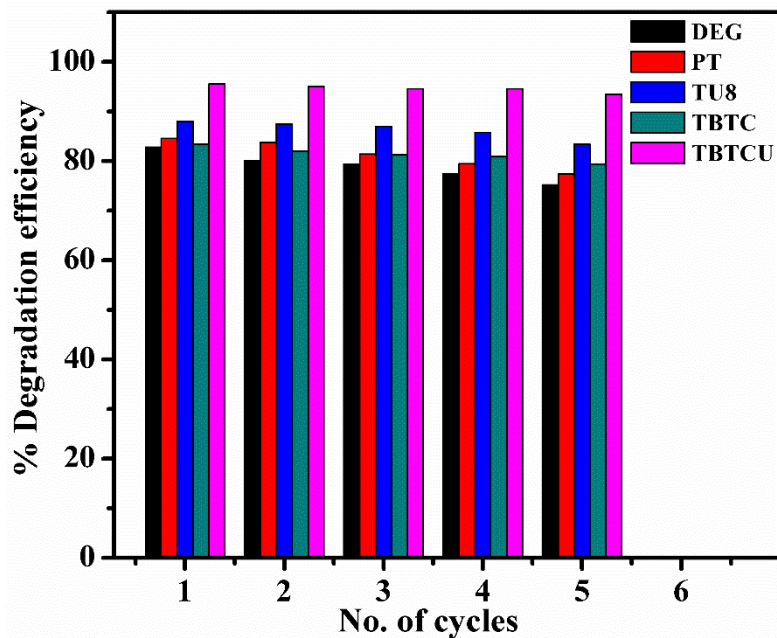


Figure 2.27: Catalyst regeneration study of Degussa P-25, PT, TU8, TBTC and TBTCU.

2.6 Conclusion.

Mesoporous anatase TiO_2 catalysts were synthesized using reflux assisted sol-gel method. The effect of urea on surface area of TiO_2 was investigated. TiO_2 synthesized using Ti:U ratio of 1:8 exhibited highest surface area of $186 \text{ m}^2.\text{g}^{-1}$ with pore size of 7.5 nm and pore volume of 0.35 cc.g^{-1} thus confirming the role of urea in inducing porosity in TiO_2 . In addition to this, the effect of different carboxylic acids as SDA on pore size distribution and surface area of the TiO_2 was investigated. It was confirmed that with the increase in the number of $-\text{COOH}$ groups in the SDA, the porous TiO_2 with wider pore size distribution are formed. This porosity is largely due to the randomly oriented agglomerated nanoparticles. The stronger interaction between the carboxylate groups and Ti^{4+} also lead to longer calcination times for their complete removal from the TiO_2 . Such increased heat treatments probably also lead to partial collapse of pore structure in TiO_2 . In an innovative strategy, suitable combination of carboxylic acid with urea was used as a mixed SDA which assisted in facile removal of carboxylic acids during combustion further assisting in tailoring the agglomerate porosity into structurally robust, ordered mesoporosity especially in the case of TTCU and TBTCU. Structurally robust mesoporous TiO_2 with highest surface area of $238 \text{ m}^2.\text{g}^{-1}$, and average pore size and pore volume of 4.8 nm and 0.84 cc.g^{-1} was obtained using

butanetetracarboxylic acid and urea as SDA. All the synthesized TiO₂ catalysts were then tested for adsorptive removal of Amaranth dye from water. The experimental data was analyzed using various adsorption isotherms and adsorption kinetic models were fitted to understand the interaction between Amaranth dye and TiO₂. Amaranth adsorption on all the synthesized TiO₂ exhibited Sips adsorption model and the maximum adsorption capacity of 87.8 mg.g⁻¹ was obtained for TBTCU which was greater than PT by a factor of 2. Furthermore, TBTCU also exhibited the highest Amaranth dye photodegradation efficiency of 95.6 % (in 15 minutes) with a rate constant of $2.05 \times 10^{-1} \text{ min}^{-1}$ which is the best photocatalytic Amaranth degradation performance reported till date in the literature. Therefore, the first objective of designing a novel synthesis process to produce highly robust, mesoporous TiO₂ catalyst of high surface area and catalytic activity was successfully achieved.

2.7 References

- [1] N. Kumar, H. Mittal, S.M. Alhassan, S.S. Ray, Bionanocomposite Hydrogel for the Adsorption of Dye and Reusability of Generated Waste for the Photodegradation of Ciprofloxacin: A Demonstration of the Circularity Concept for Water Purification, *ACS Sustain. Chem. Eng.* 6 (2018) 17011–17025.
- [2] R. Baccar, P. Blázquez, J. Bouzid, M. Feki, H. Attiya, M. Sarrà, Modeling of adsorption isotherms and kinetics of a tannery dye onto an activated carbon prepared from an agricultural by-product, *Fuel Process. Technol.* 106 (2013) 408–415.
- [3] N. Ayawei, A.N. Ebelegi, D. Wankasi, Modelling and Interpretation of Adsorption Isotherms, *J. Chem.* 2017 (2017) 1–11.
- [4] M.A. Al-Ghouti, D.A. Da'ana, Guidelines for the use and interpretation of adsorption isotherm models: A review, *J. Hazard. Mater.* 393 (2020) 122383.
- [5] B.M. Marwa, S. Bruno, B. Mongi, F. Tran Van, B.L. Abdelmottaleb, Modeling of adsorption isotherms of dye N719 on titanium oxide using the grand canonical ensemble in statistical physics for dye sensitized solar cells, *Sol. Energy.* 135 (2016) 177–187.
- [6] L.S. Chougala, M.S. Yatnatti, R.K. Linganagoudar, R.R. Kamble, J.S. Kadadevarmath, A simple approach on synthesis of TiO₂ nanoparticles and its application in dye sensitized solar cells, *J. Nano- Electron. Phys.* 9 (2017) 1-6.
- [7] T. V. Gerasimova, O.L. Evdokimova (Galkina), A.S. Kraev, V.K. Ivanov, A. V. Agafonov, Micro-mesoporous anatase TiO₂ nanorods with high specific surface area possessing enhanced adsorption ability and photocatalytic activity, *Microporous and Mesoporous Materials.* Elsevier Ltd. 235 (2016), 185-194.
- [8] P. Cheng, J. Qiu, M. Gu, Y. Jin, W. Shangguan, Synthesis of shape-controlled titania particles from a precursor solution containing urea, *Mater. Lett.* 58 (2004) 3751–3755.
- [9] J.Y. Zheng, J. Bin Pang, K.Y. Qiu, Y. Wei, Synthesis and characterization of mesoporous titania and silica-titania materials by urea templated sol-gel reactions, *Microporous Mesoporous Mater.* 49 (2001) 189–195.

- [10] D.C.L. Vasconcelos, E.H.M. Nunes, A.C.S. Sabioni, P.M.P. Vasconcelos, W.L. Vasconcelos, Optical characterization of 316L stainless steel coated with sol-gel titania, *J. Non. Cryst. Solids*. 358 (2012) 3042–3047.
- [11] S.S. Muniandy, N.H. Mohd Kaus, Z.T. Jiang, M. Altarawneh, H.L. Lee, Green synthesis of mesoporous anatase TiO₂ nanoparticles and their photocatalytic activities, *RSC Adv.* 7 (2017) 48083–48094.
- [12] M. Thommes, K. Kaneko, A. V. Neimark, J.P. Olivier, F. Rodriguez-Reinoso, J. Rouquerol, K.S.W. Sing, Physisorption of gases, with special reference to the evaluation of surface area and pore size distribution (IUPAC Technical Report), *Pure Appl. Chem.* 87 (2015).
- [13] S.M. Deshmukh, M.S. Tamboli, H. Shaikh, S.B. Babar, D.P. Hiwarale, A.G. Thate, A.F. Shaikh, M.A. Alam, S.M. Khetre, S.R. Bamane, Nanoparticles and their photocatalytic activity, (2021) 1–12.
- [14] I. Sopyan, N. Hafizah, Nanosized TiO₂ photocatalyst powder via sol-gel method: Effect of hydrolysis degree on powder properties, *Int. J. Photoenergy*. 2009 (2009) 8–10.
- [15] L. Ye, J. Mao, J. Liu, Z. Jiang, T. Peng, L. Zan, Synthesis of anatase TiO₂ nanocrystals with {101}, {001} or {010} single facets of 90% level exposure and liquid-phase photocatalytic reduction and oxidation activity orders, *J. Mater. Chem. A*. 1 (2013) 10532–10537.
- [16] L.H. Kao, T.C. Hsu, H.Y. Lu, Sol-gel synthesis and morphological control of nanocrystalline TiO₂ via urea treatment, *J. Colloid Interface Sci.* 316 (2007) 160–167.
- [17] A.L. Castro, M.R. Nunes, A.P. Carvalho, F.M. Costa, M.H. Florêncio, Synthesis of anatase TiO₂ nanoparticles with high temperature stability and photocatalytic activity, *Solid State Sci.* 10 (2008) 602–606.
- [18] J. Marques, T.D. Gomes, M.A. Forte, R.F. Silva, C.J. Tavares, A new route for the synthesis of highly-active N-doped TiO₂ nanoparticles for visible light photocatalysis using urea as nitrogen precursor, *Catal. Today*. (2019) 36–45.

- [19] K. Sivaranjani, S. Agarkar, S.B. Ogale, C.S. Gopinath, Toward a quantitative correlation between microstructure and DSSC efficiency: A case study of $\text{TiO}_{2-x}\text{N}_x$ nanoparticles in a disordered mesoporous framework, *J. Phys. Chem. C*. 116 (2012) 2581–2587.
- [20] K. Sivaranjani, C.S. Gopinath, Porosity driven photocatalytic activity of wormhole mesoporous $\text{TiO}_{2-x}\text{N}_x$ in direct sunlight, *J. Mater. Chem.* 21 (2011) 2639–2647.
- [21] S. Du, J. Lian, F. Zhang, Visible light-responsive N-doped TiO_2 photocatalysis: synthesis, characterizations, and applications, *Trans. Tianjin Univ.* 28 (2022) 33–52.
- [22] G.B. Soares, B. Bravin, C.M.P. Vaz, C. Ribeiro, Facile synthesis of N-doped TiO_2 nanoparticles by a modified polymeric precursor method and its photocatalytic properties, *Appl. Catal. B Environ.* 106 (2011) 287–294.
- [23] A. Pandikumar, K. Sivaranjani, C.S. Gopinath, R. Ramaraj, Aminosilicate sol-gel stabilized N-doped TiO_2 -Au nanocomposite materials and their potential environmental remediation applications, *RSC Adv.* 3 (2013) 13390–13398.
- [24] B. Jiang, H. Yin, T. Jiang, J. Yan, Z. Fan, C. Li, J. Wu, Y. Wada, Size-controlled synthesis of anatase TiO_2 nanoparticles by carboxylic acid group-containing organics, *Mater. Chem. Phys.* 92 (2005) 595–599.
- [25] B.R. Srinivasan, S.Y. Shetgaonkar, M. Saxena, C. Näther, A new calcium(II) coordination polymer based on a μ 2-bridging tridentate 4-nitrobenzoate, *Indian J. Chem. - Sect. A Inorganic, Phys. Theor. Anal. Chem.* 51 (2012) 435–443.
- [26] B.R. Srinivasan, Synthesis, characterization and properties of a water-rich calcium (II)-4-nitrobenzoate, *Indian J. Chemistry.* 49A (2010) 1468–1477.
- [27] P. V. Bakre, S.G. Tilve, Dicarboxylic acids as soft templates for the sol-gel synthesis of mesoporous nano TiO_2 with enhanced photocatalytic activity, *ChemistrySelect.* 2 (2017) 7063–7072.
- [28] S. Challagulla, S. Roy, The role of fuel to oxidizer ratio in solution combustion synthesis of TiO_2 and its influence on photocatalysis, *J. Mater. Res.* 32 (2017) 2764–2772.

- [29] M.Y. Nassar, E.I. Ali, E.S. Zakaria, Tunable auto-combustion preparation of TiO₂ nanostructures as efficient adsorbents for the removal of an anionic textile dye, *RSC Adv.* 7 (2017) 8034–8050.
- [30] S.-L. Chung, C.-M. Wang, Solution combustion synthesis of TiO₂ and its use for fabrication of photoelectrode for dye-sensitized solar cell, *J. Mater. Sci. Technol.* 28 (2012), 713-722.
- [31] C.C. Travis, E.L. Etnier, A Survey of sorption relationships for reactive solutes in Soil, *J. Environ. Qual.* 10 (2010) 1-8.
- [32] I. Anastopoulos, A. Hosseini-Bandegharai, J. Fu, A.C. Mitropoulos, G.Z. Kyzas, Use of nanoparticles for dye adsorption: Review, *J. Dispers. Sci. Technol.* 39 (2018) 836–847.
- [33] H. Mittal, P.P. Morajkar, A. Al Alili, S.M. Alhassan, In-Situ synthesis of ZnO nanoparticles using gum arabic based hydrogels as a self-template for effective malachite green dye adsorption, *J. Polym. Environ.* (2020).
- [34] H. Mittal, S.M. Alhassan, S.S. Ray, Efficient organic dye removal from wastewater by magnetic carbonaceous adsorbent prepared from corn starch, *J. Environ. Chem. Eng.* 6 (2018) 7119–7131.
- [35] T.H. Tran, A.H. Le, T.H. Pham, D.T. Nguyen, S.W. Chang, W.J. Chung, D.D. Nguyen, Adsorption isotherms and kinetic modeling of methylene blue dye onto a carbonaceous hydrochar adsorbent derived from coffee husk waste, *Sci. Total Environ.* 725 (2020) 138325.
- [36] T.S. Kim, H.J. Song, M.A. Dar, H.J. Lee, D.W. Kim, Fast adsorption kinetics of highly dispersed ultrafine nickel/carbon nanoparticles for organic dye removal, *Appl. Surf. Sci.* 439 (2018) 364–370.
- [37] W. Konicki, A. Hełminiak, W. Arabczyk, E. Mijowska, Adsorption of cationic dyes onto Fe@graphite core-shell magnetic nanocomposite: Equilibrium, kinetics and thermodynamics, *Chem. Eng. Res. Des.* 129 (2018) 259–270.
- [38] V. Vadivelan, K. Vasanth Kumar, Equilibrium, kinetics, mechanism, and process

- design for the sorption of methylene blue onto rice husk, *J. Colloid Interface Sci.* 286 (2005) 90–100.
- [39] H. Eskandarloo, A. Badiei, C. Haug, Enhanced photocatalytic degradation of an azo textile dye by using TiO₂/NiO coupled nanoparticles: Optimization of synthesis and operational key factors, *Mater. Sci. Semicond. Process.* 27 (2014) 240–253.
- [40] S. Sakulphaemaruehai, T. Sreethawong, Synthesis of mesoporous-assembled TiO₂ nanocrystals by a modified urea-aided sol-gel process and their outstanding photocatalytic H₂ production activity, *Int. J. Hydrogen Energy.* 36 (2011) 6553–6559.
- [41] L. Gomathi Devi, K. Eraiah Rajashekhar, K.S. Anantha Raju, S. Girish Kumar, Influence of various aromatic derivatives on the advanced photo Fenton degradation of Amaranth dye, *Desalination.* 270 (2011) 31–39.
- [42] V.K. Gupta, R. Jain, A. Mittal, T.A. Saleh, A. Nayak, S. Agarwal, S. Sikarwar, Photocatalytic degradation of toxic dye amaranth on TiO₂/UV in aqueous suspensions, *Mater. Sci. Eng. C.* 32 (2012) 12–17.
- [43] A.K. Jain, S. Sharma, R. Ameta, Enhanced photocatalytic activity of N, S-doped titania for degradation of amaranth, *Merit Res. J. Environ. Sci. Toxicol.* 3 (2015) 25–30.
- [44] H. Sudrajat, S. Babel, Rapid photocatalytic degradation of the recalcitrant dye amaranth by highly active N-WO₃, *Environ. Chem. Lett.* 14 (2016) 243–249.
- [45] M. Karkmaz, E. Puzenat, C. Guillard, J.M. Herrmann, Photocatalytic degradation of the alimentary azo dye amaranth: Mineralization of the azo group to nitrogen, *Appl. Catal. B Environ.* 51 (2004) 183–194.
- [46] A.P. Naik, A. V. Salkar, M.S. Majik, P.P. Morajkar, Enhanced photocatalytic degradation of Amaranth dye on mesoporous anatase TiO₂: Evidence of C-N, N=N bond cleavage and identification of new intermediates, *Photochem. Photobiol. Sci.* 16 (2017) 1126–1138.
- [47] H. Sudrajat, S. Babel, H. Sakai, S. Takizawa, Rapid enhanced photocatalytic degradation of dyes using novel N-doped ZrO₂, *J. Environ. Manage.* 165 (2016) 224–

234.

- [48] N. Divya, A. Bansal, A.K. Jana, Photocatalytic activity of transition metal ion doped titania for Amaranth dye degradation, *Mater. Sci. Forum.* 712 (2012) 85–104.
- [49] R. Ameta, N. Jain, S. Kothari, Photocatalytic bleaching of amaranth dye over ZnO powder, *Indian J. Chem. Technol.* 11 (2004) 423–426.

CHAPTER III:

SYNTHESIS,

CHARACTERIZATION AND

CATALYTIC APPLICATION OF

NANOPOROUS Ni_{1-x}O CATALYTS

3.1 PROLOGUE

This chapter deals with synthesis, characterization and catalytic application of Ni_{1-x}O nanostructures. The nanoporous Ni_{1-x}O catalysts have been synthesized by combustion of different nickel coordination compounds:

- i) Hexaaquanickel(II) bis(p-nitrobenzoate) dihydrate
- ii) Tetra-aquobis(para-nitrobenzoato)nickel(II) dihydrate
- iii) Diaquabis(imidazole- κN)bis(nitrobenzoate- κO)nickel(II)
- iv) Hexakis(imidazole)nickel(II) bis(4-nitrobenzoate) dehydrate

Furthermore, sol-gel synthesis method has been employed wherein Ni_{1-x}O has been prepared using Ni^{2+} precursors, with and without urea as SDA as detailed in section 3.3. The detailed characterization of Ni_{1-x}O synthesized by the above methods is discussed in section 3.4.1. Finally, its catalytic efficiency for the adsorptive removal and photocatalytic degradation of Amaranth dye is presented in section 3.4.2 and 3.4.3 followed by the conclusion of this study in section 3.5.

3.2 CHEMICALS USED

The chemicals such as Nickel chloride hexahydrate (99 %), Sodium bicarbonate (99%), para-Nitrobenzoic acid (4-nbaH) (99 %), Ammonia solution (25 % in water), Urea (99.5 %) were purchased from Alfa Aesar. Imidazole (99 %) was purchased from Spectrochem Pvt Ltd. All these chemicals were used for the experimental work without any further purification.

3.3 EXPERIMENTAL: SYNTHESIS STRATEGY AND PROCEDURES

3.3.1 Synthesis of Ni_{1-x}O from $[\text{Ni}(\text{H}_2\text{O})_6](4\text{-nba})_2 \cdot 2\text{H}_2\text{O}$ and $[\text{Ni}(\text{H}_2\text{O})_4(4\text{-nba})_2] \cdot 2\text{H}_2\text{O}$

The chemical structures of $[\text{Ni}(\text{H}_2\text{O})_6](4\text{-nba})_2 \cdot 2\text{H}_2\text{O}$ referred to as compound I and $[\text{Ni}(\text{H}_2\text{O})_4(4\text{-nba})_2] \cdot 2\text{H}_2\text{O}$ labeled as compound II are shown in Figure 3.1. The synthesis of nickel coordination compounds I and II was carried out as per the procedure reported in references [1, 2]. The schematic representation of synthesis procedure for I & II and its subsequent transformation into Ni_{1-x}O is depicted in Figure 3.2. The reaction of freshly precipitated nickel hydroxide with 4-nitrobenzoic acid (4-nbaH) dissolved in ammonia (at pH = 12.0) resulted in the formation of the blue hexaquo Ni(II) compound $[\text{Ni}(\text{H}_2\text{O})_6](4\text{-$

$\text{nba})_2 \cdot 2\text{H}_2\text{O}$ (I) in agreement with Ref. [1]. The detailed characterization and crystal structure elucidation of compounds I is available in references [1–3]. The synthesized crystals were calcined at 400°C . The Ni_{1-x}O obtained post-calcination is labeled as N1.

Subsequently, the reaction of $[\text{Ni}(\text{H}_2\text{O})_6]\text{Cl}_2$ with the sodium salt of 4-nitrobenzoic acid resulted in the formation of the green compound $[\text{Ni}(\text{H}_2\text{O})_4(4\text{-nba})_2] \cdot 2\text{H}_2\text{O}$ (II) which is in good agreement with the reported observations [2]. The synthesized crystals were calcined by following a controlled two-step calcination strategy. The detailed characterization and crystal structure elucidation of compounds I and II are available in references [1–3] and hence are not repeated here. The synthesized crystals were calcined at 400°C . The Ni_{1-x}O obtained post-calcination is labeled as N2.

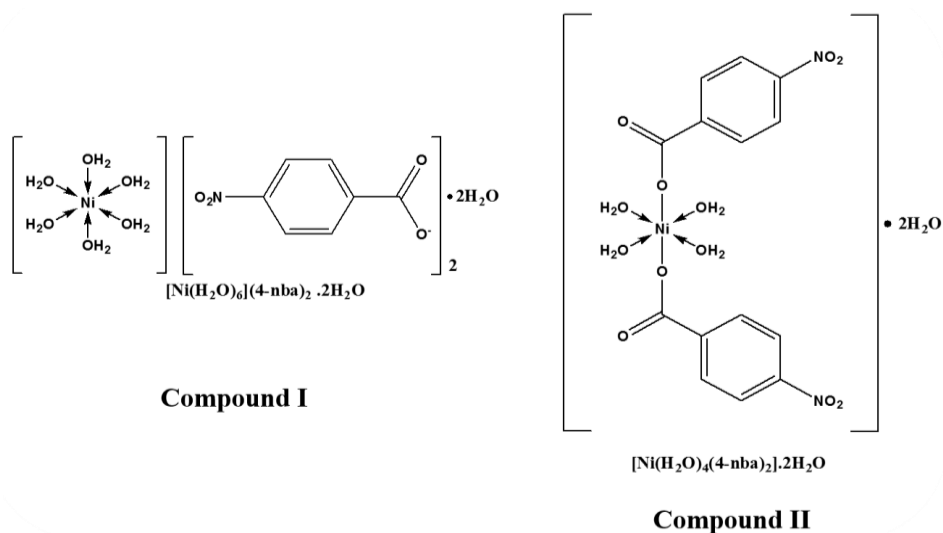


Figure 3.1: Structure of (I) $[\text{Ni}(\text{H}_2\text{O})_6](4\text{-nba})_2 \cdot 2\text{H}_2\text{O}$ and (II) $[\text{Ni}(\text{H}_2\text{O})_4(4\text{-nba})_2] \cdot 2\text{H}_2\text{O}$

3.3.1 Synthesis of Ni_{1-x}O from $[\text{Ni}(\text{Im})_6](4\text{-nba})_2 \cdot 2\text{H}_2\text{O}$ and $[\text{Ni}(\text{Im})_2(4\text{-nba})_2(\text{H}_2\text{O})_4] \cdot 2\text{H}_2\text{O}$

The chemical structure of $[\text{Ni}(\text{H}_2\text{O})_2(\text{Im})_2(4\text{-nba})_2]$ labeled as III and $[\text{Ni}(\text{Im})_6](4\text{-nba})_2 \cdot 2\text{H}_2\text{O}$ labeled as IV is shown in Figure 3.3. The synthesis of nickel coordination compounds III and IV is carried out as per the procedure reported in [4, 5]. The schematic representation of synthesis procedure for III and IV and their subsequent transformation into Ni_{1-x}O is depicted in Figure 3.4.

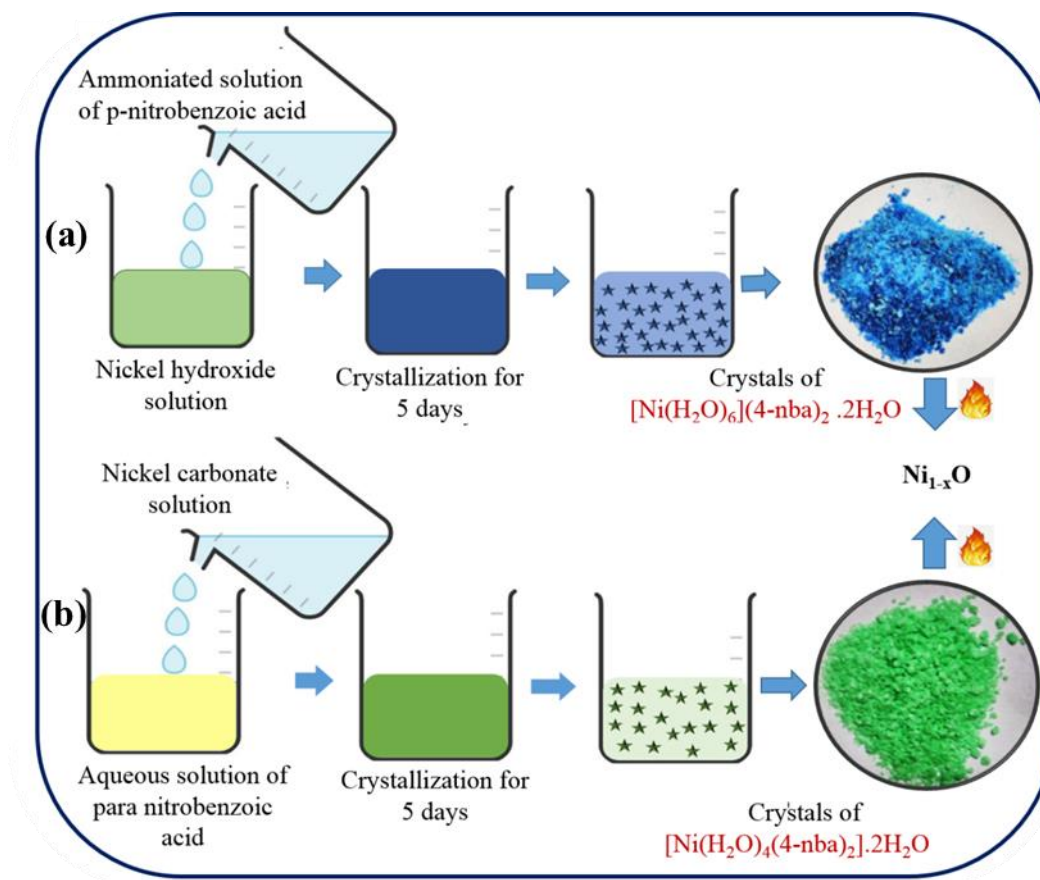


Figure 3.2: Schematic representation of synthesis of Ni_{1-x}O from compounds a) I and b) II.

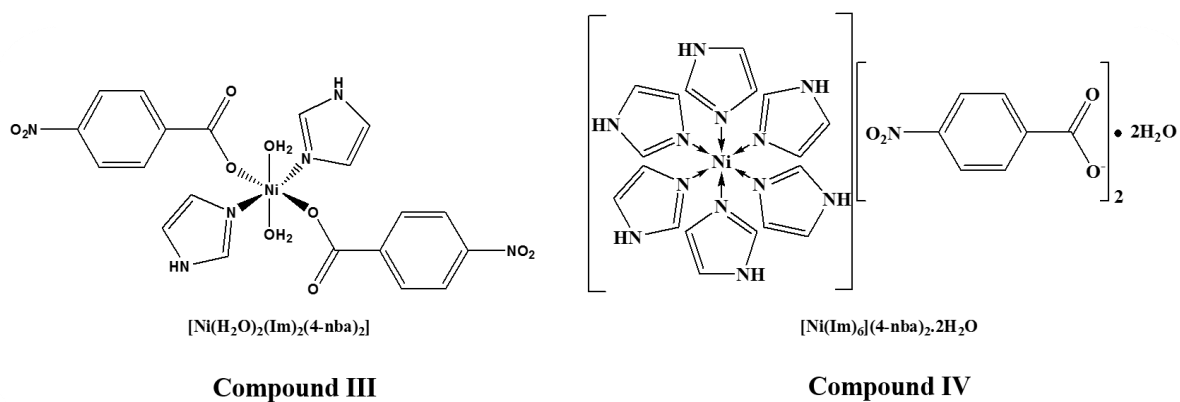


Figure 3.3: Structures of (III) $[\text{Ni}(\text{Im})_2(4\text{-nba})_2(\text{H}_2\text{O})_4] \cdot 2\text{H}_2\text{O}$ and (IV) $[\text{Ni}(\text{Im})_6](4\text{-nba})_2 \cdot 2\text{H}_2\text{O}$

Briefly, the sodium salt of 4-nitrobenzoic acid (4-nbaH) was synthesized by reacting 4-nbaH with sodium bicarbonate in an aqueous medium and added to $[\text{Ni}(\text{H}_2\text{O})_6]\text{Cl}_2$ solution to obtain a green coloured mixture. Further to this solution mixture, imidazole in the ratio Ni: Im = 1:2 was added, resulting in the formation of dark green coloured crystals of $[\text{Ni}(\text{H}_2\text{O})_2(\text{Im})_2(4\text{-nba})_2]$ which is in good agreement with reference [6]. The synthesized crystals were calcined at 400°C . The Ni_{1-x}O obtained post-calcination is labeled as N3. Similarly, the reaction $[\text{Ni}(\text{H}_2\text{O})_6]\text{Cl}_2$ with the sodium salt of 4-nitrobenzoic acid and Imidazole in the ratio Ni: Im = 1:6 resulted in the formation of blue coloured crystals of $[\text{Ni}(\text{Im})_6](4\text{-nba})_2 \cdot 2\text{H}_2\text{O}$ which is in agreement with reference [4]. The detailed characterization and crystal structure elucidations of III and IV is reported in the references [2–4, 6] and therefore it is not repeated here. The post calcined material was labeled as N4.

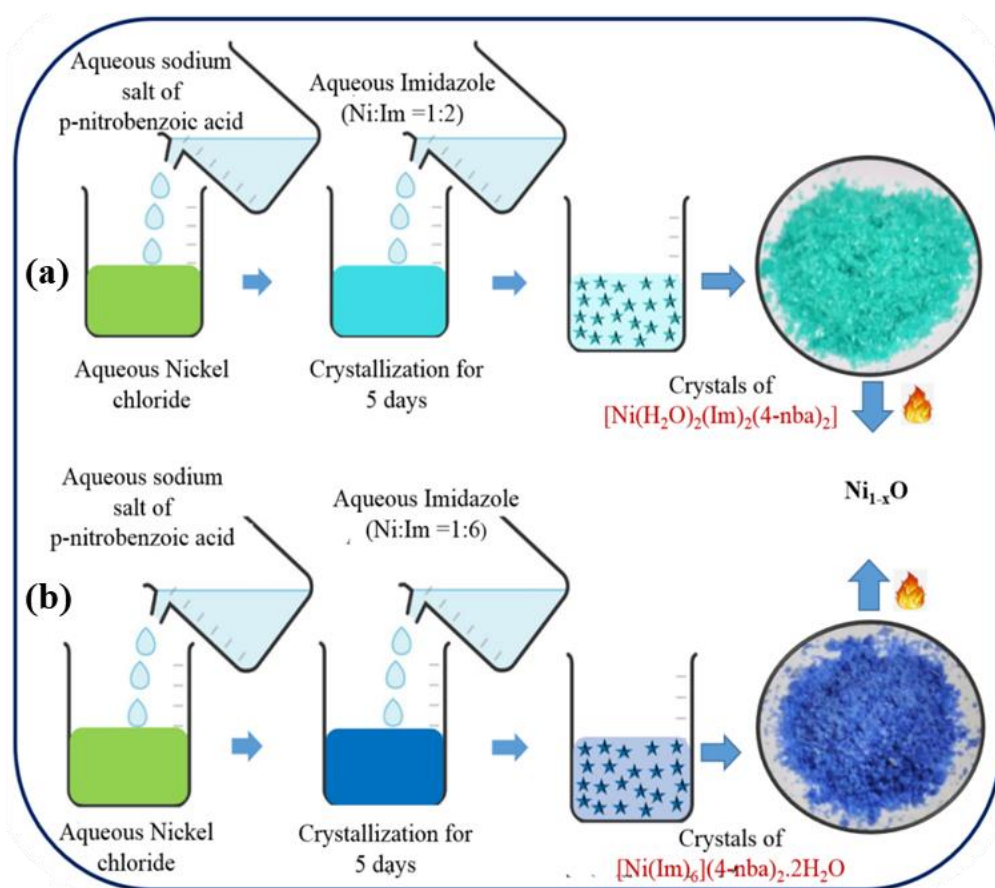


Figure 3.4: Synthesis of Ni_{1-x}O from compounds a) III and b) IV.

3.3.2 Synthesis of Ni_{1-x}O from $\text{Ni}(\text{OH})_2$ –urea mixture.

A solution was prepared by dissolving 3.89 g of the nickel nitrate in 20 mL deionized water. To this solution 1M NH_4OH was added to form nickel hydroxide precipitate which was then digested at 100 °C and calcined at 400°C to obtain pristine Ni_{1-x}O hereafter referred to as PN. Subsequently, in another synthesis, nickel hydroxide was precipitated in a similar procedure as above and was further modified using urea as structure directing agent. The obtained mixture was digested at 100 °C to get a dried precipitate. The precipitate was then calcined at 400°C to obtain Ni_{1-x}O referred to as NU. The temperature for calcination was chosen based on TG-DTA analysis, more details of which are presented in the result and discussion section. A schematic representation of the above synthesis strategy is shown in Figure 3.5.

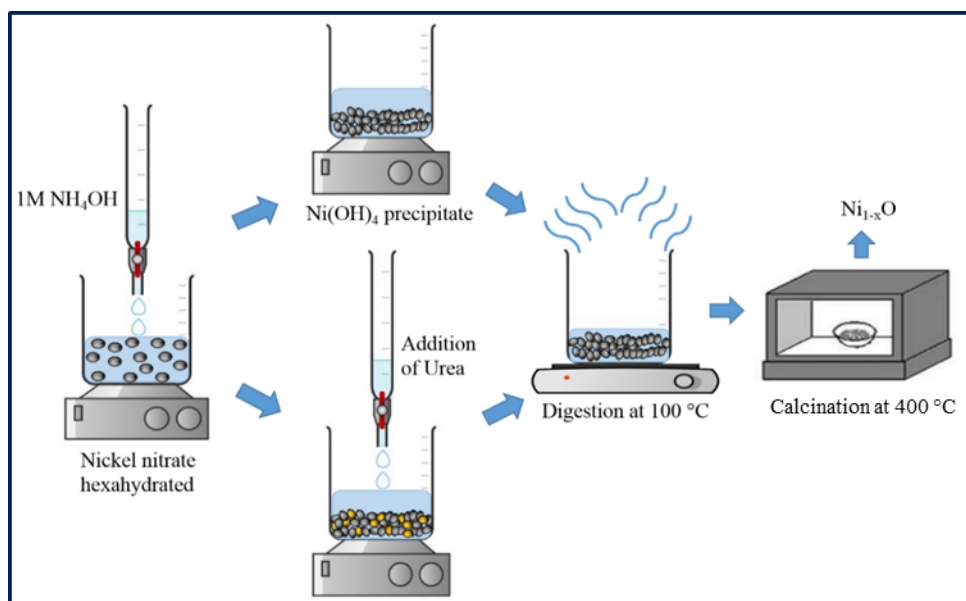


Figure 3.5: Schematic of Ni_{1-x}O synthesis by precipitation method.

3.3.3 Protocol of Amaranth dye adsorption isotherm and kinetic studies.

In a typical adsorption experiment, the pre-activated Ni_{1-x}O catalyst (0.3 g) was dispersed in 1L Amaranth dye solution of varied concentrations from 10 to 110 ppm. The solution was kept on shaker for 24 hours at room temperature. The absorbance of each of the solution was recorded at 520 nm using UV-Visible spectrophotometer. The adsorption capacity at equilibrium (q_e), and the Amaranth removal efficiency of each of the Ni_{1-x}O catalyst was determined using the standard adsorption isotherm models. [1,2] The graph of q_e as a function

of initial concentration of Amaranth dye was fitted using non-linear forms of different adsorption isotherm models such as Langmuir, Freundlich, Sips and Temkin models [3–5].

Similarly, the adsorption kinetic experiments were performed to know the reaction rate and the adsorption mechanism. In a typical experiment 0.3 g of each of the Ni_{1-x}O catalysts were dispersed in 1L of 30 ppm Amaranth dye solution. At regular interval of time, aliquots were taken and the absorbance of the solution was recorded using UV-Visible spectrophotometer at 520 nm. The obtained experimental data was fitted using different adsorption kinetic models such as pseudo first order, pseudo second order, Elovich model and intraparticle diffusion model. The mathematical equations of all the above-mentioned isotherm models and adsorption kinetic models is already presented in Table 2.1 and Table 2.2 respectively in section 2.4.4 of Chapter 2 and hence are not repeated here. The obtained results are discussed in detail in section 3.4

3.4 RESULT AND DISCUSSION

3.4.1 Characterization of synthesized Ni_{1-x}O catalysts

The effect of para-nitrobenzoate (4-nba) ligation with Ni^{2+} on the phase purity, morphology, particle size and the surface area of Ni_{1-x}O has been investigated using different characterization techniques. These results are discussed in detail in this section.

➤ Effect of p-nitrobenzoate ligation with Ni^{2+} on properties of Ni_{1-x}O catalyst.

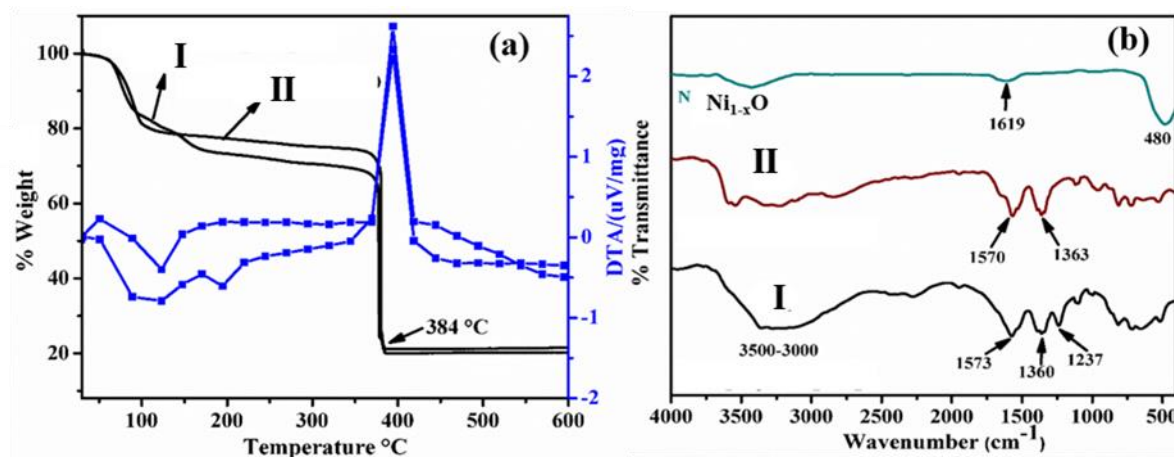


Figure 3.6: (a) TG-DTA and (b) IR analysis of compounds I and II

Figure 3.6 (a) represents the TG-DTA analysis of $[\text{Ni}(\text{H}_2\text{O})_6](4\text{-nba})_2 \cdot 2\text{H}_2\text{O}$ and $[\text{Ni}(\text{H}_2\text{O})_4(4\text{-nba})_2] \cdot 2\text{H}_2\text{O}$. The initial weight loss in both the precursors was due to loss of coordinated and uncoordinated water molecules. The second major weight loss up to 400°C is due to the exothermic decomposition of para-nitrobenzoate ligand. At temperature beyond 400°C , no significant weight loss is observed which indicates formation of stable phase of Ni_{1-x}O . To further confirm this observation IR analysis was carried out. Figure 3.6 (b) shows the IR spectra of compound I and II illustrating a characteristic broad band of O-H stretching vibrations in the region $3600\text{--}2800\text{ cm}^{-1}$. Similarly, the characteristics vibration bands were obtained for carbonyl (~ 1570) and nitro group (~ 1360) in both the compounds which is in good agreement with the literature reports [6]. However, the exact binding modes of the carboxylate ligand to the nickel cannot be confirmed through single infrared spectrum. Upon calcination of samples in air, no characteristic peaks of organic moiety were observed which confirmed the complete removal of organic components. The synthesized Ni_{1-x}O was further characterized for its phase purity using powdered X-ray diffraction study.

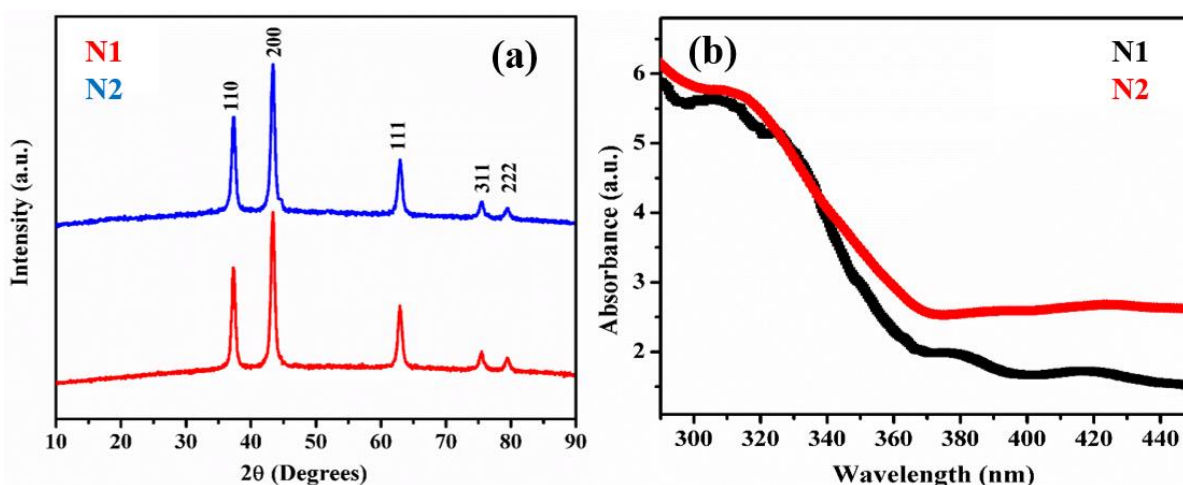


Figure 3.7: (a) XRD and (b) UV-DRS spectra of N1 and N2

Figure 3.7 (a) represents the powder X-ray diffraction pattern of synthesized Ni_{1-x}O . Both the diffractograms showed characteristic peaks at 2θ values of 37.28° , 43.23° , 63.20° , 76.60° , 79.22° corresponding to the plane 111, 200, 220, 311 and 222 which confirmed the cubic phase formation of Ni_{1-x}O and this is in good agreement with the JCPDS data 78-0429 [7,8]. Furthermore, the effect of 4-nba coordination to nickel on band gap of Ni_{1-x}O was analyzed

using UV-DRS analysis. Figure 3.7 (b) shows the UV-DRS plots of N1 and N2. The band gap was calculated to be 3.33 eV for N1 and 3.30 eV for N2 which indicates no significant change in the band gap of synthesized Ni_{1-x}O . Furthermore the effect of 4-nba coordinated to nickel on morphology of Ni_{1-x}O was determined using FESEM analysis.

Figure 3.8 represents the FESEM images of calcined Ni_{1-x}O (N1 and N2). N1 showed mixed aggregates of flake-like and aggregates of spherical particles whereas N2 showed a fully grown nanosponge like morphology. The difference in the morphology could be due to the greater degree of charge stabilization because of direct coordination of 4-nba with Ni^{2+} and hydrogen bonding in case of compound II as compared to compound I wherein 4-nba is outside the coordination sphere. To get more insight into the particle size distribution and surface planes, HRTEM and SAED analysis were carried out. Figure 3.9 represents the HRTEM micrographs along with particle size distribution histogram which was built up by analyzing approx.100 particles using Image J software. The average particle size obtained is 19.6 nm for N1 and 13.8 nm for N2. The d-spacing value of 0.21 nm was obtained using HRTEM micrographs (Figure 3.9 a and b inset), corresponding to (200) plane of Ni_{1-x}O .

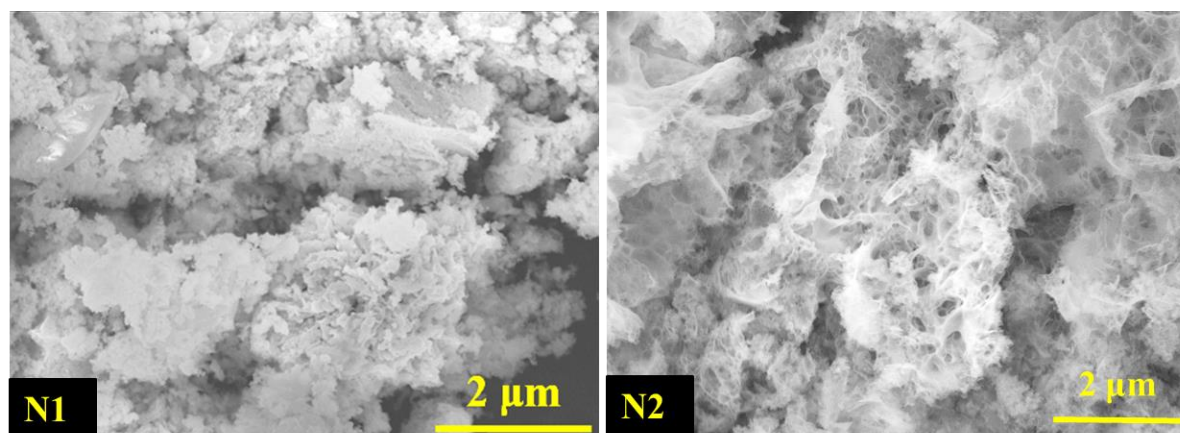


Figure 3.8: Morphological analysis of N1 and N2 using FESEM.

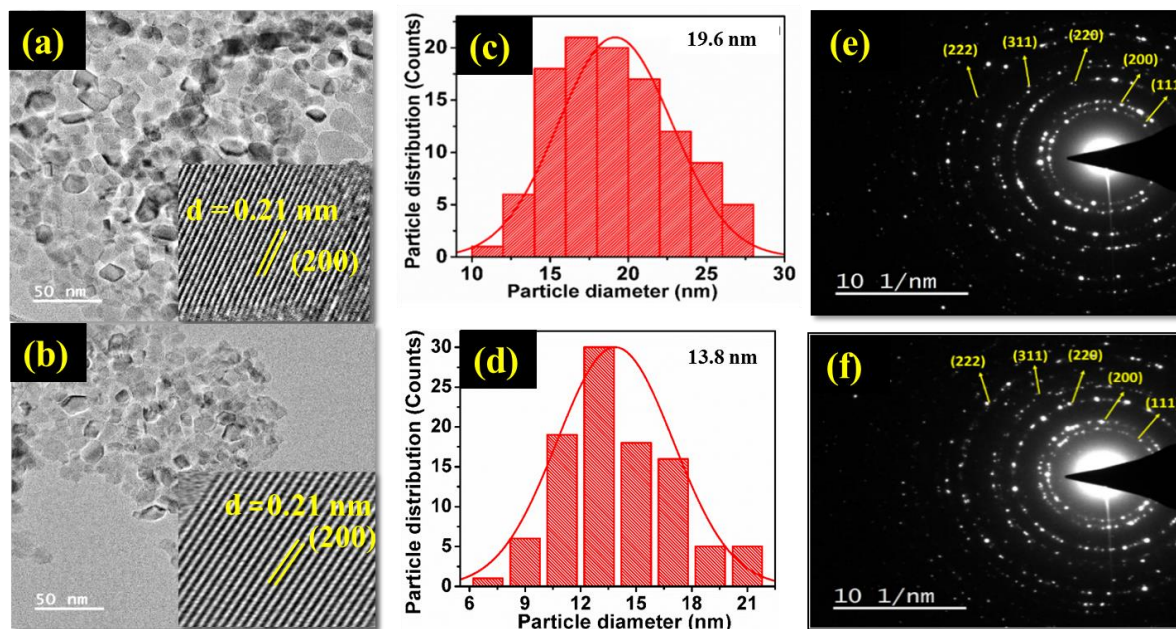


Figure 3.9: (a, b) HRTEM, (c, d) particle size distribution and (e, f) SAED analysis of N1 and N2 respectively.

The surface area of nanosponge-like Ni_{1-x}O is further investigated using BET N_2 adsorption–desorption isotherm experiments and BJH pore analysis method. As evident from Figure 3.10 both N1 and N2 showed type IV isotherms with H1-type hysteresis loop. At low relative pressure i.e. the initial part of isotherm represents monolayer-multilayer adsorption followed by capillary condensation/pore-filling mechanism. Ni_{1-x}O obtained from compound I (with uncoordinated 4-nba) has a relatively lower surface area of $46.2 \text{ m}^2\cdot\text{g}^{-1}$ with largely microporous and mixture of micro-mesoporous (pore size = 5.67 nm , pore volume = $0.082 \text{ cc}\cdot\text{g}^{-1}$) structure, due to the particle aggregates.

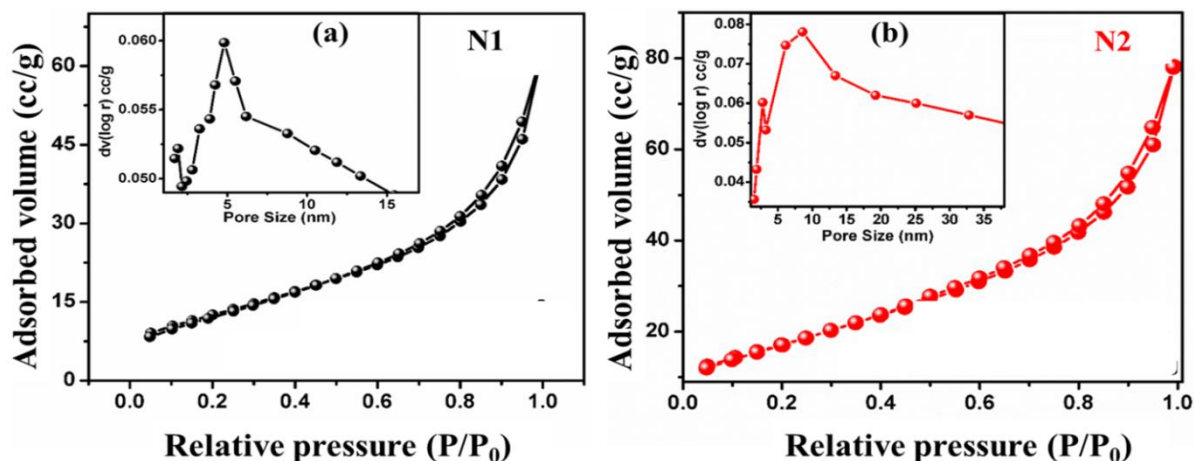
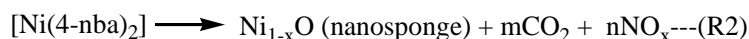


Figure 3.10: N₂ adsorption-desorption and the pore size distribution in N1 and N2.

However, Ni_{1-x}O obtained from compound II, which showed fibrous sponge-like structure in FESEM, exhibited greater degree of mesoporous network with relatively larger average pore diameter of 14.3 nm and greater pore volume of 0.113 cc.g⁻¹, leading to higher surface area of 63.7 m².g⁻¹. Therefore, the BET results are in good agreement with FESEM and TEM results. The probable decomposition process of compound II for the formation of fibrous mesoporous Ni_{1-x}O nanosponge occurs via reactions R1 & R2 as follows:



The formation of a mesoporous, fibrous sponge-like structure in N2 can be attributed to the role of 4-nba ligand which is in direct coordination with Ni²⁺ in compound II. The compound [Ni(H₂O)₄(4-nba)₂].2H₂O is isostructural with [Mn(H₂O)₄(4-nba)₂].2H₂O as reported by Kristiansson et al. [9], in which 4-nba coordinates to Ni²⁺ in a monodentate trans mode. The interplanar distance of aromatic rings in this compound indicates aromatic g-g stacking interactions suggesting a non-bonded crystal organization. The repeating units are assembled into hydrophobic and hydrophilic domains wherein the aromatic stacking into columns constitute the hydrophobic part and act as separators across the alternating planes. These spacers separate each coordinating unit from the other, while the extensive array of hydrogen bonds due to the coordinated water molecules acts as a “glue” to hold together [Ni(4-nba)₂] units [9,10]. Therefore, such a structural arrangement is probably suitable for generating porous structure. Upon calcination in air at temperature 400 °C, exothermic decomposition of

coordinated 4-nba into CO, CO₂ and NO_x gases induces differential porosity into the growing Ni_{1-x}O structure. This exothermic heat produced during 4-nba ligand decomposition process is possibly utilized to fuse Ni_{1-x}O particles into fiber-like structures, which grow in three dimensions forming a highly porous, nanosponge-like network. Thus a fibrous and porous, spongy Ni_{1-x}O is obtained upon calcination of compound II at 400 °C.

➤ **Effect of imidazole ligation with Ni²⁺ on properties of Ni_{1-x}O.**

In the next synthesis scheme the effect of imidazole ligation on properties of Ni_{1-x}O investigated. Figure 3.11 (a) represents the TG-DTA curve for [Ni(H₂O)₂(Im)₂(4-nba)₂] and [Ni(Im)₆](4-nba)₂.2H₂O. The decomposition induced weight loss pattern observed for both the compounds are in accordance with the literature reports [11,12]. All the compounds show typical weight losses due to i) loss of water molecules (coordinated and uncoordinated) followed by thermal decomposition of ligands. The probable global decomposition reactions are represented by R3-R4. A striking difference between these thermal profiles is that the imidazole ligand decomposition follows a gradual weight loss compared to the rapid fall-off observed in case of 4-nba ligand coordinated to Ni²⁺, confirming that Ni²⁺ undergoes stronger chemical bonding with imidazole ligand and that the evolution of gas-phase products like CO_x and NO_x is not as rapid as that of compounds I and II.

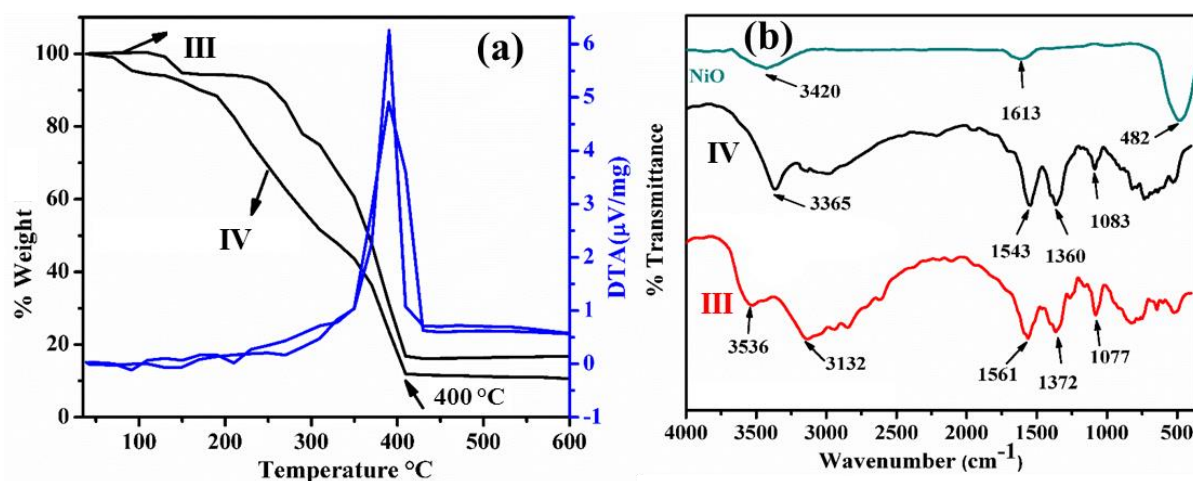
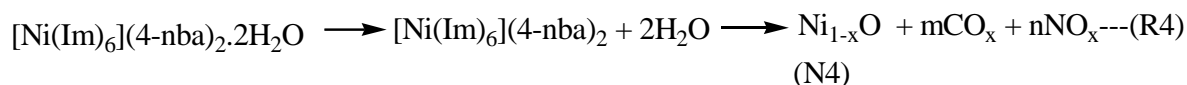
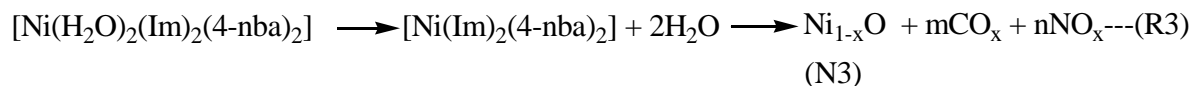


Figure 3.11: (a) TG-DTA analysis and (b) IR spectra of III & IV respectively.

Moreover, the complete decomposition of the ligands coordinated to Ni^{2+} leading to the formation of Ni_{1-x}O in the case of compound **III** and **IV** occurs over a larger temperature range of 200-400°C compared to rapid, lower decomposition temperature span of 364-386°C in case of compound **I** and **II**. The formation of stable Ni_{1-x}O is indicated by the plateau parallel to the x-axis observed in all thermograms.



The IR analysis of the as-synthesized Ni compounds **III** and **IV** (see Figure 3.11 (b)) depicted a characteristic O-H and N-H stretching vibrations at $3300\text{-}3550\text{ cm}^{-1}$ and $3148\text{-}3152\text{ cm}^{-1}$. The obtained values for characteristics vibration bands of carboxylate and nitro groups for compounds **III** and **IV** are in line with the literature reports [6]. Furthermore, no characteristic peaks of organic moiety were observed upon calcination in air, this confirms the complete removal of ligands from the final oxide.

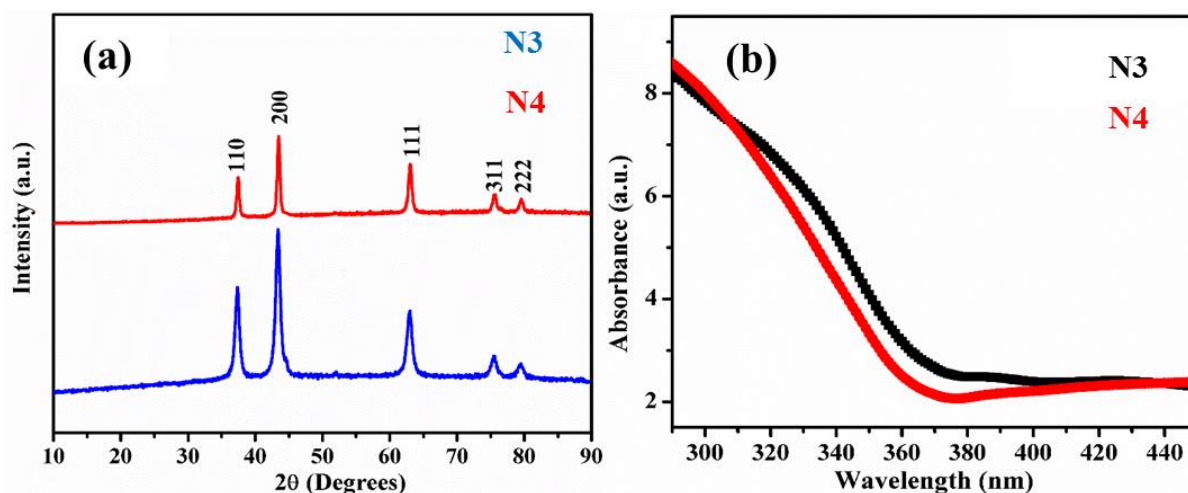


Figure 3.12: (a) XRD and (b) UV-DRS of N3 & N4.

The phase formation of all the Ni_{1-x}O catalysts were analyzed using powder X-ray diffraction studies. All the diffraction patterns of the calcined Ni_{1-x}O showed cubic phase formation with characteristic peaks observed at 2θ values of 37.28° , 43.23° , 63.20° , 76.60° , 79.22°

corresponding to the plane 111, 200, 220, 311 and 222 (see Figure 3.12 (a)) which is in good agreement with the JCPDS file data 78-0429 [13]. Since, six imidazoles coordinate to Ni^{2+} via one N-atom each, the possibility of N-doping in Ni_{1-x}O could result in a lowering of the band gap. Therefore, UV-diffuse reflectance spectroscopic analysis was carried out. The optical band gap energy was calculated using formula $E_g = 1239.8/\lambda$ wherein E_g is the band gap (eV) and λ (nm) is the absorption edge wavelength. The calculated band energy values are as follows: N3 (3.33 eV) and N4 (3.35 eV) which are very much similar within the error limit of ± 0.05 eV, as depicted in Figure 3.12 (b). As evident from the results, the replacement of imidazole by 4-nba ligand does not influence the band gap energy of the synthesized Ni_{1-x}O . Therefore, the possibility of N-doping in Ni_{1-x}O due to N-Ni coordination in compound **III** and **IV** does not seem likely at this stage. Furthermore, the influence of imidazole

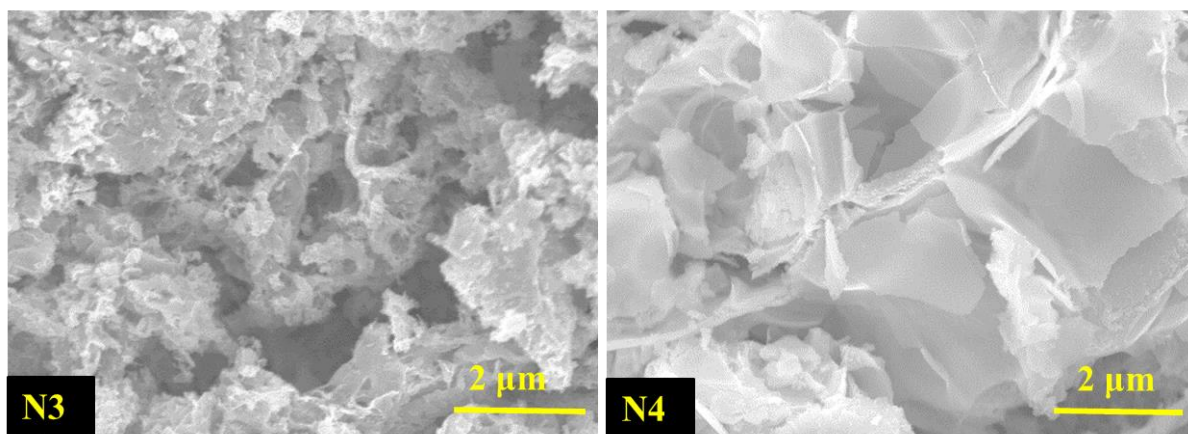


Figure 3.13: FESEM analysis of N3 and N4.

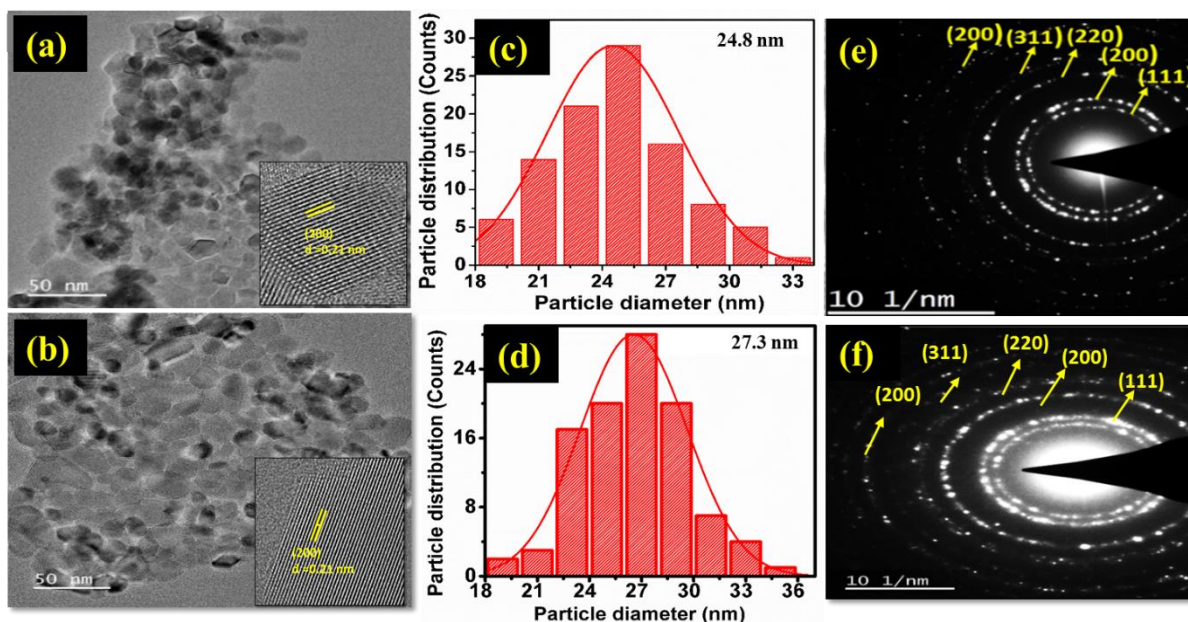


Figure 3.14: (a, b) HRTEM analysis, (c, d) particle size distribution, (e, f) SAED of N3 and N4 respectively.

and its combination with 4-nba coordinated to Ni^{2+} on morphology of Ni_{1-x}O was determined using FESEM analysis. Figure 3.13 represents the FESEM images of calcined Ni_{1-x}O obtained from compound **III** and **IV** respectively. The N3 shows sintered sheet-like aggregates while N4 showed nanoflakes-like morphology. Furthermore, the particle size of the synthesized Ni_{1-x}O catalysts was determined using low-resolution TEM images (Figure 3.14 (a) and (b)). The d-spacing of lattice fringes (0.21 nm) which corresponds to the dominant (200) plane was obtained from the HRTEM images (see inset of Figure 3.14 (a) and (b)) for N3, and N4 respectively. The particle size distribution histogram (Figure 3.14 (c) and (d)) was built by analyzing approximately 100 particles using Image J software. The average particle diameter of 24.8 and 27.3 (± 2) nm was obtained for N3 and N4 respectively.

The corresponding selected area electron diffraction (SAED) pattern indicates the polycrystalline nature of all the synthesized Ni_{1-x}O (Figure 3.14 (e) and (f)). The observed diffraction rings can be indexed to (111), (200), (220), (311) and (222) diffractions of cubic Ni_{1-x}O . Furthermore, surface area and pore size distribution analysis were conducted and these results are discussed in detail in the next section.

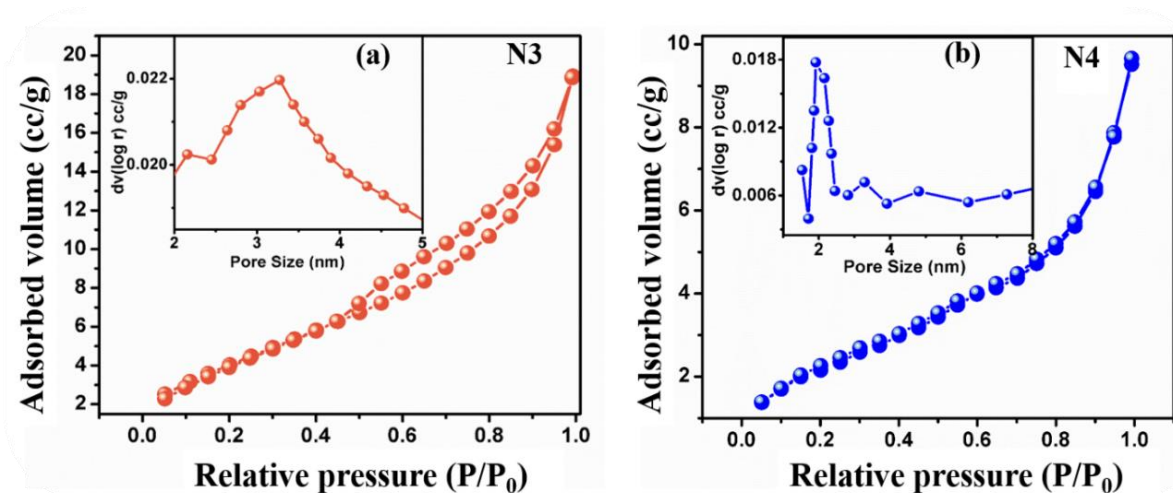


Figure 3.15: BET surface area analysis of (a) N3 and (b) N4.

The porosity analysis of all the calcined Ni_{1-x}O was carried out using N_2 -adsorption-desorption isotherm studies and BJH porosity analysis. As evident from Figure 3.15 (a and b) all the synthesized Ni_{1-x}O catalysts showed type IV isotherms with H1 type hysteresis loop [14]. Initially, there is monolayer-multilayer adsorption at lower pressure followed by capillary condensation/pore-filling mechanism. The lowest surface area was obtained for N4 ($8.53 \text{ m}^2 \cdot \text{g}^{-1}$) and highest was $15.89 \text{ m}^2 \cdot \text{g}^{-1}$ in the case of N3. However, in the entire series the maximum surface area obtained was of $63.7 \text{ m}^2 \cdot \text{g}^{-1}$ recorded in the case of N2. The BJH porosity analysis confirms that N3 (pore size = 1.5 nm, pore volume = $0.026 \text{ cc} \cdot \text{g}^{-1}$) and N4 (pore size = 1.9 nm, pore volume = $0.013 \text{ cc} \cdot \text{g}^{-1}$) exhibit interparticle microporosity while mesoporous nature with a large pore volume of $0.113 \text{ cc} \cdot \text{g}^{-1}$ is observed in the case of N2. Comparing the HRTEM and BET studies of all the Ni_{1-x}O , it can be concluded that, N2 has lowest particle size with maximum surface area. The rapid evolution of gas-phase products such as CO_x and NO_x is the major reason for the induction of porosity in N2 [12,15]. Such a difference in the decomposition behavior could be attributed to different strength of hydrophobic and

hydrophilic domains coordinated to the Ni^{2+} ions, π - π stacking interaction of aromatic rings and modes of secondary interaction in terms of strength of H-bonding. The hydrated 4-nba compound (**III**) exhibits extensive O-H \cdots O interactions due to the presence of electronegative oxygen groups, while imidazole coordinated compound **IV** involves H-bonding interaction such as C-H \cdots O and N-H \cdots O within the coordination sphere. [9,11,16,17]. Furthermore, the N-atoms attached to Ni^{2+} does not support internal oxidation as efficiently as that of O-atoms attached to Ni^{2+} in compound **III**. Thus, higher combustion temperatures are needed to convert compound **IV** into Ni_{1-x}O which results in greater sintering of particles, possibly supporting the growth of nanoflakes-like morphology. The compound **III** follows a mixed pattern of decomposition behavior compared to **I** and **II** and hence has partial porosity as well as a sintered sheet-like agglomerates as seen in FESEM of N3. Furthermore, to prove the effect of ligation on the structural and morphological properties of Ni_{1-x}O , we synthesized pristine Ni_{1-x}O (labeled as PN) from decomposition of $\text{Ni}(\text{OH})_2$ and subsequently by the decomposition of $\text{Ni}(\text{OH})_2$ and urea mixture (labeled as NU), the results of which are presented in the next section.

➤ **Effect of urea as a structure directing agent on properties of Ni_{1-x}O .**

The synthesized $\text{Ni}(\text{OH})_2$ and $\text{Ni}(\text{OH})_2$ -urea precursors were analyzed using TG-DTA analysis. Figure 3.16 (a-b) shows TG-DTA plots for $\text{Ni}(\text{OH})_2$ and $\text{Ni}(\text{OH})_2$ modified with urea. The initial weight loss in both $\text{Ni}(\text{OH})_2$ and $\text{Ni}(\text{OH})_2$ -urea precursor was attributed to the loss of physically adsorbed water. The second major weight loss is due to the loss of organic moiety present in the precipitate in case of $\text{Ni}(\text{OH})_2$ modified with urea. Significantly lower initial decomposition temperature is observed in case of $\text{Ni}(\text{OH})_2$ -urea precursors (279°C) compared to $\text{Ni}(\text{OH})_2$ precursor (378°C). On further heating, there was no significant change in weight beyond 400°C which confirms the formation of stable metal oxide. To further confirm this, IR analysis was carried out which exhibit characteristic peaks of OH

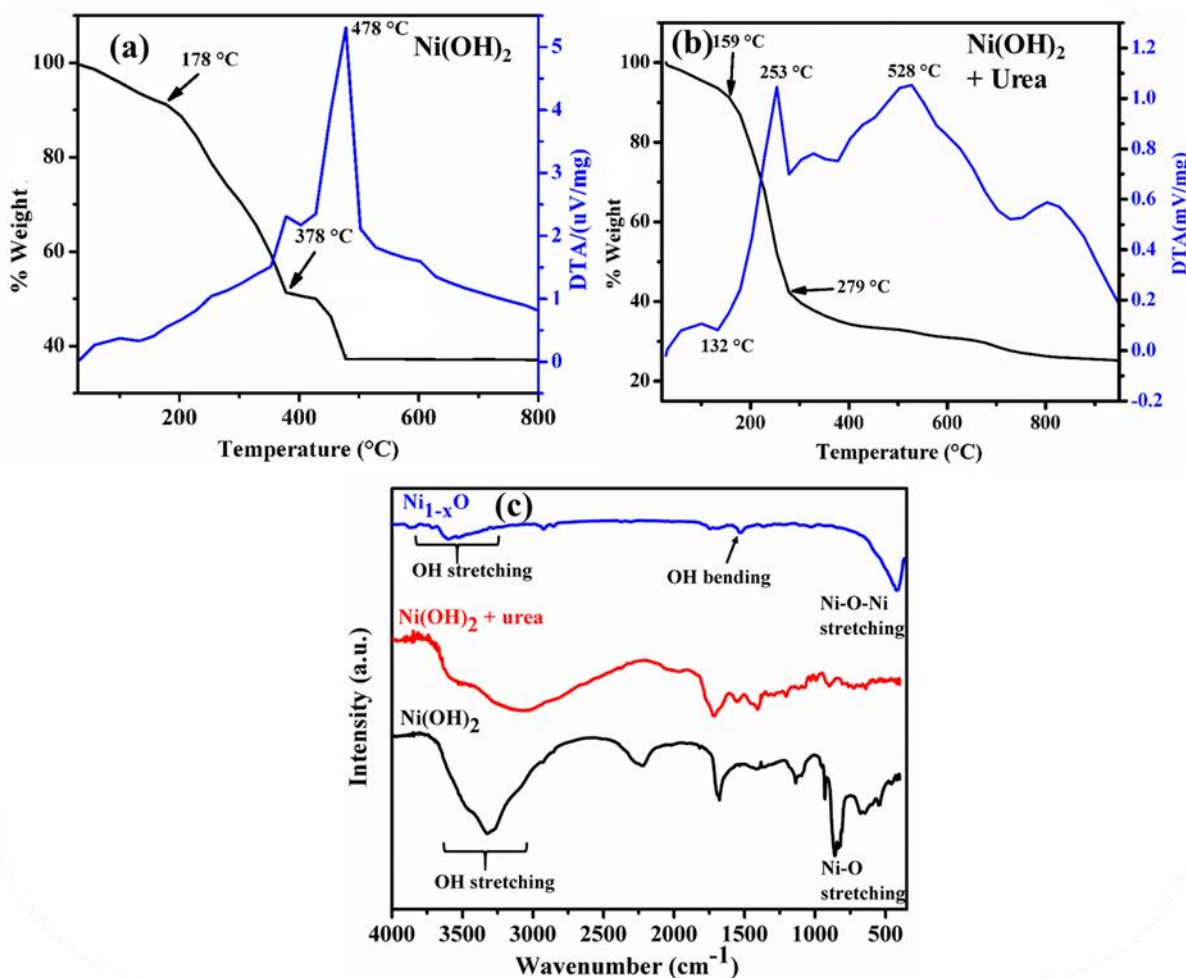


Figure 3.16: (a, b) TG-DTA and (c) IR analysis of Ni(OH)_2 , Ni(OH)_2 with urea and Ni_{1-x}O after calcination at 400°C .

stretching vibration and Ni-O stretching vibrations in the calcined sample as seen in Figure 3.16 (c). Furthermore, the phase purity of all the Ni_{1-x}O was analyzed using powder X-ray diffraction studies. All the diffraction patterns of the calcined Ni_{1-x}O showed cubic phase formation with characteristic peaks observed at 2θ values of 37.28° , 43.23° , 63.20° , 76.60° , 79.22° corresponding to the plane 111, 200, 220, 311 and 222 plane (see Figure 3.17 (a)) which is in good agreement with the JCPDS file data 78-0429 [13]. The UV-diffuse reflectance spectroscopic analysis was carried out. The optical band gap energy obtained is as follows: PN (3.41 eV) and NU (3.38 eV) $\pm 0.05\text{ eV}$, which are very much similar within the error limit, as depicted in Figure 3.17 (b).

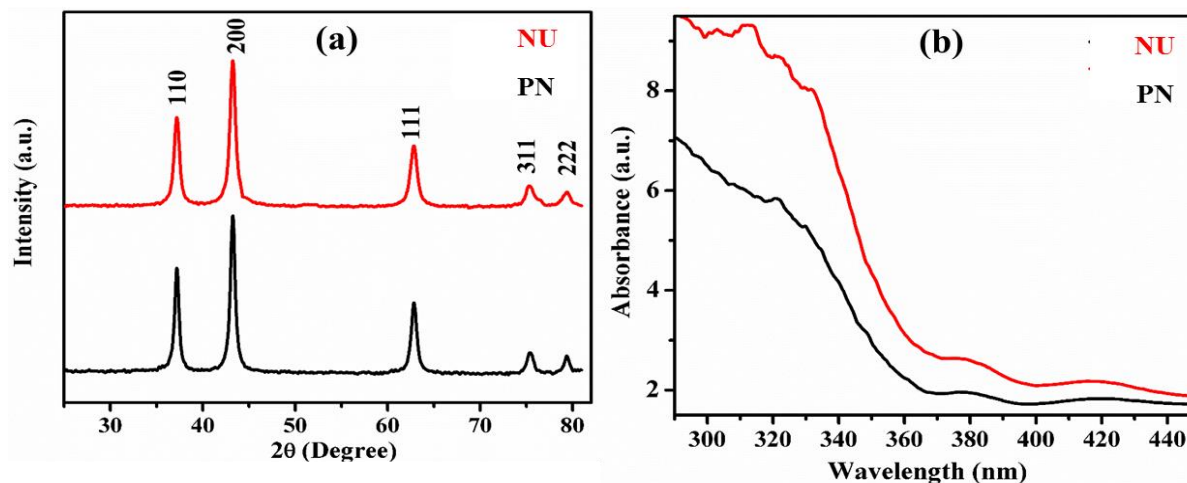


Figure 3.17: (a) XRD and (b) UV-DRS spectra of PN and NU.

The effect of urea on the morphology of the synthesized Ni_{1-x}O was studied using FESEM analysis as presented in Figure 3.18. Figure shows the FESEM images of the PN and NU wherein heavy agglomeration of the particles was observed in both the cases. Furthermore, the particle size and surface planes were determined using HRTEM and SAED analysis. Figure 3.19 (a) and (b) shows the low resolution TEM images of PN and NU. The particle size of PN and NU was analysed by measuring approximately 100 particles and plotting particle size distribution histogram. The particle size calculated is 37 nm and 34 nm \pm 5 nm for N3 and N4 respectively. The d-spacing of 0.21 nm which corresponds to 200 plane of Ni_{1-x}O was determined from the HRTEM micrographs (as shown in the inset of Figure 3.19 (a) and (b)). The corresponding selected area electron diffraction (SAED) pattern indicates the polycrystalline nature of the synthesized Ni_{1-x}O and observed diffraction rings are indexed to (111), (200), (220), (311) and (222) diffractions of cubic Ni_{1-x}O which are in good agreement with the XRD analysis.

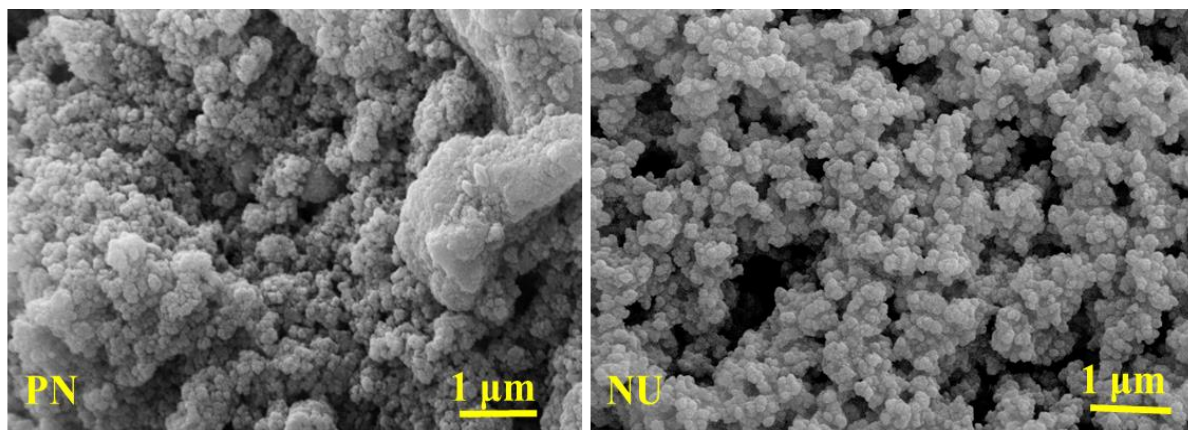


Figure 3.18: Morphological analysis of PN and NU.

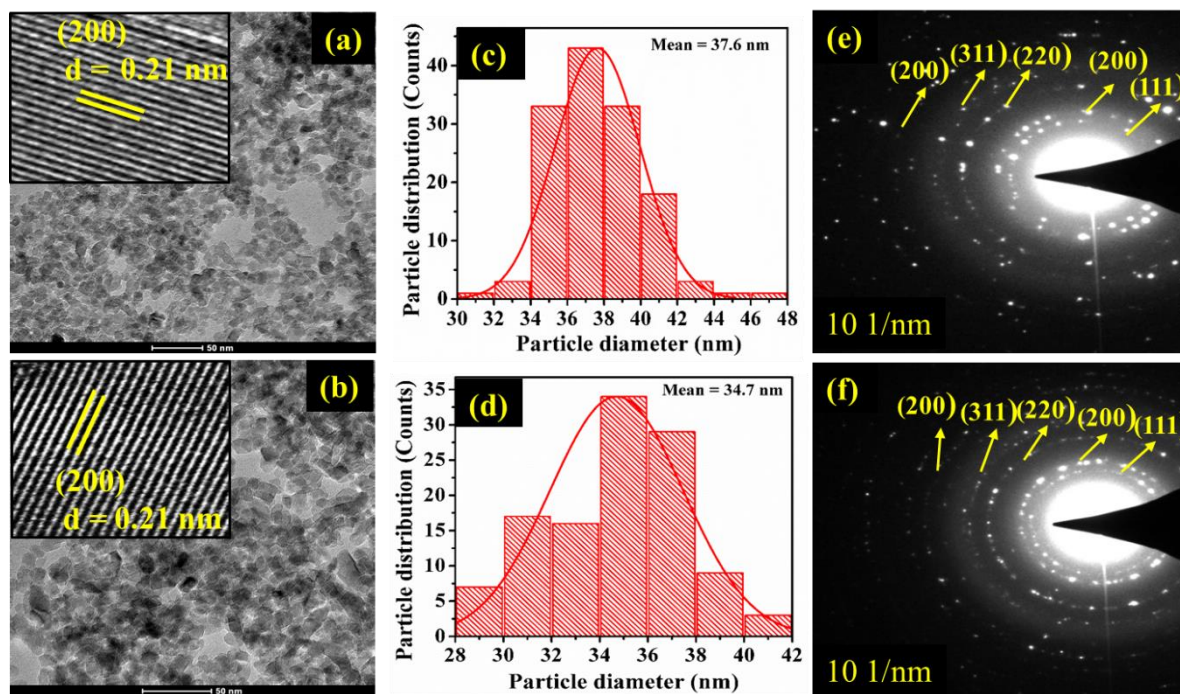


Figure 3.19: (a-b) Low resolution TEM, (c-d) Particle size distribution, (e-f) SAED analysis of PN and NU respectively

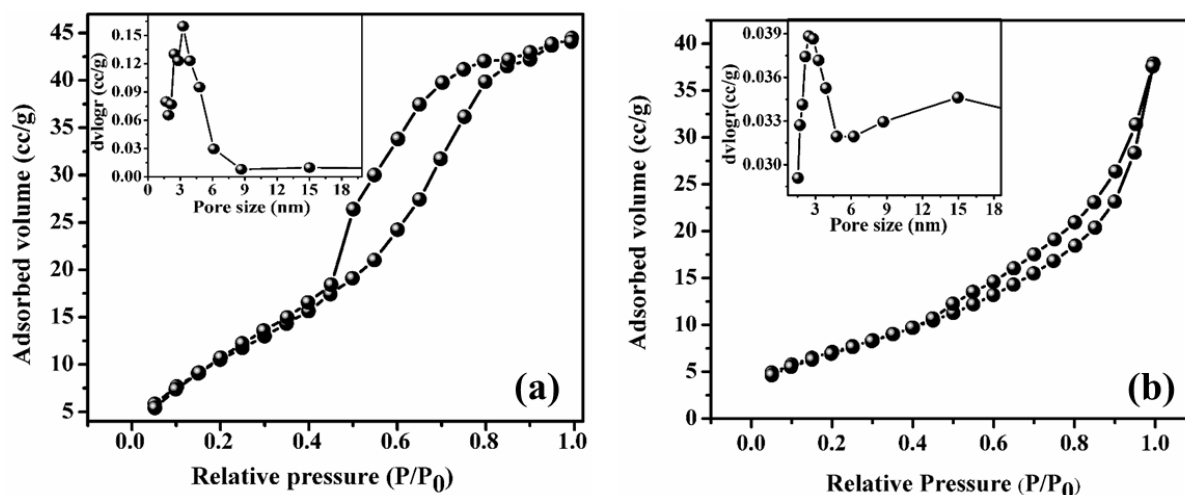


Figure 3.20: N₂ adsorption-desorption analysis of a) PN and b) NU respectively.

Further, the porosity analysis of PN and NU was carried out using N₂ adsorption-desorption analysis (Figure 3.20). The measured surface area of PN is 22.4 m².g⁻¹ and that of NU is 25.7 m².g⁻¹ which are very similar, indicating not much effect of urea on particle morphology.

➤ Effect of structure directing agents on non-stoichiometry of Ni_{1-x}O

Ni_{1-x}O is known to adopt the rock salt structure with octahedral Ni²⁺ and O²⁻ sites and is known to be highly non-stoichiometric in nature. The non-stoichiometric Ni_{1-x}O is known to exhibit different properties such as conductivity, magnetism, chromism and catalytic activity which is very useful in electrochemical application. Therefore, the effect of 4-nba ligation on the non-stoichiometric nature of Ni_{1-x}O was investigated by determining the Ni³⁺ concentration by XPS analysis. Figure 3.21 (a), (d), (g) and Figure 3.22 (j), (m) and (p) shows the full scan spectra, of all the synthesized Ni_{1-x}O. Figure 3.21 (b), (e) (h) and Figure 3.22 (k), (h) (q) shows the high-resolution (narrow scan) XPS spectra of Ni (2p) core level for N1, N2, N3, N4, PN and NU respectively.

All XPS spectra illustrate distinct five peaks located at various binding energies and agrees well with literature reports [18,19]. A shoulder peak that represents the Ni (2p) core levels for Ni_{1-x}O has been observed in all the samples. In order to precisely determine the shoulder peak features of Ni (2p_{3/2}) and Ni (2p_{1/2}), the XPS spectra were deconvoluted using Voigt peak fitting function. The peak fitting for the 8 peaks has been marked from *a* to *h* located at the

binding energies of $853.2 (\pm 0.2)$, $855.1 (\pm 0.2)$, $860.5 (\pm 0.2)$, $865.2 (\pm 0.2)$, $870.7 (\pm 0.2)$, $872.2 (\pm 0.2)$, $877.1 (\pm 0.2)$ and $879.9 (\pm 0.2)$ eV, respectively. The peaks marked as *a*, *b*, *e* and *f* represents the core level Ni^{2+} ($2p_{3/2}$), Ni^{3+} ($2p_{3/2}$), Ni^{2+} ($2p_{1/2}$) and Ni^{3+} ($2p_{1/2}$), respectively. The shakeup satellite peaks of Ni^{2+} ($2p_{3/2}$) and Ni^{3+} ($2p_{3/2}$) are labeled as *c* and *d*, and the shakeup satellite peaks of Ni^{2+} ($2p_{1/2}$) and Ni^{3+} ($2p_{1/2}$) are labeled as *g* and *h*, respectively.

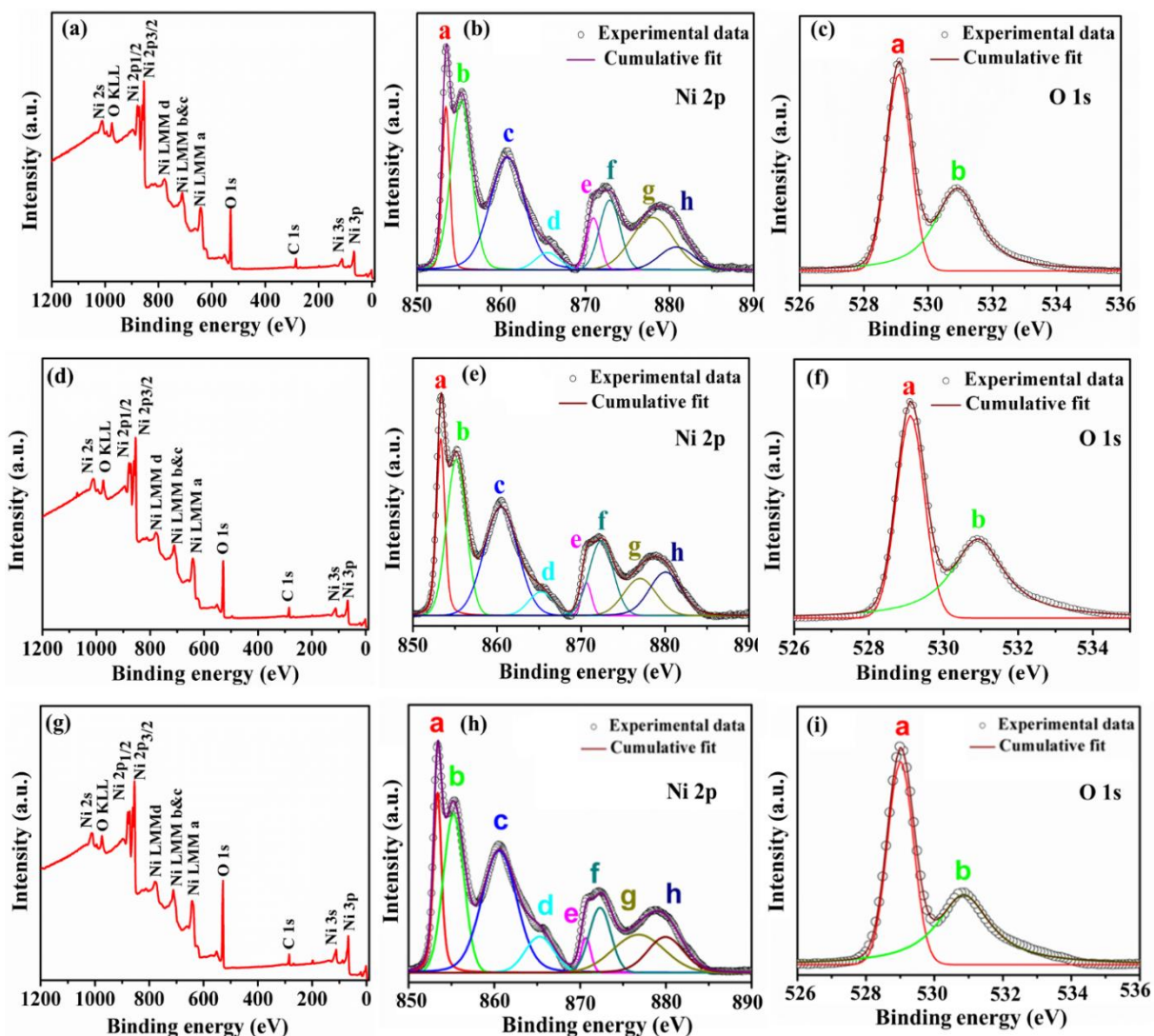


Figure 3.21: XPS spectra of N4 (a-c), PN (d-f) and NU (g-i)

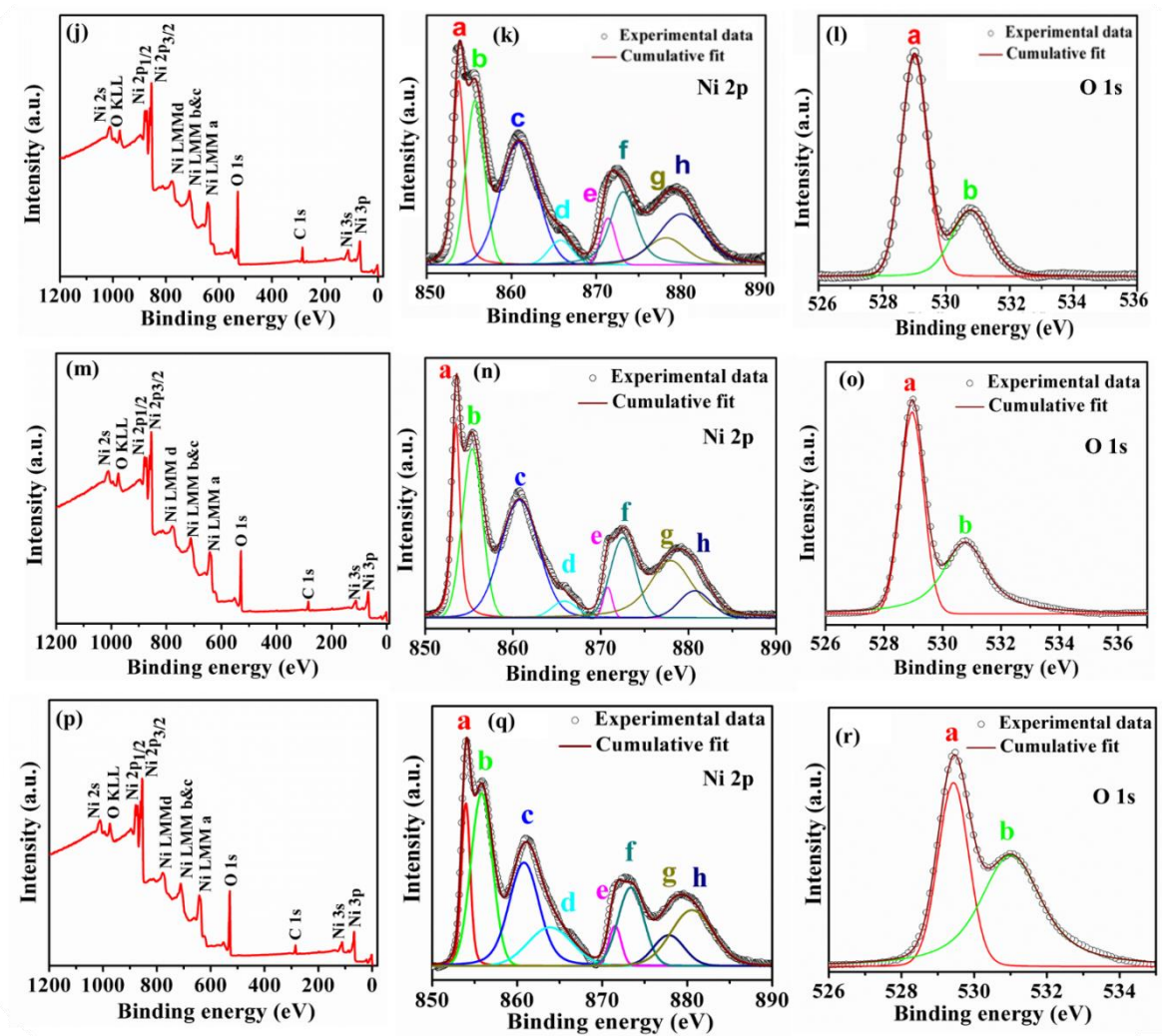


Figure 3.22: XPS spectra of N4 (j-l), PN (m-o) and NU (p-r)

The presence of these peaks confirmed the formation of non-stoichiometric Ni_{1-x}O [20]. Peak area integration revealed that the percentage of Ni^{3+} was lowest in the case of PN (36.5%) < NU (38.4%) < N1 (40.9 %) < N4 (41.1%) < N3 (41.6 %) < N2 (42.1 %) and is listed in Table 3.1. Similarly, the O (1s) XPS spectra of different Ni_{1-x}O samples were deconvoluted (see Figure 3.21 (c) (f) (i) and Figure 3.22 (l) (o) (r)). The O (1s) spectra showed an ideal fit for two peaks located at binding energies of $528.9 (\pm 0.2)$ and $530.7 (\pm 0.2)$ eV. The higher intensity at lower binding energy peak observed at 528.9 eV represents the O (1s) core level of O^{2-} anions associated with Ni–O chemical bonding, and the lower intensity at higher binding energy peak (530.7 eV) is representative of the presence of hydroxyl (–OH) groups and defect

sites on the Ni_{1-x}O surface and is thus a measure of oxygen vacancies in Ni_{1-x}O . The presence of oxygen vacancies in Ni_{1-x}O is known to improve the donor density and surface properties of Ni_{1-x}O . From the summarized peak area integration values in Table 3.1, confirms that without SDA obtained Ni_{1-x}O has the lowest non-stoichiometry ($\text{Ni}^{3+} = 36.5\%$) while the coordination of 4-nba to Ni^{2+} induces highest non-stoichiometry ($\text{Ni}^{3+} = 42.1\%$) at the same calcination temperature. Moreover, N2 is found to contain greater percentage of oxygen vacancies than PN. Thus, the presence of ligands significantly alter the non-stoichiometry in Ni_{1-x}O . Further, the influence of these morphological changes in synthesized Ni_{1-x} on its catalytic properties was tested by performing adsorptive removal and photocatalytic degradation of Amaranth dye which is presented in the next section.

Materials	Narrow Scan	Species	$\text{Ni}^{3+}/\text{Ni}^{2+}$ (Ni_{1-x}O Synthesized)	XPS area integration (%)
N1	Ni_{2p} O_{1s}	Ni^{2+}	0.69	59.1
		Ni^{3+}		40.9
		Ni-O		48.9
		Surface hydroxyl		51.1
N2	Ni_{2p} O_{1s}	Ni^{2+}	0.72	57.9
		Ni^{3+}		42.1
		Ni-O		48.1
		Surface hydroxyl		51.9
N3	Ni_{2p} O_{1s}	Ni^{2+}	0.71	58.3
		Ni^{3+}		41.6
		Ni-O		55.4
		Surface hydroxyl		44.5
N4	Ni_{2p} O_{1s}	Ni^{2+}	0.69	58.8
		Ni^{3+}		41.1
		Ni-O		52.4
		Surface hydroxyl		47.5
PN	Ni_{2p} O_{1s}	Ni^{2+}	0.57	63.5
		Ni^{3+}		36.5
		Ni-O		52.9
		Surface hydroxyl		47.1
NU	Ni_{2p} O_{1s}	Ni^{2+}	0.62	61.6
		Ni^{3+}		38.4
		Ni-O		53.7
		Surface hydroxyl		46.3

Table: 3.1: The percentage of species obtained from the XPS peak area integration of narrow scan spectra of Ni_{1-x}O catalysts.

3.4.2 Adsorptive removal of Amaranth dye from water using Ni_{1-x}O catalysts.

The catalytic efficiency of all the synthesized Ni_{1-x}O catalysts (N1, N2, N3, N4, PN and NU) were tested for adsorptive removal of Amaranth dye from waste water. The nature of interaction between the Amaranth dye (adsorbate) and Ni_{1-x}O catalyst (adsorbent) was investigated using adsorption isotherm and adsorption kinetic studies.

➤ Adsorption isotherm studies

The detailed adsorption isotherm procedures is already given in section 3.3.4. The adsorption capacity at equilibrium (q_e), and the Amaranth removal efficiency of each of the synthesized Ni_{1-x}O catalyst was determined. The experimentally obtained adsorption equilibrium (q_e), was fitted using non-linear forms of different adsorption isotherm models such as Langmuir, Freundlich, Sips and Temkin models [3]. All the equations of the respective isotherm models are given in section 2.4.4 of Chapter 2. The adsorption isotherm experiments were carried out using aqueous Amaranth dye solution at 298 K and pH = 5.6. Figure 3.23 represents the adsorption isotherm study for N1, N2, N3, N4, PN and NU. It is a plot of maximum adsorption capacity q_e as a function of adsorbate concentration c_e . We observe that at lower initial concentration of Amaranth dye there is near linear increase in the maximum adsorption capacity which subsequently enters into an equilibrium at higher initial concentration of Amaranth dye. Among all the adsorption isotherms fitted, Sips adsorption isotherm model gave a best fitted with an R² value > 0.96. The obtained adsorption capacity for the synthesized Ni_{1-x}O catalyst was in the order 61.7 mg.g⁻¹, 75 mg.g⁻¹, 53.3 mg.g⁻¹, 34.8 mg.g⁻¹, 39.9 mg.g⁻¹ and 41.6 mg.g⁻¹ for N1, N2, N3, N4, PN and NU respectively (see Table 3.2). It is very clear from the obtained adsorption capacities values that the N2 has maximum adsorption capacity of 75 mg.g⁻¹ which is almost double the value of PN. The high adsorption capacity of Ni_{1-x}O nanosponge could be attributed to its high surface area (63.67 m².g⁻¹), more number of surface active sites, and interconnected mesoporous nature (pore size=14.29 nm, pore volume=0.113 cc.g⁻¹) which allows easy diffusion of the Amaranth dye molecule throughout the nanosponge-like structure, confirming that the mesoporous, spongy nature and high surface area of N2 facilitates efficient dye diffusion and adsorption process. On the contrary, the low surface area and microporous nature in case of N3, N4, PN and NU, restricted the dye diffusion and adsorption process and hence resulted in lower adsorption capacities. Furthermore, the

adsorption kinetic study for the adsorption of Amaranth dye on the synthesized Ni_{1-x}O nanostructures was carried out to understand the rate of uptake of the Amaranth dye on Ni_{1-x}O catalyst.

Isotherm models	Parameters	Materials					
		N1	N2	N3	N4	PN	NU
Langmuir	q _m (mg.g ⁻¹)	70.2	87.4	59.17	36.2	50.9	52.3
	K _L (L.mg ⁻¹)	0.101	0.070	0.104	0.407	0.031	0.051
	R _L	0.08- 0.26	0.12- 0.35	0.06- 0.22	0.02- 0.07	0.04- 0.07	0.06- 0.12
	R ²	0.83	0.83	0.88	0.71	0.93	0.82
Freundlich	K _F (L.mg ⁻¹)	25.1	25.63	22.16	26.7	5.5	10.0
	1/n (mg.g ⁻¹)	0.207	0.244	0.197	0.061	0.426	0.325
	R ²	0.64	0.64	0.68	0.41	0.83	0.64
Sips	q _m (mg.g ⁻¹)	61.7	75.0	53.3	34.8	39.9	41.6
	K _S (L.mg ⁻¹)	0.091	0.077	0.096	0.130	0.046	0.063
	m	2.62	2.49	1.93	4.81	1.73	2.75
	R ²	0.95	0.97	0.96	0.98	0.97	0.98
Temkin	β (mg.g ⁻¹)	206.1	145.2	254.7	1152.6	199.1	200.7
	K _T (L.mg ⁻¹)	2.299	1.04	2.88	156584.6	0.2363	0.396
	R ²	0.71	0.72	0.75	0.43	0.93	0.76

Table 3.2: Parameters obtained from different adsorption isotherm models of Amaranth adsorption over Ni_{1-x}O catalysts.

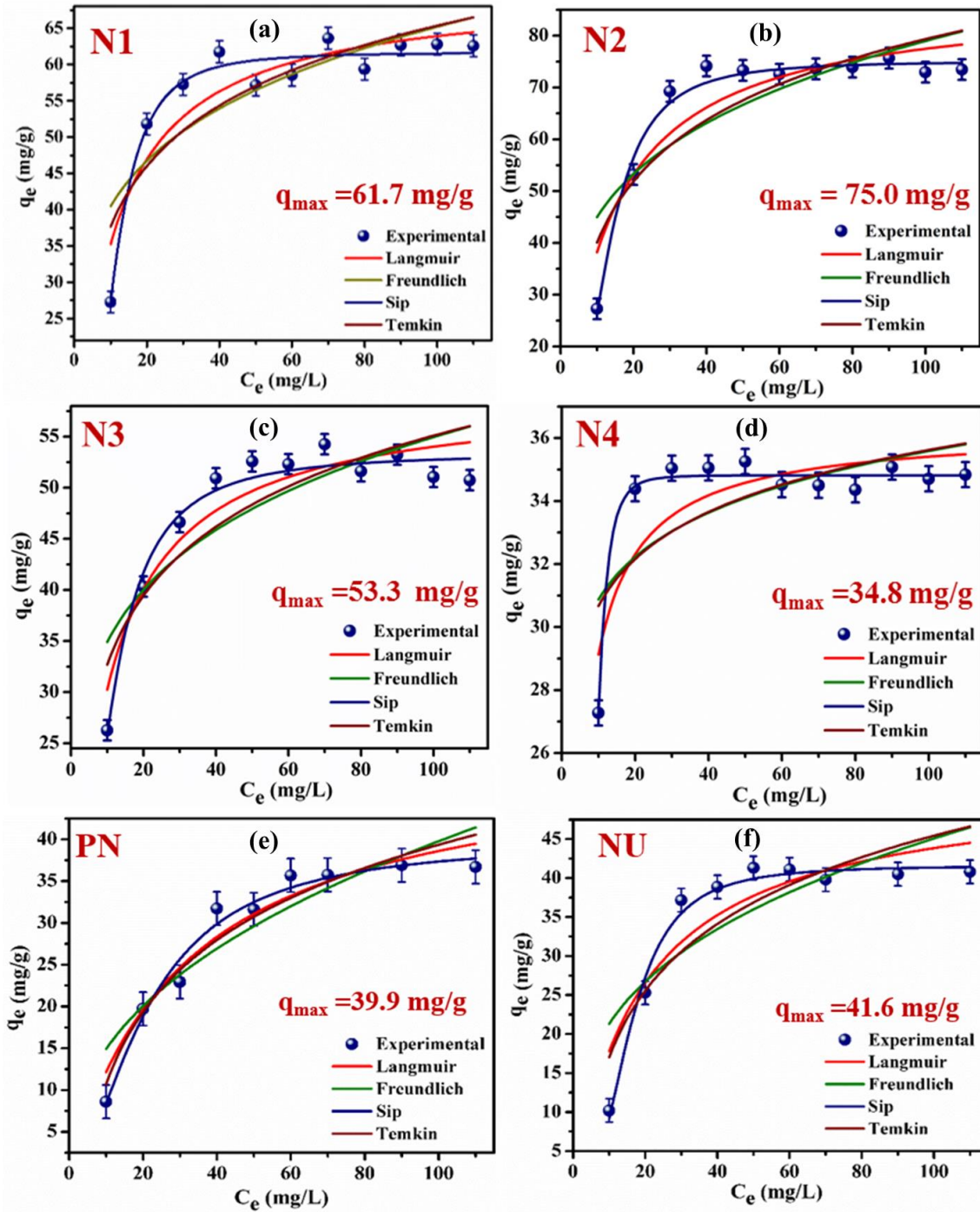


Figure 3.23: Amaranth dye adsorption isotherms profiles over Ni_{1-x}O (N1, N2, N3, N4, PN and NU) catalysts.

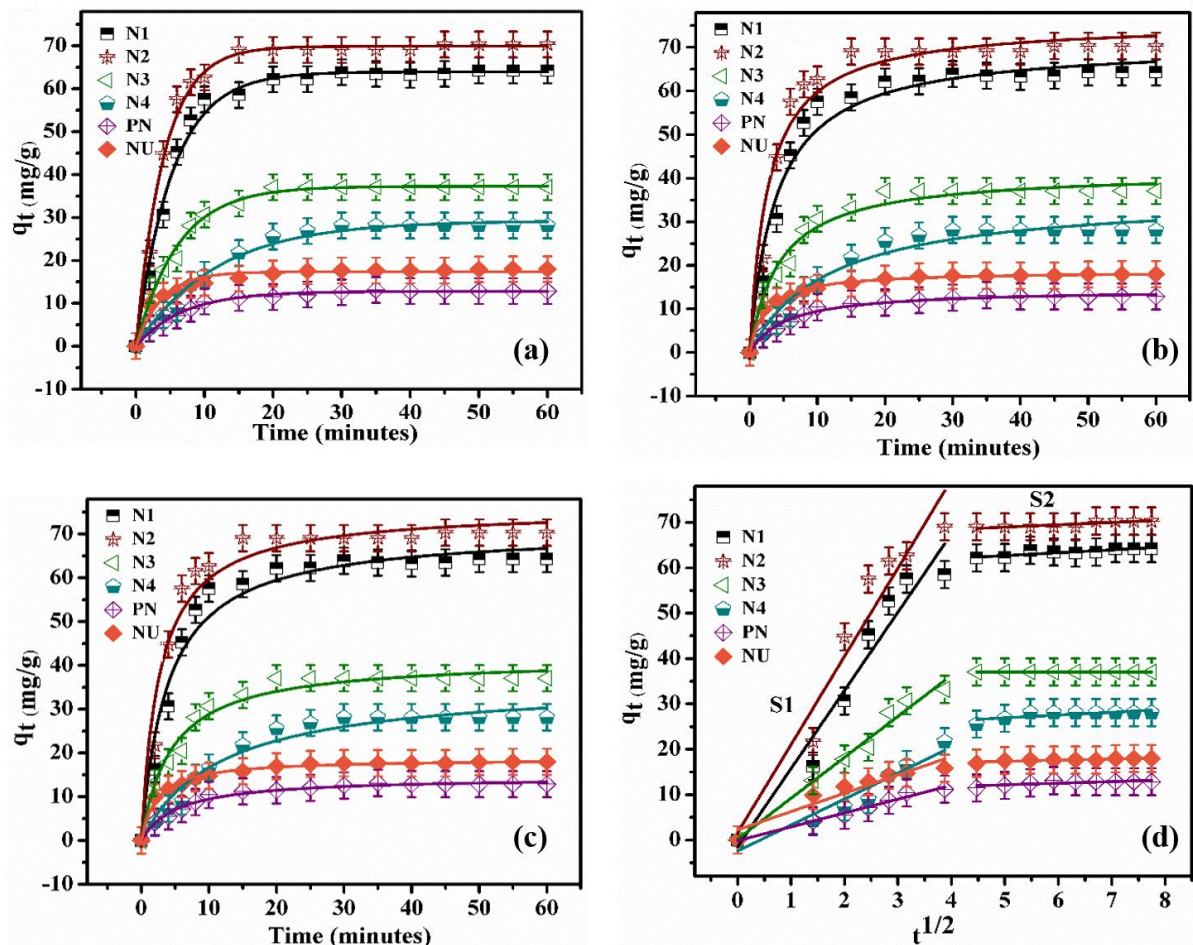


Figure 3.24: Amaranth adsorption kinetics on $Ni_{1-x}O$; a) Pseudo first order, b) Pseudo second order, c) Elovich model and d) Intra particle diffusion model

➤ Adsorption kinetic studies

The detailed experimental procedure for adsorption kinetic study has been explained in section 3.3.4. The obtained experimental data has been fitted using different adsorption kinetic models pseudo-first-order (Figure 3.24 (a)), pseudo-second-order (Figure 3.24 (b)), Elovich model (Figure 3.24 (c)) and intraparticle diffusion model (Figure 3.24 (d)).

Models Parameters	Materials						
	N1	N2	N3	N4	PN	NU	
Pseudo- first-order	k_1 (min^{-1})	0.175	0.187	0.168	0.105	0.137	0.156
	$q_{e,\text{cal}}$ ($\text{mg}\cdot\text{g}^{-1}$)	63.9	66.8	35.3	26.5	29.7	31.6
	$q_{e,\text{exp}}$ ($\text{mg}\cdot\text{g}^{-1}$)	67.5	69.2	36.5	27.6	31.5	34.2
	R^2	0.98	0.98	0.98	0.98	0.97	0.98
Pseudo- second- order	K_2 ($\text{g}\cdot\text{mg}^{-1}\cdot\text{min}^{-1}$)	3.62	3.52	6.39	3.69	2.96	2.42
		$\times 10^{-3}$					
	$q_{e,\text{cal}}$ ($\text{mg}\cdot\text{g}^{-1}$)	71.0	74.0	39.2	31.6	35.4	38.6
	R^2	0.96	0.96	0.98	0.96	0.98	0.99
Elovich	B ($\text{g}\cdot\text{mg}^{-1}$)	59.1	67.5	34.8	7.7	7.3	84.8
	k_E ($\text{mg}\cdot\text{g}^{-1}\cdot\text{min}$)	0.080	0.078	0.149	0.141	0.363	0.406
	R^2	0.90	0.91	0.95	0.93	0.95	0.98
Intrapartic le diffusion	k_{ID} (S1) ($\text{mg}\cdot\text{g}^{-1}\cdot\text{min}^{-1/2}$)	17.23	18.74	8.68	5.76	2.52	3.19
	C (S1) ($\text{mg}\cdot\text{g}^{-1}$)	59.54	1.75	0.66	1.81	0.75	3.69
	R^2 (S1)	0.93	0.98	0.98	0.93	0.94	0.85
	k_{ID} (S2) ($\text{mg}\cdot\text{g}^{-1}\cdot\text{min}^{-1/2}$)	0.62	0.45	0.33	0.07	0.14	0.21
	C (S2) ($\text{mg}\cdot\text{g}^{-1}$)	1.69	63.3	33.12	25.42	13.89	16.35
	R^2 (S2)	0.71	0.46	0.14	0.17	0.57	0.72

Table 3.3: Parameters obtained from adsorption kinetic analysis.

It was observed that for all the synthesized Ni_{1-x}O catalyst, the rate of adsorption was much higher at the beginning of the process which became comparatively slower proceeding towards the equilibrium adsorption [21]. Based on the values of the correlation coefficient i.e. R^2 , it was decided that the adsorption of Amaranth dye on all the catalysts followed pseudo-first-order kinetics which suggested that the dye molecule is attached to the adsorption sites through physical adsorption. However, the R^2 values for the pseudo-second-order rate kinetics were also found to be reasonably high which indicates that the dye molecule attaches the Ni_{1-x}O nanostructures via chemical interaction i.e. chemisorption as well which involves electrons sharing or exchange through different valence forces between the dye molecule and the catalyst surface [22,23]. Therefore, it is concluded that the Amaranth dye adsorption on all the Ni_{1-x}O

nanostructures includes the combination of both the processes i.e. physical adsorption as well as chemisorption [21]. The rate constant determined using pseudo-first order as well as pseudo-second-order rate equations followed the order $N2 > N1 > N3 > NU > PN > N4$ (see Table 3.3) which signifies the importance of mesoporous nature and nanosponge-like morphology of $Ni_{1-x}O$ for improved adsorptive separation of dye. To understand the diffusion mechanism of the dye molecule over nanostructured $Ni_{1-x}O$, the intraparticle diffusion model was tested. The experimental adsorption kinetics data was further fitted using the linear form of the intraparticle diffusion model (Figure 3.24 (d)) and the corresponding parameters calculated using this model are summarized in Table 3.3. It was observed that the plot showed multilinearity indicating the adsorption process taking place in two or more steps. It was observed that the fits of intraparticle diffusion model did not pass through the origin and had slopes which ruled-out the possibilities of the applicability of intraparticle diffusion model alone and predicted that the dye diffusion mechanism was not completely controlled by a single mechanism but it was a combination of two or more mechanisms [1]. The plots of intra-particle diffusion model showed two regions S1 and S2 and the value of the slope of region S1 is quite higher than the slope of region S2, which suggested that the contribution of the step involving the transfer of dye molecules from the bulk solution to the internal pores is quite significant. Further, the value of the slope of region S1 also followed the order $N2 > N1 > N3 > N4 > NU > PN$ (Table 3.3) which suggested that the dye uptake increased with the increasing ordered porosity. The maximum adsorption capacity was obtained for $Ni_{1-x}O$ nanosponge (N2) which is attributed to its high surface area and mesoporous nature. Further, the photocatalytic performance of all the synthesized $Ni_{1-x}O$ catalyst was investigated for degradation of Amaranth dye.

3.4.3: Photocatalytic degradation of Amaranth dye using $Ni_{1-x}O$ catalysts.

Similar to the procedure adopted in case of TiO_2 , the optimum concentration of $Ni_{1-x}O$ catalyst required for photocatalytic degradation of Amaranth dye was evaluated by varying the amount of catalyst in the photocatalytic reaction while maintaining the dye concentration constant. The amount of $Ni_{1-x}O$ catalyst (N2) taken was 25, 50, 75, 100, 125 and 150 mg. Maximum photocatalytic degradation of 93.8 % was obtained using 100 mg $Ni_{1-x}O$ catalyst

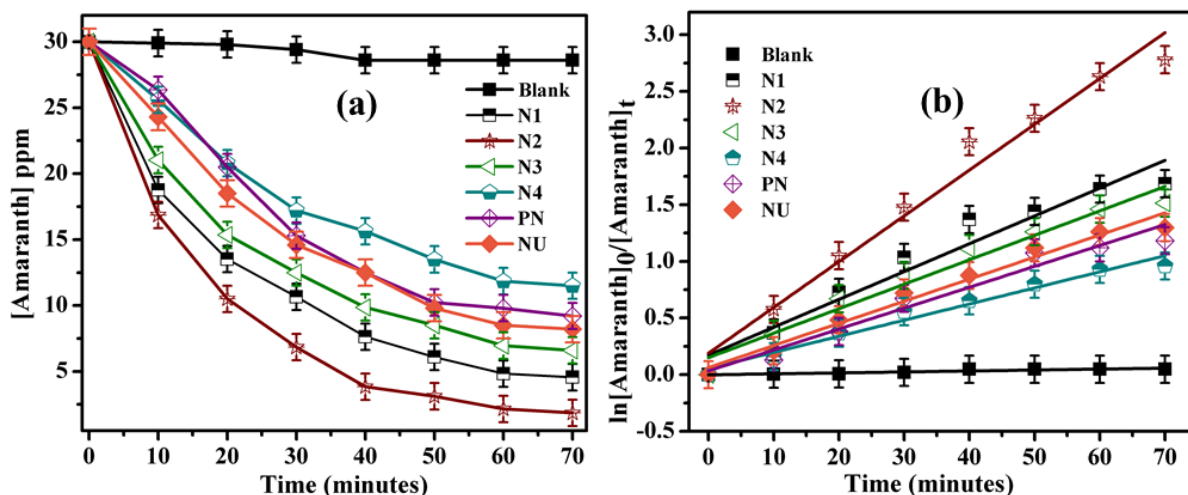


Figure 3.25: (a) Kinetic profiles, (b) Linear fit $\ln[\text{Amaranth}]_0/[\text{Amaranth}]_t$ as a function of time for Amaranth dye degradation using Ni_{1-x}O catalysts.

in 70 minutes. This optimized amount was used to carry out the photocatalytic degradation of Amaranth dye using rest of the synthesized Ni_{1-x}O catalyst. The photocatalytic degradation of Amaranth dye on synthesized nanostructured Ni_{1-x}O was carried out by irradiating an aqueous reaction mixture of dye and catalyst using 250 Watt medium pressure Hg immersion lamp and compared its activity with a control experiment wherein only dye was irradiated. Figure 3.25 represents the results of the experiment wherein it is observed that only 5 % of initial Amaranth dye concentration decreases without any catalyst. On the contrary, a significant decrease in the concentration of dye was observed in the presence of a synthesized nanostructured Ni_{1-x}O catalyst. Among all the Ni_{1-x}O catalyst, N2 exhibited maximum degradation efficiency of 93.8 % within 70 mins which is significantly higher as compared to N1 (84.8 %), N3 (78 %), N4 (61.6 %), PN (69.3%) and NU (72.6 %). The photocatalytic degradation of Amaranth dye followed the pseudo-first-order kinetic model which is defined by the equation $\ln[\text{Amaranth}]_0/[\text{Amaranth}]_t = k_{\text{app}} t$. The plot of $\ln[\text{Amaranth}]_0/[\text{Amaranth}]_t$ (see Figure 3.25 (b)) gave a straight line fit ($R^2 = 0.97$) and from the slope of which the apparent rate constant (k_{app}) of $4.04 \times 10^{-2} \text{ min}^{-1}$ was obtained. As evident from Table 3.4, the k_{app} for N2 is almost double as compared to N1, signifying that the enhanced adsorption efficiency over N2 is further assisted by photocatalytically generated charge carriers/ reactive surface species which degrade the adsorbed dye at a much faster rate and improved the photocatalytic efficiency.

Catalyst	Surface Area $\text{m}^2\cdot\text{g}^{-1}$	Band Gap (eV)	% Degradation (70 min)	$k_{\text{degd}} \times 10^{-2}$ (min^{-1})	Adsorption capacity, q_{max} ($\text{mg}\cdot\text{g}^{-1}$)
Blank	--	--	5.0	0.05	---
N1	46.1	3.33	84.8	2.45	61.7
N2	63.6	3.30	93.8	4.04	75.0
N3	15.8	3.33	78.0	2.15	53.3
N4	8.53	3.35	61.6	1.42	34.8
PN	22.4	3.41	69.3	1.84	39.9
NU	25.7	3.38	72.6	1.95	41.6

Table 3.4: Comparative analysis of the Amaranth degradation efficiency, photocatalytic rate constant, bandgap energies and surface area of synthesized N1, N2, N3, N4, PN and NU catalysts.

A comparative data on the literature reported photocatalytic Amaranth dye degradation efficiency of several catalysts is listed in Table 3.5. It is evident that the Ni_{1-x}O nanosponge (N2) outperforms other synthesized Ni_{1-x}O catalyst and reported transition metal oxide catalysts such as N- WO_3 [24], N- ZrO_2 [25] and ZnO [26,27]. This is attributed to i) spongy nature of Ni_{1-x}O which facilitates facile diffusion and adsorption of dye on to the Ni_{1-x}O surface and ii) the extensive network of structurally robust, mesoporous structure which facilitates migration of charge carriers, which in turn reduces charge carrier recombination rate and enhances photocatalytic activity [28]. This signifies the importance of the structurally robust mesoporous networks in enhancing photocatalytic degradation activity in agreement with our observations of TiO_2 presented in Chapter 2.

Catalyst	Initial dye concentration	Light source	Reaction time (min)	% Degradation
N,S-doped TiO ₂ [27]	3.90 x 10 ⁻⁵ M	200 W tungsten lamp	90	59.3
TiO ₂ [28]	84 μmol.L ⁻¹	125 W	60	75
TiO ₂ [29]	30 ppm	Solar light	90	99.1
N-WO ₃ [24]	25 mg.L ⁻¹	160 W Visible and UVA light	120	100
ZnO [26]	20 ppm	250 W Hg medium pressure lamp	120	100
N-ZrO ₂ [25]	10 ppm	Fluorescent lamp (visible) 24 W and Low pressure Hg lamp (UV) of 15 W	120 240	26.4 84.5
ZnO [27]	4.4 x 10 ⁻⁵ M	200 W tungsten lamp	300	92.5
Porous TiO ₂ (This work)	30 ppm	250 W Hg Medium pressure lamp	15	95.6
Ni _{1-x} O nanosponge (N2) (This work)	30 ppm	250 W Hg Medium pressure Lamp	70	93.8

Table 3.5 Comparison of Amaranth degradation efficiency of Ni_{1-x}O with respect to literature reported catalysts.

Moreover, the regeneration activity studies were conducted with N1, N2, N3, N4, PN and NU by reutilizing the recovered catalyst. It was observed from Figure 3.26 that N2 exhibited the highest regeneration activity over 5 catalytic cycles as compared to other synthesized Ni_{1-x}O catalyst. This was attributed to reduced charge carrier recombination rates due to ease of charge carrier migration along the walls of mesoporous structure [12], possibly improving photo corrosion stability of Ni_{1-x}O. It is to be noted that, the photocatalytic performance of fibrous Ni_{1-x}O nanosponge is relatively lower compared to the mesoporous TiO₂ reported in Chapter 2, which is largely due to its limited surface area (63.67 m².g⁻¹) compared to TiO₂

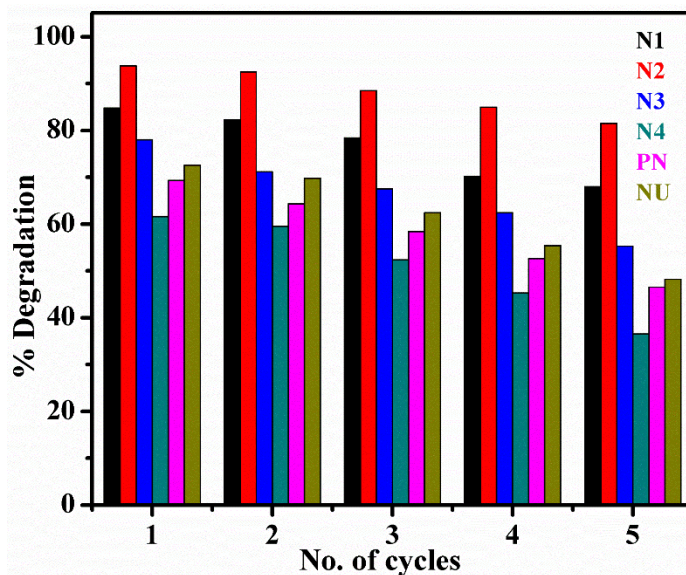


Figure 3.26: Catalyst regeneration study of all the synthesized Ni_{1-x}O catalysts.

(238 m².g⁻¹). Furthermore, the difference in photocatalytic performance could also be a result of the type of the reactive species generated over the catalyst surface and their efficiency in inducing the dye oxidation process [12]. All the above findings confirm that the fibrous, mesoporous Ni_{1-x}O nanosponge with an interconnected robust porous network, has significant advantages in terms of its superior adsorptive separation efficiency, as well as its enhanced in-situ photocatalytic dye degradation activity. Nonetheless, further improvements in its effective surface area while retaining the robust mesoporous structure and reduction in bandgap energies will be needed for achieving the development of self-sustainable, economical and highly active photocatalytic material for efficient treatment of wastewater contaminated with azo dyes.

3.5 Conclusion

The study has demonstrated the effective use of 4-nba, and imidazole in synthesizing nanostructural morphology of Ni_{1-x}O such as nanosponge and nanoflakes by utilizing simple direct calcination method. The obtained Ni_{1-x}O powders were studied for phase purity, morphology, particle size, band structure and redox states using FTIR, XRD, FESEM, TEM/HRTEM, SAED, UV-DRS, and XPS analysis. The powder X-ray diffraction study revealed a pure cubic phase of Ni_{1-x}O. The bandgap of the synthesized Ni_{1-x}O was within the range of 3.3 to 3.5 eV. A sponge-like Ni_{1-x}O with 3D interconnected porous network was obtained by controlled combustion of [Ni(H₂O)₄(4-nba)₂].2H₂O compound. The effect of 4-

nba in Ni_{1-x}O synthesis from tetra-aquobis(para-nitrobenzoato)nickel(II) dihydrate resulted in nanosponge like morphology with highest surface area of $63.67 \text{ m}^2.\text{g}^{-1}$ as compared to other synthesized Ni_{1-x}O catalyst. Furthermore, the Amaranth dye adsorption studies on all synthesized Ni_{1-x}O followed the Sip adsorption isotherm model with a maximum adsorption capacity of $75 \text{ mg}.\text{g}^{-1}$. The adsorption kinetic followed the pseudo-first-order kinetic model for all the synthesized Ni_{1-x}O . The photocatalytic degradation of Amaranth dye followed Langmuir Hinshelwood mechanism and exhibited the highest degradation of 93.8 % within 70 minutes with a maximum rate constant of $4.04 \times 10^{-2} \text{ min}^{-1}$ (at pH = 5.6). The results of stability analysis also proved that the nanosponge-like porous structure facilitated easy migration of charge carriers thus partially improving catalyst stability.

3.6 References

- [1] N. Kumar, H. Mittal, S.M. Alhassan, S.S. Ray, Bionanocomposite Hydrogel for the Adsorption of Dye and Reusability of Generated Waste for the Photodegradation of Ciprofloxacin: A Demonstration of the Circularity Concept for Water Purification, *ACS Sustain. Chem. Eng.* 6 (2018) 17011–17025.
- [2] R. Baccar, P. Blázquez, J. Bouzid, M. Feki, H. Attiya, M. Sarrà, Modeling of adsorption isotherms and kinetics of a tannery dye onto an activated carbon prepared from an agricultural by-product, *Fuel Process. Technol.* 106 (2013) 408–415.
- [3] N. Ayawei, A.N. Ebelegi, D. Wankasi, Modelling and Interpretation of Adsorption Isotherms, *J. Chem.* 2017 (2017) 1–11.
- [4] M.A. Al-Ghouti, D.A. Da'ana, Guidelines for the use and interpretation of adsorption isotherm models: A review, *J. Hazard. Mater.* 393 (2020) 122383.
- [5] B.M. Marwa, S. Bruno, B. Mongi, F. Tran Van, B.L. Abdelmottaleb, Modeling of adsorption isotherms of dye N719 on titanium oxide using the grand canonical ensemble in statistical physics for dye sensitized solar cells, *Sol. Energy.* 135 (2016) 177–187.
- [6] J. Han, Q. Geng, W. Chen, L. Zhu, Q. Wu, Q. Wang, Self-assembled liquid crystals formed by hydrogen bonding between non-mesogenic 1,3,4-oxadiazole-based pyridines and substituted benzoic acids, *Supramol. Chem.* 24 (2012) 157–164..
- [7] S. Vijayakumar, S. Nagamuthu, G. Muralidharan, Porous NiO/C nanocomposites as electrode material for electrochemical supercapacitors, *ACS Sustain. Chem. Eng.* 1 (2013) 1110–1118.
- [8] S. Vijayakumar, S. Nagamuthu, G. Muralidharan, Supercapacitor studies on NiO nanoflakes synthesized through a microwave route, *ACS Appl. Mater. Interfaces.* 5 (2013) 2188–2196.
- [9] O. Kristiansson, Crystal structure of bis(4-nitrobenzoate)tetraaquamanganese(II) dihydrate, $[\text{Mn}(\text{p-NO}_2\text{C}_6\text{H}_4\text{COO})_2(\text{H}_2\text{O})_4] \cdot 2\text{H}_2\text{O}$, bis(4-nitrobenzo-ate)tetraaquanickel(II) dihydrate, $(\text{Ni}(\text{p-NO}_2\text{C}_6\text{H}_4\text{COO})_2(\text{H}_2\text{O})_4) \cdot 2\text{H}_2\text{O}$, *Z. Kristallogr. New Cryst. Struct.* 216 (2001) 86–88.
- [10] B.R. Srinivasan, J. V Sawant, P. Raghavaiah, Synthesis, spectroscopy, thermal studies and supramolecular structures of two new alkali-earth 4-nitrobenzoate complexes

- containing coordinated imidazole, 2007.
- [11] B.R. Srinivasan, J. V Sawant, P. Raghavaiah, On the distorted $\{\text{NiN}_6\}$ octahedron in hexakis(imidazole)nickel(II) bis(4-nitrobenzoate) dihydrate, 48 (2009) 181-188.
- [12] A. Barakat, M. Al-Noaimi, M. Suleiman, A.S. Aldwayyan, B. Hammouti, T. Ben Hadda, S.F. Haddad, A. Boshala, I. Warad, One step synthesis of NiO nanoparticles via solid-state thermal decomposition at low-temperature of novel aqua(2,9-dimethyl-1,10-phenanthroline)NiCl₂ complex, *Int. J. Mol. Sci.* 14 (2013) 23941–23954.
- [13] M. Thommes, K. Kaneko, A. V. Neimark, J.P. Olivier, F. Rodriguez-Reinoso, J. Rouquerol, K.S.W. Sing, Physisorption of gases, with special reference to the evaluation of surface area and pore size distribution (IUPAC Technical Report), *Pure Appl. Chem.* 87 (2015)..
- [14] P.P. Morajkar, J.B. Fernandes, A new facile method to synthesize mesoporous $\gamma\text{-Al}_2\text{O}_3$ of high surface area and catalytic activity, *Catal. Commun.* 11 (2010) 414–418.
- [15] T.G. Xu, D.J. Xu, Diaquabis(imidazole- κN)bis(nitrobenzoato- κO)nickel(II), *Acta Crystallogr. Sect. E Struct. Reports Online.* 60 (2004) 27–29.
- [16] B.R. Srinivasan, G.K. Rane, Synthesis, properties and supramolecular structure of di(aqua)bis(ethylenediamine)nickel(II) bis(4-nitrobenzoate) *J. Chem. Sci.* 121 (2009) 145-153.
- [17] H.Q. Wang, X.P. Fan, X.H. Zhang, Y.G. Huang, Q. Wu, Q.C. Pan, Q.Y. Li, In situ growth of NiO nanoparticles on carbon paper as a cathode for rechargeable Li-O₂ batteries, *RSC Adv.* 7 (2017) 23328–23333.
- [18] C. Guan, Y. Wang, Y. Hu, J. Liu, K.H. Ho, W. Zhao, Z. Fan, Z. Shen, H. Zhang, J. Wang, Conformally deposited NiO on a hierarchical carbon support for high-power and durable asymmetric supercapacitors, *J. Mater. Chem. A.* 3 (2015) 23283–23288.
- [19] P. Dubey, N. Kaurav, R.S. Devan, G.S. Okram, Y.K. Kuo, The effect of stoichiometry on the structural, thermal and electronic properties of thermally decomposed nickel oxide, *RSC Adv.* 8 (2018) 5882–5890.
- [20] H. Mittal, S.M. Alhassan, S.S. Ray, Efficient organic dye removal from wastewater by magnetic carbonaceous adsorbent prepared from corn starch, *J. Environ. Chem. Eng.* 6 (2018) 7119–7131.

- [21] T.S. Kim, H.J. Song, M.A. Dar, H.J. Lee, D.W. Kim, Fast adsorption kinetics of highly dispersed ultrafine nickel/carbon nanoparticles for organic dye removal, *Appl. Surf. Sci.* 439 (2018) 364–370.
- [22] W. Konicki, A. Hełminiak, W. Arabczyk, E. Mijowska, Adsorption of cationic dyes onto Fe@graphite core–shell magnetic nanocomposite: Equilibrium, kinetics and thermodynamics, *Chem. Eng. Res. Des.* 129 (2018) 259–270.
- [23] H. Sudrajat, S. Babel, Rapid photocatalytic degradation of the recalcitrant dye amaranth by highly active N-WO₃, *Environ. Chem. Lett.* 14 (2016) 243–249.
- [24] H. Sudrajat, S. Babel, H. Sakai, S. Takizawa, Rapid enhanced photocatalytic degradation of dyes using novel N-doped ZrO₂, *J. Environ. Manage.* 165 (2016) 224–234.
- [25] N. Divya, A. Bansal, A.K. Jana, Photocatalytic activity of transition metal ion doped titania for Amaranth dye degradation, *Mater. Sci. Forum.* 712 (2012) 85–104.
- [26] R. Ameta, N. Jain, S. Kothari, Photocatalytic bleaching of amaranth dye over ZnO powder, *Indian J. Chem. Technol.* 11 (2004) 423–426.
- [27] A.K. Jain, S. Sharma, R. Ameta, Enhanced photocatalytic activity of N, S-doped titania for degradation of amaranth, *Merit Res. J. Environ. Sci. Toxicol.* 3 (2015) 25–30.
- [28] M. Karkmaz, E. Puzenat, C. Guillard, J.M. Herrmann, Photocatalytic degradation of the alimentary azo dye amaranth: Mineralization of the azo group to nitrogen, *Appl. Catal. B Environ.* 51 (2004) 183–194.
- [29] A.P. Naik, A. V. Salkar, M.S. Majik, P.P. Morajkar, Enhanced photocatalytic degradation of Amaranth dye on mesoporous anatase TiO₂: Evidence of C-N, NN bond cleavage and identification of new intermediates, *Photochem. Photobiol. Sci.* 16 (2017) 1126–1138.

CHAPTER IV:
SYNTHESIS,
CHARACTERIZATION
AND CATALYTIC APPLICATION
OF NANOPOROUS Ni_{1-x}O/TiO₂
CATALYTS

4.1 PROLOGUE

The nanoporous $\text{Ni}_{1-x}\text{O}/\text{TiO}_2$ catalysts have been synthesized using reflux assisted sol-gel method. The influence of addition of $[\text{Ni}(\text{H}_2\text{O})_4(4\text{-nba})_2]\cdot 2\text{H}_2\text{O}$ in $\text{Ti}(\text{OH})_4$ gel modified with butanetetracarboxylic acid and urea as SDA's has been investigated. The details of chemicals used in synthesis have already been discussed in section 2.2 and 3.2 of Chapter 2 and Chapter 3. The effect of different amount of $[\text{Ni}(\text{H}_2\text{O})_4(4\text{-nba})_2]\cdot 2\text{H}_2\text{O}$ in $\text{Ti}(\text{OH})_4$ gel modified with butanetetracarboxylic acids and urea as SDAs on porosity and morphology of $\text{Ni}_{1-x}\text{O}/\text{TiO}_2$ has been investigated and the detailed characterization is discussed in section 4.3. Finally, the catalytic efficiency of all the synthesized $\text{Ni}_{1-x}\text{O}/\text{TiO}_2$ catalysts were evaluated for adsorption and photocatalytic degradation of Amaranth dye. The novel findings of this investigation are presented in detail in the result and discussion section 4.3 along with conclusion of this study in section 4.5.

4.2 EXPERIMENTAL: SYNTHESIS STRATEGY AND PROCEDURES

4.2.1 Synthesis of $\text{Ni}_{1-x}\text{O}/\text{TiO}_2$ nanocomposites

The $\text{Ti}(\text{OH})_4$ gel with butanetetracarboxylic acid and urea was synthesized as reported in Chapter II, section 2.4.3. Subsequently crystals of $[\text{Ni}(\text{H}_2\text{O})_4(4\text{-nba})_2]\cdot 2\text{H}_2\text{O}$ were synthesized as reported in section 3.3.1. In this chapter $\text{Ni}_{1-x}\text{O}/\text{TiO}_2$ nanocomposites have been synthesized following a protocol as depicted in Figure 4.1. To a synthesized $\text{Ti}(\text{OH})_4$ gel containing butanetetracarboxylic acid – urea mixture, a predetermined amount of $[\text{Ni}(\text{H}_2\text{O})_4(4\text{-nba})_2]\cdot 2\text{H}_2\text{O}$ was added such that the final weight % of Ni_{1-x}O is 1, 3, 5, 10, 20 and 50 wt.% in $\text{Ni}_{1-x}\text{O}/\text{TiO}_2$ composite catalyst. The hybrid gel mixture containing $\text{Ti}(\text{OH})_4$, butanetetracarboxylic acid, urea and $[\text{Ni}(\text{H}_2\text{O})_4(4\text{-nba})_2]\cdot 2\text{H}_2\text{O}$ was then refluxed at $80\text{ }^\circ\text{C}$ for 24 hours. After reflux, it was then kept for digestion at $100\text{ }^\circ\text{C}$ and the obtained dried gel was calcined at $500\text{ }^\circ\text{C}$ to form $\text{Ni}_{1-x}\text{O}/\text{TiO}_2$ nanocomposite catalyst.

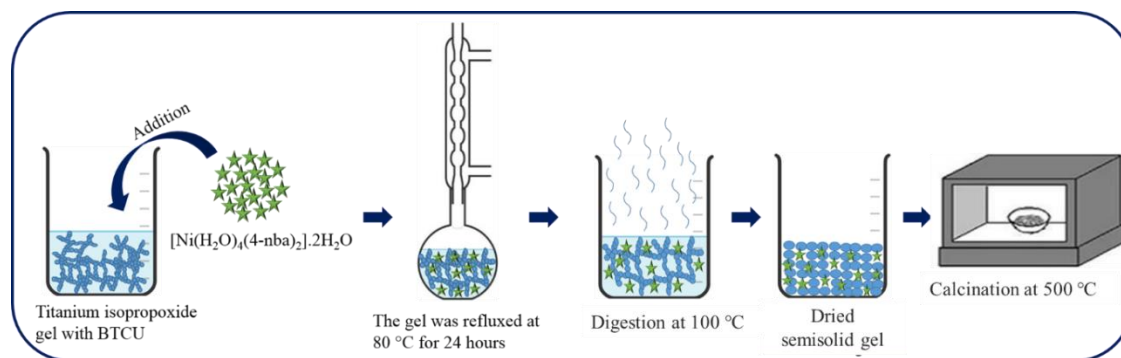


Figure 4.1: Schematic representation of $\text{Ni}_{1-x}\text{O}/\text{TiO}_2$ catalyst synthesis protocol using reflux assisted sol-gel method.

4.2.2 Protocol of adsorption isotherm and kinetic experiments.

In a typical adsorption experiment, the pre-activated $\text{Ni}_{1-x}\text{O}/\text{TiO}_2$ catalyst (0.3 g) was dispersed in 1L Amaranth dye solution of varied concentrations from 10 to 110 ppm. The solution was kept on a shaker for 24 hours at room temperature. The absorbance of each of the solution was recorded at 520 nm using UV-Visible spectrophotometer. The adsorption capacity at equilibrium (q_e), and the Amaranth removal efficiency of each of the Ni_{1-x}O catalyst was determined using the standard adsorption isotherm models. [1,2] The graph of q_e as a function of initial concentration of Amaranth dye was fitted using non-linear forms of different adsorption isotherm models such as Langmuir, Freundlich, Sips and Temkin models [3–5].

Similarly, the adsorption kinetic experiments were performed to know the reaction rate and the adsorption mechanism. In a typical experiment 0.3 g of each of the $\text{Ni}_{1-x}\text{O}/\text{TiO}_2$ catalysts were dispersed in 1L of 30 ppm Amaranth dye solution. At regular interval of time, aliquots were taken and the absorbance of the solution was recorded using UV-Visible spectrophotometer at 520 nm. The obtained experimental data was fitted using different adsorption kinetic models such as pseudo first order, pseudo second order, Elovich model and intraparticle diffusion model. The mathematical equations of all the above-mentioned isotherm models and adsorption kinetic models is already presented in Table 2.1 and Table 2.2 respectively in section 2.4.4 of Chapter 2 and hence are not repeated here. The obtained results are discussed in detail in section 4.3.

4.2.3 Protocol of photocatalytic degradation studies.

The photocatalytic performance of all the synthesized TiO₂ were evaluated for Amaranth dye degradation study. 100 mg of the pre-activated TiO₂ catalyst was dispersed in 300 mL (30 ppm) dye solution and the mixture was transferred in a photocatalytic reactor. The solution was then irradiated with 250 watt MPMVL for 60 minutes at room temperature. The reaction was monitored by sampling the solution after every five minutes and recording its absorbance using UV-Visible spectrophotometer at 520 nm as presented in Figure 4.15. The obtained results are discussed in section 4.3.3.

4.2.4 Protocol of LCMS identification of Amaranth dye degradation products.

The initial analysis of the photodegradation products of Amaranth were carried out using LC-ESI-MS (Agilent 6520) instrument. The HPLC analysis (Agilent 1200) was performed using a Phenomenex Kinetex XB C18 column (length 30 mm, internal diameter 3.0 mm). Impurity profiling of the Amaranth stock solution was performed using the LC-ESI-MS and UPLC-ESI-MS techniques (Acquity SDS mass spectrometer from Waters). The eluent gradient conditions used for the separation are listed in Table 4.1. The mass parameters were optimized using a dual spray (ESI) with positive/negative polarity operated under the full scan mode with a gas temperature of 350 °C and a flow rate of 10 L min⁻¹.

Time (min)	*A (%)	*B (%)
0	90	10
2	90	10
9	10	90
11	10	90
13	90	10
15	90	10

*A = H₂O, 0.1% formic acid + 5% acetonitrile; *B = Acetonitrile, 0.1 % formic acid, Constant flow rate = 1mL/min

Table 4.1: Optimized eluent gradient conditions for HPLC separation.

4.3 RESULT AND DISCUSSION

4.3.1 Characterization of $\text{Ni}_{1-x}\text{O}/\text{TiO}_2$ catalyst.

The effect of urea, 1,2,3,4-butanetetracarboxylic acid and p-nitrobenzoate on the phase purity, morphology, particle size and the surface area of $\text{Ni}_{1-x}\text{O}/\text{TiO}_2$ nanocomposites has been investigated using different characterization techniques which are discussed in detail in the subsequent sections.

➤ Effect of urea; 1,2,3,4-butanetetracarboxylic acid and nitrobenzoate hybrid gels on $\text{Ni}_{1-x}\text{O}/\text{TiO}_2$ catalyst

The as-synthesized hybrid gel was initially subjected to TG-DTA analysis in the temperature range of 30-800°C at the heating rate of 10°C/min. From Figure 4.2 (a) it is observed that the initial weight loss up to 255°C is due to the loss of physisorbed and chemisorbed water from the gel matrix. The weight loss in temperature range from 255°C to 500°C was predominantly due to the elimination of loss of organic species. This is supported by the significant exothermic peak at 491°C. However, after 500°C no significant change in weight loss was observed which confirms that the calcination temperature is sufficient for the formation of stable metal oxide. The post calcined $\text{Ni}_{1-x}\text{O}/\text{TiO}_2$ were labeled as 1NT, 3NT, 5NT, 10NT and 50 NT for 1, 3, 5, 10, 20 and 50 wt % of Ni_{1-x}O on TiO_2 . The formed stable metal oxide and its phase purity has been determined using IR and XRD analysis.

The IR analysis for the synthesized catalysts were carried out in the vibrational frequency range of 400 to 4000 cm^{-1} as can be observed from Figure 4.3 (a). The post-calcined metal oxide exhibited the characteristic peaks of OH-stretching at 3500 cm^{-1} , OH-bending at 1650 cm^{-1} and metal oxide stretching in the region 800-1000 cm^{-1} which confirms the complete removal of organic species from the nickel/titanium gel matrix. Furthermore, Figure 4.3 (b) shows the powder X-ray diffractograms of all the synthesized $\text{Ni}_{1-x}\text{O}/\text{TiO}_2$ nanocomposites in comparison to that of Ni_{1-x}O and TiO_2 . The observed diffraction peaks at $2\theta = 25.2, 37.8, 48.0, 53.9, 55.06, 62.7, 68.7$ and 70.2° are assigned to (101), (004), (200), (105), (211), (205) (116) and (220) planes respectively. Thus, indicating only anatase phase of TiO_2 in all the nanocomposites. However, no diffraction peaks for Ni_{1-x}O was obtained for lower % loading of Ni_{1-x}O on TiO_2 i.e. 1NT, 3NT and 5 NT.

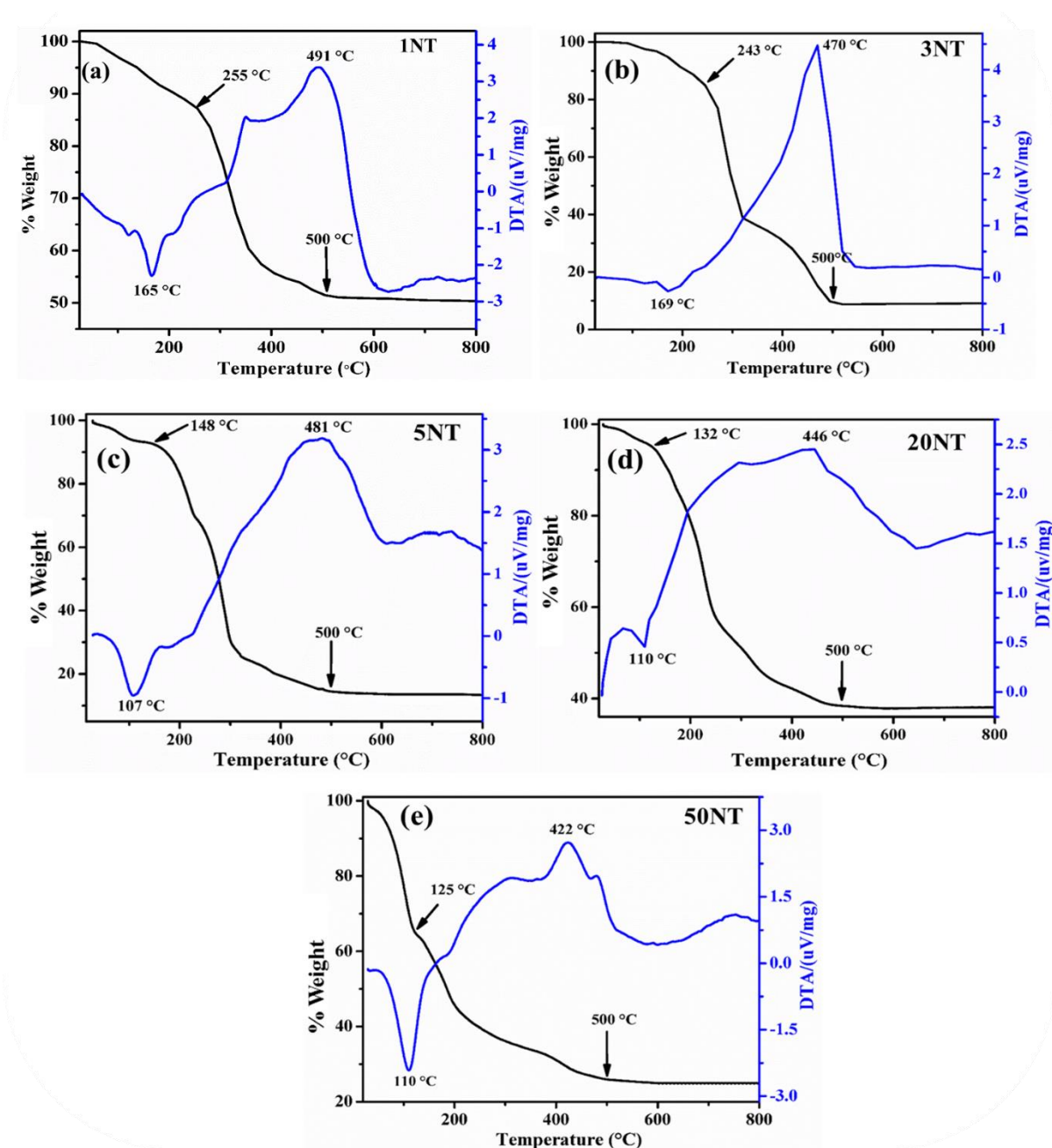


Figure 4.2: (a-e) TG-DTA analysis of titanium hydroxide hybrid gel with butanetetracarboxylic acid, urea and $[\text{Ni}(\text{H}_2\text{O})_4(4\text{-nba})_2] \cdot 2\text{H}_2\text{O}$

However, as we increase the concentration of Ni_{1-x}O as in the case of 10 NT, 20NT and 50 NT, we observe diffraction pattern at $2\theta = 43.3^\circ$ which corresponds to 200 plane of Ni_{1-x}O . Moreover, no new peaks, were observed for this composites which indicates the formation of pure $\text{Ni}_{1-x}\text{O}/\text{TiO}_2$ nanocomposites.

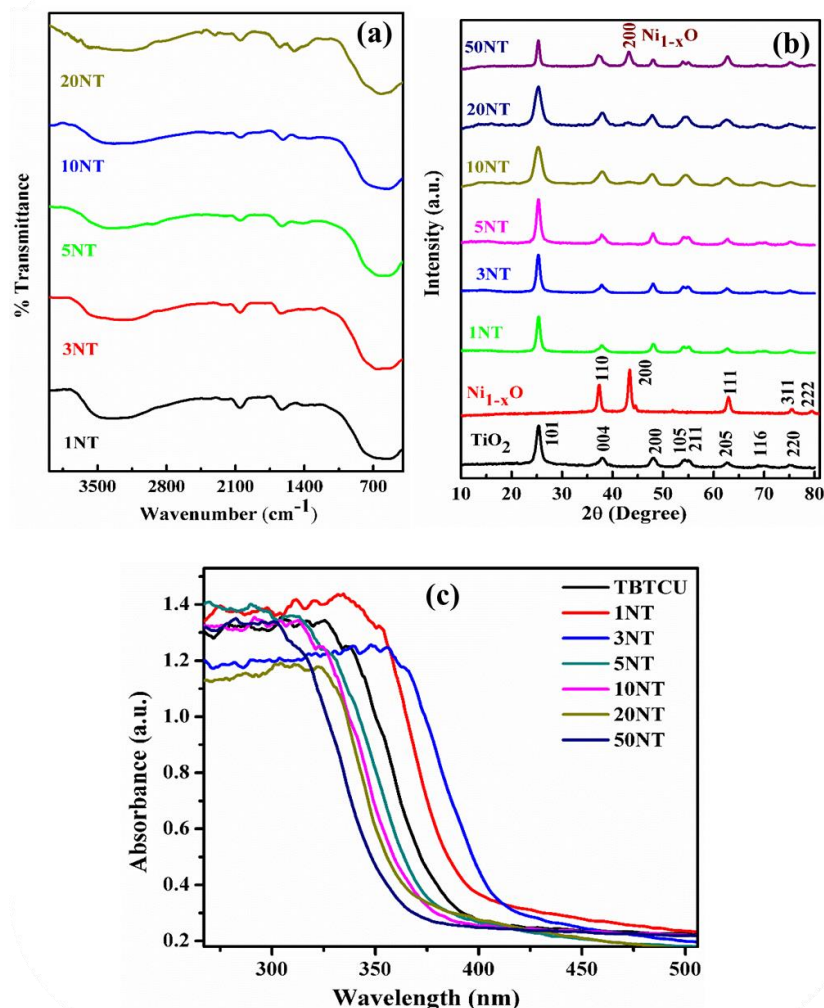


Figure 4.3: (a) IR analysis (b) XRD and (c) UV-DRS analysis of Ni_{1-x}O/TiO₂ nanocomposites.

Further, the bandgap energy of the sample was determined using UV-DRS analysis. Figure 4.3 (c) shows the diffuse reflectance spectra of all the synthesized Ni_{1-x}O/TiO₂ nanocomposites. The calculated bandgap for TBTCU was 3.19 eV. As we load Ni_{1-x}O on TiO₂ the bandgap was observed to decrease to 3.10 and 2.90 eV for 1% and 3% Ni_{1-x}O/TiO₂ nanocomposites. However, with further increase in the loading of Ni_{1-x}O from 5% to 50 % the bandgap was observed to increase from 3.19 to 3.33 eV.

The porosity of the Ni_{1-x}O/TiO₂ nanocomposites was determined using N₂ adsorption-desorption isotherm study. All the synthesized Ni_{1-x}O/TiO₂ exhibited type IV isotherm. The representative isotherm for 1NT, 3NT, 5NT, 10NT, 20NT and 50 NT are shown in the Figure

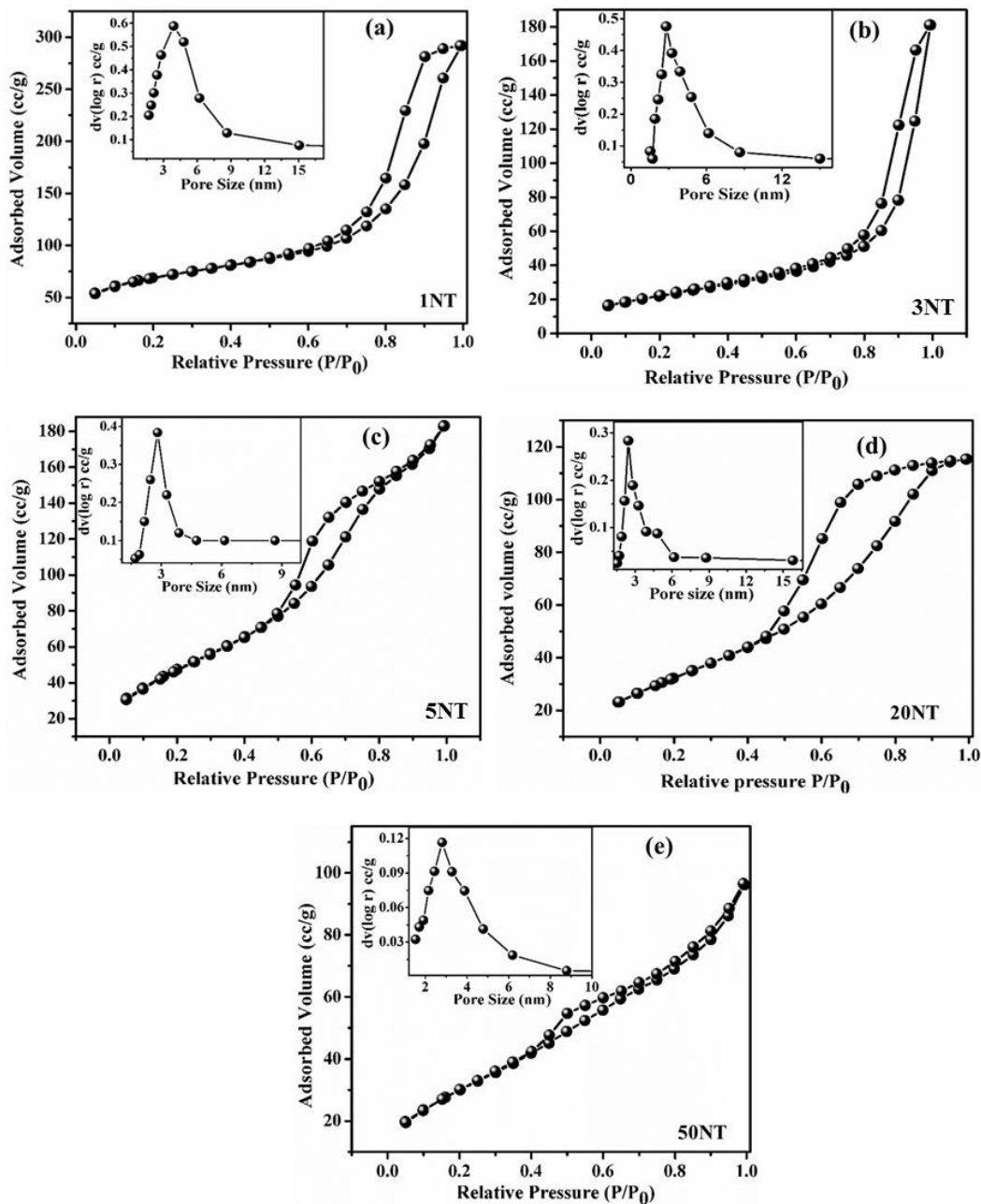


Figure 4.4: (a-e) N_2 adsorption-desorption analysis of synthesized $Ni_{1-x}O/TiO_2$ nanocomposites.

4.4 (a-e). The surface area for the synthesized $Ni_{1-x}O/TiO_2$ nanocomposites are depicted in the Table 4.2 which are observed to be lower as compared to TBTCU. In addition to this, the pore size as well as pore volume were observed to decrease. This could be due to the occupancy of the TiO_2 pores with that of $Ni_{1-x}O$ nanoparticles.

Catalyst	Surface area ($\text{m}^2\cdot\text{g}^{-1}$)	Pore size (nm)	Pore volume ($\text{cc}\cdot\text{g}^{-1}$)
TBTCU	238	4.80	0.84
N2	63	14.20	0.113
1NT	231	3.89	0.588
3NT	219	2.80	0.535
5NT	183	2.80	0.384
10NT	134	2.62	0.285
20NT	121	2.40	0.213
50NT	90	2.12	0.119

Table 4.2: Surface area, pore size and pore volume of $\text{Ni}_{1-x}\text{O}/\text{TiO}_2$ nanocomposites.

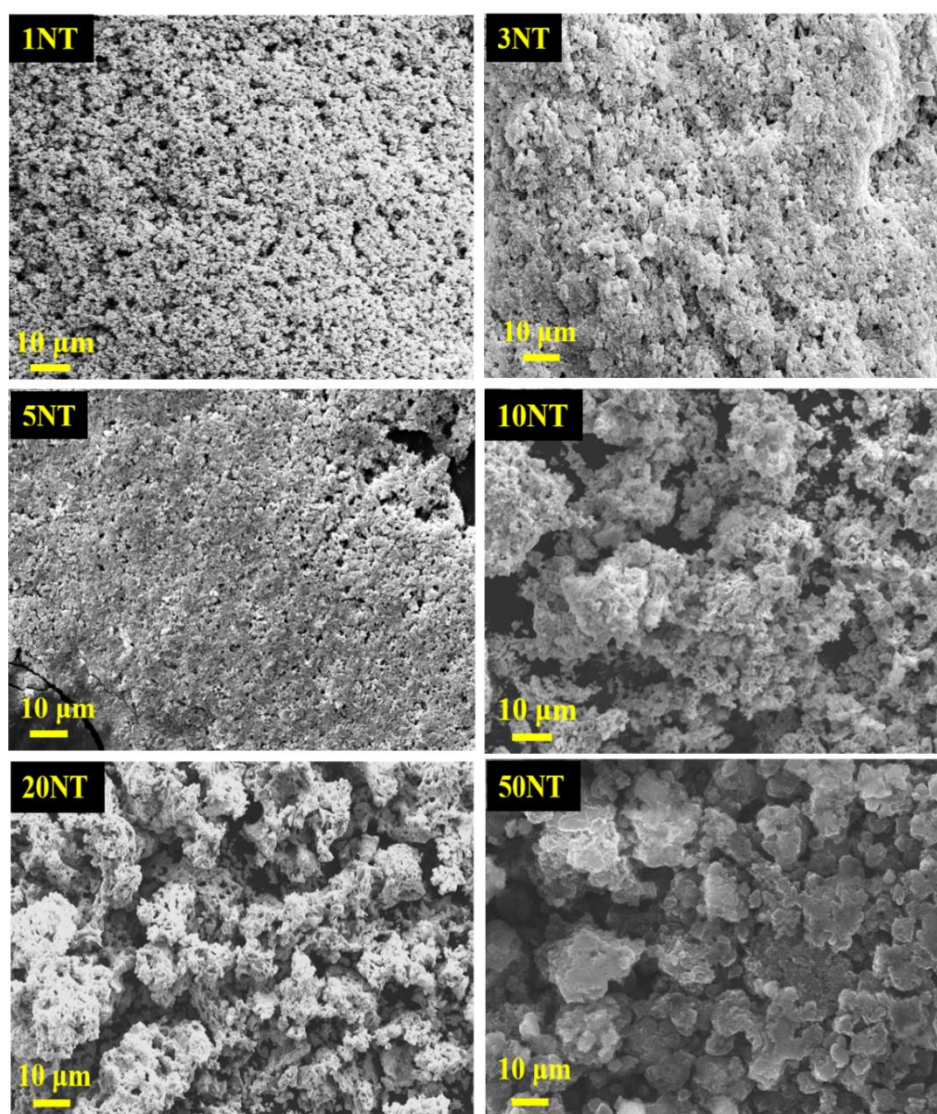


Figure 4.5: SEM analyses of synthesized $\text{Ni}_{1-x}\text{O}/\text{TiO}_2$ nanocomposites.

The surface morphology of the $\text{Ni}_{1-x}\text{O}/\text{TiO}_2$ nanocomposites was analyzed using SEM analysis (Figure 4.5). The porous nature of the sample was observed in case of 1NT, 3NT and 5NT. However, the porous structure tend to disappear as the Ni_{1-x}O loading on TiO_2 was increased (see Figure 4.5-10NT, 20NT and 50NT). This could be attributed to the sintering of the material due to exothermic decomposition of $[\text{Ni}(\text{H}_2\text{O})_4(4\text{-nba})_2]\cdot 2\text{H}_2\text{O}$. This observation was further confirmed by HRTEM analysis of the $\text{Ni}_{1-x}\text{O}/\text{TiO}_2$ nanocomposites. The particle size of the synthesized nanocomposites appeared to increase from 7 to 29 nm as we increase the concentration of Ni_{1-x}O from 1-50% as can be seen from the particle size distribution curve. The HRTEM for these synthesized nanocomposites represents the characteristic d-spacing value of 0.34 nm and 0.21 nm corresponding to 101 plane of TiO_2 and 200 plane of Ni_{1-x}O . The diffraction ring pattern observed in SAED indicates the characteristics peaks and is in accordance with that of the powder XRD.

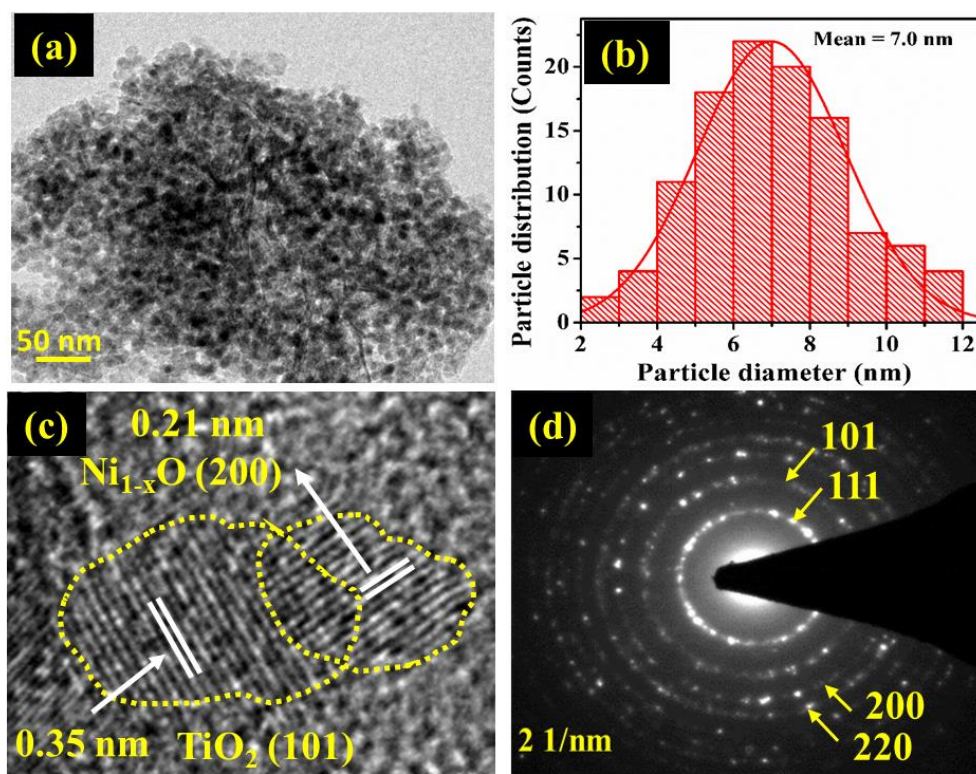


Figure 4.6: (a) Low resolution TEM, (b) particle size distribution, (c) HRTEM and (d) SAED analysis of 1NT

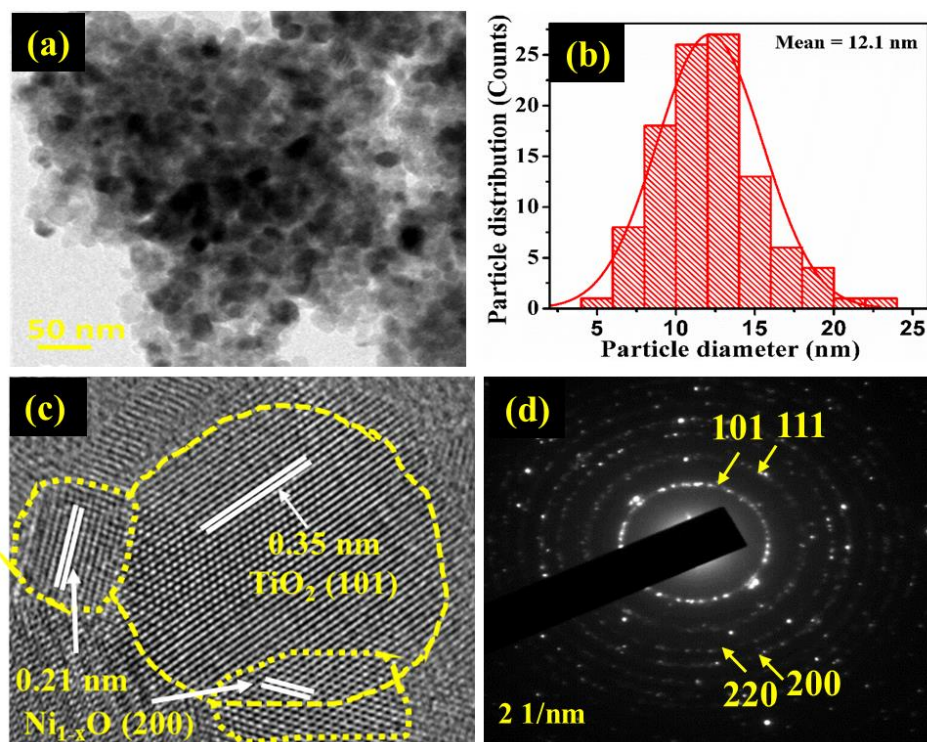


Figure 4.7: (a) Low resolution TEM, (b) particle size distribution, (c) HRTEM and (d) SAED analysis of 3NT

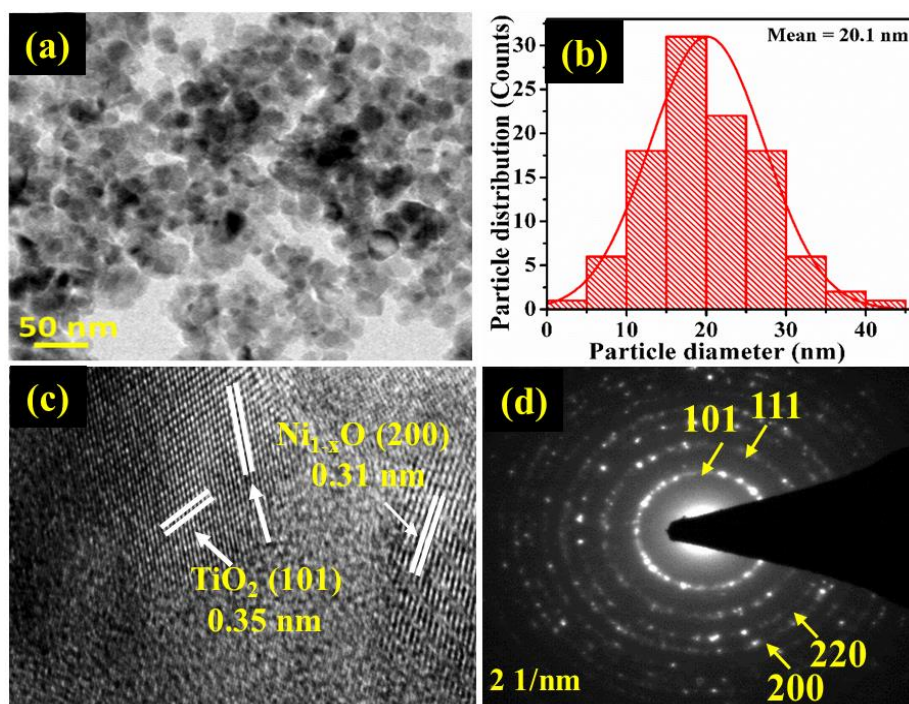


Figure 4.8: (a) Low resolution TEM, (b) particle size distribution, (c) HRTEM and (d) SAED analysis of 20NT

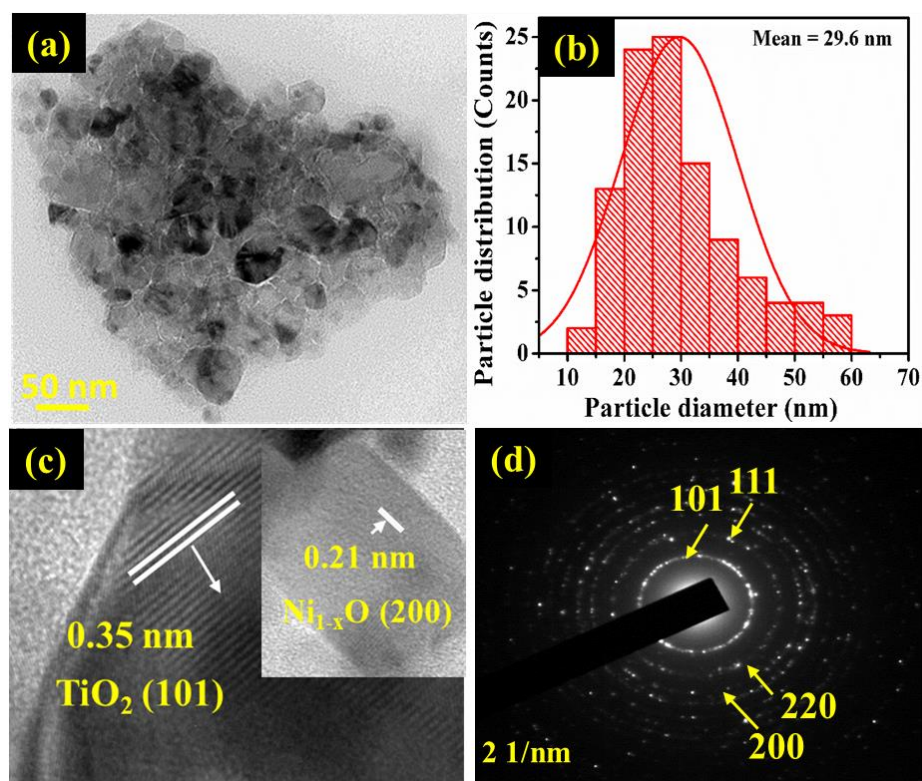


Figure 4.9: (a) Low resolution TEM, (b) particle size distribution, (c) HRTEM and (d) SAED analysis of 50NT

➤ **Non stoichiometric nature of $\text{Ni}_{1-x}\text{O}/\text{TiO}_2$ nanocomposites.**

The oxidation state and surface composition of the total number of elements present in the synthesized $\text{Ni}_{1-x}\text{O}/\text{TiO}_2$ nanocomposite was analyzed using XPS analysis. The major peaks corresponding to the binding energy of 458.7 eV, 855.8 eV and 529.3 eV in the full scan spectra were attributed to Ti, Ni and O which is in good agreement with the literature reports [6] as shown in Figure 4.10. To get more insights into the study of Ti, Ni and O, high resolution spectra were examined for each of the elements. Figure 4.10 shows full scan spectra of all the synthesized $\text{Ni}_{1-x}\text{O}/\text{TiO}_2$ catalyst. Figure 4.11 and Figure 4.12 shows the high resolution (narrow scan) XPS spectra of Ni (2p) core level, Ti (2p) core level and O (1s) core level for 1NT, 3NT, 5NT, 10NT, 20NT and 50 NT respectively.

XPS spectra of all the Ni (2p) showed five different peaks located at various binding energy and it agrees well with literature reports [7]. A well-defined shoulder peak that represents the

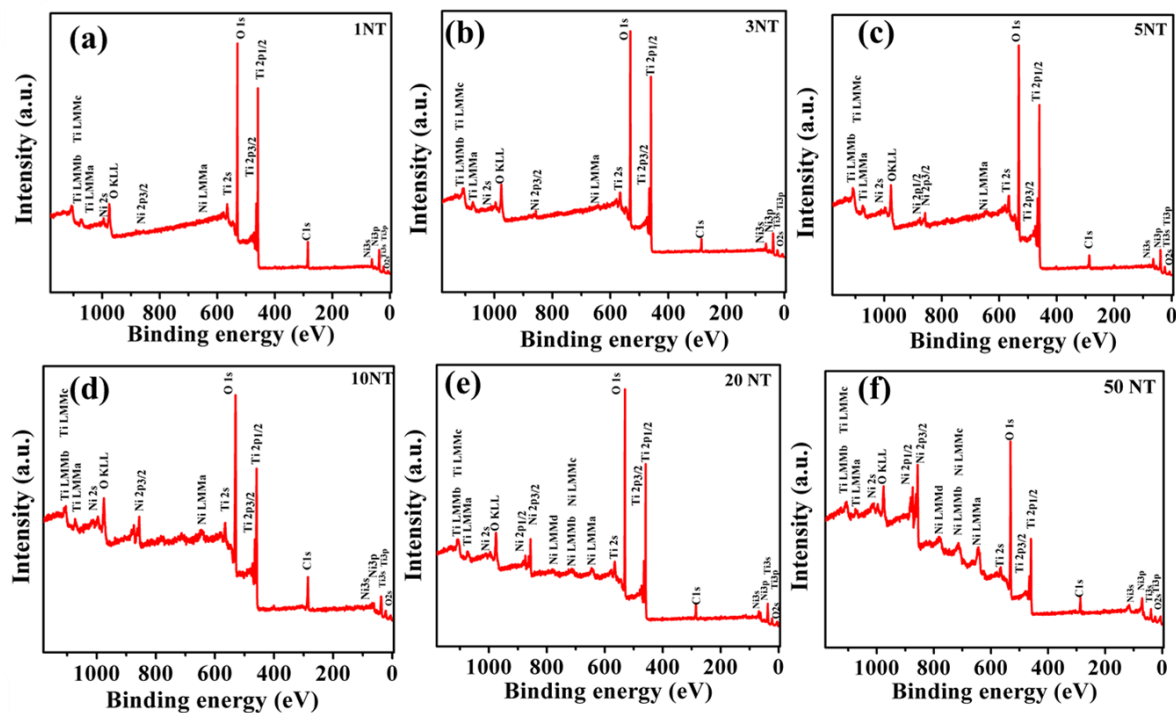


Figure 4.10: (a-f) Full scan spectra $\text{Ni}_{1-x}\text{O}/\text{TiO}_2$ nanocomposites.

Ni (2p) core levels for Ni_{1-x}O has been observed in all the $\text{Ni}_{1-x}\text{O}/\text{TiO}_2$ nanocomposite. To get further insight of the shoulder peak features of Ni ($2p_{3/2}$) and Ni ($2p_{1/2}$), the XPS spectra were deconvoluted using Voigt peak fitting functions. The peak fitting for the 8 peaks has been marked from *a* to *h* located at the binding energies of $853.2 (\pm 0.2)$, $855.1 (\pm 0.2)$, $860.5 (\pm 0.2)$, $865.2 (\pm 0.2)$, $870.7 (\pm 0.2)$, $872.2 (\pm 0.2)$, $877.1 (\pm 0.2)$ and $879.9 (\pm 0.2)$ eV, respectively. The peaks marked as *a*, *b*, *e* and *f* represents the core level Ni^{2+} ($2p_{3/2}$), Ni^{3+} ($2p_{3/2}$), Ni^{2+} ($2p_{1/2}$) and Ni^{3+} ($2p_{1/2}$), respectively. The shakeup satellite peaks of Ni^{2+} ($2p_{3/2}$) and Ni^{3+} ($2p_{3/2}$) are labeled as *c* and *d*, and the shakeup satellite peaks of Ni^{2+} ($2p_{1/2}$) and Ni^{3+} ($2p_{1/2}$) are labeled as *g* and *h*, respectively. These peaks confirmed the presence of non-stoichiometric Ni_{1-x}O [8] in the as synthesized $\text{Ni}_{1-x}\text{O}/\text{TiO}_2$ nanocomposites.

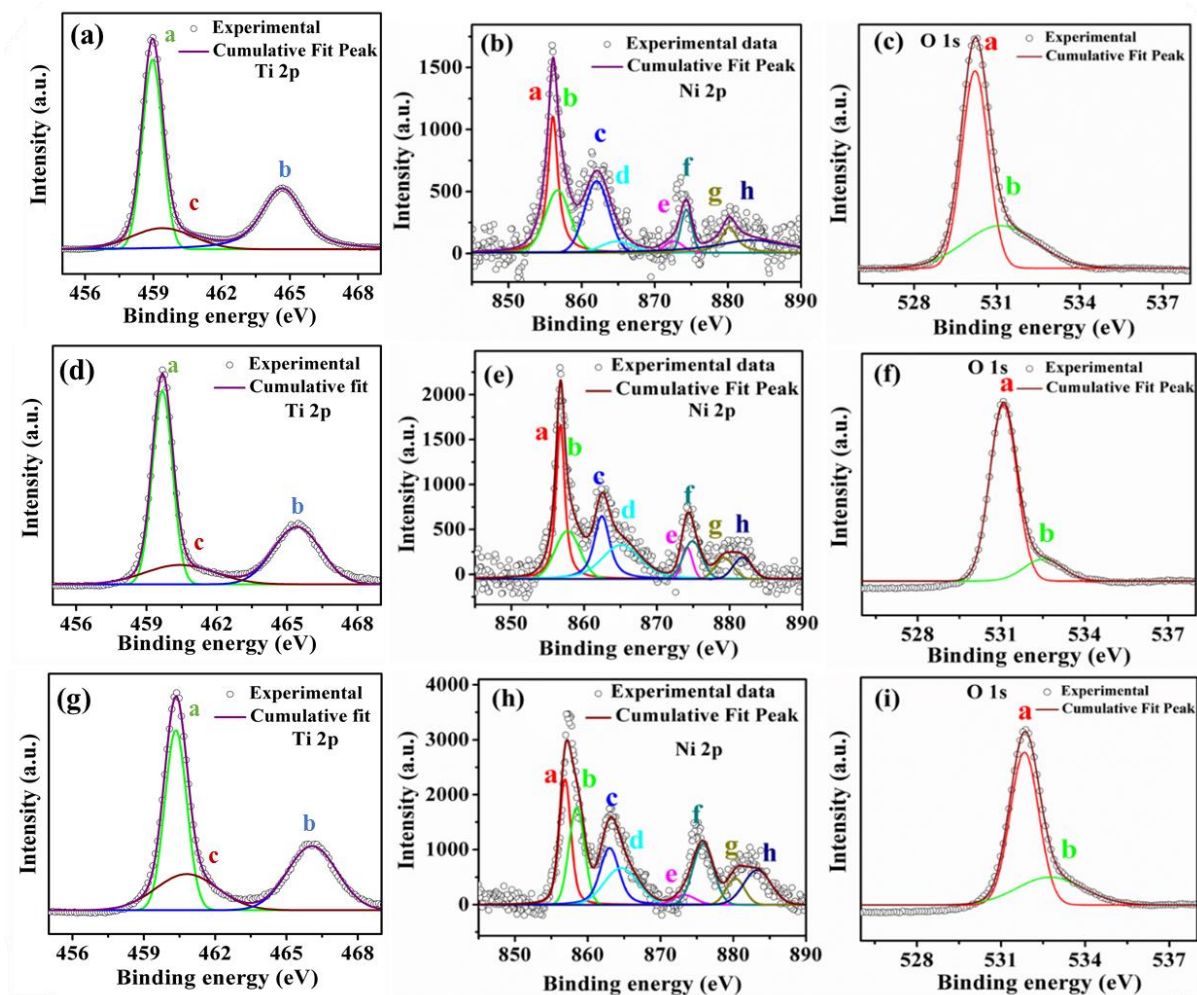


Figure 4.11: XPS spectra of 1NT (a-c), 3NT (d-f) and 5NT (g-i)

Furthermore, the Ti 2p spectrum exhibited two symmetric peaks located at binding energy 458.8 eV and 464.5 eV which arises from spin orbit –splitting and they are assigned to Ti 2p_{3/2} and Ti 2p_{1/2} core levels respectively. Peak (a and b corresponds to Ti⁴⁺ peaks) and peak c corresponds to Ti³⁺. These two peaks are in line with the literature reports for Ti⁴⁺ oxidation states in TiO₂ lattice. The shoulder peak located at binding energy 460.2 eV corresponds to Ti³⁺ in Ti₂O₃ which indicates that both TiO₂ and Ti₂O₃ are present in the Ni_{1-x}O/TiO₂ nanocomposites. Peak area integration revealed that the percentage of Ti³⁺ decreases with the increase in Ni³⁺ in the samples. The observed order of Ti³⁺ is in the order 1NT > 3NT > 5NT > 10NT > 20NT > 50NT as presented in Table 4.3.

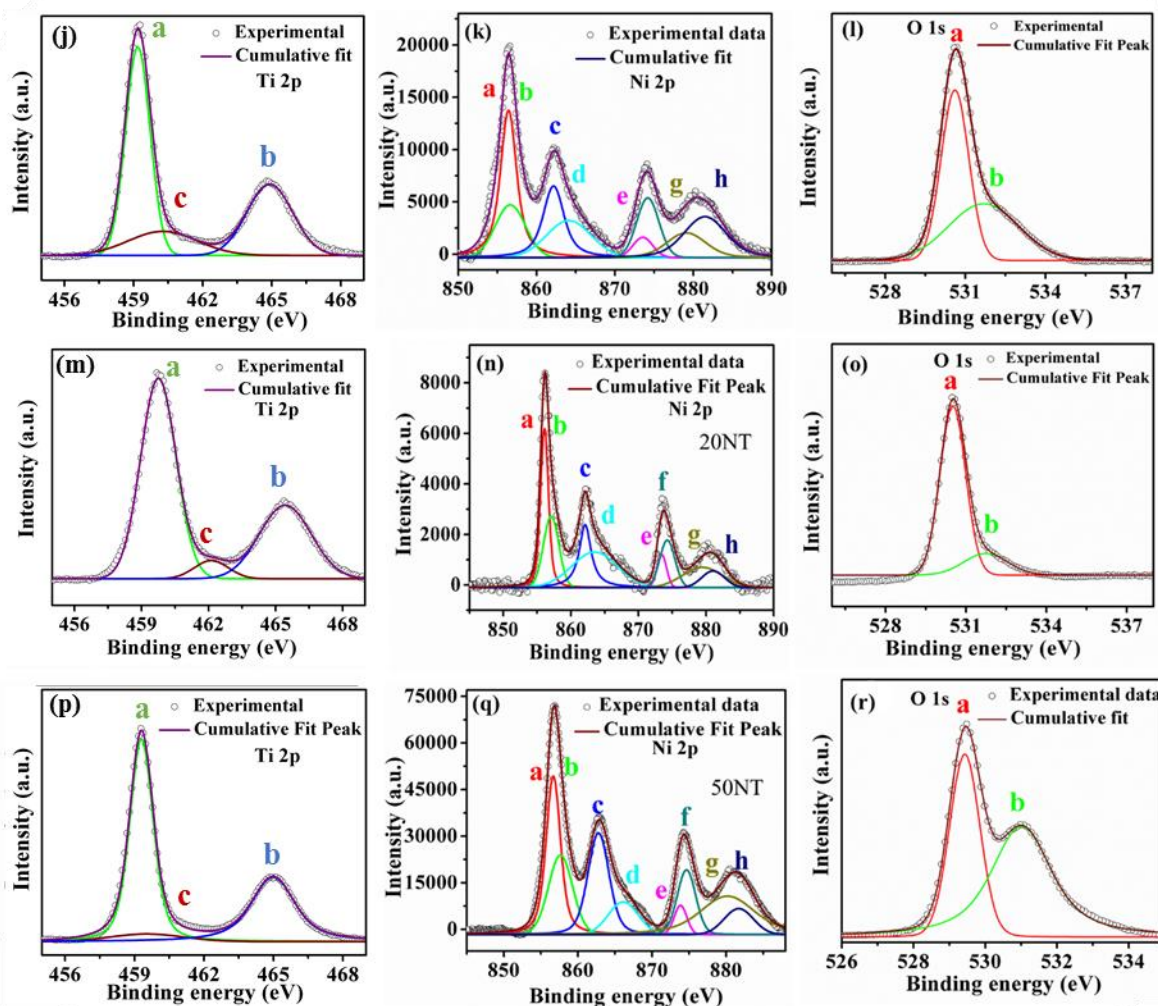


Figure 4.12: XPS spectra of 10NT (j-l), 20NT (m-o) and 50NT (p-r)

Similarly the O (1s) peaks were deconvoluted as presented in Figure 4.10 (c), (f), (i) and Figure 4.11 (l), (o), (r). The O (1s) spectra showed an ideal fit for two peaks located at the binding energy peak observed at 528.9 eV represents the O (1s) core level of O^{2-} anions associated with Ni-O chemical bonding, and the lower intensity at higher binding energy peak (530.7 eV) is representative of the presence of the hydroxyl (-OH) groups and defect sited on the $Ni_{1-x}O/TiO_2$ surface and is thus a measure of oxygen vacancies in $Ni_{1-x}O/TiO_2$. The presence of oxygen vacancies in the $Ni_{1-x}O/TiO_2$ is known to improve the donor density and surface properties of $Ni_{1-x}O/TiO_2$. The synthesized $Ni_{1-x}O/TiO_2$ nanocomposites were tested for adsorptive separation and photocatalytic degradation of Amaranth dye which is presented in the next section.

Materials	Narrow Scan	Species	Ni ³⁺ /Ni ²⁺ (Ni _{1-x} O/TiO ₂ Synthesized)	XPS area integration (%)
1NT	Ni _{2p} O _{1s}	Ni ²⁺	0.82	55.09
		Ni ³⁺		44.91
		Ti ³⁺		40.14
		Ti ⁴⁺		59.86
		Ni/Ti-O		51.6
		Surface hydroxyl		48.4
3NT	Ni _{2p} O _{1s}	Ni ²⁺	0.84	54.77
		Ni ³⁺		45.23
		Ti ³⁺		37.46
		Ti ⁴⁺		62.54
		Ni/Ti-O		50.8
		Surface hydroxyl		49.2
5NT	Ni _{2p} O _{1s}	Ni ²⁺	0.84	54.33
		Ni ³⁺		45.66
		Ti ³⁺		36.72
		Ti ⁴⁺		63.27
		Ni/Ti-O		52.3
		Surface hydroxyl		47.7
10NT	Ni _{2p} O _{1s}	Ni ²⁺	0.86	53.38
		Ni ³⁺		46.62
		Ti ³⁺		31.1
		Ti ⁴⁺		68.9
		Ni/Ti-O		49.5
		Surface hydroxyl		50.5
20NT	Ni _{2p} O _{1s}	Ni ²⁺	0.87	53.08
		Ni ³⁺		46.91
		Ti ³⁺		28.36
		Ti ⁴⁺		71.63
		Ni/Ti-O		51.2
		Surface hydroxyl		48.8
50NT	Ni _{2p} O _{1s}	Ni ²⁺	0.88	52.92
		Ni ³⁺		47.07
		Ti ³⁺		11.43
		Ti ⁴⁺		88.56
		Ni/Ti-O		52.6
		Surface hydroxyl		47.4

Table: 4.3: The percentage of species obtained from the XPS peak area integration of narrow scan spectra of Ni_{1-x}O catalysts.

4.3.2 Adsorptive removal of Amaranth dye using synthesized $\text{Ni}_{1-x}\text{O}/\text{TiO}_2$ catalysts.

The adsorption efficiency of all the synthesized $\text{Ni}_{1-x}\text{O}/\text{TiO}_2$ nanocomposites catalysts (1NT, 3NT, 5NT, 10NT, 20NT and 50NT) were tested for adsorptive removal of Amaranth dye from waste water. The type of interaction between the Amaranth dye (adsorbate) and $\text{Ni}_{1-x}\text{O}/\text{TiO}_2$ catalyst (adsorbent) was investigated using adsorption isotherm and kinetic studies. Figure 4.13 represents adsorption isotherm study for 1NT, 3NT, 5NT, 10NT, 20NT and 50NT. It is a plot of maximum adsorption capacity q_e as a function of adsorbate concentration c_e . It is observed that at lower initial concentration of Amaranth dye there is linear increase in the maximum adsorption capacity which subsequently enters into an equilibrium at higher initial concentration of Amaranth dye.

Among all the adsorption isotherm models fitted, sips adsorption isotherm model gave the experimental data with the R^2 value of > 0.98 . The obtained adsorption capacity for all the synthesized $\text{Ni}_{1-x}\text{O}/\text{TiO}_2$ catalyst was in the order 1NT ($84.5 \text{ mg}\cdot\text{g}^{-1}$) $>$ 3NT ($82.3 \text{ mg}\cdot\text{g}^{-1}$) $>$ 5NT ($81.6 \text{ mg}\cdot\text{g}^{-1}$) $>$ 10 NT ($78.2 \text{ mg}\cdot\text{g}^{-1}$) $>$ 20 NT ($77.6 \text{ mg}\cdot\text{g}^{-1}$) $>$ 50 NT ($61.2 \text{ mg}\cdot\text{g}^{-1}$) (see Table 4.4). It is very clear from the obtained adsorption capacity values that the 1NT, 3NT and 5 NT have relatively maximum adsorption capacity as compared to 10 NT, 20NT and 50NT. It is also observed that the adsorption capacity decreases as we increase the Ni_{1-x}O loading on to TiO_2 . The high adsorption capacity is due to the high surface area of 1NT, 3NT and 5NT. The subsequent decrease in adsorption capacity is due to decrease in surface area as we increase the Ni_{1-x}O content in the nanocomposites. To further understand the rate of uptake of Amaranth dye on $\text{Ni}_{1-x}\text{O}/\text{TiO}_2$ nanocomposites catalysts, adsorption kinetic study was carried out.

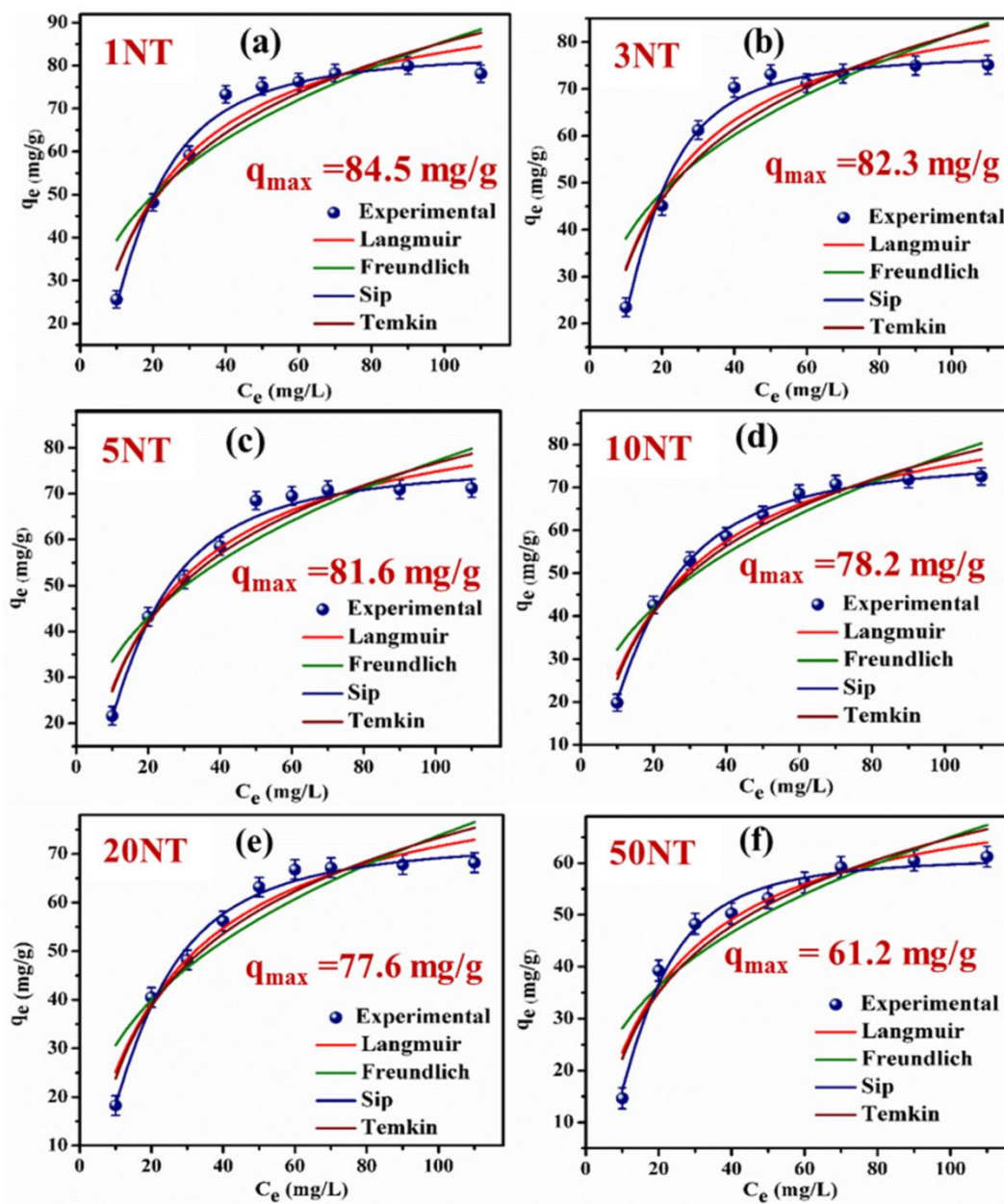


Figure 4.13: (a-f) Adsorption isotherm study of all the synthesized $\text{Ni}_{1-x}\text{O}/\text{TiO}_2$ nanocomposites.

Isotherm models	Parameters	Materials					
		1NT	3NT	5NT	10NT	20NT	50NT
Langmuir	q_m (mg.g ⁻¹)	100.42	94.70	92.40	94.15	89.99	77.29
	K_L (L.mg ⁻¹)	0.048	0.050	0.042	0.039	0.038	0.043
	R_L	0.15- 0.68	0.15- 0.62	0.13- 0.52	0.12- 0.32	0.11- 0.25	0.10- 0.15
	R^2	0.930	0.907	0.945	0.962	0.945	0.921
Freundlich	K_F (L.mg ⁻¹)	18.09	17.87	14.51	13.38	12.71	12.17
	$1/n$ (mg.g ⁻¹)	0.337	0.329	0.362	0.381	0.381	0.363
	R^2	0.79	0.75	0.82	0.85	0.83	0.80
Sips	q_m (mg.g ⁻¹)	84.5	82.3	81.6	78.2	77.6	61.2
	K_S (L.mg ⁻¹)	0.064	0.061	0.056	0.054	0.053	0.050
	m	1.81	2.04	1.66	1.64	1.74	2.04
	R^2	0.981	0.984	0.979	0.994	0.986	0.980
Temkin	β (mg.g ⁻¹)	107.66	114.10	117.75	110.86	115.14	134.28
	K_T (L.mg ⁻¹)	0.409	0.425	0.347	0.310	0.301	0.334
	R^2	0.887	0.857	0.918	0.946	0.926	0.900

Table 4.4: Parameters obtained from different adsorption isotherm study

➤ **Adsorption kinetic studies**

The detailed experimental procedure for the adsorption kinetic study has already been explained in section 4.2.2. The obtained experimental results were fitted using different adsorption kinetic models such as pseudo-first-order (Figure 4.14 (a)), pseudo-second-order (Figure 4.14 (b)), Elovich model (Figure 4.14 (c)) and intraparticle diffusion model (Figure 4.14 (d)).

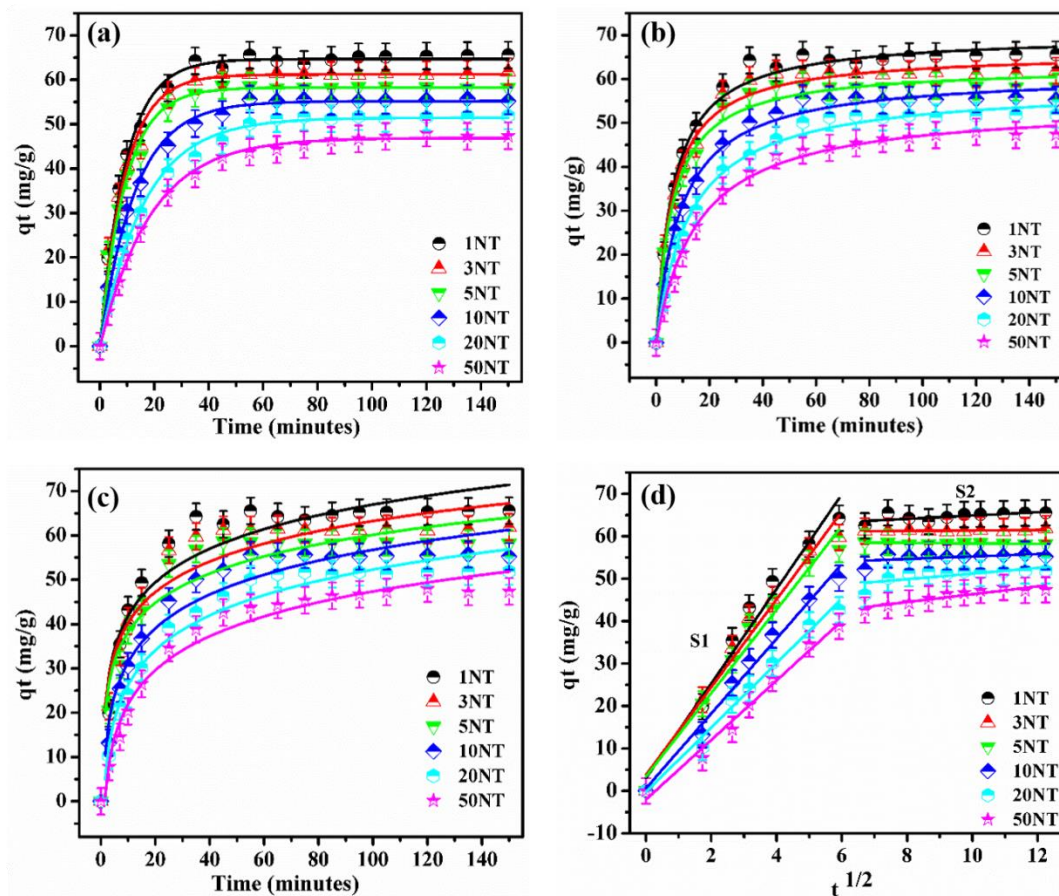


Figure 4.14: (a-d) Adsorption kinetic study of synthesized $\text{Ni}_{1-x}\text{O}/\text{TiO}_2$ nanocomposites

It was observed that for all the synthesized $\text{Ni}_{1-x}\text{O}/\text{TiO}_2$ nanocomposite catalysts, the rate of adsorption was much higher at the beginning of the process which became comparatively slower proceeding towards equilibrium adsorption [9]. Based on the values of the correlation coefficient i.e. R^2 , it was decided that the adsorption of Amaranth dye on all the catalysts followed pseudo-first-order kinetics which suggested that the dye molecules are attached to the adsorption sites through physical adsorption.

The rate constant determined using pseudo-first order rate equations followed the order $1\text{NT} > 3\text{NT} > 5\text{NT} > 10\text{NT} > 20\text{NT} > 50\text{NT}$ (see Table 4.5) which signifies the importance of porous nature of the nanocomposites in case of lower % of Ni_{1-x}O on TiO_2 . To understand the dye diffusion mechanism over nanostructured $\text{Ni}_{1-x}\text{O}/\text{TiO}_2$, the intraparticle diffusion model was studied. The obtained experimental kinetic data was further fitted using the linear form of the intraparticle diffusion model (Figure 4.14(d)) and the corresponding parameters calculated using this model are summarized in Table 4.5. It was observed that the plot

showed multi-linearity indicating the adsorption process taking place in two or more steps. It was observed that the fits of intraparticle diffusion model did not pass through the origin and had slopes which ruled-out the possibilities of the applicability of intraparticle diffusion model alone and predicted that the dye diffusion mechanism was not completely controlled by a single mechanism but it was a combination of two or more mechanisms [10]. The plots of intra-particle diffusion model showed two regions S1 and S2 and the value of the slope of region S1 is quite higher than the slope of region S2, which suggested that the contribution of the step involving the transfer of dye molecules from bulk solution to the internal pores is quite significant. Further, the value of the slope of region S1 followed the order $1NT > 3NT > 5NT > 10NT > 20NT > 50NT$ (Table 4.5) which suggested that the dye uptake increased with the increasing ordered porosity. Furthermore all the synthesized $Ni_{1-x}O/TiO_2$ nanocomposites catalysts were tested for the photocatalytic degradation of Amaranth dye.

4.3.3 Photocatalytic degradation of Amaranth dye using synthesized $Ni_{1-x}O/TiO_2$ catalysts.

➤ Kinetic Studies

The photocatalytic Amaranth dye degradation study was carried out using synthesized $Ni_{1-x}O/TiO_2$ nanocomposites. Initially the optimum concentration of the $Ni_{1-x}O/TiO_2$ nanocomposites was evaluated by varying the amount of the catalyst in the photocatalytic reaction with initial dye concentration of 30 ppm. The amount of $Ni_{1-x}O/TiO_2$ catalyst taken was 25, 50, 75, 100, 125 and 150 mg in each experiment. The maximum photocatalytic degradation activity was obtained for 100 mg 1NT catalyst with degradation efficiency of 95.4 % in 20 minutes. The obtained optimized catalyst concentration was used to carry out the photocatalytic degradation of Amaranth dye using all the synthesized $Ni_{1-x}O/TiO_2$ catalyst. In a typical reaction 100 mg of the catalyst was dispersed in 300 mL, 30 ppm Amaranth dye solution. The solution was further irradiated with 250 W mercury lamp and at regular interval of time aliquots were taken and absorbance was recorded using UV-Vis spectroscopy.

Models Parameters		Materials					
		1NT	3NT	5NT	10NT	20NT	50NT
Pseudo- first-order	k_1 (min^{-1})	0.097	0.087	0.078	0.063	0.049	0.048
	$q_{e,\text{cal}}$ ($\text{mg}\cdot\text{g}^{-1}$)	67.3	65.4	64.4	60.1	55.6	46.9
	$q_{e,\text{exp}}$ ($\text{mg}\cdot\text{g}^{-1}$)	65.2	63.4	62.3	59.4	53.2	44.6
	R^2	0.982	0.982	0.986	0.985	0.982	0.986
Pseudo- second- order	K_2 ($\text{g}\cdot\text{mg}^{-1}\cdot\text{min}^{-1}$)	1.82 $\times 10^{-3}$	1.72 $\times 10^{-3}$	1.51 $\times 10^{-3}$	1.19 $\times 10^{-3}$	0.93 $\times 10^{-3}$	0.88 $\times 10^{-3}$
	$q_{e,\text{cal}}$ ($\text{mg}\cdot\text{g}^{-1}$)	74.02	72.12	71.69	68.26	64.78	55.01
	R^2	0.97	0.96	0.96	0.97	0.97	0.98
Elovich	B ($\text{g}\cdot\text{mg}^{-1}$)	36.53	32.45	25.46	14.61	9.681	7.35
	k_E ($\text{mg}\cdot\text{g}^{-1}\cdot\text{min}$)	0.081	0.082	0.080	0.077	0.077	0.088
	R^2	0.97	0.98	0.98	0.97	0.99	0.97
Intraparticle diffusion	$k_{\text{ID}}(S1)$ ($\text{mg}\cdot\text{g}^{-1}\cdot\text{min}^{-1/2}$)	9.54	8.91	8.52	8.13	7.19	6.43
	$C(S1)$ ($\text{mg}\cdot\text{g}^{-1}$)	6.67	6.58	5.93	2.13	0.62	1.28
	$R^2(S1)$	0.91	0.94	0.94	0.97	0.98	0.97
	$k_{\text{ID}}(S2)$ ($\text{mg}\cdot\text{g}^{-1}\cdot\text{min}^{-1/2}$)	1.12	0.60	0.80	0.68	1.69	0.82
	$C(S2)$ ($\text{mg}\cdot\text{g}^{-1}$)	57.39	60.66	57.1	53.70	38.31	38.05
	$R^2(S2)$	0.95	0.74	0.94	0.54	0.91	0.54

Table 4.5: Parameters obtained from adsorption kinetic analysis.

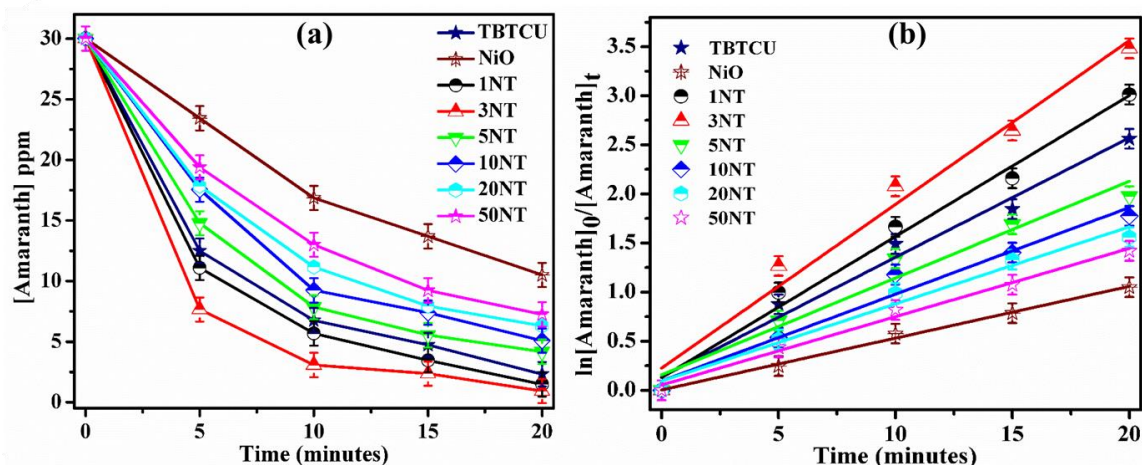


Figure 4.15: (a-b) Photocatalytic degradation study of synthesized $\text{Ni}_{1-x}\text{O}/\text{TiO}_2$ nanocomposites.

The Figure 4.15 (a) and (b) shows the kinetic profiles for the photocatalytic Amaranth dye degradation using all the synthesized $\text{Ni}_{1-x}\text{O}/\text{TiO}_2$ nanocomposite catalyst. The 1% and 3% $\text{Ni}_{1-x}\text{O}/\text{TiO}_2$ exhibited better photocatalytic activity as compared to the synthesized TiO_2 , Ni_{1-x}O , and commercial Degussa P25. The 3% $\text{Ni}_{1-x}\text{O}/\text{TiO}_2$ nanocomposites exhibited the highest Amaranth dye degradation efficiency of 97% with the rate constant of $1.628 \times 10^{-1} \text{ min}^{-1}$ (at $\text{pH} = 5.6$) within 20 minutes of irradiation which was comparatively higher than TBTCU (92.3% degradation efficiency in 20 minutes) with rate constant of $1.218 \times 10^{-1} \text{ min}^{-1}$ at $\text{pH} = 5.6$). It was also observed from the Table 4.6 that the 3NT showed better photocatalytic performance as compared to other transition metal oxide catalyst used for photocatalytic degradation of Amaranth dye. The enhanced photocatalytic activity is attributed to the synergistic effect of high surface area, lower bandgap, and greater charge carrier separation possibly due to the formation of a p-n heterojunction at the interface of mesoporous Ni_{1-x}O and TiO_2 . 3% $\text{Ni}_{1-x}\text{O}/\text{TiO}_2$ nanocomposite is considered to be the optimum photocatalyst with high photocatalytic performance. High photocatalytic activity can be attributed to the probable formed heterojunction between Ni_{1-x}O and TiO_2 . These composite oxides provides easy charge separation and overcomes the major energy loss due to recombination of electrons and hole pairs, thus enhancing the photocatalytic degradation efficiency.

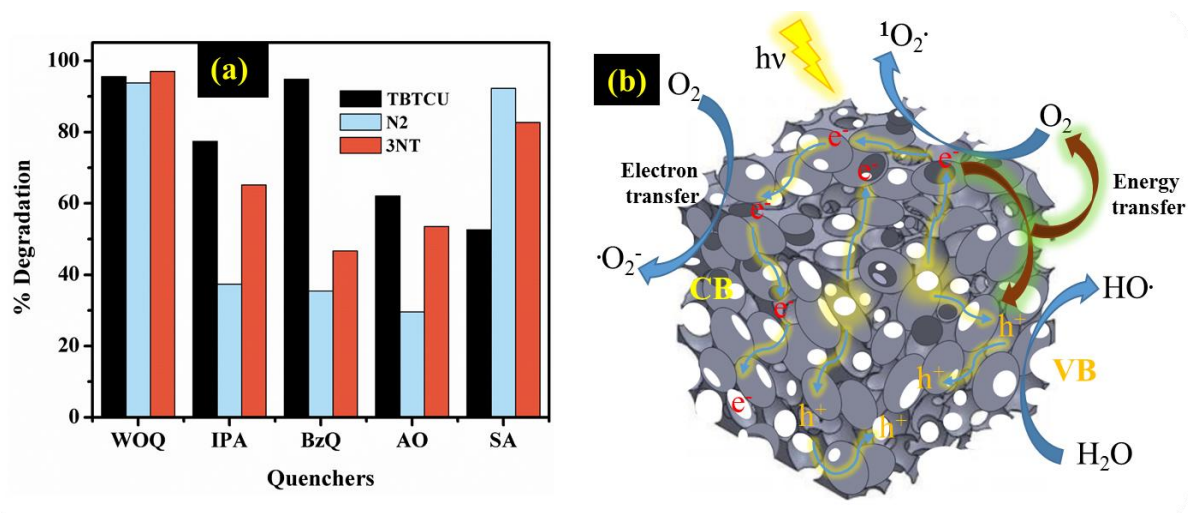


Figure 4.16 (a) Comparative free radical scavenging study of TiO₂, Ni_{1-x}O and Ni_{1-x}O/TiO₂ nanocomposites and (b) Schematic of photocatalytic degradation mechanism using free radical species.

➤ Free radical scavenging studies

It is well established that the photocatalytic action of semiconductor surfaces is initiated by the generation of h^+ , $O_2^{\cdot-}$ and OH radicals upon absorption of UV-Vis radiation. Depending on the nature of the semiconductor surface, the concentration of the active reactive species can vary. Therefore, in order to elucidate the contribution of photocatalytically generated charge carriers and radical species on Amaranth degradation activity of TiO₂, the free radical scavenging experiments were conducted using 0.1 M benzoquinone (BQ), isopropanol (IPA), ammonium oxalate (AO) and NaN₃ which serve as $\cdot O_2$, $\cdot OH$, h^+ and 1O_2 scavengers respectively. It is observed that BQ has little influence on Amaranth degradation, indicating that $\cdot O_2$ does not play any major role in the photocatalytic process. In contrast, the addition of IPA, AO, and NaN₃ lead to a decrease in degradation activity by 19%, 35%, and 45% respectively, suggesting that $\cdot OH$, h^+ , and more importantly the 1O_2 species generated at the TiO₂ surface, play a key role in the photocatalytic degradation process. Therefore, it is proposed that the photo degradation mechanism is initiated by the illumination of TiO₂ surface which produces holes in valence band which interacts with adsorbed water to form highly reactive $\cdot OH$ radicals [18–20]. Apparently, complementary to the electron-hole recombination process, energy transfer process from TiO₂ to adsorbed O₂ also takes place

Catalyst	Initial dye concentration	Light source	Reaction time (min)	% Degradation
N,S-doped [11] titania	3.90×10^{-5} M	200 W Tungsten lamp	90	59.3
N-WO ₃ [12]	25 mg.L ⁻¹	160 W Visible and UVA light	120	100
TiO ₂ [13]	84 μ mol.L ⁻¹	125 W lamp	60	75
TiO ₂ [14]	30 ppm	Solar light	90	99.1
N-ZrO ₂ [15]	10 ppm	Fluorescent lamp (visible) 24 W and Low pressure Hg lamp(UV) of 15 W	120 240	26.4 84.5
ZnO [16]	20 ppm	250 W Hg medium pressure lamp	120	100
ZnO [17]	4.4×10^{-5} M	200 W Tungsten lamp	300	92.5
TiO ₂ (TBTCU) [This work]	30 ppm	250 W Hg Medium pressure Lamp	20	92.3
Ni _{1-x} O (N2) [This work]	30 ppm	250 W Hg Medium pressure Lamp	70	93.8
Ni _{1-x} O/TiO ₂ (3NT) [This work]	30 ppm	250 W Hg Medium pressure Lamp	20	97.0

Table 4.6: Comparative analysis of Amaranth dye degradation efficiency of TBTCU, Ni_{1-x}O and Ni_{1-x}O/TiO₂ with that of literature reported catalysts.

which results in the formation of ¹O₂ species [21,22]. The negatively charged Amaranth dye (RSO₃⁻) adsorbed on the TiO₂ (101) surface, is then oxidized by ·OH, h⁺, ¹O₂ ·-O₂ via radical cleavage of RSO₃⁻ to form several intermediates such as sodium-3-hydroxynaphthalene-2, 7-disulphonate, 3-hydroxynaphthalene, sodium-4-aminonaphthalenesulphonate, and sodium-4-amino benzenesulphonate. These intermediates further convert to relatively stable phenol and malic acid before ultimately converting to CO₂ and H₂O.

Similarly, free radical scavenging study was carried out using Ni_{1-x}O (N2) catalyst. The scavengers such as 10 mM benzoquinone (BQ), tertiary Butanol (t-BuOH), ammonium

oxalate (AO) and sodium azide (NaN_3) were employed which serve as O_2^- , $\cdot\text{OH}$, h^+ and $^1\text{O}_2$ scavengers respectively for Ni_{1-x}O (N2) catalyst. It was observed that the addition of sodium azide had a negligible influence on Amaranth degradation activity, indicating that $^1\text{O}_2$ species does not play any major role in the photocatalytic degradation process over Ni_{1-x}O nanosponge unlike in the case of TiO_2 [23]. Similarly, the addition of t-butanol leads to a moderate decrease in the activity which indicates the appreciable contribution of $\cdot\text{OH}$ radical in the photocatalytic degradation process. However, the addition of ammonium oxalate leads to a significant decrease in the activity of N2 (66.66 %). Similarly, the addition of benzoquinone also leads to decrease in the activity of N3 by (60.6 %), confirming that both h^+ and $\cdot\text{O}_2^-$ radical species play a major role in the photocatalytic degradation of Amaranth dye over synthesized Ni_{1-x}O nanostructures. This observation is in good agreement with Harraz et al. [24] and Ramesh et al.[25]

Furthermore, photodegradation activity of $\text{Ni}_{1-x}\text{O}/\text{TiO}_2$ nanocomposite catalyst was evaluated through free radical scavenging experiment so as to identify the active radical species. In a typical experiment, 0.01 M ammonium oxalate (AO): h^+ scavenger, Benzoquinone, sodium azide and isopropyl alcohol were separately added to Amaranth dye solution. A noticeable decrease in amaranth dye photodegradation was detected in the presence of ammonium oxalate (53.5 %) and with benzoquinone (46.7 %) which suggest that h^+ and O_2^- are the major active species contributing in the photocatalytic process. The minor contributions from $\cdot\text{OH}$ and $^1\text{O}_2$ were also observed.

From the above results, a photocatalytic reaction mechanism is proposed. The surface modification of mesoporous TiO_2 with Ni_{1-x}O nanoparticles causes the enhancement of light absorption. As reported by Lin et al. [26], the combination of the Ni^{2+} with Ti^{4+} at the p-n junction induces an electric field at the contact potential. When UV radiation falls on $\text{TiO}_2/\text{Ni}_{1-x}\text{O}$ heterojunction, it excites electrons from valence band of both the oxides to their respective conduction bands. Under the influence of the internal field, the electrons from CB of Ni_{1-x}O migrate towards the CB of TiO_2 leading to higher population of electrons in TiO_2 . Subsequently, the h^+ from V.B of TiO_2 are pulled towards the V.B of Ni_{1-x}O at the contact surface, resulting in increased population of h^+ in Ni_{1-x}O . This results in effective separation of e^- and h^+ as reported by Lin et al. [26] A similar effect could occur in our nanocomposites. These surface electrons then result in generation of O_2^- radicals and h^+ which together

promote the photocatalytic Amaranth dye degradation efficiency of the $\text{Ni}_{1-x}\text{O}/\text{TiO}_2$ nanocomposite catalyst.

➤ **Catalyst regeneration studies**

The $\text{Ni}_{1-x}\text{O}/\text{TiO}_2$ (3NT) catalyst was subjected to regeneration studies under optimized conditions for five consecutive cycles. After each reaction the dye adsorbed on the catalyst was desorbed by boiling it in a hot water for one hour with continuous stirring. Catalyst was reactivated at 200 °C, and then the photocatalytic degradation was carried out. The obtained decrease in the photocatalytic degradation activity is from 97 % to 92.4% for 3NT confirming excellent stability of the composite catalyst

➤ **Identification of Amaranth dye degradation products**

i) *Percentage purity and impurity profiling of Amaranth dye*

The LC-ESI-MS analysis of an Amaranth stock solution showed a major peak on the chromatogram due to Amaranth dye with minor unresolved impurity bands which were below the mass detection limit (as seen from Figure 4.17). Hence, further analyses were performed with an ultra-performance LC-ESI-MS under the positive scan mode (as seen from Figure 4.18). Two impurity peaks at retention times of 0.18 min (11%) and 1.27 (7%) corresponding to m/z peaks of 144.2 and 301.3, respectively, were detected (see Figure 4.19 and Figure 4.20). The former impurity was identified to be α -naphthylamine; however, no particular structure could be assigned to the second impurity.

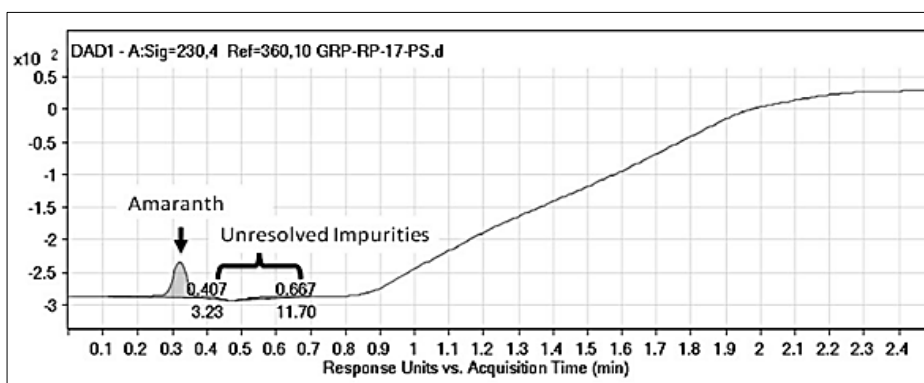


Figure 4.17: Liquid chromatogram of the Amaranth dye

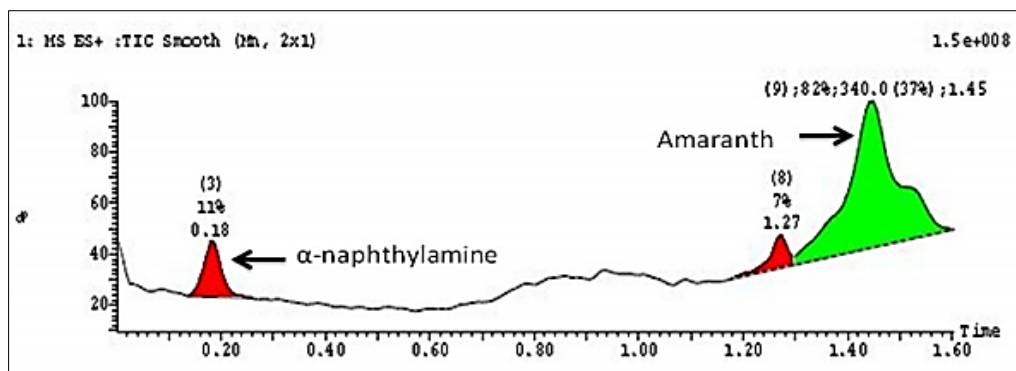


Figure 4.18: Ultra performance chromatogram of the Amaranth dye.

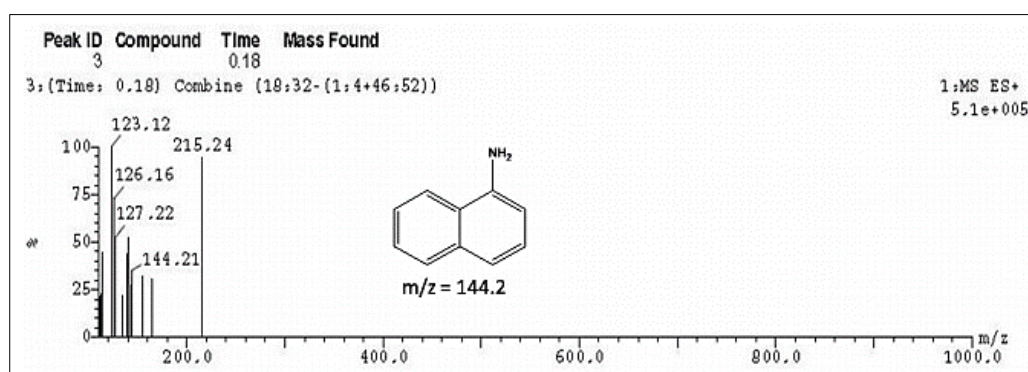


Figure 4.19: Impurity peak corresponding to m/z value 144

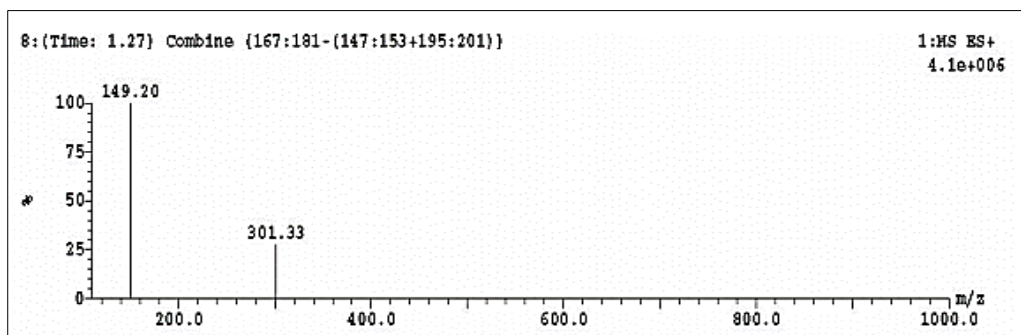


Figure 4.20: Impurity peak corresponding to m/z value 301.33

ii) Amaranth degradation products catalyzed by TiO₂ photocatalyst

The following products of Amaranth degradation over TiO₂ surface (TBTCU) were identified using LC-ESI-MS. These products are as follows: Sodium 4-aminonaphthalene-2,7-disulfonate, 5,6,7-trihydroxynaphthalene-2-sulfonic acid; Sodium 3,4-dihydroxynaphthalene-2,7-disulfonate; 2- 1-Aminonaphthalene-2-ol, Naphthalene-1,2-diol;

Sodium 4-aminonaphthalene 1-sulfonate; Sodium 4-aminobenzenesulfonate, phenol, 2-Hydroxymalonic acid and 2-Hydroxysuccinic acid. A typical mass spectrum of sodium 4-aminobenzenesulfonate is shown in Figure 4.21 (more details are given in appendix I)

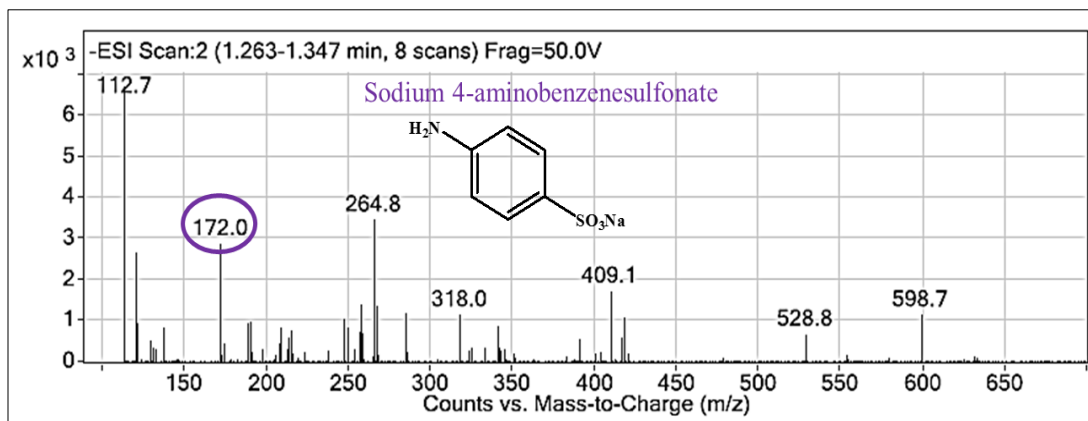


Figure 4.21: Sodium 4-aminobenzenesulfonate corresponding to m/z value 172.

iii) Amaranth degradation products catalyzed by $Ni_{1-x}O$ photocatalyst

The Amaranth degradation products obtained using $Ni_{1-x}O$ (N2) as catalyst were identified using LC-ESI-MS. These are as follows: Sodium 3, 4-dihydroxynaphthalene-2, 7-disulfonate; Sodium 3,4-dioxo-3,4-dihydronaphthalene-2,7-disulfonate; 6,7-dihydroxynaphthalene-2-sulfonic acid; phenol; 2-Hydroxymalonic acid and 2-Hydroxysuccinic acid. A typical mass spectrum of 5, 6, 7-trihydroxynaphthalene-2-sulfonic acid is shown in Figure 4.22 (more details are given in appendix I).

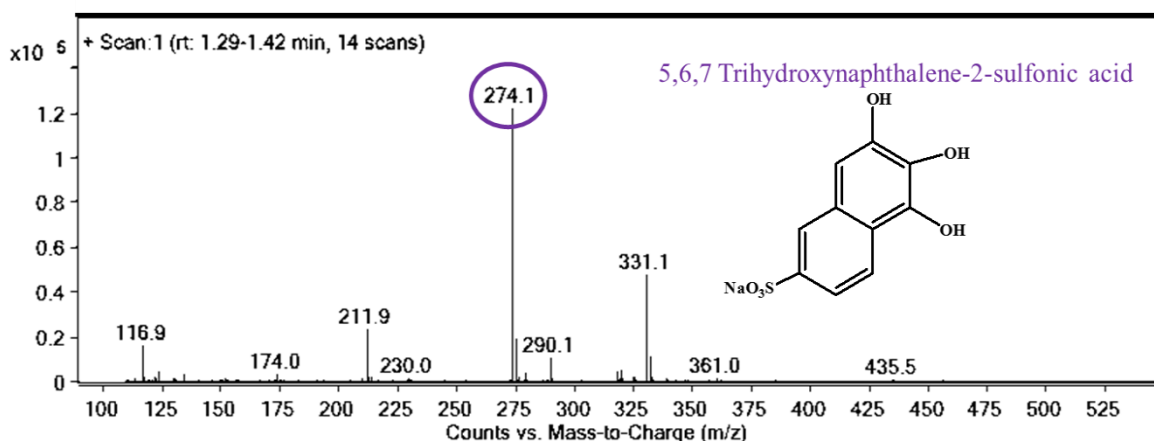


Figure 4.22: 5, 6, 7 Trihydroxynaphthalene-2-sulfonic acid corresponding to m/z value 274.

iv) Amaranth degradation products catalyzed by Ni_{1-x}O/TiO₂ photocatalyst

The Amaranth degradation products obtained using Ni_{1-x}O/TiO₂ (3NT) as catalyst were identified using LC-ESI-MS as follows: Sodium 3,4-dihydroxynaphthalene-2,7-disulfonate; 5,6,7 Trihydroxynaphthalene-2-sulfonic acid; Phenol A typical mass spectrum of 2-hydroxymalonic acid is shown in Figure 4.23 (more details are given in appendix I).

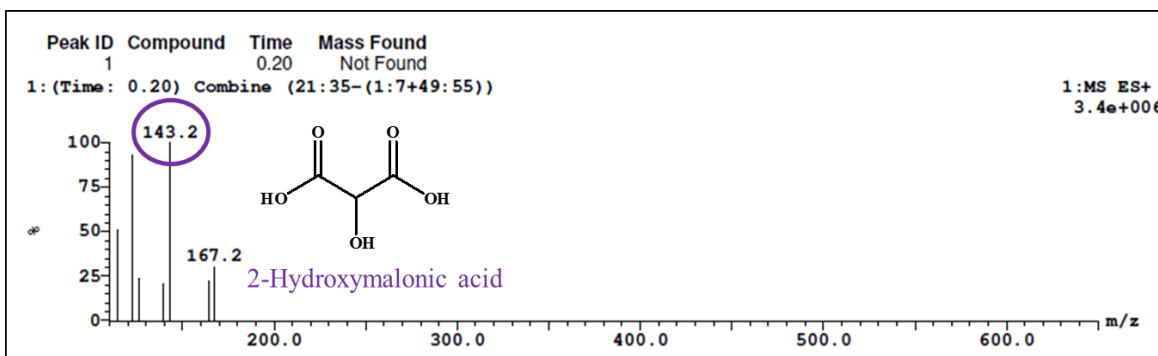


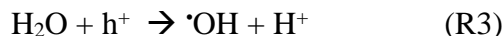
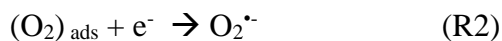
Figure 4.23: 2-Hydroxymalonic acid corresponding to m/z value 143.

Based on the intermediates and products detected via LC-ESI-MS, the following global mechanism of photocatalytic degradation is proposed:

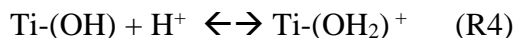
➤ **Plausible degradation mechanism**



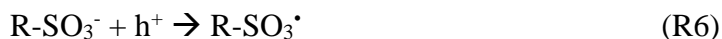
(Effective separation of charge carriers due to p-n junction)



According to the studies by Karkmaz et al. [13] under acidic conditions, the surface of TiO₂ gets positively charged.



Adsorption of Amaranth on the surface of Ti-(OH₂)⁺ occurs via interaction of the sulphonyl group at the ortho position with respect to the OH group on the naphthalene ring. The formation of ·OH radicals, O₂^{·-} radical anion and holes (h⁺) on the catalyst surface is believed to initiate the radical degradation of Amaranth according to the following reactions:



where R-SO_3^- represents Amaranth dye. The radical reactions of $\text{R}\cdot$ initiates the dye degradation process via ring rupture, and leads to the formation of phenol and organic acids which ultimately at long reaction times would transform into gaseous CO_2 along with mineralization of the azo group to gaseous N_2 . Steter et al. [16] performed sono-electrochemical degradation of Amaranth dye and product identification by LC-MS and suggested that the Amaranth degradation occurs by cleavage of the $-\text{N}=\text{N}-$ bond (pathway A and B in Figure 4.17) leading to sodium 3-hydroxy-4-imino- 4,4a dihydronaphthalene-2,7-disulfonate (A) and sodium-4-amino naphthalene-1-sulphonate (B).

In the present study, the qualitative identification of primary intermediates and products using the LC-ESI-MS technique was performed. The detected m/z values and their comparison with the mechanisms proposed by Steter et al. and Karkmaz et al. confirmed that the degradation mechanism is initiated by the $\text{N}=\text{N}$ bond cleavage leading to intermediates A and B, as shown in Figure 4.17.

The intermediate A1 (Sodium 4-aminonathalene-2,7-disulfonate with $m/z = 370$) can be formed from the intermediate A as reported by Stater et al. [16]. A1 subsequently can undergo oxidative loss of NH_3 leading to the formation of tautomer A2 (Sodium 3, 4-dihydroxynaphthalene-2,7-disulfonate, $m/z = 406$). A2 can also be formed directly from compound A, however, since A1 is detected in LC-ESI-MS while A is not, the former pathway for formation of A2 is considered. Subsequent oxidation of A2 gives A3 (5,6,7-Trihydroxynaphthalene-2-sulfonic acid, detected at m/z 274) which loses an $\cdot\text{OH}$ group to form A4 (6,7-dihydroxynaphthalene-2-sulfonic acid, $m/z = 279$).

It is important to note here that, the compound A' (1-aminonaphthalene-2-ol, detected at $m/z = 198$) could have formed from compound A, which subsequently undergoes oxidative loss of NH_3 to give tautomer A'1 (Naphthalene-1, 2-diol, $m/z = 176$). Both A'1 and A4 would then lead to the formation of products P1 (2-hydroxysuccinic acid, $m/z = 152$) and P2 (2-hydroxymalonic acid, $m/z = 143$) through intermediates such as Catechol and 2-hydroxybenzoic acid via ring rupture mechanism. Similarly, the formation of product P3

4.4 Conclusion:

$\text{Ni}_{1-x}\text{O}/\text{TiO}_2$ nanocomposites were synthesized using $\text{Ti}(\text{OH})_4$ /urea/butanetetracarboxylic acid/nickel p-nitrobenzoate hybrid gel by reflux assisted sol-gel method. The effect of Ni_{1-x}O loading on morphology, surface area, and non-stoichiometry of $\text{Ni}_{1-x}\text{O}/\text{TiO}_2$ nanocomposites was investigated. It was observed that as we increase the Ni_{1-x}O loading on TiO_2 (0-50 wt %) the surface area tends to decrease from $231 \text{ m}^2.\text{g}^{-1}$ to $90 \text{ m}^2.\text{g}^{-1}$. Similarly, the pore size and pore volume also decreases with the increase the Ni_{1-x}O loading. The $\text{Ni}_{1-x}\text{O}/\text{TiO}_2$ nanocomposites exhibited porous morphology for lower % loading of Ni_{1-x}O while agglomeration and sintering of the particles is observed with the increase in % Ni_{1-x}O loading. Low resolution TEM analysis revealed smaller particle size distribution for lower % loading of Ni_{1-x}O and large particle size for higher % Ni_{1-x}O loading which is in good agreement with SEM and BET analysis. Further, the non-stoichiometric analysis of all the synthesized $\text{Ni}_{1-x}\text{O}/\text{TiO}_2$ nanocomposites exhibited significant change in $\text{Ni}^{3+}/\text{Ni}^{2+}$ ratio as compared to pure Ni_{1-x}O . Amaranth dye adsorption on all the synthesized TiO_2 exhibited Sips adsorption model with maximum adsorption capacity of $84.5 \text{ mg}.\text{g}^{-1}$ in case of 1NT was observed. This was attributed to its high surface area. Furthermore, 3NT exhibited the highest Amaranth dye photodegradation efficiency of 97 % (in 20 minutes) with a rate constant of $1.218 \times 10^{-1} \text{ min}^{-1}$, which is the best photocatalytic Amaranth degradation performance reported till date in the literature. Therefore, the third objective of designing $\text{Ni}_{1-x}\text{O}/\text{TiO}_2$ nanocomposite for enhanced photocatalytic degradation of Amaranth dye was successfully achieved.

4.6 References:

- [1] N. Kumar, H. Mittal, S.M. Alhassan, S.S. Ray, Bionanocomposite Hydrogel for the Adsorption of Dye and Reusability of Generated Waste for the Photodegradation of Ciprofloxacin: A Demonstration of the Circularity Concept for Water Purification, *ACS Sustain. Chem. Eng.* 6 (2018) 17011–17025..
- [2] R. Baccar, P. Blánquez, J. Bouzid, M. Feki, H. Attiya, M. Sarrà, Modeling of adsorption isotherms and kinetics of a tannery dye onto an activated carbon prepared from an agricultural by-product, *Fuel Process. Technol.* 106 (2013) 408–415.
- [3] N. Ayawei, A.N. Ebelegi, D. Wankasi, Modelling and Interpretation of Adsorption Isotherms, *J. Chem.* 2017 (2017) 1–11.
- [4] M.A. Al-Ghouti, D.A. Da'ana, Guidelines for the use and interpretation of adsorption isotherm models: A review, *J. Hazard. Mater.* 393 (2020) 122383.
- [5] B.M. Marwa, S. Bruno, B. Mongi, F. Tran Van, B.L. Abdelmottaleb, Modeling of adsorption isotherms of dye N719 on titanium oxide using the grand canonical ensemble in statistical physics for dye sensitized solar cells, *Sol. Energy.* 135 (2016) 177–187.
- [6] K. Sakamoto, F. Hayashi, K. Sato, M. Hirano, N. Ohtsu, XPS spectral analysis for a multiple oxide comprising NiO, TiO₂, and NiTiO₃, *Appl. Surf. Sci.* 526 (2020).
- [7] E. Arciga-Duran, Y. Meas, J.J. Pérez-Bueno, J.C. Ballesteros, G. Trejo, Effect of oxygen vacancies in electrodeposited NiO towards the oxygen evolution reaction: Role of Ni-Glycine complexes, *Electrochim. Acta.* 268 (2018) 49–58.
- [8] P. Dubey, N. Kaurav, R.S. Devan, G.S. Okram, Y.K. Kuo, The effect of stoichiometry on the structural, thermal and electronic properties of thermally decomposed nickel oxide, *RSC Adv.* 8 (2018) 5882–5890.
- [9] S.J. Allen, G. McKay, J.F. Porter, Adsorption isotherm models for basic dye adsorption by peat in single and binary component systems, *J. Colloid Interface Sci.* 280 (2004) 322–333.
- [10] H. Mittal, P.P. Morajkar, A. Al Alili, S.M. Alhassan, In-Situ Synthesis of ZnO

- Nanoparticles using Gum Arabic Based Hydrogels as a Self-template for Effective Malachite Green Dye Adsorption, *J. Polym. Environ.* (2020).
- [11] A.K. Jain, S. Sharma, R. Ameta, Enhanced photocatalytic activity of N, S-doped titania for degradation of amaranth, *Merit Res. J. Environ. Sci. Toxicol.* 3 (2015) 25–30.
- [12] H. Sudrajat, S. Babel, Rapid photocatalytic degradation of the recalcitrant dye amaranth by highly active N-WO₃, *Environ. Chem. Lett.* 14 (2016) 243–249.
- [13] M. Karkmaz, E. Puzenat, C. Guillard, J.M. Herrmann, Photocatalytic degradation of the alimentary azo dye amaranth: Mineralization of the azo group to nitrogen, *Appl. Catal. B Environ.* 51 (2004) 183–194.
- [14] A.P. Naik, A. V. Salkar, M.S. Majik, P.P. Morajkar, Enhanced photocatalytic degradation of Amaranth dye on mesoporous anatase TiO₂: Evidence of C-N, N=N bond cleavage and identification of new intermediates, *Photochem. Photobiol. Sci.* 16 (2017) 1126–1138.
- [15] H. Sudrajat, S. Babel, H. Sakai, S. Takizawa, Rapid enhanced photocatalytic degradation of dyes using novel N-doped ZrO₂, *J. Environ. Manage.* 165 (2016) 224–234.
- [16] N. Divya, A. Bansal, A.K. Jana, Photocatalytic activity of transition metal ion doped titania for Amaranth dye degradation, *Mater. Sci. Forum.* 712 (2012) 85–104.
- [17] R. Ameta, N. Jain, S. Kothari, Photocatalytic bleaching of amaranth dye over ZnO powder, *Indian J. Chem. Technol.* 11 (2004) 423–426.
- [18] G. Dong, Y. Wang, H. Lei, G. Tian, S. Qi, D. Wu, Hierarchical mesoporous titania nanoshell encapsulated on polyimide nanofiber as flexible, highly reactive, energy saving and recyclable photocatalyst for water purification, *J. Clean. Prod.* 253 (2020) 120021.
- [19] G. Vincent, A. Aluculesei, A. Parker, C. Fittschen, O. Zahraa, P.M. Marquaire, Direct detection of OH radicals and indirect detection of H₂O₂ molecules in the gas phase near a TiO₂ photocatalyst using LIF, *J. Phys. Chem. C.* 112 (2008) 9115–9119.

- [20] J. Yi, C. Bahrini, C. Schoemaeker, C. Fittschen, W. Choi, Photocatalytic decomposition of H_2O_2 on different TiO_2 surfaces along with the concurrent generation of HO_2 radicals monitored using cavity ring down spectroscopy, *J. Phys. Chem. C*. 116 (2012) 10090–10097.
- [21] T. Daimon, Y. Nosaka, Formation and behavior of singlet molecular oxygen in TiO_2 photocatalysis studied by detection of near-infrared phosphorescence, *J. Phys. Chem. C*. 111 (2007) 4420–4424.
- [22] A. Jańczyk, E. Krakowska, G. Stochel, W. Macyk, Singlet oxygen photogeneration at surface modified titanium dioxide, *J. Am. Chem. Soc.* 128 (2006) 15574–15575.
- [23] A.P. Naik, H. Mittal, V.S. Wadi, L. Sane, A. Raj, S.M. Alhassan, A. Al Alili, S. V. Bhosale, P.P. Morajkar, Super porous TiO_2 photocatalyst: Tailoring the agglomerate porosity into robust structural mesoporosity with enhanced surface area for efficient remediation of azo dye polluted waste water, *J. Environ. Manage.* 258 (2020).
- [24] F.A. Harraz, R.M. Mohamed, A. Shawky, I.A. Ibrahim, Composition and phase control of Ni/NiO nanoparticles for photocatalytic degradation of EDTA, *J. Alloys Compd.* 508 (2010) 133–140.
- [25] M. Ramesh, M.P.C. Rao, S. Anandan, H. Nagaraja, Adsorption and photocatalytic properties of NiO nanoparticles synthesized via a thermal decomposition process, *J. Mater. Res.* 33 (2018) 601–610.
- [26] J. Lin, J. Shen, R. Wang, J. Cui, W. Zhou, P. Hu, D. Liu, H. Liu, J. Wang, R.I. Boughton, Y. Yue, Nano-p-n junctions on surface-coarsened TiO_2 nanobelts with enhanced photocatalytic activity, *J. Mater. Chem.* 21 (2011) 5106–5113.

CHAPTER V:
SUPERCAPACITOR
APPLICATIONS OF Ni_{1-x}O, TiO₂
AND Ni_{1-x}O/TiO₂

5.1 PROLOGUE

All the synthesized Ni_{1-x}O catalysts, TiO_2 (TBTCU) and $\text{Ni}_{1-x}\text{O}/\text{TiO}_2$ catalyst have been tested for their supercapacitor application. The chemicals used and the experimental procedure is explained in section 5.2 and 5.3. The effect of ligation of the structure directing agent on the supercapacitor efficiency of Ni_{1-x}O catalyst and $\text{Ni}_{1-x}\text{O}/\text{TiO}_2$ have been discussed in detail in section 5.4, followed by the conclusion in section 5.5 and references in section 5.6.

5.2 CHEMICALS USED

Potassium hydroxide (99.9%), Acetylene black (99.9%), Polytetrafluoroethylene (99.9%), N-methylpyrrolidone (99.9%). All chemicals purchased were of AR grade and used without any further purifications.

5.3 EXPERIMENTAL PROCEDURES:

The electrochemical analysis were carried out using standard three-electrode system in 6M KOH using CHI 660 E series potentiostate with Ag/AgCl as reference electrode and platinum plate as counter electrode. The working electrode was prepared by mixing active material, acetylene black and PTFE in a mass ratio of 80:15:5. The mixture was then homogenized using N-methylpyrrolidone as a solvent which was sonicated for 30 minutes. The slurry was then pressed on Ni foam ($1 \times 1 \text{ cm}^2$) and dried at 90°C for complete removal of solvent. The mass of active material was 2 mg. The CV measurements were taken in the potential range of -0.2 to 0.4 V at a scan rate of $5\text{-}200 \text{ mV}\cdot\text{s}^{-1}$. The galvanostatic charge/discharge curves were recorded for the same electrode system at variable current densities of $0.5\text{-}9 \text{ A}\cdot\text{g}^{-1}$ in the potential range of -0.2 to 0.4 V in 6 M KOH. Following this, cyclic stability analysis was carried out at a current density of $6 \text{ A}\cdot\text{g}^{-1}$ in 6 M KOH solution for 10000 cycles.

5.4 RESULT AND DISCUSSION

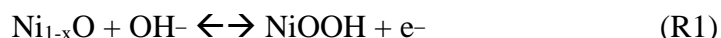
5.4.1 Effect of ligation on supercapacitor behavior of Ni_{1-x}O catalysts.

The synthesized Ni_{1-x}O with different ligands on structural and morphological properties of Ni_{1-x}O has been discussed earlier in detail in Chapter 3. The obtained changes in structural

and morphological properties on supercapacitor application have been studied in detail in this chapter.

➤ **Cyclic voltammetry study**

The Ni_{1-x}O/acetylene black/PTFE supported on nickel foam electrodes were fabricated (used as working electrode), and their electrochemical performances were characterized by cyclic voltammetry (CV) and galvanostatic charge/discharge (GCD) measurements. Figure 5.1 shows the CV curve of the synthesized Ni_{1-x}O in the potential window of -0.2 to 0.4 V (vs Ag/AgCl) at various scan rates from 5 to 200 mV.s⁻¹ in 6.0 M KOH. A pair of strong redox current peaks are observed from the CV curves at 0.19 V and 0.33 V, which corresponds to the faradic oxidation/reduction reactions and also indicates the pseudocapacitive behavior of the Ni_{1-x}O /acetylene black/PTFE composites. According to the redox mechanism, the faradic reaction can be described by reaction (R1).[1,2]



Furthermore, as the peak intensity increases with the increasing scan rate, the CV results continue to display an obvious pair of redox peaks, suggesting good reversibility of the involved faradic reactions. Moreover, along with the increase in scan rate from 5 to 200 mV.s⁻¹, the anodic peaks shift positively, while the cathodic peaks shift negatively, which are attributed to the polarization of the electrodes at higher scan rates. In addition, as shown in Figure 5.1 the Ni_{1-x}O/acetylene black/PTFE prepared from N2 exhibits much larger area under the CV curve in comparison with N1, N3, N4, PN and NU indicating the capacitive behavior to be in the order of N2 > N1 > N3 > N4 > PN > NU. The greater integral area of N2 indicates that the mesoporous nature of the nanosponge morphology enables higher electrochemical activity by providing an improved contact at the electrode/electrolyte interface, which can be associated with a richer faradaic reaction; and this observation is similar to the literature reports for porous Ni_{1-x}O electrodes.[3–5]

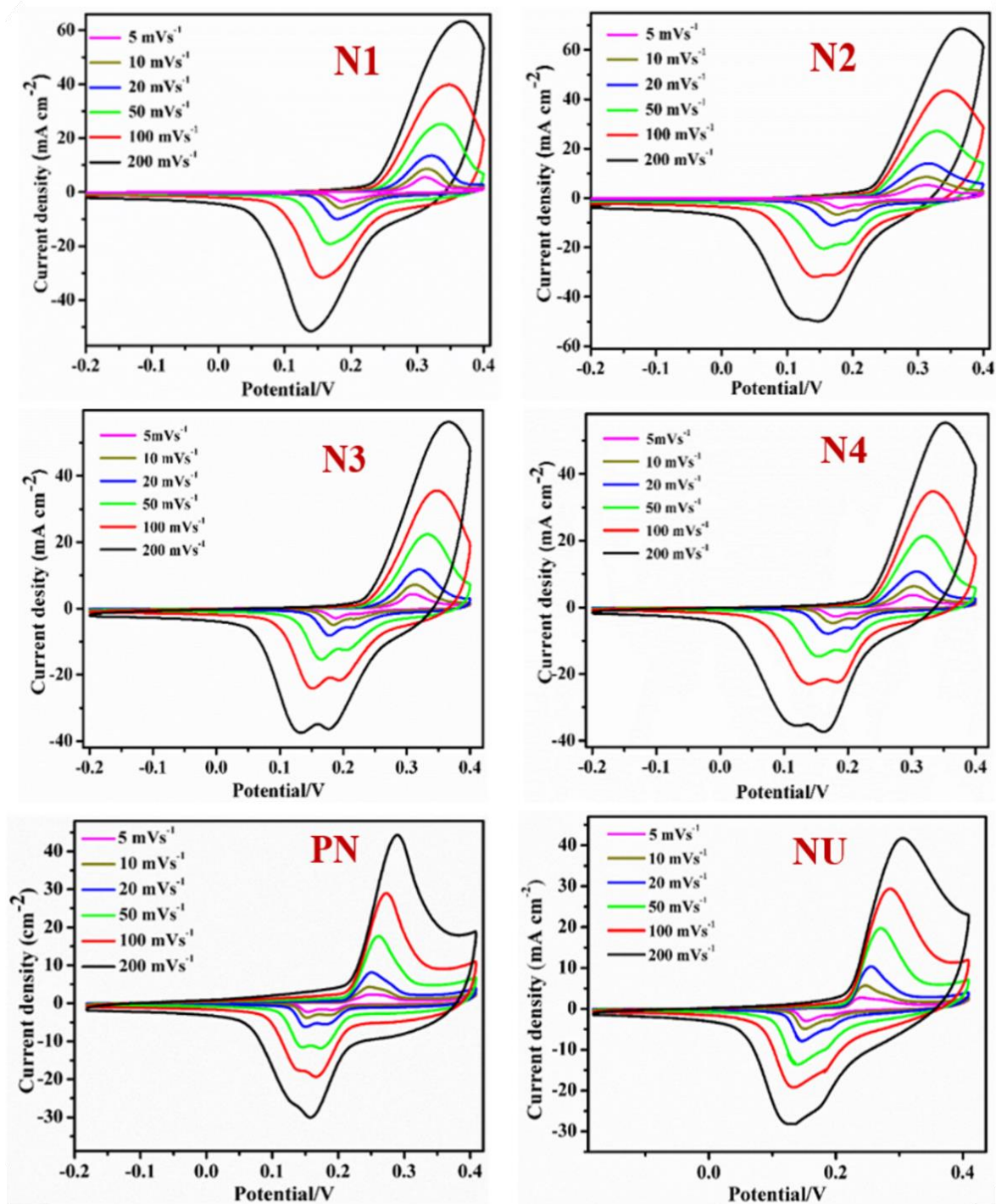


Figure 5.1 Cyclic voltammogram of the Ni_{1-x}O samples N1, N2, N3, N4, PN and NU

Catalyst	Surface area (m ² .g ⁻¹)	Specific capacitance (F.g ⁻¹) at current density 1 A.g ⁻¹
N1	46.1	713.3
N2	63.6	1236.8
N3	15.8	356.1
N4	8.5	196.3
PN	22.4	98.6
NU	25.7	105.3

Table 5.1: Comparative surface area and specific capacitance values of N1, N2, N3, N4, PN and NU

➤ **Galvanostatic charge discharge study**

To further examine the pseudocapacitive performance, a series of charge/discharge measurements were performed on synthesized electrodes at various charge/discharge current densities from 0.5 to 9 A.g⁻¹, as shown in Figure 5.2. Unlike in the case of electric double-layer capacitors with linear charge/discharge characteristics, the charge/discharge curves of synthesized Ni_{1-x}O electrodes exhibit the typical pseudocapacitive behavior, which is in good agreement with the CV results as well as with literature reports [6,7]. Based on the discharge curves the specific capacitance values were calculated. It can be clearly seen from Table 5.1 that the mesoporous Ni_{1-x}O nanosponge (N2) exhibits excellent specific capacitance of 1236.8 F.g⁻¹ at a current density of 1 A.g⁻¹.

This superior electrochemical performance of mesoporous Ni_{1-x}O nanosponge confirms the importance of robust structural porosity in providing additional electroactive contact sites at the electrode/electrolyte interfaces, enhancing ionic diffusion, leading to faster electrode kinetics [8,9]. Thus, along with morphology, other factors such as surface area, average pore size and average pore volume play a vital role in improving the capacitive performance. This obtained results are in good agreement with FESEM, BET surface area and porosity analysis reported in Chapter 3.

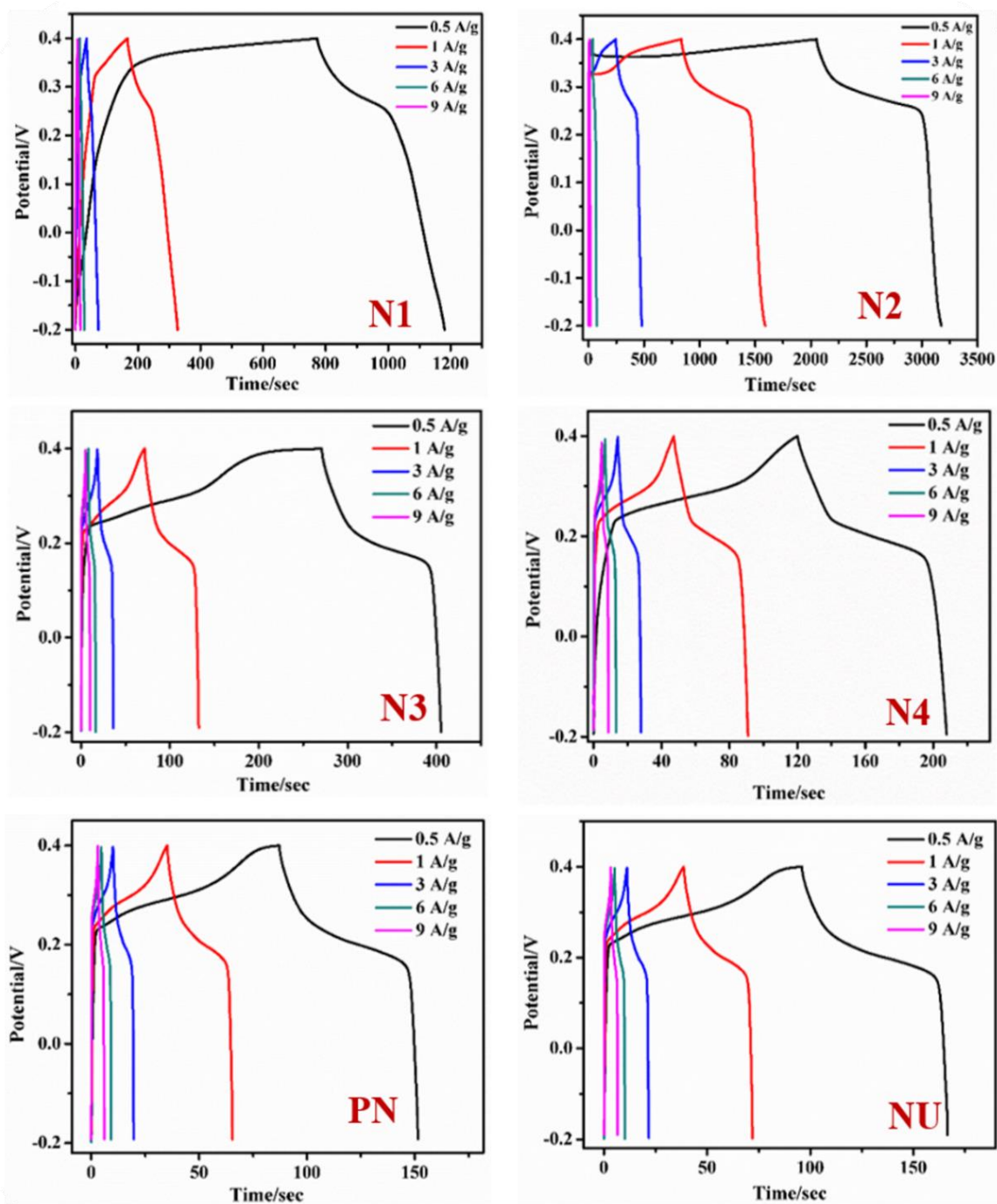


Figure 5.2 Galvanostatic charge discharge study of the Ni_{1-x}O samples N1, N2, N3, N4, PN and NU.

Catalyst	Specific capacitance (F.g ⁻¹) at current density 1 A.g ⁻¹	Capacitance retention
Ultrathin nickel oxide [10]	600	98 % after 3000 cycles
NiO nanotube [11]	919	95 % after 2000 cycles
NiO/mesoporous carbon nanospheres [12]	406	91 % after 10000 cycles
Porous thin film NiO nanowire [9]	750	88 % after 1000 cycles
NiO/carbon fibers [13]	929	88 % after 5000 cycles
NiO hierarchical microsphere/nanofibers [14]	809	85 % after 2000 cycles
Ultrathin porous NiO nanoflakes [15]	2014	100 % after 5000 cycles
Ni_{1-x}O nanosponge (N2) (This work)	1237	95 % after 10,000 cycles.

Table 5.2: Comparative analysis of specific capacitance and cyclic performance of synthesized mesoporous Ni_{1-x}O nanosponge with that of literature reported Ni_{1-x}O catalysts.

➤ **Cyclic stability study**

The electro-corrosion effects (i.e., structural instability) in Ni_{1-x}O are known to retard its electrochemical cyclic stability as a result of continuous rapid charging and discharging process [16]. Thus, the cyclic stability analysis was carried out at a current density of 6 A.g⁻¹ in 6 M KOH solution for 10000 cycles. Notably, the excellent specific capacity retention of more than 95% was observed from Figure 5.3 that for N2, nearly 78 % for N1 and 76% for N3 75% for N4, PN and NU. Thus, the excellent cyclic stability up to 10000 cycles with capacitance retention of 95% for the Ni_{1-x}O nanosponge (N2) is attributed to its robust structural mesoporosity with interconnected porous channels which provides the efficient pathway for ion diffusion throughout the charging and discharging process as compared to the rest of the synthesized catalyst as well as the reported nanostructures of Ni_{1-x}O such as nanotubes, nanowires, microspheres as shown in Table 5.2. The existence of mesoporous structure is known to reduce photo-corrosion effects in semiconductor materials by providing

easy migration of charge carriers along the walls of the mesopores [15,17]. A similar effect was observed to reduce the corrosion effects in N2 resulting in an exceptionally high cyclic rate of 10000 cycles which is extremely essential for device scale applications. However, there is slight decrease in capacitance after 10000 cycles, which can be ascribed to the film deterioration as an effect of fast electrochemical cyclic.

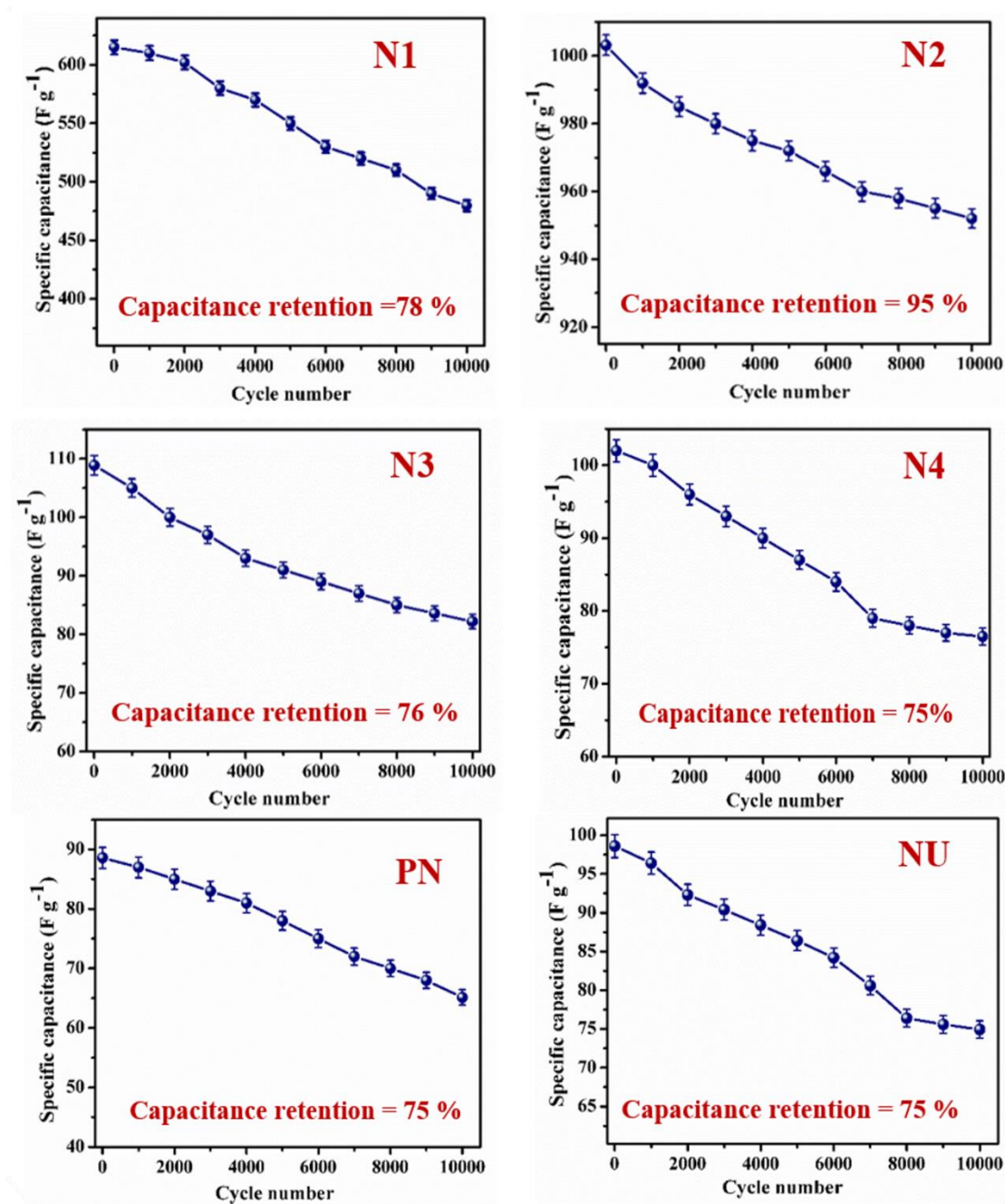


Figure 5.3 Cyclic stability study of the $Ni_{1-x}O$ samples N1, N2, N3, N4, PN and NU

A comparison of the capacitance values of N2 with respect to literature reports is presented in Table 5.2. Liu et al. reported the specific capacitance of only 600.3 F.g⁻¹ for ultrathin Ni_{1-x}O at a current density of 1 A.g⁻¹. Moreover, their synthesized Ni_{1-x}O was reported to retain cyclic stability only up to 3000 cycles [5]. Guo et al. [18] reported a specific capacitance of 929 F.g⁻¹ for NiO microspheres at a current density of 1 A.g⁻¹ with capacitance retention up to 88% for merely 2000 cycles. Zeng et al. [19] recorded the specific capacitance for NiO/carbon nanodisk electrode as 261 F.g⁻¹ at a current density of 0.25 A.g⁻¹. Han et al. [20] have reported the specific capacitance for MOF-derived NiO architectures as 322 F.g⁻¹ at a current density of 1 A.g⁻¹, while Kim et al. [21] reported the specific capacitance for NiO/NiS hybrids as 386.7 F.g⁻¹ at a current density of 1 A.g⁻¹. Xiang et al. [13] reported specific capacitance for NiO/carbon fibers as 929 F.g⁻¹ at a current density of 1 A.g⁻¹, while Qi et al. [22] reported specific capacitance of 1280 F.g⁻¹ at a current density of 1 A.g⁻¹ for multishelled NiO hollow microspheres. Although, the reported materials have capacitance on par with the NiO synthesized in this study, the use of expensive synthesis techniques such as chemical vapor deposition, hydrothermal autoclaves or complex synthetic routes serve as a limiting factor for their large-scale production and practical applicability. On the contrary, in this study the fibrous mesoporous nanosponge-like active Ni_{1-x}O is obtained via a fairly simple and scalable method for the first time. More importantly, the encouraging results obtained in the present investigation demonstrate that the 4-nba coordinated compound II can be effectively utilized to synthesize robust, fibrous, mesoporous Ni_{1-x}O nanosponge with excellent specific capacitance and extremely high cyclic stability, with potential application as electrode materials in high-performance pseudocapacitors. The next section presents a similar set of studies performed on the super porous TiO₂, the synthesis and characterization of which is already presented in Chapter 2.

5.4.2 Supercapacitor performance of TiO₂ catalysts

TiO₂ have attracted a great attention from various fields of researchers because of their low cost and excellent stability and also due to its non-toxicity. They are widely studied in the field of energy and environment like water splitting, photocatalytic degradation studies, supercapacitors, in lithium ion batteries etc. In recent times one dimensional TiO₂ has also considered to be a promising material for various electrochemical application because of its

high specific surface area, chemical stability, nanostructuring effect etc. High surface area basically provides diffusion of electrons and ions. However the major limitations of TiO_2 are poor electrical conductivity which results in low electrochemical activity. Therefore, the electrochemical performance of DEG, TU and TBTCU was evaluated using cyclic voltammetry, galvanostatic charge discharge study and cyclic stability study.

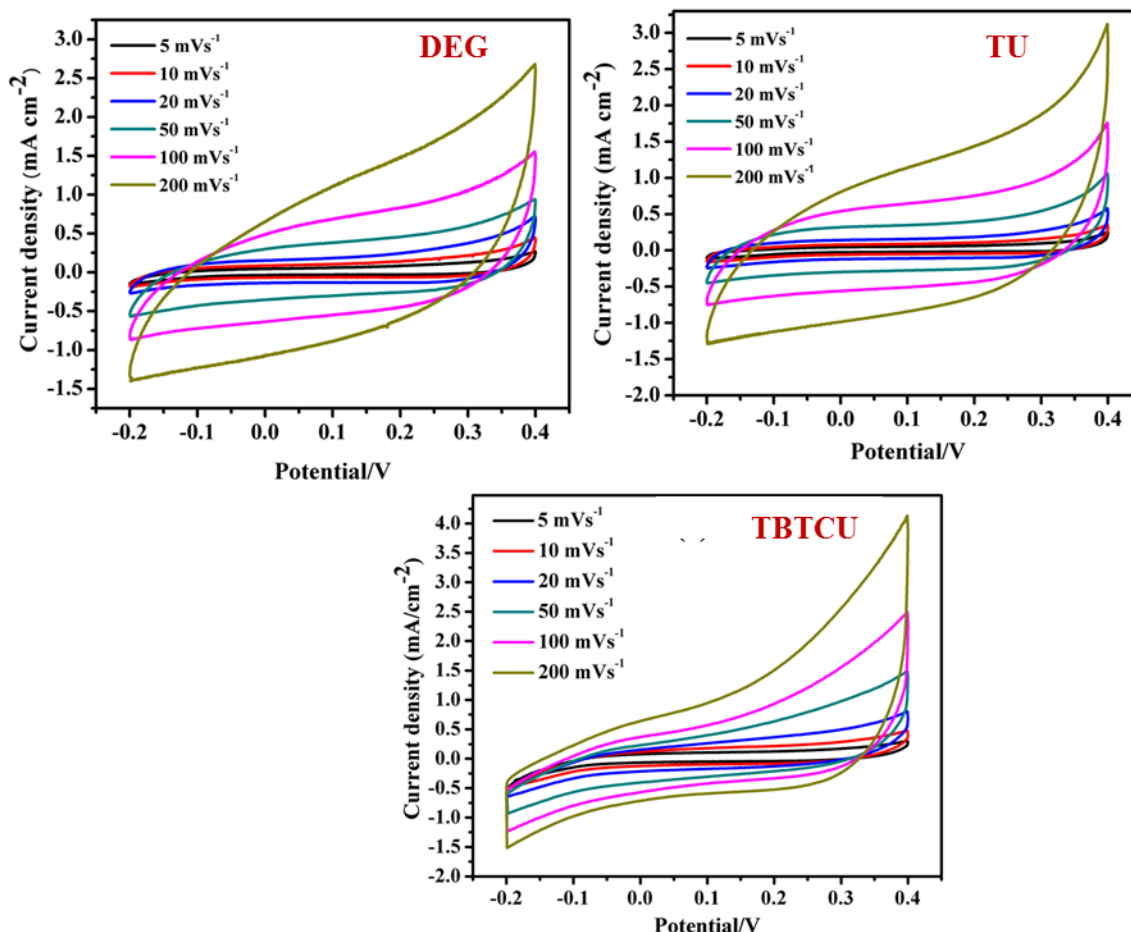


Figure 5.4 Cyclic voltammogram of the TiO_2 samples DEG, TU and TBTCU.

➤ Cyclic voltammetry study

The TiO_2 /acetylene black/PTFE supported on nickel foam electrodes were fabricated (used as working electrode), and their electrochemical performances were characterized by cyclic voltammetry (CV) and galvanostatic charge/discharge (GCD) measurements. Figure 5.4 shows the representative CV curve of the TiO_2 in the potential window of -0.2 to 0.4 V (vs Ag/AgCl) at various scan rates from 5 to 200 $\text{mV}\cdot\text{s}^{-1}$ in 6.0 M KOH. The CV curve exhibited EDLC like behavior for all the TiO_2 samples. The area under the CV curve was observe to

increase as we increase the scan rate from 5 to 200 $\text{mV}\cdot\text{s}^{-1}$. TBTCU showed slightly high area under the CV curve as compared to DEG and TU which indicated more charge storage capacity in case of TBTCU. This could be attributed to its high surface area and porosity as compared to DEG and TU. In order to confirm this behavior of TBTCU galvanostatic charge discharge measurements were carried out which are presented in the next section.

➤ Galvanostatic charge discharge study

For all the TiO_2 samples a series of charge/discharge measurements were carried out at different charge/discharge current densities from 0.5 to 9 $\text{A}\cdot\text{g}^{-1}$ in 6 M KOH solution.

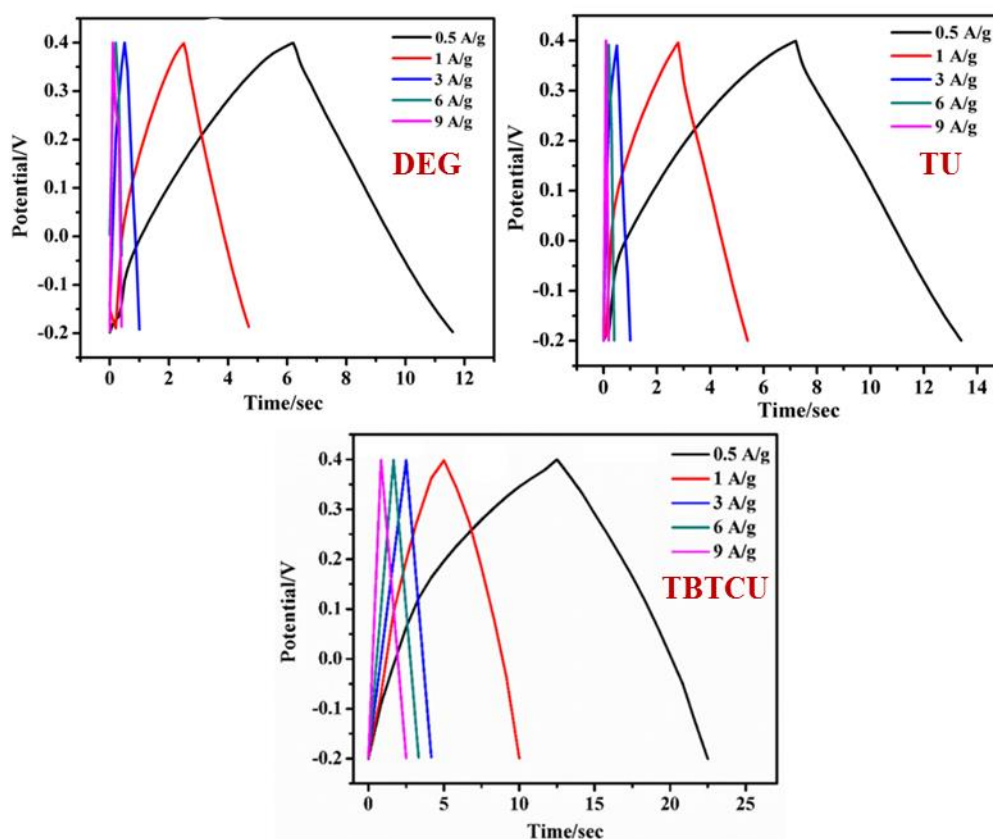


Figure 5.5 Galvanostatic charge discharge study of the TiO_2 samples DEG, TU and TBCTU.

Figure 5.5 shows galvanostatic charge discharge study in all the TiO_2 samples. It is observed that all the TiO_2 sample showed EDLC like behavior and with increase in current density from 0.5 to 9 $\text{A} \cdot \text{g}^{-1}$ there was increase in charging and discharging rates of the electrode. The specific capacitance was calculated at 1 $\text{A} \cdot \text{g}^{-1}$ for each of the TiO_2 samples and the obtained specific capacitance are 16.5 $\text{F} \cdot \text{g}^{-1}$, 19.8 $\text{F} \cdot \text{g}^{-1}$ and 24.6 $\text{F} \cdot \text{g}^{-1}$. The maximum specific capacitance of 24.6 $\text{F} \cdot \text{g}^{-1}$ was obtained for TBTCU which was in good agreement with the CV profiles and the literature reports. [23]

➤ Cyclic stability study

The electrode stability was tested using cyclic stability experiments at current density 6 $\text{A} \cdot \text{g}^{-1}$ in 6 M KOH solution for 1000 cycles.

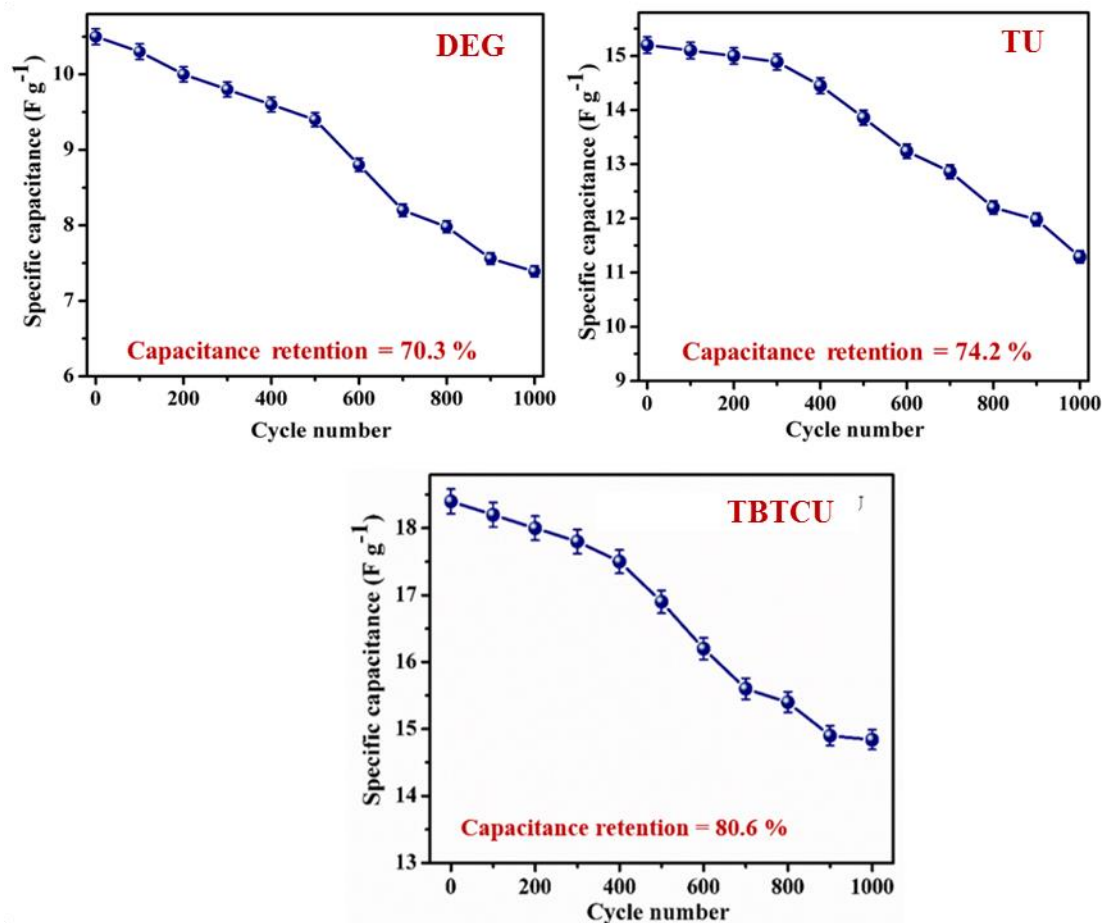


Figure 5.6: Cyclic stability study of TiO_2 samples, DEG, TU and TBTCU.

Approximately 80.7 % specific capacitance retention was observed for TBTCU while that of TU and DEG showed 74.2 and 70.3 % specific capacitance retention for 1000 cycles as presented in Figure 5.7. The maximum capacitance retention of 80.7 % for TBTCU is

attributed to its high surface area along with the porous structure which helps in increasing the charge storage capacity of the TBTCU.

Thus, it is evident that, TBTCU shows slightly better performance than DEG and TU which could be an effect of its porous structure. Nonetheless, it is to be noted that in spite of its extremely high surface area of $238 \text{ m}^2.\text{g}^{-1}$, its supercapacitor performance is lower by a factor of 5 compared to Ni_{1-x}O nanosponge. Therefore, in order to improve the activity of TBTCU, its synthesis was modified to incorporate Ni_{1-x}O particles resulting in formation of $\text{Ni}_{1-x}\text{O}/\text{TiO}_2$ nanocomposites. The details of synthesis and characterization have already been presented in chapter 4 and hence only the effect of loading Ni_{1-x}O over TiO_2 on the electrochemical performance of the composite is discussed in the next section.

5. 4. 3 Supercapacitor performance of $\text{Ni}_{1-x}\text{O}/\text{TiO}_2$ nanocomposites.

The $\text{Ni}_{1-x}\text{O}-\text{TiO}_2/\text{acetylene black}/\text{PTFE}$ supported on nickel foam electrodes were fabricated (used as working electrode), and their electrochemical performances were characterized by cyclic voltammetry (CV) and galvanostatic charge/discharge (GCD) measurements. Figure 5.5 shows the representative CV curve of the $\text{Ni}_{1-x}\text{O}/\text{TiO}_2$ in the potential window of -0.2 to 0.4 V (vs Ag/AgCl) at various scan rates from 5 to $200 \text{ mV}.\text{s}^{-1}$ in 6.0 M KOH.

➤ Cyclic voltammetry study

For lower percentage loading of Ni_{1-x}O , i.e. 1NT, 3NT and 5NT, the CV graph showed EDLC type behavior whereas at higher percentage loading of Ni_{1-x}O i.e 10 NT, 20 NT and 50 NT, a pair of redox current peaks were observed at 0.19 V and 0.33 V which corresponds to faradic oxidation/reduction reaction and represents the pseudocapacitive behavior of Ni_{1-x}O . Furthermore, as the peak intensity increases with the increasing scan rate, the CV results continue to display an obvious pair of redox peaks, suggesting good reversibility of the involved faradic reactions. Moreover, along with the increase in scan rate from 5 to $200 \text{ mV}.\text{s}^{-1}$, the anodic peaks shift positively, while the cathodic peaks shift negatively, which are attributed to the polarization of the electrodes at higher scan rates. Moreover, as shown in Figure 5.5, with an increase in % of Ni_{1-x}O in TiO_2 , the area under the CV curve increases due to increase in the charge storage capacity of the synthesized nanocomposites (1NT-

10NT). The greater integral area indicates that the higher % of Ni_{1-x}O enables higher electrochemical activity by providing greater percentage of electroactive sites at the electrode/electrolyte interface, which can be associated with a richer faradaic reaction, in agreement with the literature reports [24–26]. In order to confirm the above observation, the enhancement in electrochemical rates at the electrode interface were studied using Galvanostatic charge discharge measurements which are presented in the next section.

➤ **Galvanostatic charge discharge study**

To further examine the pseudocapacitive performance, a series of charge/discharge measurements were performed on synthesized electrodes at various charge/discharge current densities from 0.5 to 9 A.g^{-1} , as shown in Figure 5.6. For lower % of Ni_{1-x}O in case of 1NT, 3NT, and 5NT, the nanocomposite showed EDLC type behavior and as we increase the concentration of Ni_{1-x}O from 10 NT to 50 NT it exhibited pseudocapacitive like behavior which is in good agreement with the CV results as well as with literature reports [27].

Furthermore, the effect of as the current density is increased from 0.5 to 9 A.g^{-1} , the material shows increase in charging and discharging rates while maintaining the nature of the GCD curve. This indicates excellent stability of the material even during fast charge-discharge process. Furthermore, if the performance of all the composites are evaluated at the same current density, it is observed that both charging and discharging time increases from 1NT to 50NT which confirms that the charge storage capacity of the composite increases as a function of Ni_{1-x}O loading.

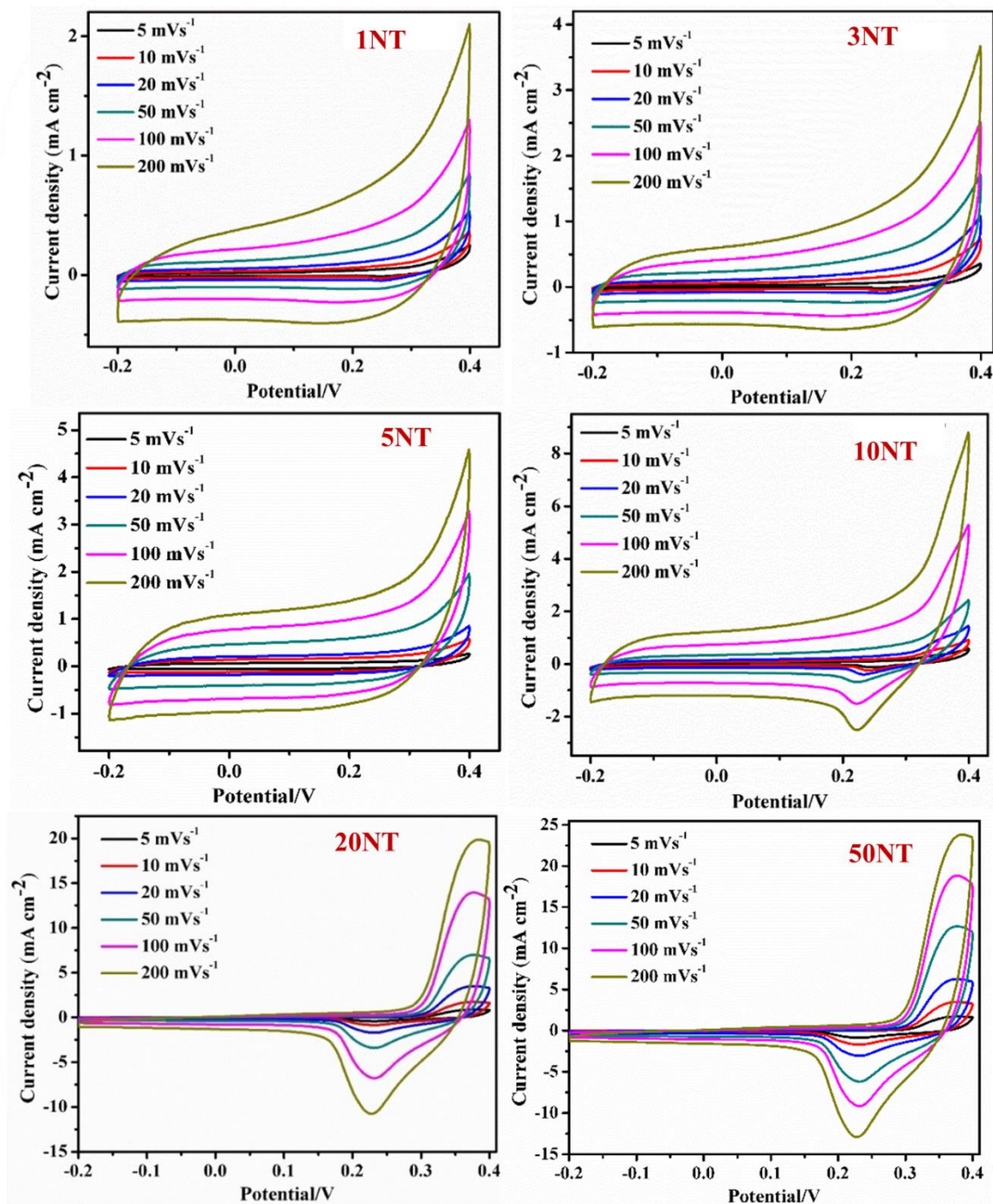


Figure 5.7 Cyclic voltammogram of the synthesized $\text{Ni}_{1-x}\text{O}/\text{TiO}_2$ nanocomposites.

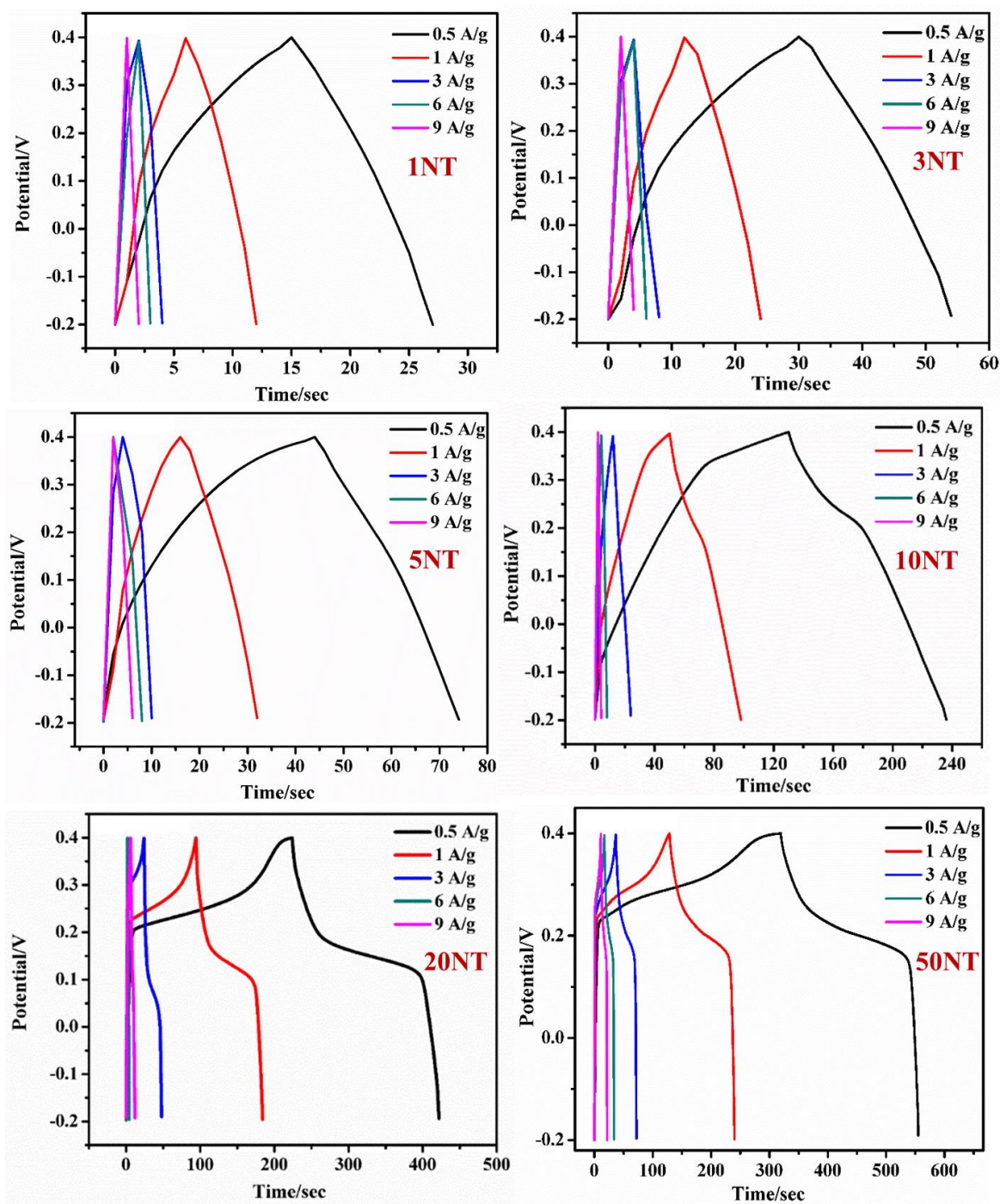


Figure 5.8: Galvanostatic charge discharge study of all synthesized $\text{Ni}_{1-x}\text{O}/\text{TiO}_2$ nanocomposites.

Depending upon the discharge rates, the specific capacitance were calculated and tabulated in Table 5.3. The obtained values indicates that up to 20% loading of Ni_{1-x}O , the specific capacitance values of the composite increases and it almost remains similar or constant up to 50 NT. This increase cannot be justified based on the surface area of the composites listed in Table 5.3. Therefore, such an enhancement in the supercapacitive behavior of the nanocomposite could be due to the increase in the electroactive sites in the composite. A comparison of the ratio of $\text{Ni}^{3+}/\text{Ni}^{2+}$ redox state shows as presented in Table 5.3 shows that there is a gradual increase in Ni^{3+} concentration in the composite with the increase in Ni_{1-x}O loading in TiO_2 . Though the increase in the values is marginal, it gives an indication that the $\text{Ni}_{1-x}\text{O}/\text{TiO}_2$ heterostructure could be responsible for the enhancement in the redox states and hence the electroactive sites.

➤ **Cyclic stability study**

The cyclic stability analysis was carried out at a current density of 6 A.g^{-1} in 6 M KOH solution for 1000 cycles. Notably, approximately 90 % specific capacitance retention was observed for 20 NT and 50 NT nanocomposites while for the rest of the catalyst it varied between 78-87% as seen in Figure 5.7. The observed trend also confirms that with the increase in Ni_{1-x}O loading, the stability of the composite is enhanced.

In order to confirm this effect, $\text{Ni}_{1-x}\text{O}/\text{TiO}_2$ mixtures were synthesized by physically mixing the two metal oxides and its cyclic voltammetry and galvanostatic charge-discharge study was conducted. The results obtained were compared with that of synthesized composites. Figure 5.8 and 5.9 shows the CV and GCD results for the physically mixed $\text{Ni}_{1-x}\text{O}/\text{TiO}_2$ mixtures and synthesized nanocomposites at a scan rate of at 5 mV.s^{-1} and current density of 1 A.g^{-1} . The calculated specific capacitance values are compared in Table 5.3 and depicted in Figure 5.10.

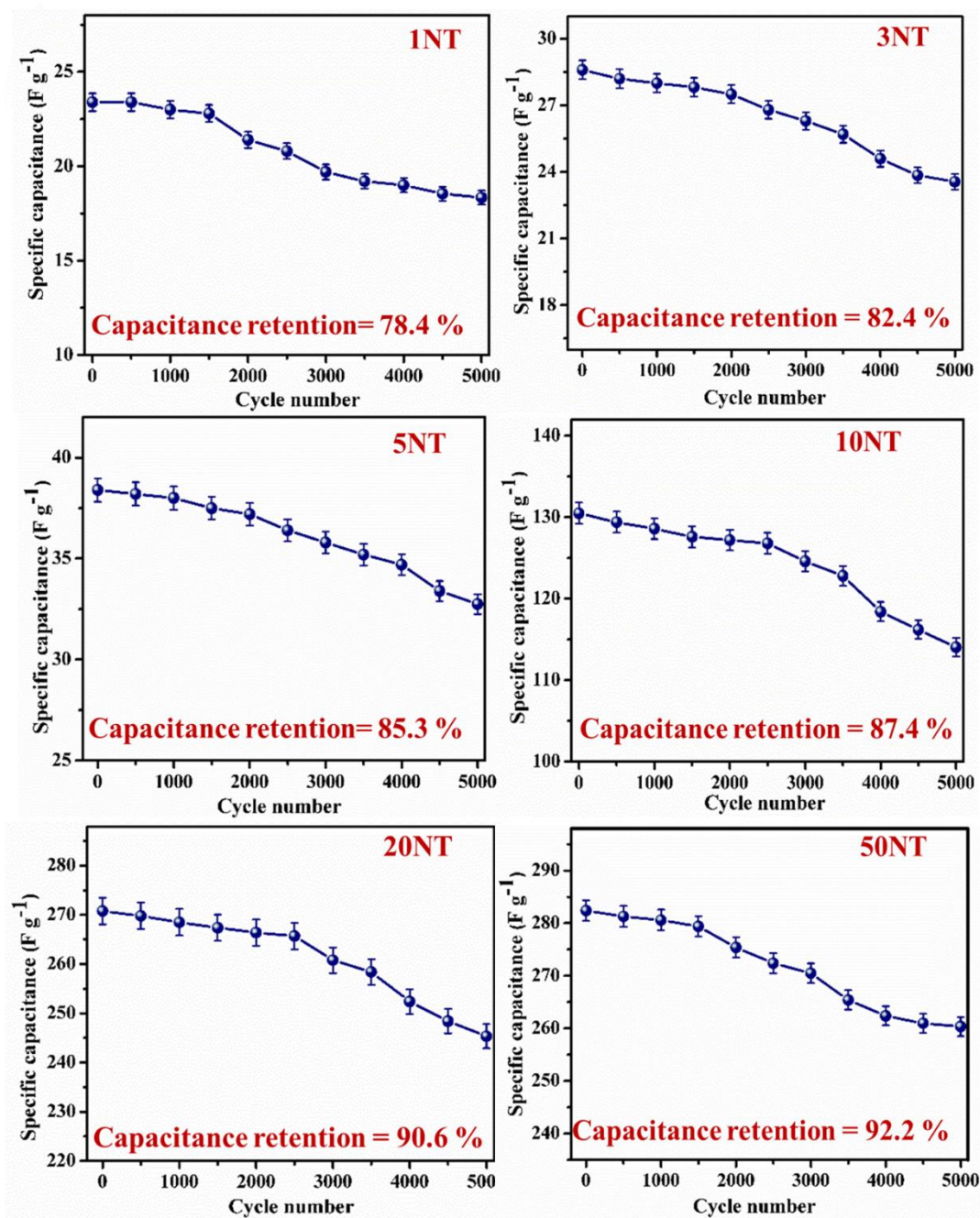


Figure 5.9: Cyclic stability study of all synthesized $Ni_{1-x}O/TiO_2$ nanocomposites.

It is clear from the Figure 5.10 that, the as-synthesized $\text{Ni}_{1-x}\text{O}/\text{TiO}_2$ nanocomposite exhibits much higher charge storage capacity (> by a factor of 3) as compared to its physically mixed counterpart at 50% Ni_{1-x}O loading on TiO_2 , which confirms that the heterostructure formation in synthesized nanocomposites could have a significant impact on the electroactive states which augments the electrode kinetics and charge storage performance of the composite.

Catalyst	BET Surface area ($\pm 5 \text{ m}^2.\text{g}^{-1}$)	SC (F.g^{-1}) ($\text{Ni}_{1-x}\text{O}/\text{TiO}_2$ Synthesized)	$\text{Ni}^{3+}/\text{Ni}^{2+}$ ($\text{Ni}_{1-x}\text{O}/\text{TiO}_2$ Synthesized)	SC (F.g^{-1}) ($\text{Ni}_{1-x}\text{O}/\text{TiO}_2$ Physically mixed)
N2	63	1236.8	---	---
1NT	231	30.9	0.82	20.6
3NT	219	37.0	0.84	20.4
5NT	183	49.3	0.84	21.6
10NT	134	147.6	0.86	23.5
20NT	121	298.5	0.87	52.6
50NT	90	310.6	0.88	106.5

Table 5.3: Comparative analysis of BET surface area specific capacitance and $\text{Ni}^{3+}/\text{Ni}^{2+}$ ratio of synthesized and physically mixed synthesized $\text{Ni}_{1-x}\text{O}/\text{TiO}_2$ nanocomposites.

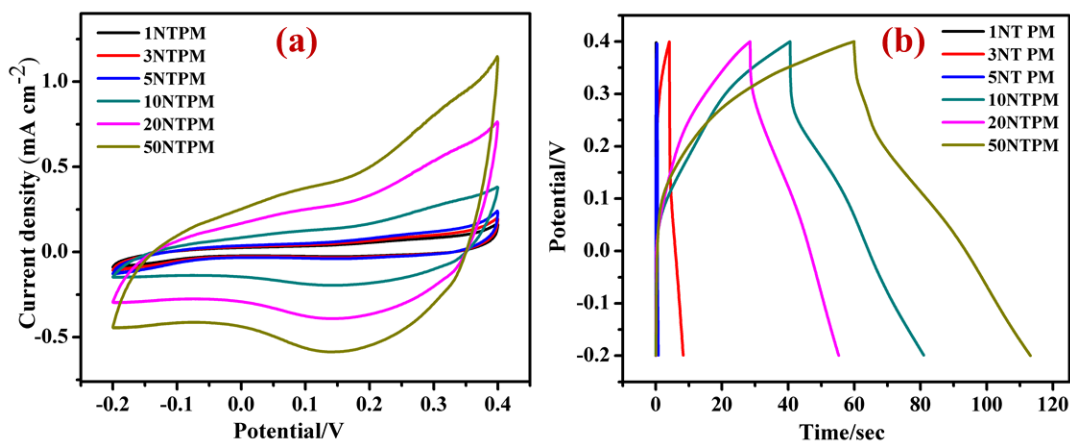


Figure 5.10: (a) Comparative CV and (b) GCD plots of 1-50 % $\text{Ni}_{1-x}\text{O}/\text{TiO}_2$ nanocomposites at 5 mV.s^{-1} and 1 A.g^{-1} .

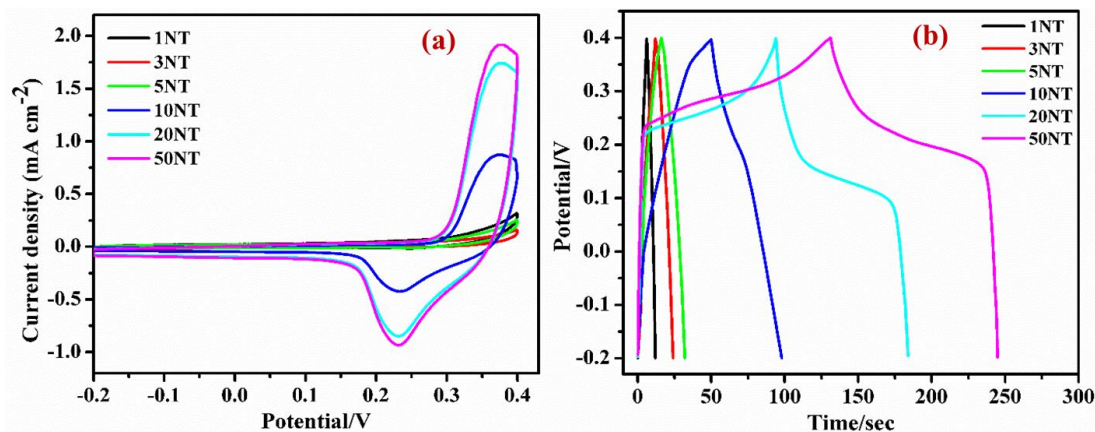


Figure 5.11: (a) Comparative cyclic voltammetry at 5 mV.s⁻¹ (b) Galvanostatic charge discharge at 1 A.g⁻¹.

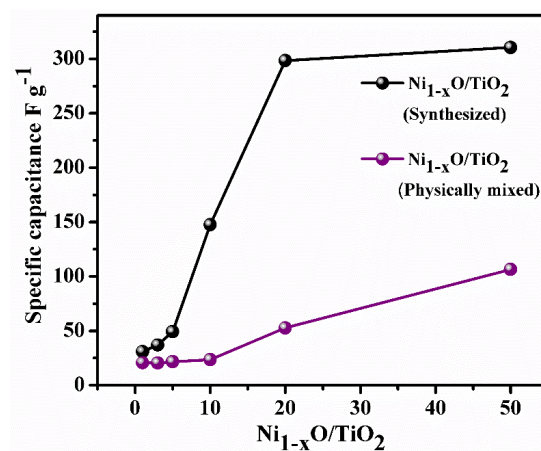


Figure 5.12: Specific capacitance of 1-50 % Ni_{1-x}O/TiO₂ nanocomposites.

5.5 Conclusion

The present study has evaluated the supercapacitor performance of Ni_{1-x}O, TiO₂ and their nanocomposites. It has been confirmed that Ni_{1-x}O exhibits much superior electrochemical performance as compared to TiO₂ catalyst. In spite of a lower surface area of Ni_{1-x}O (N2) as compared to TiO₂ (TBTCU), the nanosponge-like Ni_{1-x}O exhibits high specific capacitance of 1236.8 F.g⁻¹ at a current density 1 A.g⁻¹ along with exceptional electrochemical stability even after 10000 cycles and appreciable capacitance retention of 95% at a current density of 6 A.g⁻¹. This is attributed to improved electrode kinetics as a result of greater electrode–electrolyte interaction, fast charging- discharging rates within the mesopores facilitated by the greater distribution of Ni³⁺/Ni²⁺ redox states which results in increased electroactive sites

is probably responsible for the superior charge storage performance of Ni_{1-x}O . An improvement in the charge storage capacity of TiO_2 is observed as the % of Ni_{1-x}O loading on TiO_2 is increased. The cyclic voltammetry study showed EDLC like behavior for lower % loading of Ni_{1-x}O on TiO_2 i.e 1NT, 3NT and 5NT. However, for higher % loading of Ni_{1-x}O it exhibited pseudocapacitive behavior. The maximum specific capacitance 310 F.g^{-1} was obtained for 50% Ni_{1-x}O loading on TiO_2 . The activity of as-synthesized 50 NT was further confirmed with that of physically mixed 50% $\text{Ni}_{1-x}\text{O}/\text{TiO}_2$ mixture and it was observed that the specific capacitance obtained was 106.5 F.g^{-1} which is lower by almost 3 times compared to the former case. Thus, it is concluded that the heterostructure formation in synthesized $\text{Ni}_{1-x}\text{O}/\text{TiO}_2$ nanocomposites could have a significant impact on the electroactive sites which augments the electrode kinetics and charge storage performance of the composite.

5.6 References

- [1] G. Cheng, W. Yang, C. Dong, T. Kou, Q. Bai, H. Wang, Z. Zhang, Ultrathin mesoporous NiO nanosheet-anchored 3D nickel foam as an advanced electrode for supercapacitors, *J. Mater. Chem. A*. 3 (2015) 17469–17478.
- [2] S. Wu, K.S. Hui, K.N. Hui, K.H. Kim, Ultrathin porous NiO nanoflake arrays on nickel foam as an advanced electrode for high performance asymmetric supercapacitors, *J. Mater. Chem. A*. 4 (2016) 9113–9123.
- [3] S.K. Meher, P. Justin, G. Ranga Rao, Nanoscale morphology dependent pseudocapacitance of NiO: Influence of intercalating anions during synthesis, *Nanoscale*. 3 (2011) 683–692.
- [4] S.K. Meher, G.R. Rao, Ultralayered Co_3O_4 for high-performance supercapacitor applications, *J. Phys. Chem. C*. 115 (2011) 15646–15654.
- [5] W. Liu, C. Lu, X. Wang, K. Liang, B.K. Tay, In situ fabrication of three-dimensional, ultrathin graphite/carbon nanotube/NiO composite as binder-free electrode for high-performance energy storage, *J. Mater. Chem. A*. 3 (2015) 624–633.
- [6] S. Goel, A. Kumar Tomar, R. Kishore Sharma, G. Singh, Highly Pseudocapacitive NiO Nanoflakes through Surfactant-Free Facile Microwave-Assisted Route, *ACS Appl. Energy Mater.* 1 (2018) 1540–1548.
- [7] A.K. Singh, D. Sarkar, G.G. Khan, K. Mandal, Hydrogenated NiO nanoblock architecture for high performance pseudocapacitor, *ACS Appl. Mater. Interfaces*. 6 (2014) 4684–4692.
- [8] S. Xiong, C. Yuan, X. Zhang, Y. Qian, Mesoporous NiO with various hierarchical nanostructures by quasi-nanotubes/nanowires/nanorods self-assembly: Controllable preparation and application in supercapacitors, *CrystEngComm*. 13 (2011) 626–632..
- [9] A. Paravannoor, R. Ranjusha, A.M. Asha, R. Vani, S. Kalluri, K.R.V. Subramanian, N. Sivakumar, T.N. Kim, S. V. Nair, A. Balakrishnan, Chemical and structural stability of porous thin film NiO nanowire based electrodes for supercapacitors, *Chem. Eng. J.* 220 (2013) 360–366.

- [10] Q. Liu, C. Lu, Y. Li, Controllable synthesis of ultrathin nickel oxide sheets on carbon cloth for high-performance supercapacitors, *RSC Adv.* 7 (2017) 23143–23148.
- [11] A. Liu, H. Che, Y. Mao, Y. Wang, J. Mu, C. Wu, Y. Bai, X. Zhang, G. Wang, Template-free synthesis of one-dimensional hierarchical NiO nanotubes self-assembled by nanosheets for high-performance supercapacitors, *Ceram. Int.* 42 (2016) 11435–11441.
- [12] P. Zhang, M. Chen, X. Shen, Q. Wu, X. Zhang, L. Huan, G. Diao, Preparation of $\text{Li}_4\text{Ti}_5\text{O}_{12}$ nanosheets/carbon nanotubes composites and application of anode materials for lithium-ion batteries, *Electrochim. Acta.* 204 (2016) 92–99.
- [13] D. Xiang, X. Liu, X. Dong, A facile synthetic method and electrochemical performances of nickel oxide/carbon fibers composites, *J. Mater. Sci.* 52 (2017) 7709–7718.
- [14] X. Guo, K. Yan, F. Fan, Y. Zhang, Y. Duan, J. Liu, Controllable synthesis of a NiO hierarchical microspheres/nanofibers composites assembled on nickel foam for supercapacitor, *Mater. Lett.* 240 (2019) 62–65.
- [15] Y. Lv, J. Lin, S. Peng, L. Zhang, L. Yu, Effective ways to enhance the photocatalytic activity of ZnO nanopowders: High crystalline degree, more oxygen vacancies, and preferential growth, *New J. Chem.* 43 (2019) 19223–19231.
- [16] B. Sun, X. He, X. Leng, Y. Jiang, Y. Zhao, H. Suo, C. Zhao, Flower-like polyaniline-NiO structures: A high specific capacity supercapacitor electrode material with remarkable cyclic stability, *RSC Adv.* 6 (2016) 43959–43963.
- [17] L. Yu, G. Li, X. Zhang, X. Ba, G. Shi, Y. Li, P.K. Wong, J.C. Yu, Y. Yu, Enhanced Activity and Stability of Carbon-Decorated Cuprous Oxide Mesoporous Nanorods for CO_2 Reduction in Artificial Photosynthesis, *ACS Catal.* 6 (2016) 6444–6454.
- [18] C. Guan, Y. Wang, Y. Hu, J. Liu, K.H. Ho, W. Zhao, Z. Fan, Z. Shen, H. Zhang, J. Wang, Conformally deposited NiO on a hierarchical carbon support for high-power and durable asymmetric supercapacitors, *J. Mater. Chem. A.* 3 (2015) 23283–23288.
- [19] D. Zeng, Y. Yang, F. Yang, F. Guo, S. Yang, B. Liu, S. Hao, Y. Ren, Versatile

- NiO/mesoporous carbon nanodisks: controlled synthesis from hexagon shaped heterobimetallic metal–organic frameworks, *Nanoscale*. 9 (2017) 11851–11857.
- [20] Y. Han, S. Zhang, N. Shen, D. Li, X. Li, MOF-derived porous NiO nanoparticle architecture for high performance supercapacitors, *Mater. Lett.* 188 (2017) 1–4.
- [21] S.Y. Kim, C.V.V.M. Gopi, A.E. Reddy, H.J. Kim, Facile synthesis of a NiO/NiS hybrid and its use as an efficient electrode material for supercapacitor applications, *New J. Chem.* 42 (2018) 5309–5313.
- [22] X. Qi, W. Zheng, X. Li, G. He, Multishelled NiO hollow microspheres for high-performance supercapacitors with ultrahigh energy density and robust cycle life, *Sci. Rep.* 6 (2016) 1–10.
- [23] X. Liu, P. Carvalho, M.N. Getz, T. Norby, A. Chatzitakis, Black Anatase TiO₂ Nanotubes with Tunable Orientation for High Performance Supercapacitors, *J. Phys. Chem. C*. 123 (2019) 21931–21940.
- [24] J.B. Wu, R.Q. Guo, X.H. Huang, Y. Lin, Construction of self-supported porous TiO₂/NiO core/shell nanorod arrays for electrochemical capacitor application, *J. Power Sources*. 243 (2013) 317–322.
- [25] P. Anandhi, V.J.S. Kumar, S. Harikrishnan, Preparation and Improved Capacitive Behavior of NiO/TiO₂ Nanocomposites as Electrode Material for Supercapacitor, *Curr. Nanosci.* 16 (2019) 79–85.
- [26] J.H. Kim, K. Zhu, Y. Yan, C.L. Perkins, A.J. Frank, Microstructure and pseudocapacitive properties of electrodes constructed of oriented NiO-TiO₂ nanotube arrays, *Nano Lett.* 10 (2010) 4099–4104.
- [27] W. Bao, Y. Wu, Y. Xie, C. Yao, Fabrication and electrochemical performance of nickel oxide nanoparticles anchored titanium dioxide nanotube array hybrid electrode, *Funct. Mater. Lett.* 13 (2020) 1–7.

CHAPTER VI:
CONCLUSION OF THE THESIS

CONCLUSION OF THE THESIS

The increasing energy needs and the associated environmental pollution led to the genesis of this thesis and the underlying research investigations herein. The demand for highly active, smart nanomaterials which can play a vital role in both environmental and energy applications were researched in detail. Two independent catalyst systems, namely TiO_2 and Ni_{1-x}O with unique crystal structures and physico-chemical properties, were identified so that their combinations to produce a highly active hybrid catalyst system ($\text{Ni}_{1-x}\text{O}/\text{TiO}_2$) could be synthesized.

TiO_2 was chosen to be the primary catalyst for environmental applications mainly due to its highly active semiconductor properties, photocatalytic activity and environmental compatibility. In spite of the vast research and available literature on TiO_2 , it was observed that its low surface area owing to randomly agglomerated nanostructures leads to agglomerate porosity which limits facile reactant diffusion pathways for catalytic applications. This problem was addressed in the present thesis via a systematic trial and error method. Firstly, mesoporous anatase TiO_2 catalysts were synthesized using reflux assisted sol-gel method. The effect of urea on surface area of TiO_2 was investigated. TiO_2 synthesized using Ti:U ratio of 1:8 exhibited highest surface area of $186 \text{ m}^2.\text{g}^{-1}$ with pore size of 7.5 nm and pore volume of $0.35 \text{ cc}.\text{g}^{-1}$ thus confirming the role of urea in inducing porosity in TiO_2 . In addition to this, the effect of different carboxylic acids as SDA on pore size distribution and surface area of the TiO_2 was investigated. It was confirmed that with the increase in the number of $-\text{COOH}$ groups in the SDA, the porous TiO_2 with wider pore size distribution are formed. This porosity was primarily due to the randomly oriented agglomerated nanoparticles. The stronger interaction between the carboxylate groups and Ti^{4+} also led to longer calcination time for their complete removal from the titanium hydroxide gel. Such increased heat treatments probably lead to a partial collapse of pore structure in TiO_2 .

The above results led to the formulation of an innovative strategy, which included a suitable combination of carboxylic acid with urea as a mixed SDA, which assisted in facile removal of carboxylic acids during combustion while preserving the porous structure. Thus, further assisting in tailoring the agglomerate porosity into structurally robust, ordered mesoporosity

especially in the case of TTCU and TBTCU. Structurally robust mesoporous TiO₂ with a highest surface area of 238 m².g⁻¹, and average pore size and pore volume of 4.8 nm and 0.84 cc.g⁻¹ was obtained using butanetetracarboxylic acid and urea as SDA. All the synthesized TiO₂ catalysts were tested for adsorptive removal of Amaranth dye from water and subsequent kinetic modeling analysis were performed. These analysis revealed that Amaranth adsorption on all the synthesized TiO₂ obeyed Sips adsorption model and the maximum adsorption capacity of 87.8 mg.g⁻¹ was obtained for TBTCU which was greater than PT by a factor of 2. Furthermore, TBTCU also exhibited the highest Amaranth dye photodegradation efficiency of 95.6 % (in 15 minutes) with a rate constant of $2.05 \times 10^{-1} \text{ min}^{-1}$, which is the best photocatalytic Amaranth degradation performance reported till date in the literature. This enhanced adsorptive separation capacity and increased photocatalytic activity of TiO₂ was attributed to the highly robust, ordered mesoporous nature and high surface area of TiO₂.

A detailed literature survey on Ni_{1-x}O concluded that it is one of the prominent materials with potential for application in energy storage devices. However, its electro-corrosion issues limit its utilization in the industrial sector. Furthermore, its applicability in photocatalysis in particular for environmental remediation of organic pollutants, is extremely limited due to its wide band gap and photo-corrosion effects. In order to improve the stability and applicability of Ni_{1-x}O in photocatalysis, attempts were made to design simple and scalable methodologies to produce highly porous Ni_{1-x}O nanostructures. In this study, it was demonstrated that ligands such as p-nitrobenzoic acid and imidazole are highly effective in tuning the nanostructural growth of Ni_{1-x}O into nanosponge and nanoflake-like morphologies, respectively.

Detailed material characterization revealed that a pure cubic phase of Ni_{1-x}O with a band gap of 3.3 to 3.5 eV was achieved. A sponge-like Ni_{1-x}O with 3D interconnected porous network could be obtained by controlled combustion of [Ni(H₂O)₄(4-nba)₂].2H₂O compound leading to a nanosponge-like morphology with a highest surface area of 63.67 m².g⁻¹ as compared to other synthesized Ni_{1-x}O catalyst. Furthermore, the Amaranth dye adsorption studies on all synthesized Ni_{1-x}O followed the Sip adsorption isotherm model with a maximum adsorption

capacity of 75.0 mg.g⁻¹. The adsorption kinetics followed the pseudo-first-order kinetic model for all the synthesized Ni_{1-x}O. The photocatalytic degradation of Amaranth dye followed the Langmuir- Hinshelwood mechanism and exhibited the highest degradation of 93.8 % within 70 minutes with a maximum rate constant of 4.04 × 10⁻² min⁻¹ (at pH = 5.6). The results of stability analysis also proved that the nanosponge-like porous structure facilitated easy migration of charge carriers, thus partially improving catalyst stability. Though the activity of the synthesized Ni_{1-x}O was lower in comparison to TiO₂, a significant improvement in its activity was achieved as compared to pristine Ni_{1-x}O. Furthermore, the simplicity of this synthesis strategy could further pave the way for the industrial scalability of Ni_{1-x}O catalyst for varied applications.

The findings of the above two studies were amalgamated to devise a new simple strategy to produce Ni_{1-x}O/TiO₂ nanocomposite catalyst. The composite catalyst was synthesized using a hybrid gelatinous mixture of Ti(OH)₄, urea, butanetetracarboxylic acid and nickel p-nitrobenzoic acid via reflux assisted sol-gel method. The effect of Ni_{1-x}O loading on morphology, surface area, and non-stoichiometry of Ni_{1-x}O/TiO₂ nanocomposites was investigated. It was concluded that as we increase the Ni_{1-x}O loading on TiO₂ (0-50 wt %) the surface area tends to decrease from 231 m².g⁻¹ to 90 m².g⁻¹ while the pore size and pore volume also decreases with the increase in Ni_{1-x}O loading. This effect was attributed to the increased sintering of the particles at higher 4-nba concentrations, partly reducing the pore size with simultaneous incorporation of Ni_{1-x}O particles into the pore wells. Further, the non-stoichiometric analysis of all the synthesized Ni_{1-x}O/TiO₂ nanocomposites showed a slight increase in Ni³⁺ content in the nanocomposites as the Ni_{1-x}O loading on TiO₂ is increased.

The Amaranth dye adsorption capacity of the composite catalyst was found to decrease with the increase in Ni_{1-x}O loading in the composite with a maximum adsorption capacity of 84.5 mg.g⁻¹ in case of 1NT. This trend was attributed to the decreases in the surface area of the composite catalyst. Interestingly, the 1% and 3 % Ni_{1-x}O/TiO₂ composites exhibited better photocatalytic activity as compared to the synthesized TiO₂, Ni_{1-x}O, and commercial Degussa P25. The 3% Ni_{1-x}O/TiO₂ nanocomposites exhibited the highest Amaranth dye degradation efficiency of 97 % with the rate constant of 1.628 × 10⁻¹ min⁻¹ (at pH = 5.6) within 20 minutes of irradiation, which was comparatively higher than TBTCU (92.3 % degradation efficiency

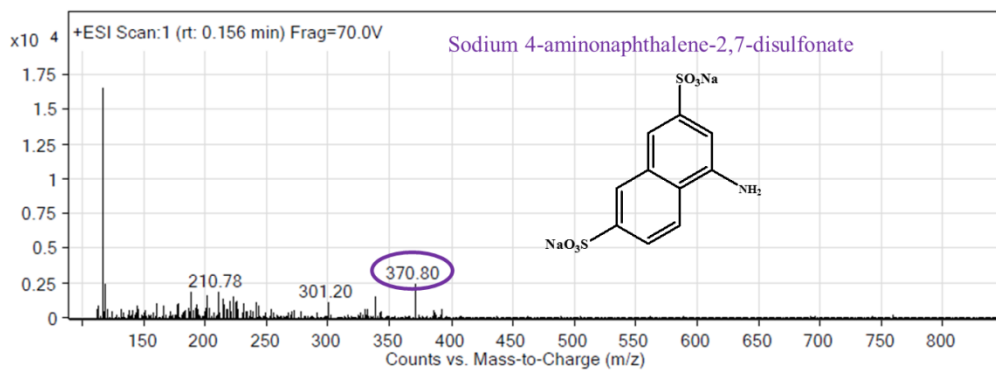
in 20 minutes) with a rate constant of $1.218 \times 10^{-1} \text{ min}^{-1}$ at $\text{pH} = 5.6$) in spite of the lower surface area in the former case. The enhanced photocatalytic activity is attributed to the synergistic effect of reduction in bandgap, and greater charge carrier separation possibly due to the formation of a p-n heterojunction at the interface of mesoporous Ni_{1-x}O and TiO_2 . Furthermore, qualitative analysis of Amaranth degradation using LC-ESI-MS led to identifying some novel products such as sodium 4-aminonaphthalene-2,7-disulphonate, sodium 3, 4-dioxo-3,4-dihydronaphthalene-2,7-disulphonate, trihydroxynaphthalene-2-sulfonic acid, 2-hydroxy succinic acid and 2-hydroxy malonic acid which were reported in this study for the very first time. Two reactive species dominating the surface of the p-n heterojunction namely, $\text{O}_2^{\cdot-}$ and h^+ played a major role in effectively degrading the Amaranth dye. Thus, it can be concluded that all the above investigations led to the designing of novel strategies to effectively produce hybrid p-n junction photocatalyst of high catalytic activity for mitigation of dye pollutants from wastewater.

From the outset, the primary aim of this thesis was to design, synthesize, characterization a highly active material that can have significant activity and applicability in both the environmental and energy sector. Therefore, the best of the synthesized catalyst, namely, TiO_2 , Ni_{1-x}O and $\text{Ni}_{1-x}\text{O}/\text{TiO}_2$ were further evaluated for their energy storage performance in supercapacitor devices. In this study, it was confirmed that Ni_{1-x}O exhibits superior electrochemical performance as compared to TiO_2 catalyst. In spite of a lower surface area of Ni_{1-x}O as compared to TiO_2 , the nanosponge-like Ni_{1-x}O exhibited extremely high specific capacitance of 1236.8 F.g^{-1} at a current density 1 A.g^{-1} along with exceptional electrochemical stability even after 10000 cycles and appreciable capacitance retention of 95% at a current density of 6 A.g^{-1} . This high activity was attributed to the improved electrode kinetics as a result of greater electrode–electrolyte interaction due to the mesopores, fast charging-discharging rates facilitated by the greater distribution of $\text{Ni}^{3+}/\text{Ni}^{2+}$ redox states, which resulted in increased electroactive sites. All these factors together contributed to the superior charge storage performance of Ni_{1-x}O . An improvement in the charge storage capacity of TiO_2 was observed as the % of Ni_{1-x}O loading on TiO_2 was increased. The cyclic voltammetry study showed EDLC-like behavior for TiO_2 , which persisted even in 1NT, 3NT and 5NT. However, for higher % loading of Ni_{1-x}O , it exhibited pseudocapacitive behavior. The maximum specific capacitance of 310 F.g^{-1} was obtained for

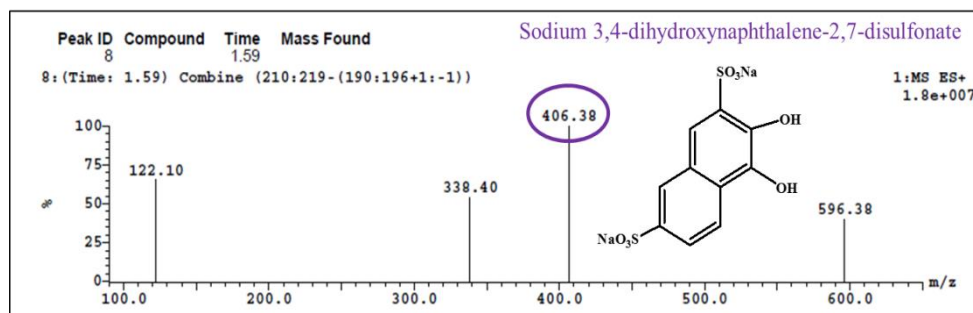
50% Ni_{1-x}O loading on TiO₂. The activity of as-synthesized 50 NT was further confirmed by comparing it with that of a physically mixed 50% Ni_{1-x}O/TiO₂ mixture, which had a lower capacitance by almost three times compared to the former case. Thus, it is concluded that the hetero-junction formation in synthesized Ni_{1-x}O/TiO₂ nanocomposite could have increased the surface distribution of redox states (Ni²⁺/Ni³⁺/Ti⁴⁺). This increase in the electroactive sites, therefore, augmented the electrode kinetics and hence the charge storage performance of the composite catalyst. Therefore, it can be concluded that this thesis made an honest preliminary attempt to synthesize a highly active superporous TiO₂, Ni_{1-x}O nanosponge and Ni_{1-x}O/TiO₂ composite nanocatalysts which are highly efficient in photocatalytic mitigation of organic azo dye pollutants as well as, can store high electrochemical energy for device scale application in supercapacitors.

Appendix I

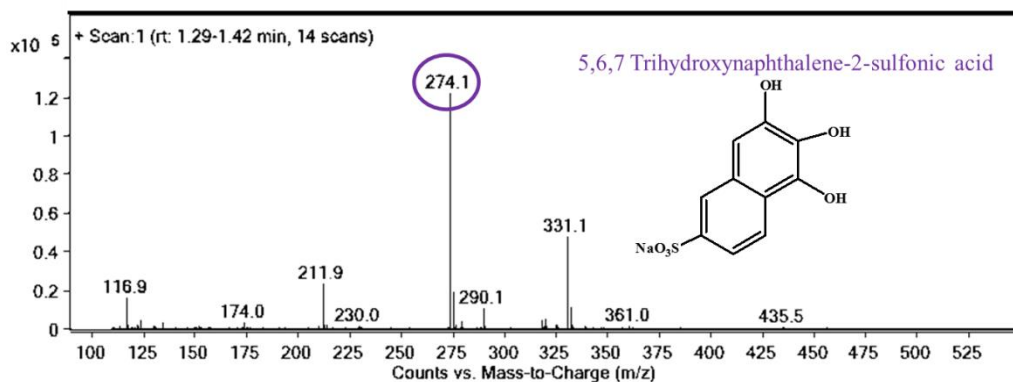
Mass spectra of Amaranth degradation products identified using LCMS analysis



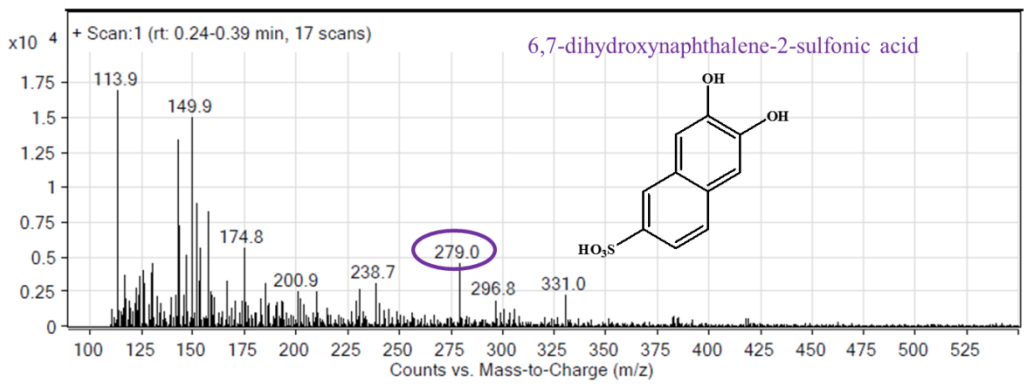
SF1: Peak corresponding to m/z = 370



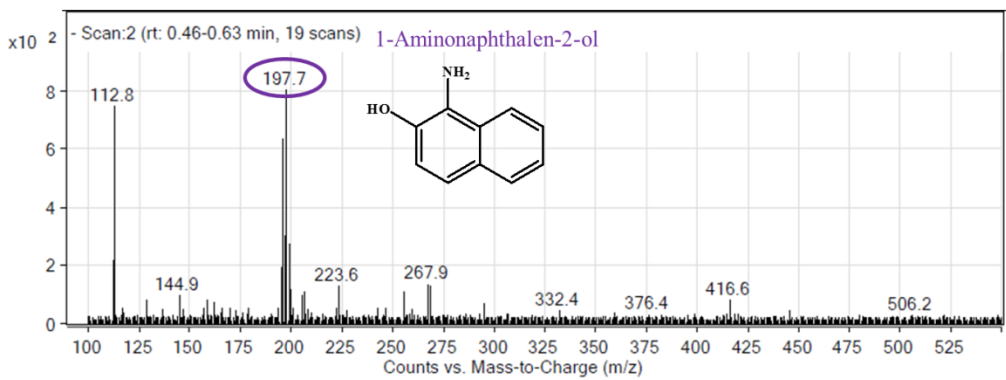
SF2: Peak corresponding to m/z = 406



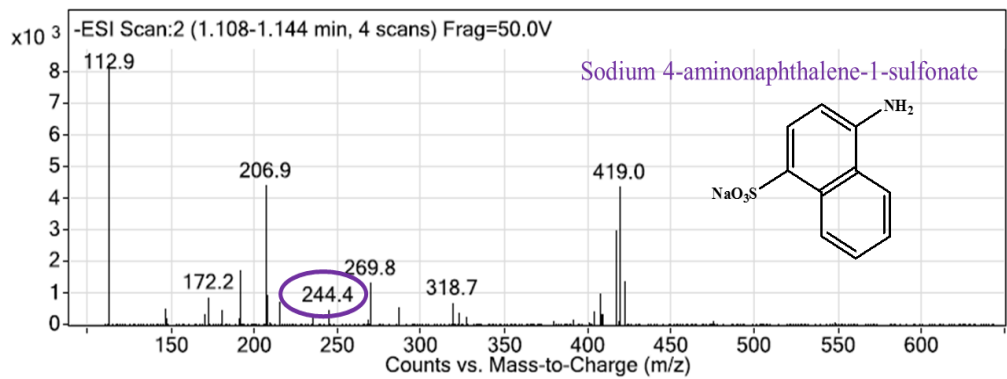
SF3: Peak corresponding to m/z = 274



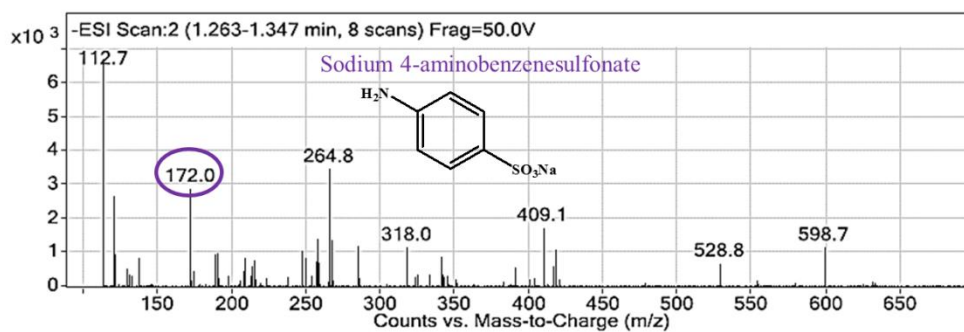
SF4: Peak corresponding to $m/z = 279$



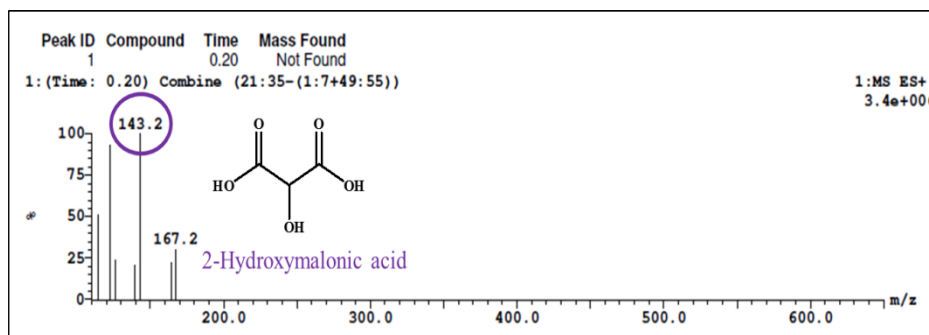
SF5: Peak corresponding to $m/z = 198$



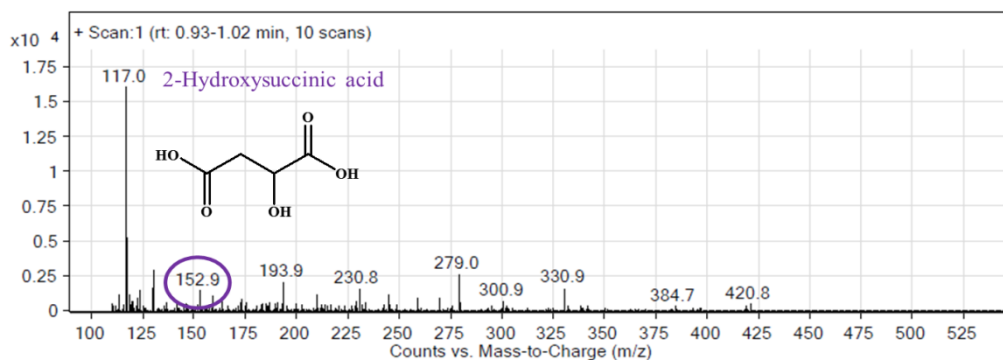
SF6: Peak corresponding to $m/z = 244$



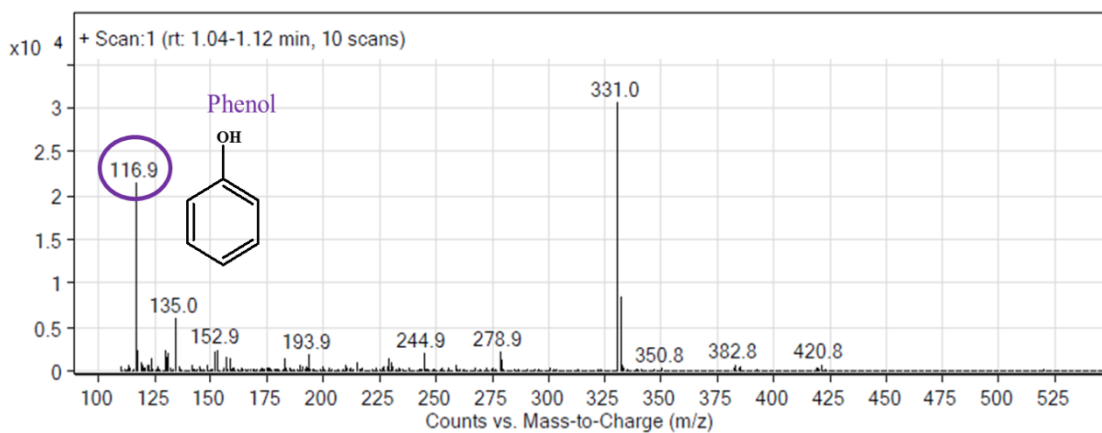
SF7: Peak corresponding to m/z = 172



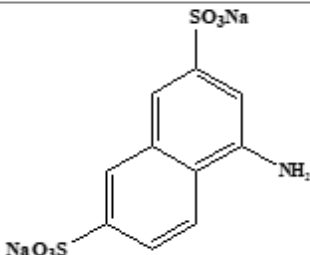
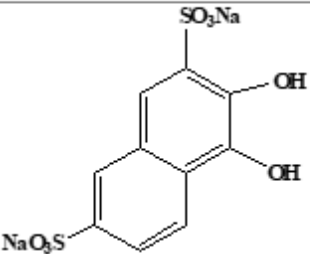
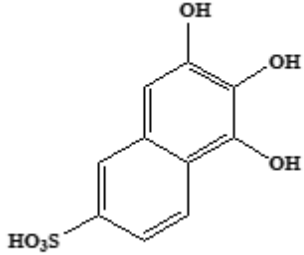
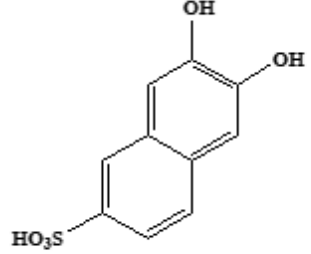
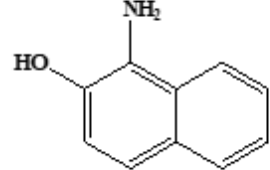
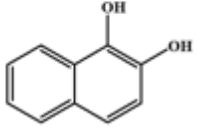
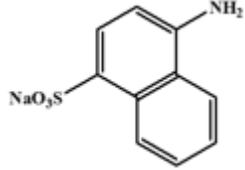
SF8: Peak corresponding to m/z = 143

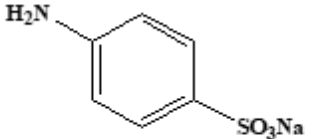
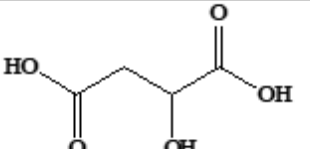
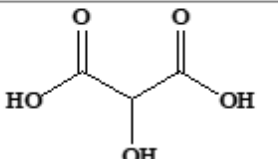
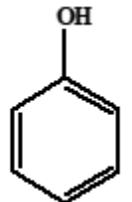


SF9: Peak corresponding to m/z = 152



SF10: Peak corresponding to m/z = 117

Product code	Mass Calculated	Mass obtained	Products
A1	347	[M+23] = 370	
A2	364	[M+CH3CN+H] = 406	
A3	256	[M+Na] = 274	
A4	240	[M+K] =279	
A'	159	[M+K] =198	
A'1	160	[M+H2O] =176	
B	245	[M-H] = 244	

B1	195	[M-Na] =172	
P1	134	[M+18] =152	
P2	120	[M+23] = 143	
P3	94	[M+23] = 117	

ST1: List of products of photocatalytic degradation of Amaranth dye.

Appendix II

List of publications:

Appended to thesis:

1. **A. P. Naik**, A. V. Salkar, M. S. Majik, **P. P. Morajkar***, Enhanced photocatalytic degradation Amaranth dye on mesoporous anatase TiO₂: evidence of C-N, N=N bond cleavage and identification of new intermediates **Photochemical Photobiological Sciences**, 2017, 16, 1126-1138. (IF = 3.982)
2. **A. P. Naik**, H. Mittal, V. S. Wadi, L. Sane, A. Raj, S. Alhassan, A. A. Alili S. V. Bhosale and **P. P. Morajkar***, Super porous TiO₂ photocatalyst: tailoring the agglomerate porosity into robust structural mesoporosity with enhanced surface area for efficient remediation of azo dye polluted waste water. **Journal of Environmental Management**, 2020, 258, 110029. (IF = 6.789)
3. **A. P. Naik**, A. V. Salkar G. D. J. Guerrero Pena, J. V. Sawant, G. Bharath, F. Banat, S.V. Bhosale and **P.P. Morajkar***, Facile synthesis of fibrous, mesoporous Ni_{1-x}O nanosponge supported on Ni foam for enhanced pseudocapacitor applications. **Journal of Materials Sciences**, 2020, 55, 12232-12248. (IF = 4.220)
4. **A. P. Naik**, J. V. Sawant, H. Mittal, A. A. Alili, **P. P. Morajkar***, Facile synthesis of 2D nanoflakes and 3D nanosponge-like Ni_{1-x}O via direct calcination of Ni (II) coordination compounds of imidazole and 4-nitrobenzoate: Adsorptive separation kinetics and photocatalytic removal of Amaranth dye contaminated wastewater, **Journal of Molecular Liquids**, 2021, 325, 115235. (IF = 6.165)
5. **P. P. Morajkar***, **A. P. Naik**, S. T. Bugde, B. R. Naik Photocatalytic and microbial degradation of Amaranth dye Surya N. Meena, Milind M. Naik (Eds.), *Advances in Biological Sciences Research: A Practical Approach*, Elsevier 2019, 327-357.

Other publications through sponsored research projects which provided research fellowship:

1. A. V. Salkar, **A. P. Naik**, V. S. Joshi, S. K. Haram and **P. P. Morajkar***, Designing a 3D nanoporous network: via self-assembly of WO₃ nanorods for improved electrocapacitive performance. *Crystal Engineering Communication*, 2018, 20, 6683–6694. (IF = **3.545**)
2. A. V. Salkar, **A. P. Naik**, S.V. Bhosale and **P. P. Morajkar***, Designing a rare DNA-like double helical microfiber superstructure via self-assembly of in situ carbon fiber-encapsulated WO_{3-x} nanorods as an advanced supercapacitor material *ACS Applied Materials Interfaces*, 2021, 13, 1288-1300. (IF = **9.229**)

Manuscript under preparation:

1. **A.P. Naik, P. P. Morajkar***, Enhanced supercapacitor performance of mesoporous Ni_{1-x}O/TiO₂ nanocomposites.

Appendix III

Participation and presentation at National & International conferences:

- 1) **A. P. Naik**, A. V. Salkar & **P. P. Morajkar**, Enhanced photocatalytic degradation of Amaranth dye on mesoporous anatase TiO₂: evidence of C-N,N=N bond cleavage and Identification of new intermediates (Poster), “Conference on Advances in Catalysis For Energy and Environment (CACEE-2018)” organized by Tata Institute of Fundamental Research (TIFR), Mumbai India on 10th -12th January 2018. (Poster No. 116)
- 2) **A. P. Naik**, A. V. Salkar & **P. P. Morajkar**, Temperature controlled synthesis of CuO loaded TiO₂ nanocatalyst for photocatalytic oxidation of benzyl alcohol (Poster), 21st “Worshop & Symposium on Thermal Analysis (Thermans-2018)” organized by Department of Chemistry Goa University, Goa, India on 16th -20th January 2018. (Poster No. E-9)
- 3) **A. P. Naik**, CO₂/O₂/Octane reactivity under reservoir conditions, “Workshop on Gas phase chemistry of hydrocarbon oxidation” organized by Physikalisch-Technische Bundesanstalt Germany on 14th -19th May 2018. (Oral)
- 4) **A. P. Naik**, A.V. Salkar S. V. Bhosale & **P. P. Morajkar**, Photocatalytic degradation of Amaranth dye using super porous TiO₂, “Two- day workshop on Material Science between University of Porto, University of Coimbra and Goa University” organized by School of Chemical Sciences Goa University, Goa, India on 18th-19th November, 2019. (Poster)
- 5) **A. P. Naik**, A. V. Salkar, S. V. Bhosale & **P. P. Morajkar**, Super porous TiO₂ photocatalyst with enhanced surface area for efficient remediation of azo dye polluted wastewater, “New Frontiers In Chemistry-From Fundamentals To Applications (NFCFA-2019)” organized by Department of Chemistry BITS Pilani, Goa, India on 20th-22nd December, 2019. (Poster No.74)

- 6) **A. P. Naik**, A. V. Salkar, S. V. Bhosale & **P. P. Morajkar**, Super porous TiO₂ photocatalyst with enhanced surface area for efficient remediation of azo dye polluted wastewater, “Advanced Materials for Renewable Energy and Sustainable Environment (AMRESE -2020)” organized by Govt. College of Arts, Science & Commerce Khandola, Marcela, Goa, India on 31st January -1st February 2020. (Poster No. P-3).
- 7) Participated in conference on “Advances in Materials Science and Applied Biology (AMSAB 2019)” organized by Narsee Monjee Institute of Management Studies (NMIMS), Mumbai, India on 8th-10th January 2019.
- 8) Participated in National Conference on “Advancement in Science and Technology (NCAST 2019)” organized by Govt. College of Arts, Science & Commerce Khandola, Marcela Goa India on 9th February 2019.
- 9) Participated in Virtual Conference on “Materials for Energy Harvesting and Catalysis” organized by Tata Institute of Fundamental Research (TIFR), Mumbai, India and Indian Institute of Science Education and Research (IISER), Kolkata, India on 1st-3rd May 2020.
- 10) Participated in National Conference (Virtual) on “Nanomaterials for Environmental Applications” organized by Post-Graduate Department of Chemistry, P.E.S’s R. S.N. College of Arts and Science, Framagudi, Ponda Goa, India on 28th-29th December 2020.
- 11) Participated in International Virtual Conference on “Advances in Molecular Materials Research (AMMR 2021)” organized by Visva-Bharati, India, Jadavpur University, India and Osaka University, Japan on 3rd-5th February 2021.
- 12) Participated in State level web based lecture series on “Insights of Instrumentation & Characterization techniques” organized by Cluster Research Centre, PG & UG Department of Chemistry, Government College of Arts Science and Commerce Khandola Marcela-Goa, India on 10th May and 16-17th June 2021.

- 13) Participated in International Conference (Virtual) on “Solution Grown Crystal and Their Useful Applications (SGCA-2021)” organized by SSN Research Centre, SSN Institutions (Autonomous) and Indian Association for Crystal Growth (IACG) Tamil Nadu, India on 13th-15th September 2021.

- 14) Participated in Two day Industry-Academia International Symposium (Virtual) on “Fuels for Environmental Sustainability” organized by Department of Chemistry, Government College of Arts, Science and Commerce, Khandola Goa, India on 8th- 9th October 2021.

- 15) Participated in International Webinar Series on “Two-Dimensional Semiconductor Applications for Green Energy (2D-SAGE)” organized by School of Chemical Sciences Goa University, Taleigao Plateau, Panaji, Goa, India on 10th November 2021.